Theoretical and Experimental Investigation on the Use of Surface Acoustic Wave Sensors for Evaluating the Adhesion of SU-8 Thin Films

by

Mohamed Mahmoud Taher EL Gowini

A thesis submitted in partial fulfillment of the requirements for the degree of

Doctor of Philosophy

Department of Mechanical Engineering
University of Alberta

Abstract

This research investigates the use of a SU-8/AlN/Si SAW sensor for evaluating the adhesion of SU-8 thin films. A theoretical model is developed to plot the wave dispersion profile for the SU-8/AlN/Si configuration. A spring interface model is utilized to represent the SU-8/AlN interface using a series of massless springs with stiffness K (N/m^3). The value of the interface spring stiffness K is changed to represent different levels of SU-8 adhesion. The wave dispersion profiles for the intermediate adhesion levels are plotted using the theoretical model. The change in wave velocity due to the change in adhesion of the SU-8 thin film is evaluated. The sensitivities of different configurations of the SU-8/AlN/Si SAW sensors are investigated. Four SAW sensor designs are selected to evaluate the adhesion of the SU-8 thin film. The four SAW sensors operate in the frequency range of 84-208MHz. A process flow for fabricating the SAW sensors at the University of Alberta micro-and nanofabrication facility "nanofab" is developed. The fabricated sensors are packaged using wire bonding to allow measurement of their frequency responses using a Vector Network Analyzer.

For each of the four SAW sensor designs two sensor configurations will be developed. In one configuration the SU-8 film will be patterned on top of a thin gold film on the surface of the AlN/Si layers and in the second configuration the gold film will be coated with an Omnicoat layer prior to patterning the SU-8 film. Omnicoat is an adhesion promoter that is widely used to improve the adhesion of SU-8 to gold. The frequency responses from both sensor configurations are measured for each of the four SAW sensor designs and the frequency shift is evaluated. The frequency shift illustrates the change in adhesion of the SU-8 film with and without omnicoat. The phase velocity values also shift to a higher value for the sensor configurations without omnicoat. As the adhesion of the SU-8 film drops in the absence of omnicoat the stresses transferred to the SU-8 layer drop and

accordingly the wave propagation is concentrated in the AlN/Si layers, which have a higher wave velocity than SU-8. However, in the presence of omnicoat the adhesion of the SU-8 layer improves and the surface acoustic wave propagates in the SU-8 layer, which leads to a drop in the phase velocity.

The theoretical model is used to find the equivalent interface spring stiffness values for the two cases of SU-8 adhesion i.e. with and without omnicoat. This is accomplished by curve fitting the dispersion curves to the phase velocity values for from both sensor configurations. The equivalent interface spring stiffness values are found to be 8.0992×10^9 N/m^3 and 7.9492×10^9 N/m^3 for the SAW sensors with omnicoat and without omnicoat, respectively. These values indicate that when omnicoat is used as an adhesion promoter for SU-8 the interface spring stiffness increases due to the improved adhesion. However, without omnicoat the adhesion of the SU-8 layer drops, which corresponds to the lower interface spring stiffness value.

Preface

The research work related to modeling the wave dispersion characteristics of the three configurations of the SU-8/AlN/Si SAW sensor i.e. free surface, perfect bond and spring interface and the work related to investigating the sensitivitiy of the different sensor configurations, which are included in Chapter 3 have been published in EL Gowini, M. M. and Moussa, W. A. "Theoretical and Experimental Investigation on the use of a Surface Acoustic Wave Sensor for SU-8 Thin Film Adhesion Characterization", *IEEE Sensors Journal*, 2015, 15(8): 4667-4676. This publication also includes the evaluation of the adhesion of the SU-8 thin film, which is included in Chapter 6.

The research work related to the microfabrication and packaging of the SAW sensor, which are included in Chapter 4 and the frequency response measurements of the SAW sernsors, which are included in Chapter 6 have been published in EL Gowini, M. M. and Moussa, W. A. "Evaluating the Adhesion of SU-8 Thin Films using an AlN/Si Surface Acoustic Wave Sensor", *Journal of Micromechanics & Microengineering*, 2015; 25: 035031. This publication also includes the analysis of the frequency and velocity shifts from the measurements of the SAW sensors, which are included in Chapter 6.

The research work related to calculating the stress at the SU-8/Aluminum Nitride interface, the change in the stress field with the wave dispersion profile at nultiple values of the interface spring stiffness and the contour plots of the stress and displacement fields in the SU-8 layer for different values of the interface spring stiffness, which are included in Chapter 3 and Chapter 6 have been submitted in a manuscript for publication, EL Gowini, M. M. and Moussa, W. A. "Investigating the change in surface acoustic wave velocity due to the change in adhesion of a SU-8 thin film using a SU-8/AlN/Si SAW sensor", *International Journal of Adhesion & Adhesives,* 2015 (submitted). The manuscript is currently under review.

I was responsible for the theoretical modeling, microfabrication, packaging and testing of the SAW sensors as well as analyzing the results and composition of the published manuscripts. Dr Walied A. Moussa is the supervising author for this research work. In addition, the theoretical modeling, packaging and the frequency response measurements of the SAW sensors were conducted using the resources available in Dr Moussa's MEMS/NEMS Advanced Design Lab.

*To my parents whose love, support and encouragement made me the man
I am today and whom I owe everything to*

&

To my wonderful wife who taught me the meaning of unconditional love

Acknowledgments

First and foremost I am grateful to God for giving me everything I needed to reach this far with my life. I hope that I have made the best use of the opportunities he bestowed upon me.

I sincerely thank my supervisor and mentor Dr Walied Moussa for so many things. It has been a long journey and without his patience, encouragement and support I certainly would not have been able to continue this difficult path. I would also like to thank him for providing all the resources to complete this work with the highest quality. I would like to thank my supervisory committee memebers, Dr Edmond Lou and Dr Ming Zuo for their insights and constructive criticism that were vital for the completion of this work.

I would also like to thank my colleagues at the MEMS/NEMS Advanced Design Lab for their continuous encouragement, support and insights. Special thanks are due to my dear friend Dr Hossam Gharib who has always listened to me and supported my throughout this journey. I would also like to thank my dear friend Ahmed Badr for his encouragement especially during the final phase of this research. I would also like to thank Dr Ryan Saunders, Dr David Benfield, Dr Jonathan leuke, Dr Else Gallagher, Dr Mehdi Rezaisaray, Aliaa Nabih, Suzan EL Shaer, Shichao Yue, Mohamed Haridy and Amr Balbola for their very useful insghts and feedback especially during the group meetings.

I would like to thank all the staff members at the University of Alberta micro and nanofabrication facility for their support. I am truly grateful to Les Schowalter who has helped me significantly in developing a reactive sputtering process for Aluminum Nitride.

I would like to thank the faculty memebers of the mechanical engineering department at the University of Alberta. Their knowledge and excellent teaching skills have increased my intellectual curiosity and made the coursework phase a highly rewarding experience. I would also like to thank the administrative team in the department, especially Gail Dowler.

I would like to thank the Auto21 Network of Centers of Excellence, the Canadian National Science and Engineering Research Council (NSERC), the Alberta Government and CMC Microsystems for their financial support.

Table of Contens

List of Tables

List of Figures

xvii

List of Symbols

α_j :   Relative wave amplitude

AE: Acoustic emission

A_o: Amplitude of the incident transverse wave

A_i: Amplitude of the reflected longitudinal wave

A_r: Amplitude of the reflected transverse wave

AlN: Aluminum Nitride

$BaTiO_3$:   Barium Titanate

b: Wave decay parameter

c_i: Wave velocity of the incident wave

c_r: Wave velocity of the reflected wave

c_L: Velocity of the longitudinal wave

c_T: Velocity of the transverse wave

C_n: Weighting factor

c_{ijkl}:   Stiffness constant

CP: Cyclopentanone solvent

DI: De-ionized water

$\bar{d}$:   Propagation direction

D_i: Electric displacement field

δ_{ij} :	Kronecker delta function
E_j:	Electric field component
e_{ijk}:	Piezoelectric stress coefficients
ε_{ij} :	Dielectric permittivity constant
EDF:	Forward Directivity error
EDR:	Reverse Directivity error
ESF:	Forward Source Match error
ESR:	Reverse Source Match error
ERF:	Forward Reflection Tracking error
ERR:	Reverse Reflection Tracking error
ELF:	Forward Load Match error
ELR:	Reverse Load Match error
ETF:	Forward Transmission Tracking error
ETR:	Reverse Transmission Tracking error
EXF:	Forward Crosstalk error
EXR:	Reverse Crosstalk error
F:	Force density per unit volume
f_o :	Center frequency
G:	Fracture energy
G_0:	Refers to the work of adhesion and work of cohesion

γ_1:	Surface energy of phase 1
γ_2:	Surface energy of phase 2
γ_{12}:	Interfacial surface energy of between phases 1 and 2
Γ_{ij}:	Christoffel constants
h:	Film thickness
h_{AlN}/λ:	Normalized AlN film thickness
HAR:	High Aspect Ratio
IDT:	Inter-digital electrodes
k:	Wavenumber
K:	Interface spring stiffness
λ:	Wavelength
LLW:	Leaky Lamb Waves
LPCVD:	Low Pressure Chemical Vapor Deposition
ν:	Poisson ratio
MEMS:	Micro-Electromechanical Systems
MIBK:	Methyl iso-butyl ketone
N_p:	Number of electrode pairs
NDT:	Non-destructive testing
NEMS:	Nano-Electromechanical Systems
ψ:	Energy absorbing processes in interface fracture

PZT:	Lead Zirconate Titanate
PCB:	Printed Circuit Board
$\overline{P}$:	Propagation vector
φ:	Electric potential
PGMEA:	Propylene glycol methyl ether acetate
PAG:	Photo-acid generator
PEB:	Post-exposure bake
ρ:	Density
RIE:	Reactive Ion Etch
SAW:	Surface Acoustic Wave
S_{11}:	Forward reflection scattering parameter
S_{21}:	Forward transmission scattering parameter
S_{12}:	Reverse transmission scattering parameter
S_{22}:	Reverse reflection scattering parameter
Si:	Silicon
SH:	Shear Horizontal wave
SAM:	Scanning acoustic microscope
SIALON:	Silicon Alumina Nitride
S_{kl}:	Mechanical strain components
t:	Time
ϑ_i:	Angle of the incident wave

ϑ_r :   Angle of the reflected wave

ϑ_{cr} :   Critical incident angle for transverse wave

TiN: Titanium Nitride

T_{ij}:   Stress component on plane i in direction j

u_i: i^{th} displacement component

v: Phase velocity

v_R :   Rayleigh wave velocity

VNA: Vector Network Analyzer

W_A: Work of adhesion

W_C: Work of cohesion

XRD: X-Ray Diffraction

ZnO: Zinc Oxide

CHAPTER 1.   INTRODUCTION

The earliest mankind must have been baffled by the manifestations of joined materials in nature. Since the dawn of history mankind has been involved in joining dissimilar materials to build useful objects such as projectile points hafted in to a spear or arrow and the use of natural resins to seal woven baskets for carrying water or to repair broken pottery vessels. The earliest adhesives used by mankind came from nature such as animal and fish glue, natural fibers and birch resin and pitch. With the passage of time and the discovery of new materials and technology numerous methods were developed for joining materials such as welding, brazing, riveting and bolting. Adhesives based on synthetic polymers were developed in the early 20th century for applications that required more durable and load bearing joints, which cannot be achieved with natural adhesives. The wide range of synthetic adhesives available has been used to join a wide range of material combinations such as metal-metal, metal-plastic, metal-composite, plastic-plastic and composite-composite, which facilitates the creation of structures and products with more tailored properties for specific applications. Today, it is difficult to imagine a product that does not use some kind of adhesive and/or sealant.

Joining materials creates structures with improved functionality and their properties combine the advantages of each individual material. Joining also facilitates creating more intricate and/or larger structures in a timely and cost efficient manner. While the joining process offers great possibilities and increases the functionality of bonded structures, the failure of the joint can be catastrophic. There are numerous factors that can affect the quality of the bonded structure during operation such as moisture content, temperature or exposure to aggressive chemical attack, fatigue or aging of the structure. Any of these factors can lead to significant joint degradation and/or failure, which will deteriorate the integrity of the structure and diminish its functional characteristics. Therefore, inspection of bonded joints is an essential procedure to ensure the reliability and durability of the bonded structure. Any damage to the bonded joint can be catastrophic since it can lead to the damage of the entire structure. Replacing the damaged components can be both time consuming and

expensive. Therefore, regular monitoring of the bonded structures will certainly prevent failure and would allow for sufficient time to take precautionary measures.

A wide range of adhesion monitoring techniques has been developed to accommodate the numerous material properties of bonded structures and their applications. Not all materials and bonded structures can be used with any kind of test. Selecting a specific test to monitor the adhesion of a structure involves the following considerations; cost, time constraint, test applicability and accessibility to the structure and whether to use a destructive or nondestructive technique. Therefore there is no test that is suitable for all applications. Discretion is required when selecting a test to investigate the adhesion of bonded structures. As will be illustrated in the following chapter, adhesion monitoring techniques can be divided into two main groups, destructive and non-destructive. Destructive techniques involve applying a force to the bonded structure and analyzing the resulting failure that took place. Some of the widely used destructive testing techniques include peel, scratch, nano-indentation and four point bending tests. A load needs to be applied to the bonded structure to induce damage. The different techniques differ in their application of the load to the bonded structure. Non-destructive techniques involve investigating the reliability of the bonded structure without damaging it. The structure can continue to be used after non-destructive testing. Some of the non-destructive testing techniques include visual inspection, x-ray imaging, acoustic emission and eddy currents. The most commonly used non-destructive testing technique is ultrasonic inspection. Ultrasonic techniques have been used for adhesion monitoring for a very long time. There are numerous ultrasonic techniques, which will be discussed in the following chapter. The main advantage of these techniques is that they allow the structure to be reused and can be applied when the structure is in service.

1.1 Motivation

The significant development in the field of Micro/Nanoelectromechanical system (MEMS/NEMS) design and microfabrication in recent years has lead to a wide range of new applications that are revolutionizing numerous industries. The small size, low cost, reliability and durability of MEMS/NEMS devices are among the most desirable features that have led to their vast range of applications. The use of MEMS/NEMS devices in structures and components has led to the development of smarter structures i.e. structures that provide users with access to more in depth information that would allow them to make more informed decisions. Some of these exciting

applications include implanting miniature sensors in the human body to allow surgeons to monitor all parameters of interest *in-vivo*. Developing a MEMS sensor that monitors the adhesion between two bonded structures would certainly have numerous potential applications. The reduced size of these sensors allows them to be included within the structures, hence making them "smarter" and facilitating their inspection.

1.1.1 *Thin Film Applications*

Applications utilizing thin film technology are spreading across various industries. Thin film applications include protective coatings for magnetic storage devices [1], automotive components [2] and cutting tools [3, 4] to improve hardness, corrosion and wear resistance and also for decorative purposes [5]. Thin films are also used as active components in sensors for analyte detection [6], micro-pumps [7] and micro-actuators [8]. The significant development in thin film deposition technologies has led to the widespread use of thin film applications. Thin film deposition technologies include spin-coating, physical vapor deposition, chemical vapor deposition, electro-chemical deposition and pulsed laser deposition. Due to the wide range of thin film applications there is a significant interest in monitoring the properties of thin films such as their crystal orientation, stiffness constants, density, thermal conductivity, thickness and chemical composition. Degradation in the functional properties of thin films reduces the yield and reliability of microelectronic devices and can lead to failure and damage of components and/or systems. The ability to deposit a wide range of materials as thin films on various substrates with sufficient adhesion is certainly one of the main factors that increased the possibilities of thin film applications. Adhesion is a vital characteristic of thin film technology that has led to the wide range of thin film applications. It significantly affects the reliability and durability of components and structures utilizing thin film technology.

There are many reasons for thin film delamination and de-bonding. Some of these occur during the fabrication and processing of the thin film structure or during the service period. Stress buildup during the microfabrication of the thin film device or structure is classified as either intrinsic stress or thermal stress [9-11]. Intrinsic stress can arise due to the lattice mismatch between the film and the underlying substrate during fabrication, which leads to crystallographic defects and stress build-up. Thermal stresses can also occur due to the difference in coefficient of thermal expansion between the film and the underlying substrate. After a high deposition process as the film and substrate cool

down the difference in thermal expansion coefficients restricts the expansion and contraction of the film and substrate, which leads to stress build-up. The residual stress that builds-up in the thin film can be high enough to cause poor adhesion by introducing interface cracks and interface delamination [12-14]. In addition to the intrinsic and thermal stresses, exposure of the thin film structure to harsh environmental conditions during service can lead to thin film delamination and de-bonding. High temperature and moisture often lead to thin film de-bonding and cracking [15, 16].

1.1.2 *Embedded Sensors' Applications*

Due to the reduced size of MEMS sensors they possess a major advantage, which is the ability to embed them in structures. There is a huge potential for embedded MEMS sensors in biomedical applications. Several researchers are currently working on developing MEMS sensors to monitor the adhesion at the bone-implant interface. This would lead to more tailored prescriptions, accurate assessments and early prediction of possible complications. According to Benzel *et al.* [17] each patient would become a biomechanics laboratory. Various researchers have utilized bio-implantable MEMS sensors for *in-vivo* analyses. Ferrara *et al.* [18] investigated the biocompatibility and wound healing behavior of bone tissue by implanting a piezoresistive MEMS sensor in an animal spine. Alfaro *et al.* [19] and Hsieh *et al.* [20] utilized piezoresistive MEMS sensors to measure the stresses at the bone implant interface in hip and knee implants respectively. Both approaches infer healing progression from the stress measurements since it is expected that the loads measured by the sensor will increase as healing progresses. The proposed MEMS sensor in this study has the potential to be embedded at the bone-implant interface to monitor bone-healing progression. As the bone properties strengthen during healing and the bone attaches firmly to the implant surface, the sensor would detect these changes with high sensitivity. Figure 1-1 illustrates a prosthetic implant inserted in a human femur and the bone-implant interface is enlarged to show where the MEMS sensor would be placed.
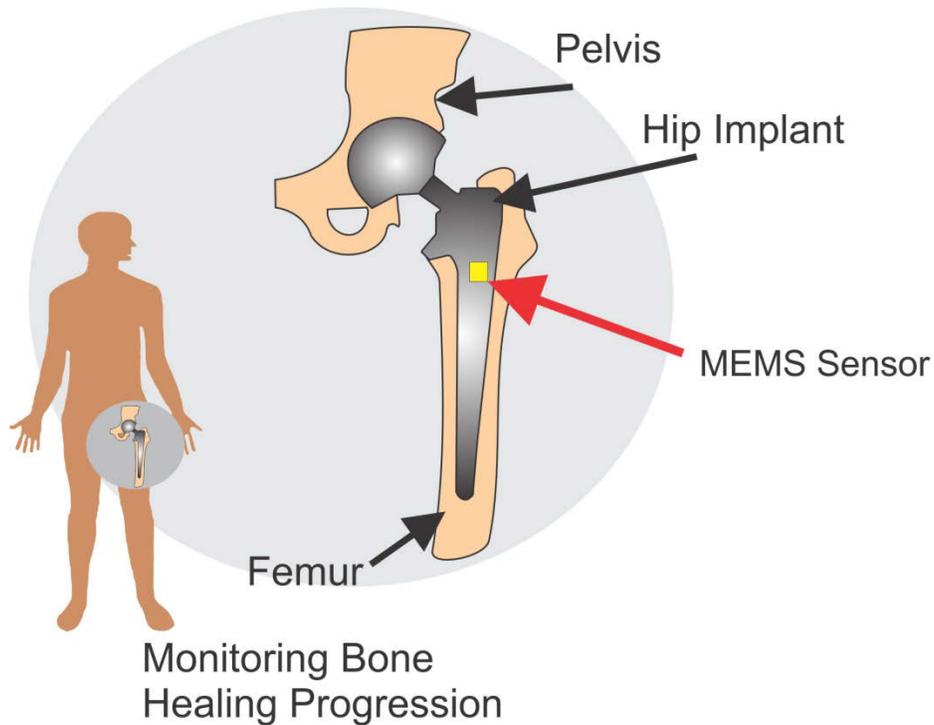
Figure 1-1: Potential application of the proposed MEMS sensor in monitoring bone-healing progression

Bonded patches are a common repair solution for cracked structures and are widely used to repair aircraft skin. Adhesive bonded patches have numerous advantages over mechanically fastened bonded patches such as their increased strength and fatigue life, ease of installation, reduced cost of installation and reduced stress concentration [21]. However, adhesively bonded patches require adhesive bond inspection since adhesive degradation is a common problem, which sometimes leads to de-bonding of the patch. Therefore an accurate inspection technique that can monitor the changes in adhesive bond pr operties and allows early detection of the bond de gradation would certainly increase the reliability of bonded patches. Various sensing technologies have been developed to monitor the degradation of adhesives in bonded patch applications. Some of the developed sensors include optical fiber sensors [22, 23], piezoelectric sensors [24] and electromechanical impedance sensors [25]. These sensors are macro-size and require long installation periods, do not offer quick measurement results and are costly. However, using an array of MEMS sensors implanted at the adhesive structure interface as illustrated in Figure 1-2 would lead to more accurate results, allow early detection of bond degradation, allow more frequent inspection and reduce cost. The sensors

can monitor the changes in material properties of the adhesive, the change in adhesive strength over time and provide a more accurate assessment of the bonded patch reliability.
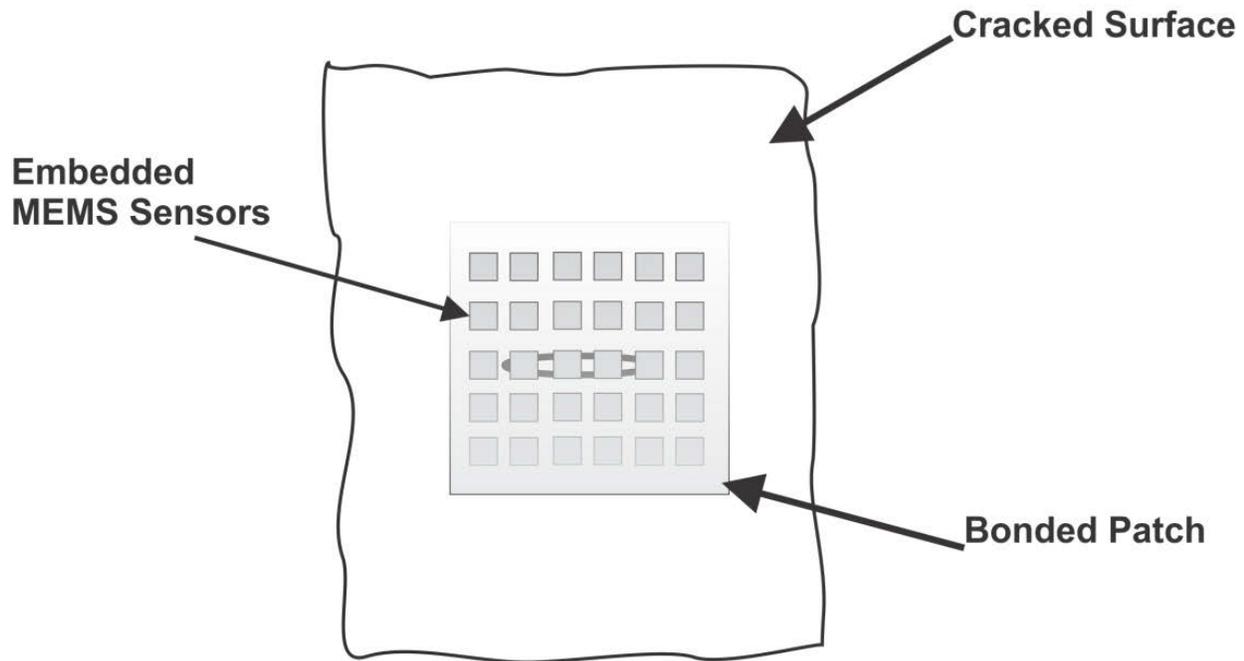
Figure 1-2: Illustration of the potential application of embedded MEMS sensors in a bonded patch

1.2 Research Objectives

This research aims at developing a Surface Acoustic Wave (SAW) sensor that can evaluate the adhesion of a thin SU-8 film. In order to achieve this goal, several phases need to be successfully accomplished. The following are the objectives of this research:

1. Develop a theoretical model that calculates the wave dispersion profile for the SAW sensor. Utilize the interface spring boundary condition to change the adhesion of the SU-8 film on the surface of the SAW sensor. Investigate the effect of changing the adhesion of the SU-8 film on the wave dispersion profile. This will validate the hypothesis that the proposed SAW sensor can be used to evaluate the adhesion of the SU-8 film. Different configurations of the SAW sensor will be investigated to select the designs with highest sensitivity. Finally, due to the intermediate adhesion level of the SU-8 film the stresses generated will also be calculated using the theoretical model. Understanding the change in the stress field as a result of the change in adhesion of the SU-8 film will provide a

more in-depth understanding of the change in the wave velocity due to the change in adhesion of the SU-8 film.

2. A process flow for the SAW sensor will be developed using bulk microfabrication techniques such that the sensor can be developed at the University of Alberta micro- and nanofabrication facility "Nanofab". One of the main objectives at this stage is to select a piezoelectric material that can be successfully deposited as a thin film using the deposition techniques available at the nanofab. Once this material is selected a recipe for depositing it as a thin piezoelectric film would be developed. The piezoelectric properties of the thin film will also be investigated using x-ray diffraction (XRD) techniques to ensure that the film adopts the piezoelectric property. Several microfabrication runs will be carried out at the nanofab until a reliable and repeatable process can be used to develop operational SAW sensors that can be tested successfully. Four designs of SAW sensors will be fabricated and for each design two sensor configurations will be fabricated. The two SAW sensor configurations will represent different levels of adhesion for the SU-8 film.

3. Testing the SAW sensors to investigate the change in SAW velocity due to the change in adhesion of the SU-8 film. The scattering parameters of the SAW sensors will be measured using a vector network analyzer. For each design of the SAW sensors the frequency response (S_{21} parameter) from both configurations will be measured and compared. The shift in the center frequency values from both configurations of each of the four SAW sensors will be used as an indicator of the change in adhesion. The center frequency values will be used to calculate the SAW wave velocities for both configurations of each design. Therefore, the change in wave velocity due to the change in adhesion of the SU-8 film for the four SAW sensor designs will be determined.

4. Upon successfully determining the velocity values for both configurations of the four SAW sensor designs, the theoretical model will be used to find the dispersion curves that best fit the experimentally determined wave velocities. This will provide both states of SU-8 adhesion with quantitative values that corresponds to the adhesion level of the SU-8 film.

1.3 Thesis organization

This thesis illustrates the methodology implemented to achieve the goals described above. For each of the different phases of this research the underlying background will be presented as well as the steps taken to achieve the desired objective. The results of each phase of this research will be presented in the corresponding chapter. This thesis consists of seven chapters and the contents of each chapter are described below.

Chapter 1 presents an introduction to this research project and illustrates the motivation for the current research study. The need for a MEMS based sensor for monitoring the adhesion of thin film structures is presented. In addition, some of the potential applications for adhesion characterization using an embedded micro sensor are also illustrated.

Chapter 2 presents an introduction to adhesion and the different adhesion theories. It also presents a literature review to some of the non-destructive adhesion testing techniques. It then focuses on the adhesion techniques for thin films; both destructive and non-destructive. Finally, it presents the latest techniques for thin film adhesion characterization. These are MEMS based techniques that characterize the adhesion of thin films destructively.

Chapter 3 presents the theoretical background for acoustic wave propagation in isotropic, anisotropic and piezoelectric layers. The theoretical model for calculating the wave dispersion profile for the SAW sensor is presented. The calculated dispersion profiles are presented for several configurations of the SAW sensors. In addition, the effect of changing the adhesion of the SU-8 thin film on the surface of the sensor on the wave dispersion profile is also presented. The sensitivity of different configurations of the SAW sensors to the change in adhesion of the SU-8 film is also presented. Finally, the stresses generated in the SU-8 film at different adhesion levels of the SU-8 film are calculated and plotted.

Chapter 4 presents the microfabrication process for the SAW sensor. Background information on the chemical structure of SU-8, its material properties and processing techniques are presented. The piezoelectric thin film used in the SAW sensor for excitation of acoustic waves is presented in terms of its crystal structure, material properties and deposition techniques. Reactive sputtering is discussed in detail since this is the deposition technique used in this study to deposit the thin piezoelectric film. In addition, background information on x-ray diffraction is presented since this

technique is used to characterize the crystal structure of the thin piezoelectric film. The XRD plot for the piezoelectric film is illustrated. Finally, wire bonding of the SAW sensor is discussed since this is the packaging technique implemented in this study for the SAW sensors.

Chapter 5 presents the experimental set-up used for measuring the frequency response of SAW sensors using a vector network analyzer (VNA). The operating principle of SAW sensors using inter-digital electrodes is presented. This is followed by a detailed discussion of the vector network analyzer architecture and calibration technique. Finally, background information on the scattering parameters of SAW sensors is presented and the measurement of the scattering parameters of a sensor is presented for illustration.

Chapter 6 presents the testing of the SAW sensors for evaluating the adhesion of SU-8 films. The scattering parameters of both configurations for each of the four SAW sensor designs are presented. The results of the frequency response measurements are plotted as well as the SAW velocities, which were calculated from the center frequency values. The shifts in the velocity values due to the change in SU-8 adhesion are plotted. The curve fitting of the theoretical dispersion curves to the experimental velocity values are illustrated. Finally, the stress and displacement fields generated in the SU-8 layer at different levels of adhesion are plotted.

Chapter 7 presents the conclusions of this research study as well as the proposed future work.

CHAPTER 2.   LITERATURE REVIEW

2.1 Overview

This chapter starts by defining adhesion followed by a discussion of the four different theories of adhesion currently available. Some of the non-destructive techniques for investigating the adhesion of bonded structures are then introduced and a literature review illustrating the application of these techniques is presented. The non-destructive techniques for investigating the adhesion of thin film structures and components are also presented. Finally, the latest developments in MEMS based adhesion characterization techniques are introduced.

2.2 Mechanisms of Adhesion

The state in which two phases of different materials are held in contact via interfacial forces such that mechanical work needs to be applied to separate them is referred to as Adhesion. When the two phases in contact represent the same material this state is referred to as Cohesion. The force acting on a given area required to separate the two phases is the Adhesion Strength or Cohesion Strength and is measured in N/m^2. The energy required to form new surfaces is Surface Energy. When failure occurs at the interface of phase 1 and phase 2 the surface energy term corresponds to the work of adhesion W_A given by

$$W_A = \gamma_1 + \gamma_2 - \gamma_{12} \qquad\qquad \text{(2-1)}$$

where γ_1 and γ_2 are the surface energies of phases 1 and 2, respectively and γ_{12} is the interfacial surface energy between phases 1 and 2. When the adhesive failure occurs within one of the two phases the surface energy term is the work of cohesion and is given by

$$W_C = 2\gamma_1 \qquad\qquad \text{(2-2)}$$

Although W_A and W_C refer to the energy required to create two surfaces, the fracture energy G is always greater than the work of adhesion or work of cohesion (both will be referred to as G_0). This

is because interface fracture involves energy absorbing processes such as plastic and viscoelastic deformation. The relationship between G and G_0 is given by

$$G = G_0 + \psi \tag{2-3}$$

where ψ refers to the energy absorbing processes. Due to the distinction between G and G_0 two types of adhesion are defined. Fundamental adhesion is concerned with the mechanisms and forces involved in joining the components of an adhesive joint at the molecular scale. Practical adhesion refers to loading an adhesive joint can withstand until failure. Equation (2-3) refers to the relation between fundamental and practical adhesion. The discussion that follows pertains to fundamental adhesion.

Multiple theories exist to describe the interfacial phenomena that allow adhesion of two dissimilar materials. The reason for the presence of more than one theory is the different interactions that occur across an interface. The type of interaction that occurs along the interface of two adhered components depends on the chemical and physical structure of both materials. There are four widely accepted theories that describe the mechanisms of adhesion at an interface and it has been proven that more than one mechanism is involved in the adhesion of two dissimilar materials. A description of the mechanisms of adhesion will be presented.

2.2.1 *Physical Bonding*

This type of bonding arises due to the presence of secondary or van der waal forces, dipolar interactions, hydrogen bonding and other low energy forces. These bonding forces are weak and the bonding energy lies within 8-16 kJ/mol [26]. Physical bonding includes adsorption and electrostatic adhesion.

2.2.1.1 Adsorption Theory

This theory states that provided sufficient intimate inter-molecular contact exists between two layers adhesion will take place due to the surface forces acting between the atoms in both surfaces. The most common of such forces are the van der Waal forces, which are considered to be secondary bonds.

2.2.1.2 Electrostatic Theory

This theory states that when an adhesive and adherend with different band structures come in contact electrons will transfer across the interface to balance the fermi levels of both layers. A double layer of electric charges develops at the interface and the resulting electrostatic forces contribute significantly to the adhesion between both layers.

2.2.2   Chemical Bonding

A chemical bond is formed between the adhesive and the adherend when a chemical group in the adhesive forms a chemical bond with another compatible group in the adherend. The strength of the bond is proportional to the number of bonds and the type of bond that takes place. Interface failure must involve bond breaking. This type of bonding involves ionic, covalent and metallic bonding. Chemical bonding involves primary forces and the bond energy lies within 40-400 kJ/mol [26].

2.2.3   Diffusion or Interdiffusion

This type of bonding involves the diffusion of molecules across the interface from one layer to the other. The molecules must possess sufficient mobility and should be mutually soluble for diffusion to take place across the interface. The interface consists of a gradual change from one material into the other i.e. there is no distinct interface layer separating both layers. The bond strength is proportional to the number of molecules involved and the molecular entanglement that occurs at the interface [26].

2.2.4   Mechanical Bonding or Mechanical Interlocking

This type of bonding occurs when two surfaces are mechanically interlocked. When a liquid adhesive is spread on the surface of the adherend and penetrates the crevices and pores on the surface. An increased surface roughness improves the mechanical bonding. This type of bonding is a low energy bond even lower than chemical bonding [26].

2.3 Ultrasonic Techniques for Adhesion Characterization

Ultrasonic techniques are widely used for non-destructive inspection of the interfacial defects in adhesively bonded structures. Multiple transducer configurations can be implemented depending on the inspection requirements and accessibility to the structure being investigated.

- Pulse-Echo: when the transmitting transducer is used for transmitting the ultrasonic wave and detecting the reflected wave. This method is suitable for detecting the defects in the top adhesive bond line with high sensitivity.

- Through transmission: when two transducers are placed on the top and bottom surfaces of the adhesively bonded structures. One transducer is used for generating the ultrasonic wave and the second transducer receives the signal on the other side of the structure. This method can be used to detect the defects in the top and bottom adhesive bond lines. However, access to both ends of the structure may not be always possible.

- Pitch-catch: when two transducers are used for inspection of the adhesively bonded structure and placed on the same side of the adhesive bond but separated by a certain distance. One of the transducers is used for transmitting the ultrasonic wave and the second for receiving the wave.

The amplitudes of the reflection/transmission coefficients are measured during ultrasonic inspection and are determined by the mismatch in acoustic impedances at the interfaces of the structure being examined. The presence of defects, which may be assumed to contain air or other low density substance, will lead to a ch ange in the acoustic impedance, which affects the transmission/reflection coefficients. There are multiple techniques for displaying the amplitudes of the reflection/transmission coefficients from ultrasonic measurements [27, 28]. A-scans are the simplest form of illustrating the response of ultrasonic measurements, which show the amplitude of the reflection/transmission coefficients displayed with time. By shifting the time axis of the A-scan to be the y-axis and taking multiple measurements a cross-sectional image can be generated, which is referred to as a B-scan. Finally, scanning the entire surface of the structure and displaying the amplitude of the reflection/transmission coefficients an acoustical image can be generated and is referred to as a C-scan.

Ultrasonic inspection requires the use of a coupling agent since the acoustic impedance mismatch between a solid and air is significant, which can lead to significant attenuation of the ultrasonic wave [29]. Water is commonly used as the coupling agent; therefore the structure could be immersed in a water bath for conducting the test. There are four basic categories of ultrasonic inspection techniques [30]:

2.3.1   Ultrasonic reflection coefficient measurements at normal and/or oblique incidence

Normal/Oblique incidence inspection technique has been widely utilized in the inspection of adhesively bonded aluminum joints [30, 31], adhesively bonded automotive components [28, 32], composite adhesive joints [33, 34], dental cements [35] and in the inspection of contact between two surfaces [29, 36, 37]. This technique involves excitation of ultrasonic waves in in adhesively bonded structures using piezoelectric transducers. Normal incidence occurs when the transducer is placed parallel to the surface normal. Oblique incidence occurs when the transducer is inclined at an angle θ_i to the surface normal as illustrated in Figure 2-1. Oblique incidence inspection is more complicated than normal incidence inspection since multiple echoes are generated at the receiving transducer. This occurs due to the acoustic impedance mismatch at the interface of two media, which leads to wave reflection, refraction and mode conversion. However, oblique incidence inspection is widely utilized because shear waves generated have a higher sensitivity to interfacial properties [31]. For the case illustrated in Figure 2-1 the transducer generates a longitudinal wave in the water and when the wave encounters the water/adherend interface longitudinal and shear waves are generated at angles θ_L and θ_S; respectively in the adherend and longitudinal waves are reflected in the water. The first wave received by the receiving transducer is due to the reflection at the water/adherend interface. Four additional echoes will be received by the transducer due to the reflection at the adherend/adhesive interface. These are longitudinal-shear, shear-longitudinal, longitudinal-longitudinal and shear-shear waves. The longitudinal and shear waves generated in the adherend will propagate as longitudinal waves in water until they reach the receiver. Various studies have demonstrated the varying sensitivities of the reflected waves to the interfacial defects. The user should have an understanding of which mode to utilize for inspection of the structure and how to differentiate among the multiple reflected echoes.
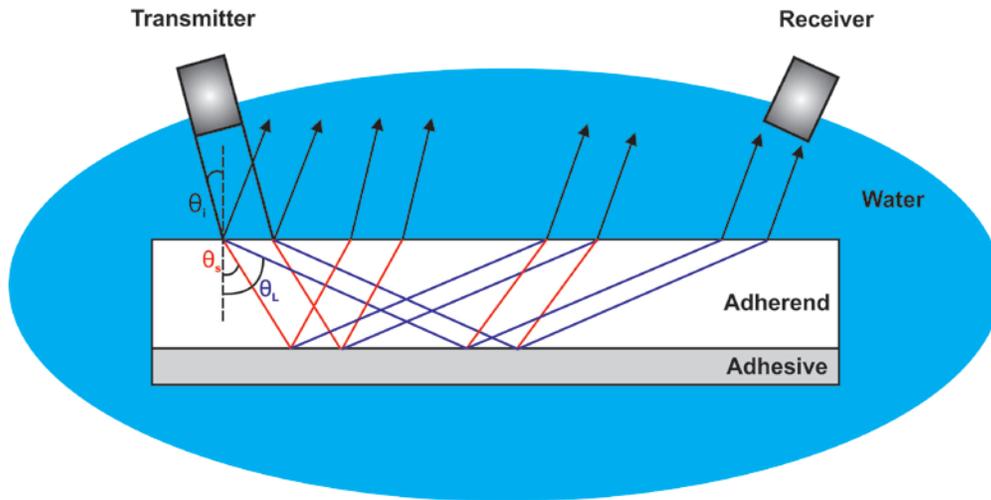
Figure 2-1: Schematic illustration of oblique incidence ultrasonic testing of an adhesively bonded structure.

2.3.2 *Lamb wave measurements*

Lamb waves are elastic waves that propagate in thin plates with traction free surfaces. Lamb waves result from the superposition of the longitudinal and shear waves that exist in a plate. The wave propagation characteristics of lamb waves is quite complex. The wave propagation characteristics depend on the angle of incidence, numerous modes of lamb wave propagation can exist and they are dispersive. Lamb waves are considered to be guided waves because their wavelength is comparable to the plate thickness and hence the wave is guided by both surfaces of the plate. As the frequency of the lamb wave changes, its wavelength also changes and the degree of confinement of the wave in the plate changes as well. This leads to the dispersive characteristics of lamb waves where the wave velocity changes with frequency. Lamb wave mods can be separated into two major groups; symmetric and anti-symmetric. Symmetric wave modes S_i, where $i = 0, 1, 2, 3, ..., n$ to designate the symmetrical mode number, generate a displacement field that is symmetrical about the median plane of the plate as illustrated in Figure 2-2. The antisymmetric modes A_i generate a displacement profile in the plate that is antisymmetric about the median plane of the plate i.e. both plate surfaces are displaced in the same direction Figure 2-2.

Figure 2-2: Symmetric and antisymmetric lamb wave modes

The particle displacement in symmetric mode wave propagation is predominantly in-plane radial displacement; therefore symmetric modes are referred to as compressional modes. However, in the antisymmetric wave modes the particle displacement is primarily normal to the plate surface and these modes are referred to as flexural modes. When both modes are excited under the same conditions the magnitude of the particle displacement of the symmetric modes is normally less than that for the antisymmetric modes [38].

Lamb waves are widely used for damage detection and inspection of components since they possess many desirable features such as the ability to propagate a wide range of modes, which allows selecting the mode that is most sensitive to the damage under inspection, the ability to inspect structures while maintaining their coating and insulation, the ability to monitor long structural components with a single measurement and the high sensitivity of lamb waves to various defects [39]. Lamb waves are commonly used to detect the changes in adhesion strength by measuring the mode attenuation, reflection and/or transmission coefficients or by measuring the change in wave dispersion profile [40].

di Scalea, *et. al.* [40] utilized lamb waves to detect two types of defects in adhesively bonded aluminum joints with dimensions in comparison to aircraft fuselage and wing panels. S_0 and A_0 lamb wave modes are generated using air-coupled capacitive transducers to detect de-bonds and poorly cured adhesive defects in the aluminum sample. The lamb waves propagate through the aluminum sample, however, both types of defects lead to wave attenuation. The attenuation in the transmission coefficient varies according to the defect type, hence it was possible to identify whether the defect in the sample is a de-bond or poor cohesive strength. Huo [41] estimated the adhesion strength of laminated safety glass for automobiles using lamb waves. The laminated safety glass samples used in this study consisted of two glass plates bonded together using a layer of polyvinyl butyral (PVB). Samples with five different adhesion levels were manufactured and investigated with

lamb waves. The energy velocity for the lamb waves was measured and interfacial spring constants were estimated by fitting the energy velocity values from a theoretical model to the experimental measurements. The change in the values of the interfacial spring constants illustrated the change in adhesion strength of the samples. Cerniglia *et al.* [42] utilized lamb wave propagation for the inspection of the adhesive bond qua lity of a t hree-layered aluminum plate bonded with an epoxy adhesive. Teflon inserts were introduced in the adhesive layers to simulate the effect of disbands. The change in lamb wave velocity was used as an indicator of the presence of defects in the adhesive layer.

2.3.3   *Measurement of the zeros of the reflection coefficient*

The use of Lamb wave techniques for adhesive bond characterization has been described above. Another variation of the Lamb wave technique is the Leaky Lamb Wave (LLW) technique. The difference with respect to the method described above is that the sample being investigated is submerged in a fluid; commonly water. Two transducers are used in a pitch-catch arrangement as illustrated in Figure 2-3. The transmitting transducer generates acoustic waves at an oblique angle in the coupling fluid, which propagates in the fluid.
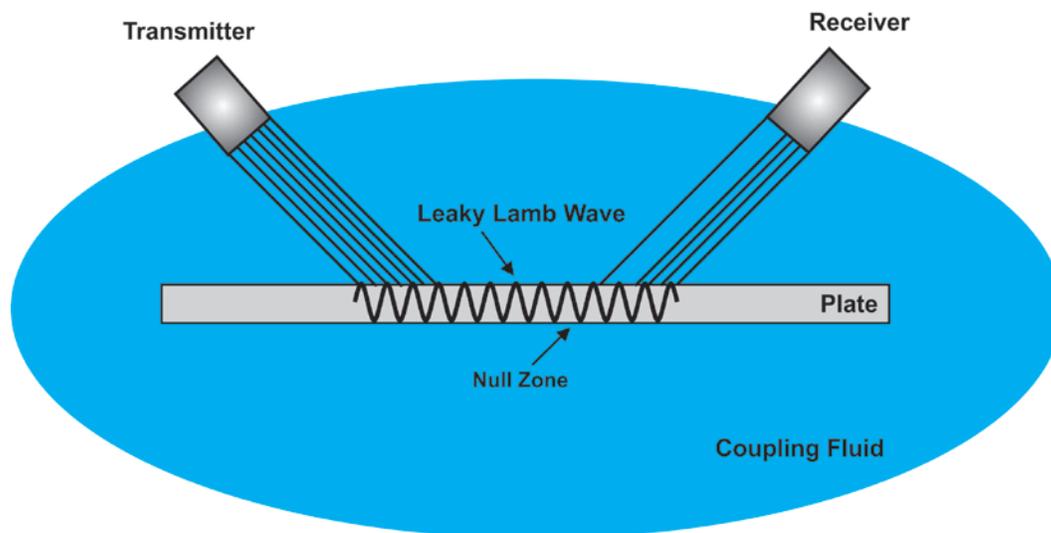
Figure 2-3: Pitch-catch configuration for leaky lamb wave generation

As the waves in the fluid reach the structure being investigated reflection, refraction and mode-conversion takes place. Due to the mode-conversion occurring at the fluid/sample interface a lamb wave propagates in the sample. The lamb wave leaks its energy into the coupling fluid and the waves

generated by the leaky Lamb wave interfere with the specularly reflected waves [43]. The destructive interference between the leaky Lamb wave and the specular component of the reflected wave leads to a null zone, which is illustrated as a minimum point in the reflection spectrum. The condition for phase matching between the incident and refracted wave is satisfied by Snell's law [44]:

$$\frac{c_i}{\sin \vartheta_i} = \frac{c_r}{\sin \vartheta_r} \qquad \text{(2-4)}$$

where c_i and c_r are the wave velocities of the incident and refracted waves, respectively, and ϑ_i and ϑ_r are the angles of the incident and refracted waves, respectively. When Lamb waves propagate in the test specimen the angle of the refracted wave ϑ_r is 90°, c_i is the longitudinal wave speed in water and the refracted wave velocity is the phase velocity of the Lamb wave c_p. Therefore, Snell's law reduces to [43]

$$c_p = \frac{c_i}{Sin \vartheta_i} \qquad \text{(2-5)}$$

this implies that the Lamb wave velocity is determined from the angle of incidence. The wavelength of the LLW is proportional to the thickness of the test specimen this allows the wave to be guided by the test specimen. The wave velocity changes with the frequency therefore a dispersion profile can be generated, which illustrates the change in wav velocity with frequency for all the possible modes that can propagate. Since there are multiple modes for Lamb wave propagation many angles of incidence can be used for Lamb wave generation. In an experimental set-up the incident angle is incremented within a range and at each angle a reflection spectrum is generated and the frequencies at which the reflection amplitude is minimum are determined. The angles of incidence are related to the Lamb wave velocities as described above and the wave dispersion profile can be generated.

Chimenti and Martin [45] utilized the LLW method to detect the presence of defects such as delamination, porosity, ply gaps and changes in fiber volume fraction in multi-ply graphyite-epoxy laminates. Two transducers in pit-catch configuration were used to generate lamb waves in the water-coupled samples at multiple angles of incidence. The reflection amplitude spectrum was recorded at multiple angles of incidence. In addition, C-scan images were generated for the

laminates with the embedded defects. Mal, Xu and Bar-Cohen [46] investigated the changes in adhesion of an aluminum-epoxy-aluminum plate using the LLW method. De-bond areas were introduced at the top and bottom aluminum-epoxy interfaces and the reflection amplitude spectra were generated as well as the dispersion curves for both cases. The dispersion curves for the de-bond cases were compared to the case with perfect bonding i.e. no defects introduced at the interfaces and significant shifts in the wave dispersion curves were observed. These results demonstrated the high sensitivity of the LLW method for detecting the changes in adhesion of bonded plates. In addition to monitoring the interfacial properties of the adhesive-adherend interface leaky lamb waves have been used to monitor the changes in the cohesive properties of the adhesive. Lowe and Cawley [47] investigated the effect of changing the adhesive's mechanical stiffness and thickness on the wave dispersion profile of the leaky lamb wave modes. Their results illustrate a shift in the dispersion profiles of the lamb wave modes with varying sensitivities due to changing the properties of the adhesive. The test specimen consisted of two Aluminum plates bonded with an adhesive layer. The effect of changing the thickness of the aluminum plates was also taken into consideration, which also led to a shift in the dispersion profiles.

Monitoring the effect of varying the adhesive-adherend interface properties on the wave dispersion profile as described above is the most commonly studied forward problem. However, using the leaky lamb wave velocity measurements the inverse problem can be solved. The inverse problem consists of measuring the phase velocity of the lamb waves and using this information to determine the material properties of the test specimen [48, 49]. This interesting problem has been investigated by Karim *et al.* [50] and Bar-Cohen and Mal [51] who utilized an inversion algorithm to characterize the elastic properties and thickness of an adhesive layer between two aluminum plates.

2.3.4 *Interface wave measurements*

Interface waves propagate along the interface of two half-spaces. The thicknesses of the two half-spaces on both sides of the interface are significantly larger than the acoustic wavelength. Two cases of interface waves will be discussed; guided interface waves and Stoneley waves; however both of these interface waves can be referred to as guided waves. The term guided interface waves used here refers to the waves that propagate in a thin layer (layer thickness is in comparison to the acoustic wavelength) embedded between two infinite half-spaces. The embedded layer guides the wave and the acoustic wave velocity changes with frequency. Stoneley waves refer to the waves that

propagate along the interface of two half-spaces whose thicknesses exceed the acoustic wavelength. Both types of interface waves have been used for monitoring adhesion between two layers as will be illustrated.

2.3.4.1 Guided Interface Waves

These are interface waves that propagate in a thin adhesive layer embedded between two infinite half-spaces i.e. adherends. The waves propagate in the adhesive layer whose thickness is comparable to the acoustic wavelength and is much smaller than the thickness of the half-spaces. The advantage of this technique is that the waves are concentrated in the thin adhesive layer. This allows the wave to be much more sensitive to any changes in the state of adhesion and less sensitive to the properties of the adherends. This technique is different than lamb wave techniques where the wave propagation is affected by the thickness and mechanical properties of the adherend plate. However, this also makes this technique very difficult to generate and detect the interface waves [52]. Nagy and Adler [52] measured the transmission coefficient for guided interface waves to monitor the presence of defects in an adhesively bonded aluminum plate. They investigated the change in interface wave transmission coefficients due to changes in adhesive thickness, the presence of partial de-bond and increased porosity of the adhesive layer. They compared the sensitivity of using lamb waves and guided interface waves to detect the presence of adhesion defects. Their results illustrated that guided interface waves are more sensitive to the adhesion defects since they are less affected by the adherend properties and more concentrated in the adhesive. Rokhlin *et al.* [53] utilized interface waves to monitor the curing process of an epoxy film embedded between two solids. The wave velocity and the attenuation of the transmission coefficient were measured during the curing process of the epoxy adhesive for seven joints with different adhesion strengths. The results illustrated different velocity and transmission coefficient profiles during the curing process as a result of the different adhesion strengths. The presence of de-bonds and/or uncured adhesive areas reduce the stresses transferred along the interface; hence the wave is more concentrated on one side of the joint. This leads to significant shifts in the wave velocity and transmission coefficient. Chen *et al.* [54] utilized analytical techniques to calculate the velocity of shear-horizontal (SH) guided interface waves propagating in a piezoceramic plate embedded between two piezoelectric half-spaces with imperfect interface conditions. Two materials for the piezoceramic plates were considered; PZT-5 and BaTiO$_3$ and the two half-spaces were assumed to consist of PZT-4. The interfaces of the

piezoceramic plate with the two half spaces were assumed to be imperfect and consist of interface springs. The springs have a stiffness K that corresponds to the bond rigidity. The dispersion profiles for the shear horizontal waves guided by the piezoceramic plate were plotted for multiple values of the interface spring stiffness. The change in bond rigidity affected the wave dispersion profile and lead to significant reduction in the values of the phase velocity indicating the high sensitivity of SH waves in monitoring the interface conditions for the presented configurations.

2.3.4.2 Stoneley waves

These are interface waves that can propagate along the boundary of two half-spaces and whose amplitude decays in both directions normal to the interface. Only certain combinations of materials can allow stoneley wave propagation. The region of existence of stoneley waves at the interface of two semi-infinite isotropic layers is defined by the ratios of their density values and shear modulus values [55]. However, the region of stoneley wave existence changes as the values of the poisson ratios of both materials change. Stoneley wave propagation can exist in anisotropic media; however calculation of the wave velocity and the displacement and stress distributions are more tedious and the existence regions depend on the direction of wave propagation [55].

Han *et al.* [56] utilized stoneley waves to detect weld and slip conditions at the interface of quartz/steel half-spaces. A laser generated stoneley wave propagates at the interface of the quartz/steel half-spaces with weld and slip boundary conditions. The weld boundary condition is implemented experimentally by bonding the quartz and steel blocks using epoxy and the slip boundary condition is implemented by introducing water at the quartz/steel interface. The stoneley wave velocity shifts to a lower value due to the change in the interface conditions from a welded to a slip boundary illustrating the ability to detect interfacial defects with high sensitivity. Claus and Kline [57] utilized stoneley waves to investigate various conditions at the interface of a pyrex mirror glass substrate bonded to a borosilicate block. Various interface conditions have been generated by polishing the borosilicate block using different grades of silicon carbide abrasive grit. Stoneley waves were generated using a piezoelectric crystal transducer. The attenuation of the stoneley wave amplitude was monitored for the different samples and the results illustrated the increase in the wave amplitude attenuation as the polishing abrasive diameter increased.

2.4 Acoustic Emission (AE)

Acoustic emission is defined as the emission of a transient stress wave due to the spontaneous release of energy resulting from the deformation or fracture of a material under loading [58]. Piezoelectric transducers attached to the structure are commonly used to detect the emitted stress waves. Most of the acoustic emission transducers operate in the 100kHz-1MHz frequency range. Different types of defects can be identified by using acoustic emission such as de-bonding, crack propagation, plastic deformation and fiber breakage in composite structures [59]. The AE technique has the advantage of inspecting the presence of defects in the entire volume of the structure during one loading cycle.

Ollendorf and Schneider [60] utilized a scratch test technique to study the adhesion of TiN films on steel substrates and recorded the acoustic emissions during the scratch test. The results indicated that the number of acoustic emissions correlated with the defect density. For the samples deposited with high adhesion strength the number of acoustic emissions decreased due to the lower number of interface defects. This indicates that the number of acoustic emissions can be used as a test parameter for thin film adhesion strength. The authors also investigated the acoustic emissions resulting from a four-point bending test equipped with an acoustic emission transducer for the TiN film on the steel substrate. The results indicated the increase in acoustic emission signals with the strain induced in the sample.

Shiwa *et al.* [61] and Swain [62] investigated the acoustic emissions during the nanoindentation of thin TiN films on silicon and sapphire substrates. Force-displacement measurements were carried out using the nanoindentation technique and an AE transducer recorded the acoustic events during the process. The number of recorded acoustic emission events increased during the loading cycle and unloading loading cycles, which continues until complete unloading. The acoustic emission results detected the onset of film cracking during loading and the film delamination during unloading. The acoustic emission response showed high sensitivity and the results varied for the silicon and sapphire substrates and even at very low loads there acoustic emission counts were recorded.

Croccolo and Cuppini [63, 64] investigated the use of the AE technique to detect different levels of defect densities in adhesively bonded structures. The AE technique can successfully detect the density of the adhesive defects if the applied load is less than the failure load of the joint. In their

study they introduced five different levels of adhesive defect densities. For each level of adhesive defect density the AE counts were recorded using an acoustic transducer as a moment is applied to the sample. The results illustrate high correlation between the AE counts recorded by the transducer and applied moment for each of the different levels of defect densities.

2.5 Eddy Currents

The Eddy Current (EC) technique is a non-destructive (NDT) used to characterize surface and bulk properties of materials by utilizing changes in electrical conductivity of the sample due to the presence of defects. The principle of operation involves applying an alternating current to a coil placed near the sample surface, which induces a magnetic field in the coil. Eddy currents are then generated in the conducting sample, which generates a secondary magnetic field that opposes the primary field. The overall change in magnetic field is usually picked by another coil and the resulting induced voltage is recorded. The presence of defects in the surface or bulk properties affects the conductivity of the surface adjacent to the coil and hence the overall change in the magnetic field. Eddy currents are used to monitor defects such as crack growth in aluminum panels bonded with a composite patch [65]. Pulsed Eddy Current technique has been used to generate C-scan images of various defects sizes and also to classify whether defects are sub-surface or not [66].

2.6 X-Ray Imaging

X-Ray imaging technique is used in monitoring the adhesion of bonded structures [41, 67]. Defects in the adhesive affect the transmission of x-rays through the bonded structure and become apparent in the resulting image. The presence of defects that are parallel to the interface can be difficult to detect with high accuracy [67]. Stevenson *et al.* [68] utilized x-ray imaging technique to detect the presence of voids in the epoxy adhesive between two aluminum plates and the average size of the voids was 100μm. A major limitation of the x-ray imaging technique is the health and safety concern.

2.7 Thin Film Adhesion Characterization

Numerous techniques have been developed for monitoring thin film adhesion in structures. Thin film adhesion measurement techniques can be classified in to two major groups; destructive and non-destructive. Destructive techniques involve applying a load to the film/substrate structure and analyzing the resulting failure that takes place to assess the film adhesion. Examples of destructive

techniques are peel [69], scratch [70], nanoindentation [71], four-point bending [72] and blister tests [73]. In all these tests a load is applied to the film substrate system, however, the method of applying and the direction of the applied load differ therefore changing the resulting failure mechanism. Non-destructive techniques involve analyzing thin film adhesion without affecting the functionality of the film/substrate system. The Scanning Acoustic Microscope (SAM) is widely used to evaluate thin film adhesion [70, 74-77].

2.7.1   *Scanning Acoustic Microscope (SAM)*

The Scanning Acoustic Microscope (SAM) technique is widely used for the characterization of thin film properties. The SAM technique utilizes high frequency SAWs for the characterization of thin film properties and the operating frequency range is 0.1-1 GHz [78]. A schematic illustration of the scanning acoustic microscope is illustrated in Figure 2-4. The heart of the SAM is the acoustic lens. The lens is made of a sapphire single crystal with its c-axis oriented along the lens axis. A piezoelectric Zinc Oxide (ZnO) transducer is placed on top of the lens and the other end of the lens is a ground refractive cavity. When a RF signal is applied to the ZnO transducer longitudinal waves are generated via the converse piezoelectric effect and propagate through the acoustic lens. The longitudinal waves propagate through the coupling fluid and strike the water/sample interface at different angles. Leaky Rayleigh waves propagate along the sample surface and re-radiates longitudinal waves into the coupling fluid. These longitudinal waves interfere with the reflected waves and propagate along the acoustic lens. The waves are converted to an electrical signal through the piezoelectric property of the ZnO transducer. The output of the SAM is illustrated as a V(z) curve, which represents the electrical signal received by the acoustic lens with respect to the distance Z from the sample surface to the focal plane of the acoustic lens.

Du *et al.* [70] utilized the SAM technique to investigate the change in adhesion of thin gold samples deposited on glass substrates. The gold film samples used in their study were 0.47-0.502μm thick. Different interface conditions between the gold films and the glass substrates were created by introducing impurities to one of the samples to weaken the adhesion between the gold film and the glass substrate. The SAW velocity of the samples were calculated from the measured V(z) curves for both samples. The velocity shifts due to the different adhesion levels of the gold/glass samples were calculated. A theoretical model was developed where the gold/glass interface is represented by a layer of distributed massless springs and the dispersion curves for different values of the interface

spring stiffness were plotted. The theoretical dispersion curves were fitted to the experimental velocity values and a quantitative assessment of the adhesion for both cases was obtained.
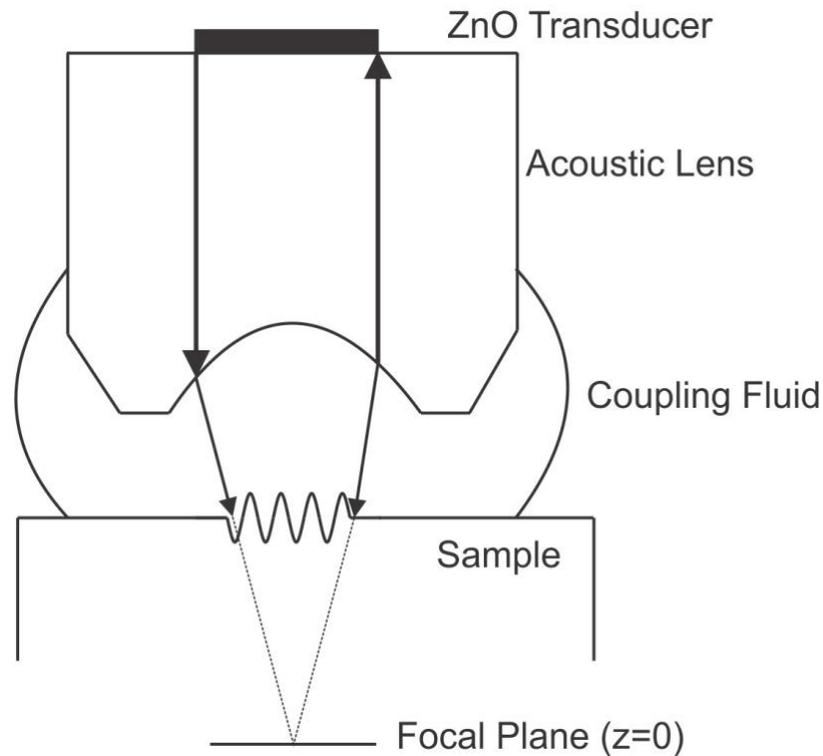
Figure 2-4: Schematic Illustration of the Scanning Acoustic Microscope (SAM)

Weglein and Mal [79] investigated the adhesion of 40µm thick titanium (Ti) films on 2mm thick beryllium (Be) substrates using the SAM technique. Different interface conditions were created at the Ti/Be interface by changing the deposition conditions and substrate treatment. Measurements were carried out using the SAM at 22-45 MHz. The wave velocities from the different samples due to the different adhesion levels were measured and shifts in wave velocity were determined. Kosbi *et al.* [80] utilized the SAM technique to investigate the change in adhesion of gold films on glass substrates at different interface conditions. The gold/glass interface was modified by introducing a layer of oil at the interface and increasing the oil thickness to deteriorate the adhesion at the gold/glass interface. Acoustic wave velocity values for the different samples were determined by the SAM. The results illustrate the shift in wave velocity due to the different interface conditions of the gold/glass sample. Parthasarathi *et al.* [81] utilized the SAM technique for non-destructive sub-surface imaging for two sets of film/substrate combinations. Diamond films with 5µm thickness were deposited on S IALON substrates and the films were indented to induce damage. The

indentation leads to film delamination. The second set of samples consisted of titanium films 3µm thick deposited on titanium alloy substrates. Laser induced spallation was introduced to the samples to create damaged regions. By mechanically scanning the surface in a raster pattern and displaying the SAM signal on a monitor an image of the induced damage is generated. Multiple sub-surface images were successfully created and the damages at the film/substrate interfaces were successfully obtained.

2.7.2   *MEMS Based Techniques*

Other MEMS based techniques for characterizing the adhesion of thin films have been developed. These techniques include a MEMS shaft-loading blister testing system [82], embedding SiO_2 microspheres in thin films and calculating the critical stress required for detaching the microspheres [83], a magnetically actuated peel test system for thin films [84] and using the deflection of micro-cantilevers to evaluate interface fracture properties [85]. These MEMS based techniques are destructive techniques that require extensive sample preparation time, external systems for load application such as using a nanoindenter system or Atomic Force Microscope and characterization techniques to assess the damaged thin film structure. However, the proposed SAW sensor technique is non-destructive; therefore it can be used to provide a quantitative assessment of thin film structures over time. In addition, the SAW sensors utilize silicon substrates and can be fabricated using simple microfabrication processes, which allows the sensor to be fabricated on the same substrate as the thin film device or structure for continuous adhesion monitoring. Finally, SAW sensors possess a very high sensitivity due to the confinement of the wave near the interface, which allows evaluating the adhesion of thin films with very high accuracy.

2.8 Conclusions

The four theories of adhesion were introduced in this chapter as well as some of the common non-destructive adhesion monitoring techniques and their applications. Destructive and non-destructive adhesion testing techniques for thin films were also discussed. Applications of the different adhesion monitoring techniques for thin film samples were also presented. Finally, the latest MEMS based adhesion monitoring techniques for thin films were introduced. It was illustrated that these MEMS based techniques are destructive; however, the proposed MEMS sensor can monitor   the   change   in   adhesion   of   thin   film   samples   non-destructively.

CHAPTER 3.   WAVE PROPAGATION IN STRUCTURES[1]

3.1 Overview

This chapter will present the fundamentals of wave propagation in isotropic, anisotropic and piezoelectric infinite media. The derivation of the Rayleigh wave solution will also be presented, which will be used for plotting the wave dispersion profile for the SU-8/AlN/Si configuration. The interface spring model will be introduced since it will be used to model the intermediate adhesion levels of the SU-8 thin film. The effect of changing the adhesion of the SU-8 film on the dispersion profile of the SU-8/AlN/Si configuration will be plotted. Finally, the sensitivity of different SAW sensors will be investigated to select the sensors with highest sensitivity for fabrication and testing.

3.2 Elastic Wave Propagation in Unbounded Media

The fundamental equation of motion for a moving body is

$$F = ma \tag{3-1}$$

The force density per unit volume is

$$f_i = \frac{\partial T_{ij}}{\partial x_j} \tag{3-2}$$

The fundamental equation of motion can be described as

$$\frac{\partial}{\partial x_j} T_{ij} = \rho \frac{\partial^2 u_i}{\partial t^2} \tag{3-3}$$

Hooke's law relates the stress to the strain as follows

$$T_{ij} = c_{ijkl} \frac{\partial u_l}{\partial x_k} \text{、} \tag{3-4}$$

Substituting Hooke's law into the equation of motion in (3-3) leads to the following format of the equation of motion

$$\rho \frac{\partial^2 u_i}{\partial t^2} = c_{ijkl} \frac{\partial^2 u_l}{\partial x_j \partial x_k}$$

(3-5)

The solution for a progressive wave that propagates in the $\overline{P}$ direction with polarization in the $\overline{d}$ direction is expressed as

$$\overline{u} = F\left(\overline{P} \cdot \overline{x} - ct\right)\overline{d}$$

(3-6)

Substituting the wave solution in the equation of motion given in (3-5) leads to the following format of the wave equation

$$\rho c^2 d_i = c_{ijkl} \, p_j \, p_k \, d_l$$

(3-7)

Introducing the second rank tensor, which is known as the Christoffel constant

$$\Gamma_{il} = c_{ijkl} \, p_j \, p_k$$

(3-8)

the wave equation can be re-written as

$$\Gamma_{il} d_l = \rho c^2 d_i$$

(3-9)

This shows that the polarization vector d_i is an eigenvector of the second rank tensor Γ_{il} and the eigenvalues are the ρc^2 values. In order to obtain the wave velocity C and the polarization d_i of a wave propagating along a direction $\overline{P}$ in a medium with stiffness constants c_{ijkl} the eigenvalues and the eigenvectors of the second rank tensor given in equation (3-8) need to be determined.

For a given wave propagation direction $\overline{P}$ there are generally three possible wave solutions propagating at three different velocity values, which can be determined by solving the following secular equation

$$\left|\Gamma_{il} - \rho c^2 \delta_{il}\right| = 0$$

(3-10)

Each value of the wave velocity is related to an eigenvector defining the polarization direction. Due to the symmetry properties of the stiffness matrix the Christoffel constants are symmetric,

therefore its eigenvalues are real and its eignevectors are orthogonal. Dieulesaint and Royer [88] illustrate that the eigenvalues ρc^2 are positive. Therefore for a given propagation direction there are three waves propagating with three different velocities and mutually orthogonal polarizations. The displacement vector u_i is not necessarily in the same direction as the wave propagation vector $\overline{P}$. The displacement vector u_i closest to the wave propagation direction is called a *quasi-longitudinal* wave and the two other waves are *quasi-transverse*. However, there are special cases in which the propagating waves are pure modes i.e. purely longitudinal and purely transverse.

In the upcoming sections the wave propagation velocity values will be calculated for isotropic, anisotropic and piezoelectric media. However, in order to utilize the formulation developed in this section for calculating the wave propagation velocities the full expressions for all Christoffel constants are presented [88]:

$$
\begin{aligned}
\Gamma_{11} &= c_{11}\, p_1^2 + c_{66}\, p_2^2 + c_{55}\, p_3^2 + 2c_{16}\, p_1\, p_2 + 2c_{15}\, p_1\, p_3 + 2c_{56}\, p_2\, p_3 \\
\Gamma_{12} &= c_{16}\, p_1^2 + c_{26}\, p_2^2 + c_{45}\, p_3^2 + \left(c_{12}+c_{66}\right) p_1\, p_2 + \left(c_{14}+c_{56}\right) p_1\, p_3 + \left(c_{46}+c_{25}\right) p_2\, p_3 \\
\Gamma_{13} &= c_{15}\, p_1^2 + c_{46}\, p_2^2 + c_{35}\, p_3^2 + \left(c_{14}+c_{56}\right) p_1\, p_2 + \left(c_{13}+c_{55}\right) p_1\, p_3 + \left(c_{36}+c_{45}\right) p_2\, p_3 \\
\Gamma_{22} &= c_{66}\, p_1^2 + c_{22}\, p_2^2 + c_{44}\, p_3^2 + 2c_{26}\, p_1\, p_2 + 2c_{46}\, p_1\, p_3 + 2c_{24}\, p_2\, p_3 \\
\Gamma_{23} &= c_{56}\, p_1^2 + c_{24}\, p_2^2 + c_{34}\, p_3^2 + \left(c_{46}+c_{25}\right) p_1\, p_2 + \left(c_{36}+c_{45}\right) p_1\, p_3 + \left(c_{23}+c_{44}\right) p_2\, p_3 \\
\Gamma_{33} &= c_{55}\, p_1^2 + c_{44}\, p_2^2 + c_{33}\, p_3^2 + 2c_{45}\, p_1\, p_2 + 2c_{35}\, p_1\, p_3 + 2c_{34}\, p_2\, p_3 \\
\Gamma_{21} &= \Gamma_{12} \quad ; \quad \Gamma_{31} = \Gamma_{13} \quad ; \quad \Gamma_{32} = \Gamma_{23}
\end{aligned} \tag{3-11}
$$

3.3 Plane Waves in Unbounded Isotropic Media

In an isotropic medium the three coordinate axes x, y and z are equivalent and every plane is a symmetry plane. The stiffness matrix for an isotropic medium has the following format

$$
\begin{bmatrix}
c_{11} & c_{12} & c_{12} & 0 & 0 & 0 \\
c_{12} & c_{11} & c_{12} & 0 & 0 & 0 \\
c_{12} & c_{12} & c_{11} & 0 & 0 & 0 \\
0 & 0 & 0 & c_{44} & 0 & 0 \\
0 & 0 & 0 & 0 & c_{44} & 0 \\
0 & 0 & 0 & 0 & 0 & c_{44}
\end{bmatrix} \tag{3-12}
$$

An isotropic medium is characterized by two independent stiffness constants, referred to as the Lame constants λ and μ and are defined by

---

$$\lambda = c_{12} \; ; \quad \mu = c_{44} \tag{3-13}$$

The stiffness constants for an isotropic medium can be expressed in terms of the Lame constants as follows

$$c_{ijkl} = \lambda \, \delta_{ij} \, \delta_{kl} + \mu \left(\delta_{ik} \, \delta_{jl} + \delta_{il} \, \delta_{jk} \right) \tag{3-14}$$

and the Christoffel constants can be expressed as

$$\Gamma_{il} = \left(\lambda + \mu \right) p_i p_l + \mu \, \delta_{il} \tag{3-15}$$

Substituting the above expression for the Christoffel constants in the wave equation (3-9) leads to

$$\left(\lambda + \mu \right) p_i p_l \, d_l + \left(\mu - \rho c^2 \right) d_i = 0 \tag{3-16}$$

which in vector format is written as

$$\left(\lambda + \mu \right) \left(\overline{P} \bullet \overline{d} \right) \overline{P} + \left(\mu - \rho c^2 \right) \overline{d} = 0 \tag{3-17}$$

Two possible wave solutions can exist.

3.3.1   *Longitudinal Wave*

The first wave solution exists when the particle polarization is in the direction of wave propagation i.e. $\overline{P} \bullet \overline{d} = \pm 1$ as illustrated in Figure 3-1. This wave is referred to as a Longitudinal wave or a P-wave (primary wave). The wave velocity for the longitudinal wave is expressed as:

$$c_L = \left(\frac{\lambda + 2\mu}{\rho} \right)^{1/2} = \left(\frac{c_{11}}{\rho} \right)^{1/2} \tag{3-18}$$
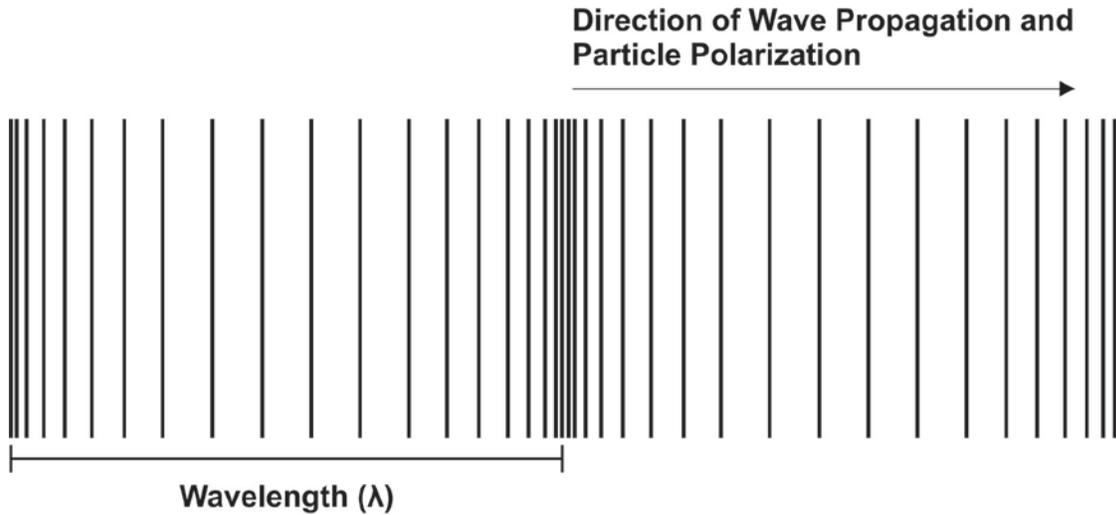
Figure 3-1: Longitudinal wave propagation

3.3.2 *Shear Wave*

The second possible wave solution can exist when the particle polarization is normal to the wave propagation direction i.e. $\overline{P} \bullet \overline{d} = 0$ as illustrated in Figure 3-2. This wave is referred to as a Shear wave or S-wave (secondary wave). The wave velocity for the shear wave is expressed as:

$$c_T = \left(\frac{\mu}{\rho} \right)^{1/2} = \left(\frac{c_{44}}{\rho} \right)^{1/2}$$

(3-19)
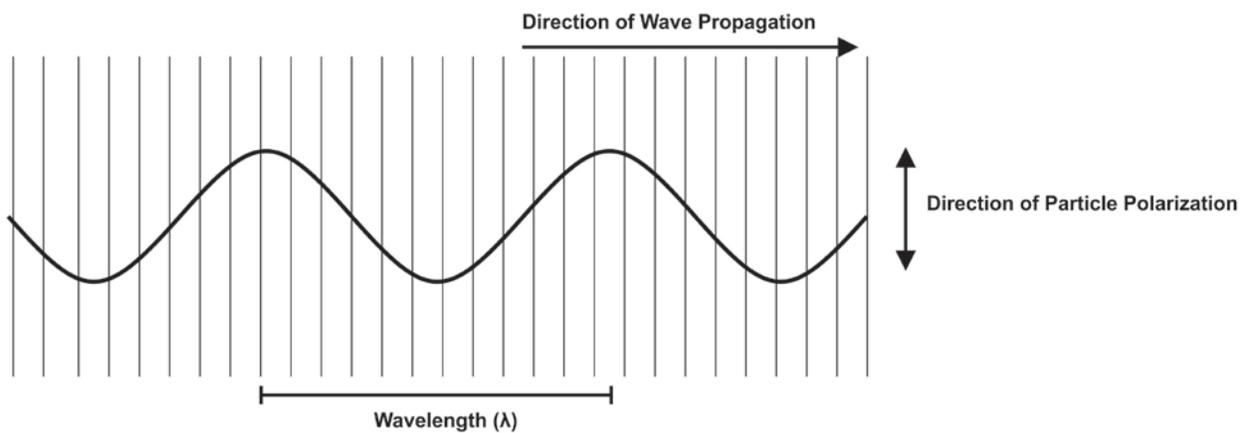
Figure 3-2: Shear wave propagation

The ratio of longitudinal to shear wave velocity can be expressed as:

$$\frac{c_L}{c_T} = \kappa = \left(\frac{\lambda + 2\mu}{\mu}\right)^{\frac{1}{2}} = \left(\frac{2(1-\nu)}{1-2\nu}\right)^{\frac{1}{2}} \tag{3-20}$$

where ν is the Poisson ratio and since $0 \le \nu \le 0.5$ then $c_L > c_T$.

3.4 Plane Waves in Unbounded Anisotropic Media

It was shown that in an isotropic medium only two waves can exist, which are a longitudinal wave and a shear wave. However, for the general case the solution of the secular equation (3-10) is a set of three eigenvectors corresponding to three wave polarization directions and three wave velocities.

There are different degrees of symmetry that affect the stiffness constants of a crystal. Two cases of anisotropic crystals will be considered in this section, which are the Cubic and Hexagonal crystal symmetry. This is because the sensor developed in this study consists of a Silicon substrate and an Aluminum Nitride film, which have cubic and hexagonal crystal structures, respectively.

3.4.1 Cubic Symmetry

A crystal with cubic symmetry has three independent stiffness constants; c_{11}, c_{12} and c_{44}. The stiffness matrix for Silicon is [89]:

$$[c] = \begin{bmatrix} 166 & 64 & 64 & 0 & 0 & 0 \\ 64 & 166 & 64 & 0 & 0 & 0 \\ 64 & 64 & 166 & 0 & 0 & 0 \\ 0 & 0 & 0 & 80 & 0 & 0 \\ 0 & 0 & 0 & 0 & 80 & 0 \\ 0 & 0 & 0 & 0 & 0 & 80 \end{bmatrix} x10^9 \quad N/m^2 \tag{3-21}$$

The symmetry of the Silicon structure leads to simplified expressions for the Christoffel constants given in equation (3-11), which can be expressed as follows:

$$\Gamma_{11} = c_{11} p_1^2 + c_{44} \left(p_2^2 + p_3^2 \right)$$

$$\Gamma_{12} = \left(c_{12} + c_{44} \right) p_1 p_2$$

$$\Gamma_{13} = \left(c_{12} + c_{44} \right) p_1 p_3$$

$$\Gamma_{22} = c_{44} \left(p_1^2 + p_3^2 \right) + c_{11} p_2^2$$ \hfill (3-22)

$$\Gamma_{23} = \left(c_{12} + c_{44} \right) p_2 p_3$$

$$\Gamma_{33} = c_{44} \left(p_1^2 + p_2^2 \right) + c_{11} p_3^2$$

Assuming that the wave propagation direction is along one of the cube faces such as the (001) plane, the components of the propagation vector are

$$p_1 = \cos\phi; \quad p_2 = \sin\phi; \quad p_3 = 0$$ \hfill (3-23)

and the Christoffel constants reduce to

$$\Gamma_{11} = c_{11} \cos^2 \phi + c_{44} \sin^2 \phi$$

$$\Gamma_{12} = \left(c_{12} + c_{44} \right) \cos\phi \sin\phi$$ \hfill (3-24)

$$\Gamma_{22} = c_{44} \cos^2 \phi + c_{11} \sin^2 \phi$$

$$\Gamma_{33} = c_{44}$$

The secular equation (3-10) is written as:

$$\begin{vmatrix} \Gamma_{11} - \rho c^2 & \Gamma_{12} & 0 \\ \Gamma_{12} & \Gamma_{22} - \rho c^2 & 0 \\ 0 & 0 & \Gamma_{33} - \rho c^2 \end{vmatrix} = 0$$ \hfill (3-25)

Expanding the determinant of the secular equation and solving for the wave velocities leads to three solutions for the wave velocities

$$2\rho c_1^2 = c_{11} + c_{44} + \sqrt{\left(c_{11} - c_{44} \right)^2 \cos^2 2\phi + \left(c_{12} + c_{44} \right)^2 \sin^2 2\phi}$$

$$2\rho c_2^2 = c_{11} + c_{44} - \sqrt{\left(c_{11} - c_{44} \right)^2 \cos^2 2\phi + \left(c_{12} + c_{44} \right)^2 \sin^2 2\phi}$$ \hfill (3-26)

$$c_3 = \sqrt{\frac{c_{44}}{\rho}}$$

The first two values of the wave velocity c_1 and c_2 correspond to the quasi-longitudinal and quasi-shear waves, respectively. The third solution for the wave velocity corresponds to a pure shear

mode with wave polarization normal to the (001) plane. Pure modes exist for cubic symmetries at $\phi = 0$ or $\pi/2$ and in these cases the velocities c_1 and c_2 reduce to

$$c_1 = \sqrt{\frac{c_{11}}{\rho}}$$

$$c_2 = \sqrt{\frac{c_{44}}{\rho}}$$

(3-27)

Using the expressions for the wave velocities along the (001) plane of Silicon in equation (3-26) the slowness curves can be plotted as illustrated in Figure 3-3. The density of Silicon used to calculate the slowness values is $2{,}320\ \text{kg/m}^3$ [89].The slowness is the inverse of the wave velocity and has units (s/m). The slowness plot for the pure shear wave is circular since the wave velocity is constant regardless of the propagation direction on the (001) plane. However, the slowness plots for the quasi-longitudinal and quasi-shear waves illustrate the change in the wave velocity as the propagation direction changes on the (001) plane. It is clear that the slowness values of the quasi-shear and pure shear waves coincide when the propagation direction is along one of the crystal axes. Due to the symmetry of the cubic crystal the wave velocity along any of the crystal axes is the same and pure modes exist. The wave velocity for pure modes can be calculated using the expressions in equation (3-27). The slowness plot illustrates the uniformity of the wave velocity values along the crystal axes.
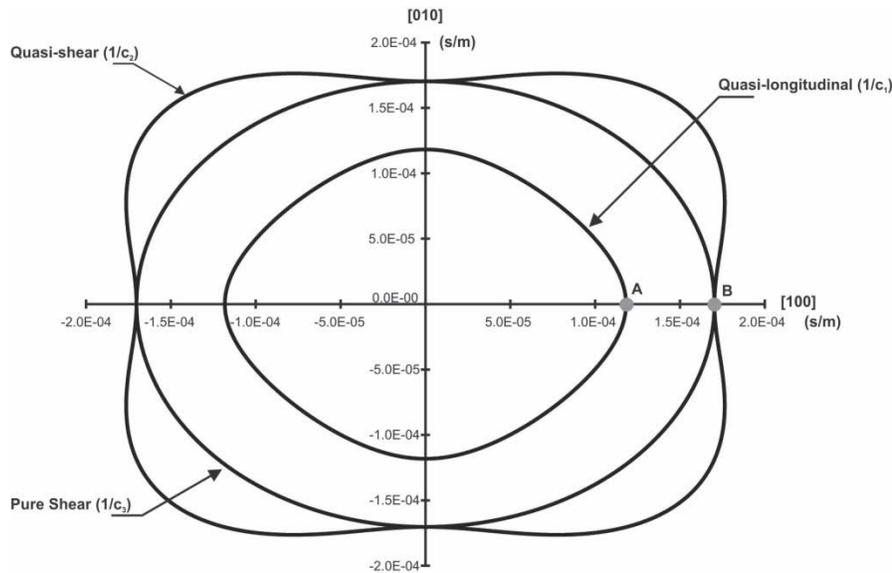
Figure 3-3: Slowness plot for the (001) plane of the cubic Silicon crystal. Point A corresponds to the pure longitudinal wave (1/1.182x10^{-4} s/m= 8458.8 m/s). Point B corresponds to the pure shear wave (1/1.703x10^{-4} s/m= 5872.2 m/s).

3.4.2 *Hexagonal Symmetry*

A crystal with Hexagonal structure possesses symmetry along the 6-fold axis, therefore all vertical planes are equivalent and along the horizontal planes the wave velocities are uniform. The stiffness matrix for a Hexagonal crystal has 6 independent stiffness constants. The stiffness matrix for Aluminum Nitride is given in equation (3-28) and the density is 3,260 kg/m^3 [90]

$$[c] = \begin{bmatrix} 345 & 125 & 120 & 0 & 0 & 0 \\ 125 & 345 & 120 & 0 & 0 & 0 \\ 120 & 120 & 395 & 0 & 0 & 0 \\ 0 & 0 & 0 & 118 & 0 & 0 \\ 0 & 0 & 0 & 0 & 118 & 0 \\ 0 & 0 & 0 & 0 & 0 & 110 \end{bmatrix} x10^9 \quad N/m^2 \tag{3-28}$$

where $c_{66} = \dfrac{345 - 125}{2}$.

Due to the symmetry of the stiffness matrix for a Hexagonal crystal the general expressions for the Christoffel constants given in equation (3-11) reduce to:

$$\begin{aligned}
\Gamma_{11} &= c_{11} p_1^2 + c_{66} p_2^2 + c_{44} p_3^2 \\
\Gamma_{12} &= (c_{12} + c_{66}) p_1 p_2 \\
\Gamma_{13} &= (c_{13} + c_{44}) p_1 p_3 \\
\Gamma_{22} &= c_{66} p_1^2 + c_{11} p_2^2 + c_{44} p_3^2 \\
\Gamma_{23} &= (c_{13} + c_{44}) p_2 p_3 \\
\Gamma_{33} &= c_{44}(p_1^2 + p_2^2) + c_{33} p_3^2
\end{aligned} \tag{3-29}$$

For the case of wave propagation along the (001) plane the propagation vector is similar to that given in equation (3-23) and the Christoffel constants reduce to:

$$\begin{aligned}
\Gamma_{11} &= c_{11} \cos^2 \phi + c_{66} \sin^2 \phi \\
\Gamma_{12} &= (c_{12} + c_{66}) \cos \phi \sin \phi \\
\Gamma_{22} &= c_{66} \cos^2 \phi + c_{11} \sin^2 \phi \\
\Gamma_{33} &= c_{44}
\end{aligned} \tag{3-30}$$

The secular equation is expressed as:

$$\begin{vmatrix} \Gamma_{11} - \rho c^2 & \Gamma_{12} & 0 \\ \Gamma_{12} & \Gamma_{22} - \rho c^2 & 0 \\ 0 & 0 & \Gamma_{33} - \rho c^2 \end{vmatrix} = 0 \qquad (3\text{-}31)$$

Three solutions exist for the three waves propagating on the (001) plane of a Hexagonal crystal:

$$2\rho c_1^2 = c_{11} + c_{66} + \sqrt{\left(c_{11} - c_{66}\right)^2 \cos^2 2\phi + \left(c_{12} + c_{66}\right)^2 \sin^2 2\phi}$$

$$2\rho c_2^2 = c_{11} + c_{66} - \sqrt{\left(c_{11} - c_{66}\right)^2 \cos^2 2\phi + \left(c_{12} + c_{66}\right)^2 \sin^2 2\phi} \qquad (3\text{-}32)$$

$$c_3 = \sqrt{\frac{c_{44}}{\rho}}$$

The slowness plots for the (001) plane in the Aluminum Nitride Hexagonal crystal are illustrated in Figure 3-4.
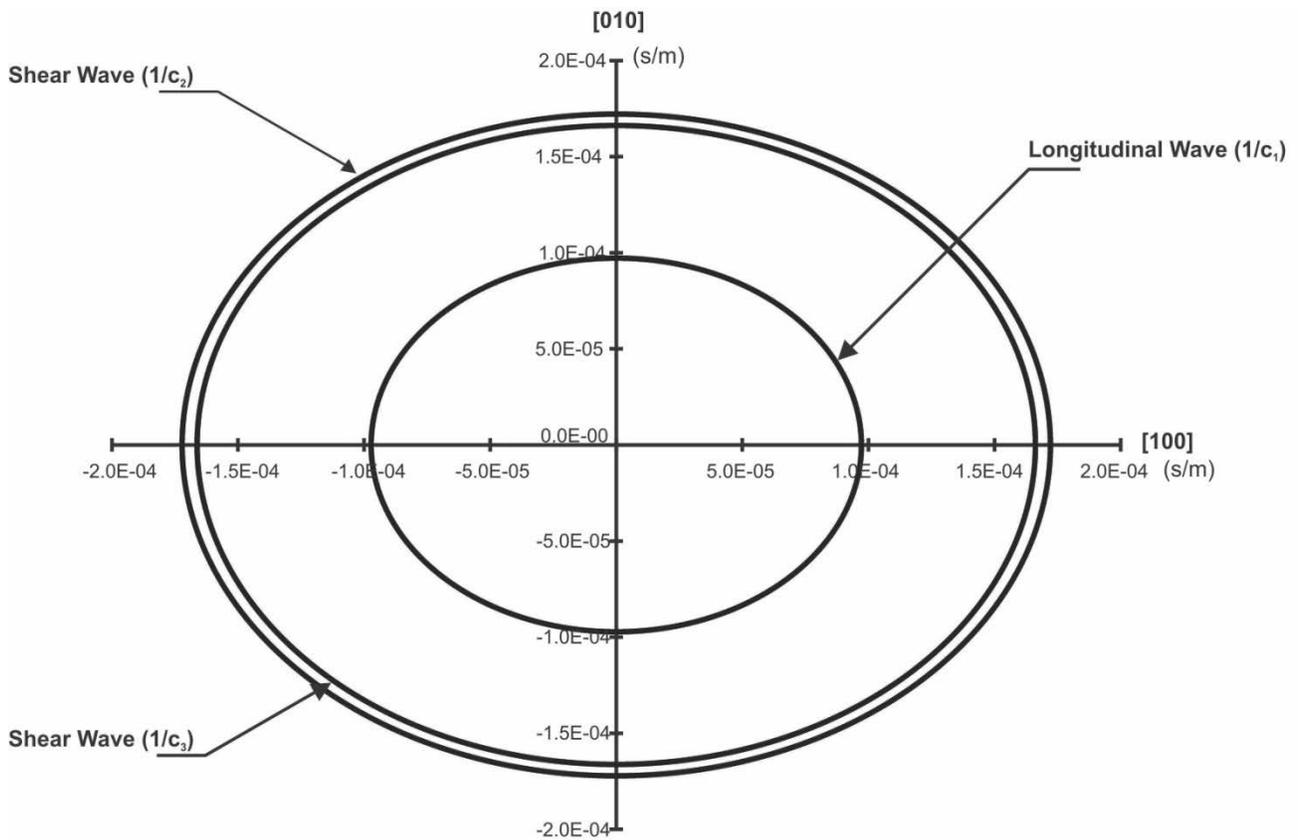
Figure 3-4: Slowness plots for the (001) plane of the Hexagonal crystal structure for Aluminum Nitride

The slowness plots for the (001) plane for Aluminum Nitride consist of three circles with radii $\sqrt{\rho/c_{11}}$, $\sqrt{\rho/c_{66}}$ and $\sqrt{\rho/c_{44}}$. Along the [100] and [010] directions pure modes propagate on the (001) plane, which consist of a longitudinal wave with velocity $c_1 = \sqrt{c_{11}/\rho}$, a shear wave with particle polarization in the (001) plane at a velocity $c_2 = \sqrt{c_{66}/\rho}$ and a shear wave with particle polarization along the 6-fold axis at a velocity $c_3 = \sqrt{c_{44}/\rho}$.

3.5 Elastic Wave Propagation in Semi-Infinite Media (Half-Space)

When considering wave propagation in unbounded media the surface effects are negligible. However, when a wave is propagating in a semi-infinite medium also known as a half-space boundary conditions need to be applied at the surface. In the cases considered in this study for wave propagation in half-spaces the adjacent medium is assumed to be vacuum and the surface of the half-space is a free surface, which means that the stress components on the free surface vanish.

In unbounded isotropic media two waves can exist, which are longitudinal and transverse waves. As the longitudinal and transverse waves encounter the free surface of a half-space they will be reflected and will generate a longitudinal wave, a transverse wave or both depending on the angle of incidence. In the following section the reflection of a transverse wave at the free surface of an isotropic half-space will be discussed.

3.5.1   Reflection of a Transverse Wave at the Boundary of a Free Surface

A transverse wave is generated from within the half-space and propagates towards the free surface at an angle ϑ_o as illustrated in Figure 3-5. Since in an isotropic half-space only a longitudinal and a transverse wave can exist these are the two possible waves that can be reflected at the free surface. The reflected waves will propagate in the half-space only since the adjacent medium is vacuum. The incident transverse wave $\left(\overline{P}_o\right)$ is expressed as:

$$\overline{u}^{(o)} = A_o \, \overline{d}^{(o)} \exp\left[ik_o \left(x_1 p_1^{(o)} + x_2 p_2^{(o)} - c_T t \right) \right] \tag{3-33}$$

where

$$p_1^{(o)} = \sin \vartheta_o \qquad\qquad p_2^{(o)} = \cos \vartheta_o$$
$$d_1^{(o)} = -\cos \vartheta_o \qquad\qquad d_2^{(o)} = \sin \vartheta_o$$
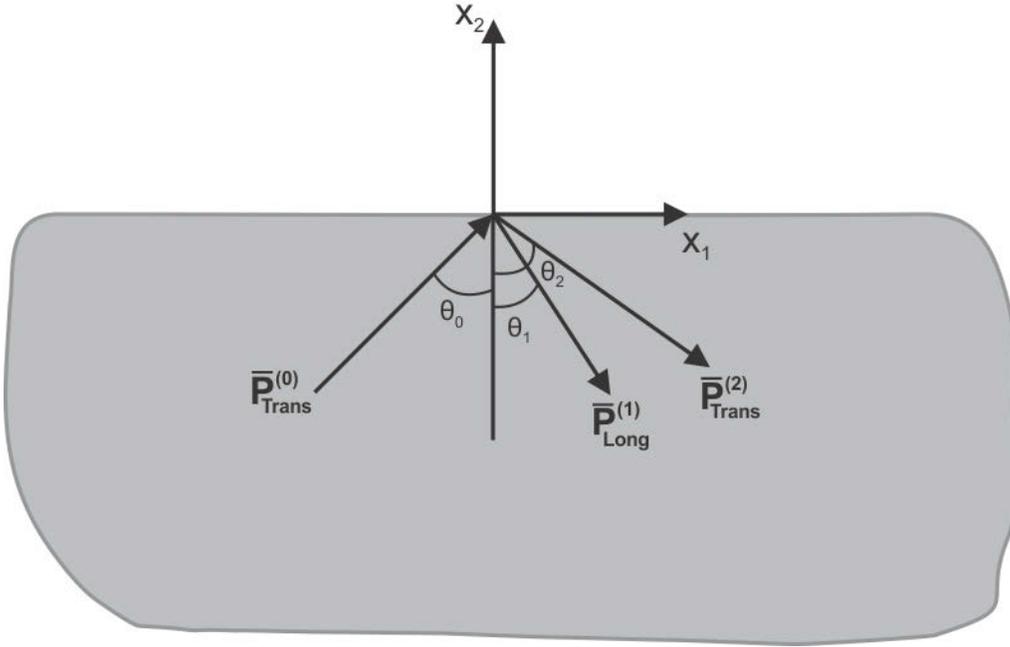
Figure 3-5: Incident transverse wave $\left(\overline{P}_0\right)$ **and reflected longitudinal** $\left(\overline{P}_1\right)$ **and transverse** $\left(\overline{P}_2\right)$ **waves in an isotropic half-space**

The reflected longitudinal wave $\left(\overline{P}_1\right)$ is expressed as

$$\overline{u}^{(1)} = A_1\, \overline{d}^{(1)} \exp\left[ik_1 \left(x_1 p_1^{(1)} + x_2 p_2^{(1)} - c_L t \right) \right]$$ (3-34)

where

$$
\begin{aligned}
&p_1^{(1)} = \sin\vartheta_1 &&p_2^{(1)} = -\cos\vartheta_1 \\
&d_1^{(1)} = \sin\vartheta_1 &&d_2^{(1)} = -\cos\vartheta_o
\end{aligned}
$$ (3-35)

The reflected transverse wave $\left(\overline{P}_2\right)$ is expressed as:

$$\overline{u}^{(2)} = A_2\, \overline{d}^{(2)} \exp\left[ik_2 \left(x_1 p_1^{(2)} + x_2 p_2^{(2)} - c_T t \right) \right]$$ (3-36)

where

$$
\begin{aligned}
&p_1^{(2)} = \sin\vartheta_2 &&p_2^{(2)} = -\cos\vartheta_2 \\
&d_1^{(2)} = \cos\vartheta_2 &&d_2^{(2)} = \sin\vartheta_2
\end{aligned}
$$ (3-37)

The boundary conditions that need to be applied at the free surface $(x_2 = 0)$ are the vanishing of the stress components T_{22} and T_{12}. Substituting the wave displacement solutions in equations (3-33), (3-34) and (3-36) into the stress-strain relation in equation (3-4) generates the expressions for the boundary conditions at the free surface. Setting $T_{22} = 0$ at $x_2 = 0$ leads to:

$$i2\mu k_o A_o \sin\vartheta_o \cos\vartheta_o \exp\left[ik_o\left(p_1^{(o)}x_1 - c_T t\right)\right] +$$
$$i\left(\lambda + 2\mu\cos^2\vartheta_1\right)k_1 A_1 \exp\left[ik_1\left(p_1^{(1)}x_1 - c_L t\right)\right] - \tag{3-38}$$
$$i2\mu k_2 A_2 \sin\vartheta_2 \cos\vartheta_2 \exp\left[ik_2\left(p_1^{(2)}x_1 - c_T t\right)\right] = 0$$

Setting $T_{12} = 0$ at $x_2 = 0$ leads to

$$i\mu k_o A_o \left(\sin^2\vartheta_o - \cos^2\vartheta_o\right)\exp\left[ik_o\left(p_1^{(o)}x_1 - c_T t\right)\right] -$$
$$i2\mu k_1 A_1 \sin\vartheta_1 \cos\vartheta_1 \exp\left[ik_1\left(p_1^{(1)}x_1 - c_L t\right)\right] - \tag{3-39}$$
$$i\mu k_2 A_2 \left(\sin^2\vartheta_2 - \cos^2\vartheta_2\right)\exp\left[ik_2\left(p_1^{(2)}x_1 - c_T t\right)\right] = 0$$

Since the boundary conditions need to be satisfied for any value of the coordinate x_1 and at any time t, the following relations must hold

$$k_o \sin\vartheta_o = k_1 \sin\vartheta_1 = k_2 \sin\vartheta_2 = k$$
$$k_o c_T = k_1 c_L = k_2 c_T = \omega \tag{3-40}$$

which lead to the following

$$k_2 = k_o$$
$$\frac{k_1}{k_o} = \frac{c_T}{c_L} = \kappa^{-1}$$
$$\vartheta_2 = \vartheta_0 \tag{3-41}$$
$$\sin\vartheta_1 = \kappa\sin\vartheta_0$$

Using these equalities the boundary condition equations (3-38) and (3-39) can be simplified to

$$\left(\lambda + 2\mu\cos^2\vartheta_1\right)\frac{A_1}{A_o} - \kappa\mu\sin2\vartheta_o\frac{A_2}{A_o} = -\kappa\mu\sin2\vartheta_o$$

$$-\mu\sin2\vartheta_1\frac{A_1}{A_o} - \kappa\mu\cos2\vartheta_o\frac{A_2}{A_o} = \kappa\mu\cos2\vartheta_o$$

(3-42)

The amplitudes of the reflected longitudinal and transverse waves are found to be

$$\frac{A_1}{A_o} = \frac{\kappa\sin4\vartheta_o}{\sin2\vartheta_o\sin2\vartheta_1 + \kappa^2\cos^2 2\vartheta_o}$$

$$\frac{A_2}{A_o} = \frac{\sin2\vartheta_o\sin2\vartheta_1 - \kappa^2\cos2\vartheta_o}{\sin2\vartheta_o\sin2\vartheta_1 + \kappa^2\cos^2 2\vartheta_o}$$

(3-43)

The equations for the amplitude ratios illustrate that some special cases may exist such as:

1. When $\vartheta_o = 0$, $\frac{\pi}{4}$ or $\frac{\pi}{2}$ the reflected longitudinal wave vanishes and the incident transverse wave is reflected only as a transverse wave.

2. If $\sin2\vartheta_o\sin2\vartheta_1 - \kappa^2\cos2\vartheta_o = 0$ and $\sin\vartheta_1 = \kappa\sin\vartheta_0$ has real solutions then $A_2/A_o = 0$ and the incident transverse wave is reflected as a longitudinal wave, which is known as *Mode Conversion*.

A real value of ϑ_1 requires that

$$\vartheta_o < \vartheta_{cr} ; \quad where \quad \vartheta_{cr} = \sin^{-1}\left(\frac{1}{\kappa}\right)$$

(3-44)

when $\vartheta_o > \vartheta_{cr}$ no real value for ϑ_1 exists; therefore:

$$P_1^{(1)} = \kappa\sin\vartheta_o$$

$$P_2^{(1)} = \sqrt{1 - \kappa^2\sin^2\vartheta_o} = \pm i\sqrt{\kappa^2\sin^2\vartheta_o - 1} = \pm ib$$

$$where \quad b = \sqrt{\kappa^2\sin^2\vartheta_o - 1}$$

(3-45)

The reflected longitudinal wave in this case is expressed as

$$\overline{u}^{(1)} = A_1\overline{d}^{(1)}\exp\left(k_1bx_2\right)\exp\left[i\left(k_o\sin\vartheta_o x_1 - \kappa^{-1}k_oc_Lt\right)\right]$$

(3-46)

This is a wave that propagates along the x_1-direction with a wavenumber $k = k_o \sin \vartheta_o$ and phase velocity $v = c_L / \kappa$. The amplitude of this wave decays exponentially along the x_2-direction. This type of wave is known as a *Surface Wave*.

3.6 Surface Wave Propagation in Elastic Media

Surface waves have been studied heavily in seismology since their discovery by Lord Rayleigh in 1885 [91]. The characteristic property of surface waves is that their amplitude decays exponentially in the depth direction, which means that most of their energy is confined within a few wavelengths from the surface. This property has allowed surface waves to be used widely in sensing applications since they are highly sensitive to changes occurring at or near the surface. The surface waves discovered by Lord Rayleigh in 1885 propagate along the free surface of a half-space with particle polarization in the sagittal plane and with decaying amplitude in the depth direction. These waves have been named Rayleigh waves after their discoverer. Another type of surface waves is Love waves, which were discovered by A. E. Love in 1911 [92]. Love waves have a shear horizontal polarization with decaying wave amplitude in the depth direction. Love waves propagate in an isotropic half-space covered with an isotropic layer of finite thickness and whose transverse wave velocity is lower than the half-space's transverse velocity. The type of surface wave that will be investigated in this study is the Rayleigh wave and it will be referred to as a surface wave. The displacement solution for a surface wave can be expressed as

$$u_j = \alpha_j \exp\left(ikbx_3\right) \exp\left[ik\left(x_1 - vt\right)\right] \tag{3-47}$$

The waves are assumed to propagate in the x_1-direction and are uniform in the x_2-driection. Substituting this wave displacement solution in the wave equation (3-5) leads to the following Christoffel equation:

$$\begin{pmatrix} \Gamma_{11} - \rho v^2 & \Gamma_{13} \\ \Gamma_{13} & \Gamma_{33} - \rho v^2 \end{pmatrix} \begin{pmatrix} \alpha_1 \\ \alpha_3 \end{pmatrix} = 0 \tag{3-48}$$

The Γ_{22} is de-coupled from the solution and the wave is a plane wave that propagates in the sagittal x_1-x_3 plane. The Christoffel constants are expressed as:

$$\Gamma_{11} = c_{44}\, b^2 + c_{11}$$

$$\Gamma_{13} = \left(c_{11} - c_{44}\right)b \tag{3-49}$$

$$\Gamma_{33} = c_{11}\, b^2 + c_{44}$$

The secular equation leads to the following:

$$\left(c_{44}\, b^2 + c_{44} - \rho v^2\right)\left(c_{11}\, b^2 + c_{11} - \rho v^2\right) = 0 \tag{3-50}$$

for an assumed value of the wave velocity v the corresponding eigenvalues and eigenvectors are:

$$b^1 = -i\left[1 - \left(v/v_t\right)^2\right]^{1/2} \quad ; \quad \overline{\alpha}^1 = \left(-b_1\,; \quad 0\,; \quad 1\right)$$

$$b^2 = -i\left[1 - \left(v/v_l\right)^2\right]^{1/2} \quad ; \quad \overline{\alpha}^2 = \left(1\,; \quad 0\,; \quad b_2\right) \tag{3-51}$$

and the wave solutions can be expressed as

$$u_j = \sum_n C_n\, \alpha_j^n \exp\left(ikb^n x_3\right)\exp\left[ik\left(x_1 - vt\right)\right] \tag{3-52}$$

Substituting the displacement solutions in the boundary conditions terms for the stress-free surface leads to the following set of homogenous equations

$$\begin{bmatrix} c_{12}\,\alpha_1^1 + c_{11}\,b^1\alpha_3^1 & c_{12}\,\alpha_1^2 + c_{11}\,b^2\alpha_3^2 \\ c_{44}\,\alpha_3^1 + c_{44}\,b^1\alpha_1^1 & c_{44}\,\alpha_3^2 + c_{44}\,b^2\alpha_1^2 \end{bmatrix}\begin{bmatrix} C_1 \\ C_2 \end{bmatrix} = \begin{bmatrix} 0 \\ 0 \end{bmatrix} \tag{3-53}$$

for a non-trivial solution

$$\begin{vmatrix} c_{12}\,\alpha_1^1 + c_{11}\,b^1\alpha_3^1 & c_{12}\,\alpha_1^2 + c_{11}\,b^2\alpha_3^2 \\ c_{44}\,\alpha_3^1 + c_{44}\,b^1\alpha_1^1 & c_{44}\,\alpha_3^2 + c_{44}\,b^2\alpha_1^2 \end{vmatrix} = 0 \tag{3-54}$$

expanding the determinant of the boundary conditions matrix in equation (3-54) leads to the following implicit equation for the Rayleigh wave velocity v_R:

$$\left(2 - \frac{v_R^2}{v_t^2}\right)^2 - 4\left(1 - \frac{v_R^2}{v_l^2}\right)^{1/2}\left(1 - \frac{v_R^2}{v_t^2}\right)^{1/2} = 0 \tag{3-55}$$

The Rayleigh wave velocity is a constant for a given propagation direction and is non-dispersive i.e. it does not change with the frequency of the wave. Using either one of the stress boundary condition equations in (3-53) the weighting factors C_1 and C_2 are related as follows:

$$C_1 = -\frac{2b^{(2)}}{1-\left(b^{(1)}\right)^2}C_2 \tag{3-56}$$

The displacement field can now be expressed as

$$u_1 = C_2\left[\exp\left(ikb^{(2)}x_3\right) - A\exp\left(ikb^{(1)}x_3\right)\right]\exp\left[ik\left(x_1 - vt\right)\right]$$

$$u_3 = -iC_2\left(1-\left(\frac{v}{v_l}\right)^2\right)^{1/2}\left[\exp\left(ikb^{(2)}x_3\right) - \frac{1}{A}\exp\left(ikb^{(1)}x_3\right)\right]\exp\left[ik\left(x_1 - vt\right)\right] \tag{3-57}$$

where

$$A = \frac{\left(1-\left(b^{(1)}\right)^2\right)}{2}$$

The physical displacements are the real parts of the expressions given in equation (3-57), which can be expressed as:

$$\text{Re}[u_1] = \overline{u_1}\cos k\left(x_1 - vt\right)$$

$$\text{Re}[u_3] = \overline{u_3}\sin k\left(x_1 - vt\right) \tag{3-58}$$

where

$$\overline{u_1} = \left[\exp\left(ikb^{(2)}x_3\right) - A\exp\left(ikb^{(1)}x_3\right)\right]$$

$$\overline{u_3} = \left(1-\left(\frac{v}{v_l}\right)^2\right)^{1/2}\left[\exp\left(ikb^{(2)}x_3\right) - \frac{1}{A}\exp\left(ikb^{(1)}x_3\right)\right] \tag{3-59}$$

The particle displacements in the x_1 and x_3 directions have a phase shift of $\pi/2$, which leads to an elliptical particle displacement. The wave amplitudes in equation (3-59) have been plotted in Figure 3-6 for an isotropic Zinc Oxide substrate with a Rayleigh wave velocity of 2,649m/s. The longitudinal and transverse components are plotted along the depth of the substrate. The transverse component is initially 1.5 times the longitudinal component and it can be seen that the longitudinal displacement changes its direction at a depth of 0.17xλ. The main feature of the displacement components is that both of them decay significantly at a depth of 1xλ, therefore indicating that most of the wave energy is confined within a wavelength from the surface. This is a characteristic property of surface waves.
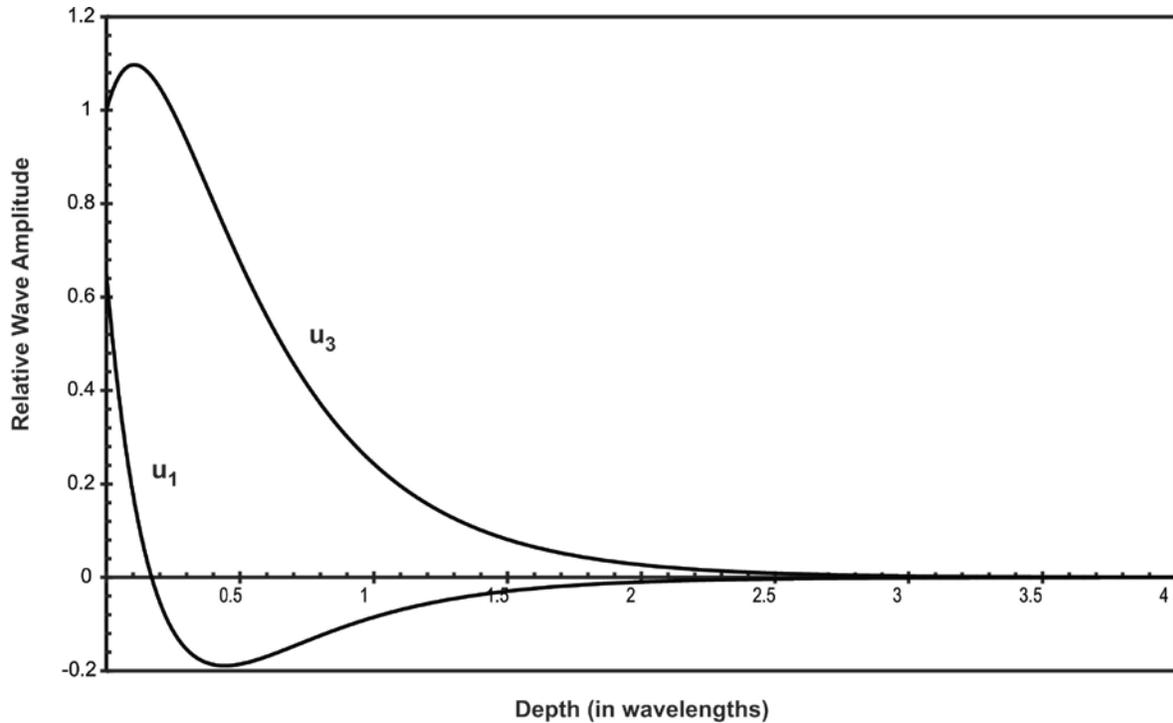
Figure 3-6: Normalized wave displacements along the depth direction (x_3) for an isotropic ZnO half-space

3.7 Wave Propagation in Piezoelectric Media

Piezoelectric materials possess the property of being electrically polarized due to the application of mechanical stress, which is the *Direct* piezoelectric effect. The *Converse* piezoelectric effect occurs when a material is placed in an electric field and experiences a mechanical strain [93-95]. On the atomic scale the polarization of a piezoelectric material due to mechanical stress occurs because the applied load leads to a relative shift between the center of the negatively charged electron cloud with respect to the positive nucleus of the atom. This shift leads to the generation of a microscopic electric dipole, which due to the crystal symmetry of the material forms a macroscopic moment i.e. the material is electrically polarized. The dipoles cancel within the material itself but generate fixed charges on the surface. Piezoelectricity occurs in 20 crystal classes out of the 32, all of which do not possess a center of symmetry.

Piezoelectric materials have been used extensively to develop acoustic wave transducers because they allow electrical excitation of acoustic waves using metal electrodes patterned on the surface of the piezoelectric material. There are numerous configurations of acoustic wave transducers utilizing piezoelectric materials that are used to generate acoustic waves. Some of these devices include the

Quartz Thickness Shear Mode transducer, the SAW Delay Line transducers, Love Wave transducers, SH-SAW transducers and Lamb Wave Transducers. Some of the common piezoelectric substrates used in acoustic wave devices are Lithiun Niobate, Quartz, Lithium Tantalate and Gallium Arsenide. Piezoelectric materials are also being deposited as thin films on Silicon substrates to create monolithic devices. Aluminum Nitride (AlN), Zinc Oxide (ZnO) and Lead Zirconate Titanate (PZT) are the commonly used piezoelectric materials for thin film deposition.

In previous sections wave propagation in isotropic and anisotropic materials have been presented and it was shown that the wave solutions consisted only for mechanical displacements. For the case of wave propagation in piezoelectric materials the wave equations illustrate the coupling that occurs between the mechanical displacement and the electrical potential. The derivation of the wave equations from the piezoelectric constitutive equations will be presented and the slowness curve for Aluminum Nitride will be plotted.

The constitutive equations for a piezoelectric material illustrate the coupling that takes place between the applied mechanical stress and the electric potential. The equations are given by:

$$T_{ij} = c_{ijkl}^E S_{kl} - e_{ijk}^T E_k \tag{3-60}$$

$$D_i = \varepsilon_{ij}^S E_j + e_{ikl} S_{kl} \tag{3-61}$$

where T_{ij} is the mechanical stress $\left(N/m^2\right)$, c_{ijkl}^E is the stiffness matrix $\left(N/m^2\right)$, e_{ikl} and e_{ijk}^T are the piezoelectric stress constants. The superscript (T) implies that the piezoelectric stress constants in both equations are transpose of each other. E_k is the electric field component (V/m), D_i is the electric displacement $\left(C/m^2\right)$, ε_{ik}^S is the dielectric permittivity (F/m). The superscripts on the stiffness constants and the dielectric permittivity imply that these are the properties measured at constants electric field and constant strain, respectively.

In order to derive the first piezoelectric wave equation, the equation of motion in (3-3), which is re-stated here for illustration;

$$\frac{\partial}{\partial x_j} T_{ij} = \rho \frac{\partial^2 u_i}{\partial t^2}$$

is substituted after taking the divergence $(\nabla \cdot)$ of the first piezoelectric constitutive equation (3-60). The velocity of electromagnetic waves is five orders of magnitude higher than acoustic wave velocities, therefore it will be assumed that the magnetic field component is de-coupled and the electric field is expressed as

$$E = -\nabla \varphi \qquad (3\text{-}62)$$

This is called the Quasi-static approximation and has negligible effect on the solution [94]. The divergence of the second piezoelectric constitutive equation (3-61) should be zero $\nabla \cdot D = 0$ due to the absence of free charges in dielectric materials. The piezoelectric wave equations can now be expressed as:

$$\rho \frac{\partial^2 u_j}{\partial t^2} - c^E_{ijkl} \frac{\partial^2 u_k}{\partial x_i \partial x_l} - e_{kij} \frac{\partial^2 \phi}{\partial x_i \partial x_k} = 0$$

$$e_{ikl} \frac{\partial^2 u_k}{\partial x_i \partial x_l} - \varepsilon^S_{ik} \frac{\partial^2 \phi}{\partial x_i \partial x_k} = 0 \qquad i,j,k,l = 1,2,3 \qquad (3\text{-}63)$$

The wave equations will be solved in the sagittal plane $x_1 - x_3$ and the wave solutions are assumed to be uniform in the out-of-plane x_2 direction. The solutions for the mechanical displacements and the electric potential in each medium are linear combinations of partial wave solutions as shown:

$$u_j = \sum_n C_n \alpha_j^n \exp\left(ikb^n x_3\right) \exp\left[ik\left(x_1 - vt\right)\right]$$

$$\varphi = \sum_n C_n \alpha_4^n \exp\left(ikb^n x_3\right) \exp\left[ik\left(x_1 - vt\right)\right] \quad ; \quad j = 1,3 \qquad (3\text{-}64)$$

where C_n are weighting factors that allow the boundary conditions to be satisfied, the subscript n refers to the number of wave solutions in the corresponding medium, α_j^n is the relative wave amplitude for the jth component, b is the decay parameter, k is the wavenumber and v is the phase velocity. By substituting the assumed wave solutions for each medium in the corresponding wave equation the following Christoffel equations are derived:

$$\begin{bmatrix} \Gamma_{11} - \rho v^2 & \Gamma_{12} & \Gamma_{13} & \vdots & \Gamma_{14} \\ \Gamma_{21} & \Gamma_{22} - \rho v^2 & \Gamma_{23} & \vdots & \Gamma_{24} \\ \Gamma_{31} & \Gamma_{32} & \Gamma_{33} - \rho v^2 & \vdots & \Gamma_{34} \\ \hdashline \Gamma_{14} & \Gamma_{24} & \Gamma_{34} & \vdots & \Gamma_{44} \end{bmatrix} \begin{bmatrix} \alpha_1 \\ \alpha_2 \\ \alpha_3 \\ \alpha_4 \end{bmatrix} = 0 \qquad \text{(3-65)}$$

The Γ_{ij}'s in the upper left block are responsible for coupling the elastic displacement components and are expressed as [96]

$$\begin{aligned}
\Gamma_{11} &= c_{55} b^2 + 2c_{15} b + c_{11} \\
\Gamma_{22} &= c_{44} b^2 + 2c_{46} b + c_{66} \\
\Gamma_{33} &= c_{33} b^2 + 2c_{35} b + c_{55} \\
\Gamma_{12} &= c_{45} b^2 + (c_{14} + c_{56})b + c_{16} \\
\Gamma_{13} &= c_{35} b^2 + (c_{13} + c_{55})b + c_{15} \\
\Gamma_{23} &= c_{34} b^2 + (c_{36} + c_{45})b + c_{56}
\end{aligned} \qquad \text{(3-66)}$$

The christoffel constants in the upper right and lower left blocks are responsible for coupling the electric potential to the mechanical displacements and are expressed as [96]

$$\begin{aligned}
\Gamma_{14} &= e_{35} b^2 + (e_{15} + e_{31})b + e_{11} \\
\Gamma_{24} &= e_{34} b^2 + (e_{14} + e_{36})b + e_{16} \\
\Gamma_{34} &= e_{33} b^2 + (e_{13} + e_{35})b + e_{15}
\end{aligned} \qquad \text{(3-67)}$$

The Γ_{44} term is a purely electrical term [96]

$$\Gamma_{44} = -\left(\varepsilon_{33} b^2 + 2\varepsilon_{13} b + \varepsilon_{11} \right) \qquad \text{(3-68)}$$

In order to have a non-trivial solution the determinant of the square matrix should be zero. This leads to the following secular equation;

$$\begin{aligned}
\left[\Gamma_{pq} - \delta_{pq} \rho v^2 \right]\left[\alpha_p \right] = 0; & \quad p, q = 1, 3, 4 \\
\delta_{44} = 0
\end{aligned} \qquad \text{(3-69)}$$

In order to have a non-trivial solution the following secular equation needs to be solved

$$\left| \Gamma_{pq} - \delta_{pq} \rho v^2 \right| = 0; \quad p, q = 1, 3, 4 \qquad \text{(3-70)}$$

For a given value of the wave velocity v the secular equation generates an eighth order polynomial in the decay parameter b. For each value of b there is a four component eigenvector $(\alpha_1, \alpha_2, \alpha_3, \alpha_4)$

that can be evaluated. Each combination of the decay parameter b and eigenvector $\bar{\alpha}$ the wave solution in equation (3-64) satisfies the piezoelectric wave equations (3-63). By imposing the boundary conditions in the problem and substituting the assumed wave solutions given in equation (3-64) into the boundary condition expressions a boundary condition matrix can be generated as follows

$$
\begin{bmatrix} & & \\ & BC's & \\ & & \end{bmatrix}_{mxm} \begin{bmatrix} C_1 \\ \vdots \\ \vdots \\ \vdots \\ C_n \end{bmatrix} = \begin{bmatrix} 0 \\ \vdots \\ \vdots \\ 0 \end{bmatrix} \tag{3-71}
$$

A non-trivial solution is calculated by finding the value of the wave velocity that minimizes the determinant of the boundary condition matrix. When the velocity is calculated, the weighting factors C_n can be calculated by solving the set of homogenous equations.

3.8 Rayleigh Wave Velocity in AlN Half-Space

This modeling approach will be applied to calculate the Rayleigh wave velocity in a piezoelectric Aluminum Nitride half-space. The Christoffel constants for Aluminum Nitride are obtained by substituting the material property constants for AlN in equations (3-66)-(3-68). The material properties for AlN, which possesses a hexagonal crystal structure are as follows [90]

$$
c = \begin{bmatrix} 345 & 125 & 120 & 0 & 0 & 0 \\ 125 & 345 & 120 & 0 & 0 & 0 \\ 120 & 120 & 395 & 0 & 0 & 0 \\ 0 & 0 & 0 & 118 & 0 & 0 \\ 0 & 0 & 0 & 0 & 118 & 0 \\ 0 & 0 & 0 & 0 & 0 & 110 \end{bmatrix} x10^9 \quad N/m^2
$$

$$
e = \begin{bmatrix} 0 & 0 & 0 & 0 & -0.48 & 0 \\ 0 & 0 & 0 & -0.48 & 0 & 0 \\ -0.58 & -0.58 & 1.55 & 0 & 0 & 0 \end{bmatrix} \quad C/m^2
$$

$$\varepsilon = \begin{bmatrix} 8 & 0 & 0 \\ 0 & 8 & 0 \\ 0 & 0 & 9.5 \end{bmatrix} x10^{-11} \quad F/m$$

The density of AlN used in this model is 3,260 kg/m³. Substituting the material properties in the expressions for the Christoffel constants leads to the following:

$$
\begin{aligned}
&\Gamma_{11} = c_{55}b^2 + c_{11} &\quad \Gamma_{12} = 0 &\quad \Gamma_{14} = (e_{15} + e_{31})b \\
&\Gamma_{22} = c_{44}b^2 + c_{66} &\quad \Gamma_{13} = (c_{13} + c_{55})b &\quad \Gamma_{24} = 0 \\
&\Gamma_{33} = c_{33}b^2 + c_{55} &\quad \Gamma_{23} = 0 &\quad \Gamma_{34} = e_{33}b^2 + e_{15}
\end{aligned}
\qquad \Gamma_{44} = -\left[\varepsilon_{33}b^2 + \varepsilon_{11}\right]
$$

(3-72)

The boundary conditions on the free surface of an AlN half-space are:

- Vanishing of the normal stress $T_{33} = 0$.

- Vanishing of the Sagittal shear stress: $T_{13} = 0$.

- Continuity of the normal component of the electrical displacement: $D = k\varepsilon_o\varphi$.

The Rayleigh wave velocity has been calculated and found to be 5,607m/s. The c-plane of AlN is an isotropic plane; hence, the wave velocity is constant along this plane.

3.9 Weak Interface Modeling

Baik and Thompson [97] developed an interface spring model to study the effect of interface imperfections on wave propagation characteristics. For the case of an interface with imperfections the displacement of two points A and B across the interface, which are illustrated in Figure 3-7 due to an applied load σ can be expressed as the summation of two displacement components. These are the displacements Δ_p that would occur in the case of a perfect interface i.e. without the presence of interface imperfections and the additional displacement Δ_I due to the imperfections along the interface. Due to the additional displacement an interface stiffness K per unit area (N/m³) can therefore be defined as

$$K = \frac{\sigma}{\Delta_I}$$

(3-73)

This stiffness can be thought of as the stiffness of a spring that joins both sides of the interface and leads to the same displacement Δ_I as illustrated in Figure 3-7b. Different levels of adhesion will have different values of interface stiffness. An additional mass can also be added at the interface to represent volumetric imperfections. For the case of interfacial cracks no mass is added and the interface is assumed to consist of a layer of distributed massless springs since the cracks have negligible openings in the direction normal to the interface. However, in the case of volumetric imperfections such as pores or inclusions the interfacial mass can be assumed to be either positive or negative.

In the general case there will be a complex pattern of imperfections along an interface. These imperfections are assumed to be much smaller than the wavelength and the overall effect of these imperfections is to change the interface stiffness. Therefore, Baik and Thompson represented such an interface with a periodic array of cracks or contacts [97]. This facilitated the use of fracture mechanics techniques to calculate the interface stiffness due to the cracks and apply it to the spring model. Tada *et al.* [98] provides a comprehensive guide for the calculation of the additional displacement Δ_I for various crack conditions
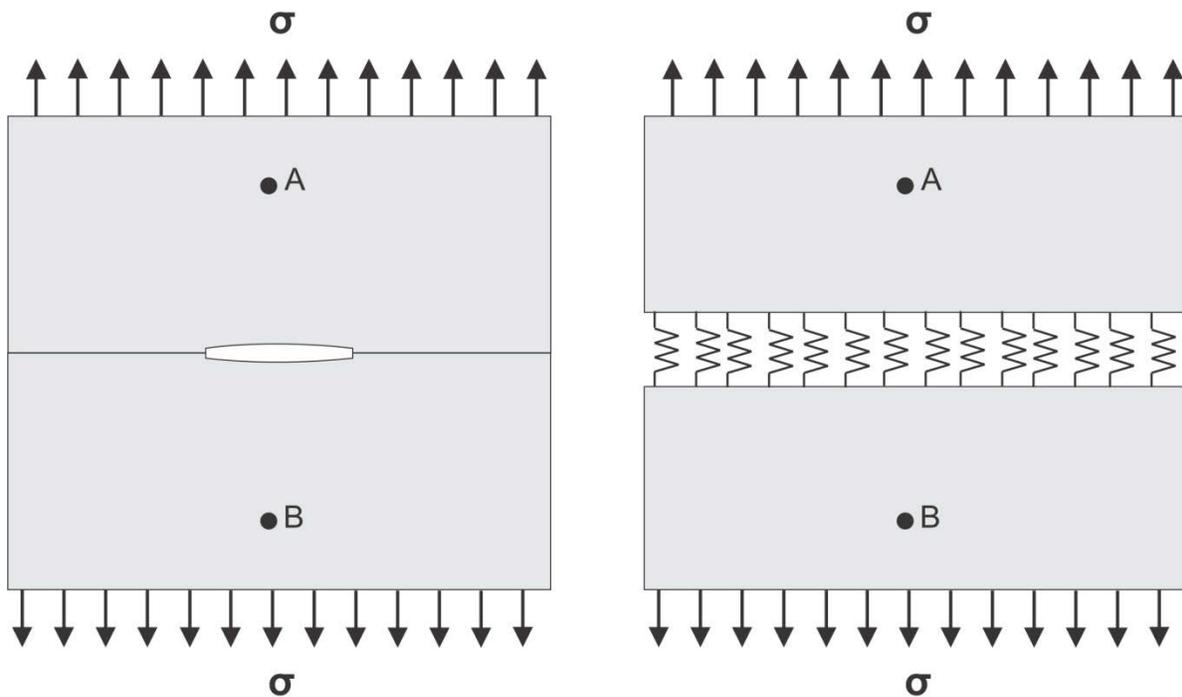
Figure 3-7: Interface spring model for weak interface modeling

Using fracture mechanics techniques multiple interface spring stiffnesses can be defined to represent Mode I, Mode II and Mode III loading conditions.
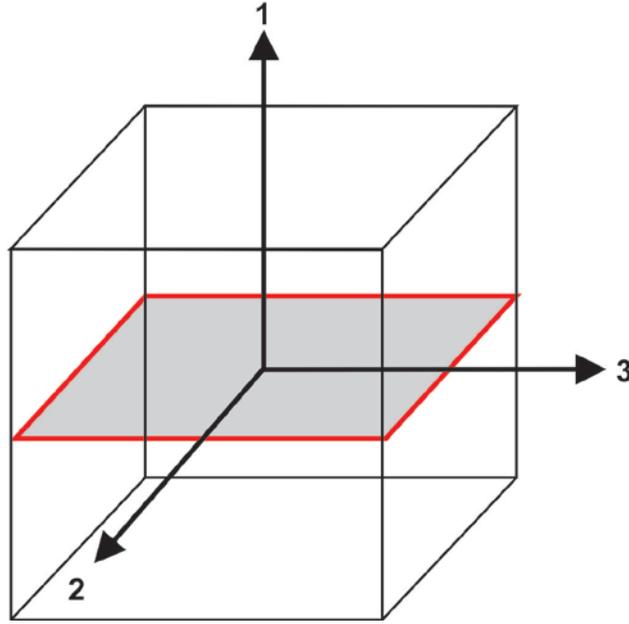
Figure 3-8: Illustration of an interface plane with its coordinate axis

The boundary conditions using the interface spring model are the continuity of the stress components, which is necessary to keep the layers intact, and the discontinuity of the displacement components. The stresses and displacements for the interface plane illustrated in Figure 3-8 in the case of an imperfect interface with spring boundary are;

$$
\begin{bmatrix} T_{11}^1 - T_{11}^2 \\ T_{12}^1 - T_{12}^2 \\ T_{13}^1 - T_{13}^2 \end{bmatrix} = \begin{bmatrix} K_{11} & K_{12} & K_{13} \\ K_{21} & K_{22} & K_{23} \\ K_{31} & K_{32} & K_{33} \end{bmatrix} \begin{bmatrix} u_1^1 - u_1^2 \\ u_2^1 - u_2^2 \\ u_3^1 - u_3^2 \end{bmatrix}
$$
(3-74)

The superscripts 1 a nd 2 r efer to the components above and below the interface plane, respectively. The K_{11} component refers to the stiffness between layers 1 and 2 i n the direction normal to the interface. K_{22} and K_{33} refer to the in-plane spring stiffnesses in the 2 and 3-directions, respectively. The K_{12} and K_{13} components refer to the shear stiffness components. For the case of isotropic media the stiffness matrix is symmetric and the off-diagonal components must vanish i.e. $K_{ij} = K_{ji} = 0$. The normal spring stiffness $K_{11} = K_N$ and $K_{22} = K_{33} = K_T$, therefore there are two

independent spring stiffness constants K_N and K_T. In this case the spring stiffness matrix has the following format

$$\begin{bmatrix} K_N & 0 & 0 \\ 0 & K_T & 0 \\ 0 & 0 & K_T \end{bmatrix}$$

(3-75)

The spring interface model will be applied to represent the adhesion of the SU-8 layer on the AlN/Si SAW sensor configuration. The spring boundary condition will be applied at the SU-8/AlN interface to represent different levels of adhesion. The values of the spring stiffness can change from zero, which is the case of complete de-bond to infinity, which represents a perfect bond i.e. an interface without any imperfections. However, in most practical cases the spring stiffness will have a finite value, which will change according to the level of adhesion of the SU-8 film. Wave dispersion profiles will be plotted for the SU-8/AlN/Si SAW sensor and multiple values for the spring stiffness will be implemented to study the effect of changing the adhesion properties of the SU-8 layer on the acoustic wave velocity.

3.10 Wave Dispersion Profiles for Multiple Configurations of the SAW Sensor

In order to plot the wave dispersion profiles for the SU-8/AlN/Si configuration with interface springs and understand the changes that take place in the dispersion profile at different values of the spring stiffness three cases for the SAW sensor need to be considered. The three cases are illustrated in Figure 3-9.
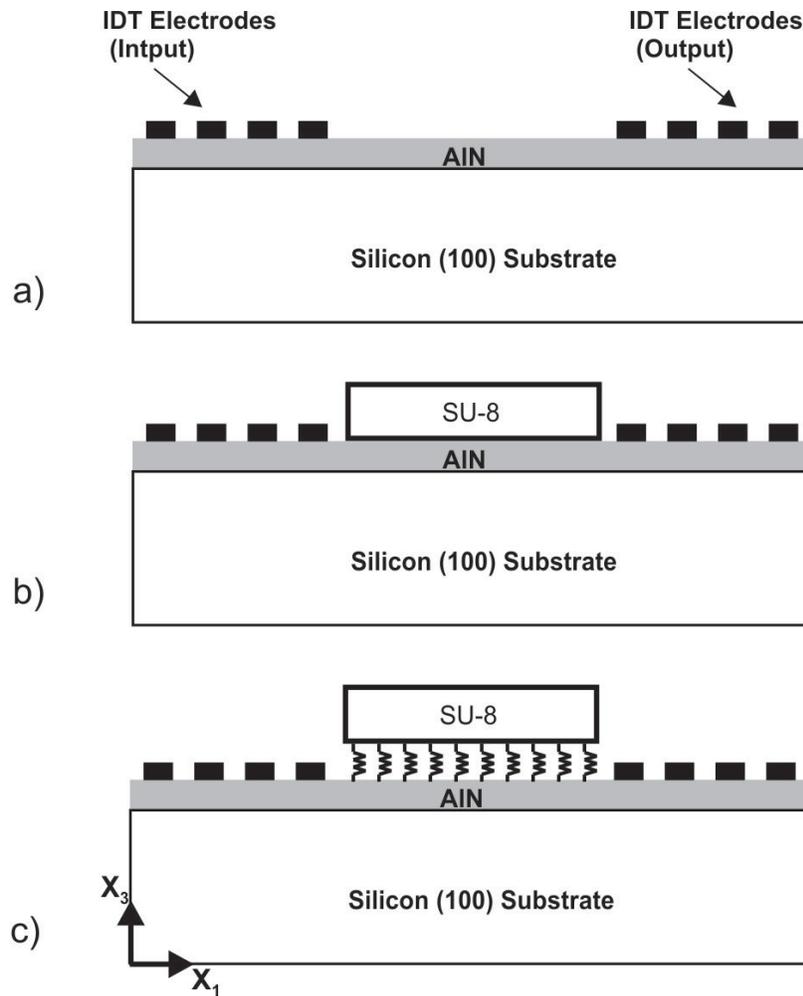
Figure 3-9: The three cases of the SAW sensor that will be considered for plotting the wave dispersion profile a) AlN/Si configuration (Case A). b) SU-8/AlN/Si configuration (Case B). c) SU-8/AlN/Si configuration with spring interface (Case C).

The material properties for the SU-8, AlN and Si layers that will be implemented in the theoretical model are listed in Table 3-1. The longitudinal, shear and Rayleigh wave velocities have been calculated for the three layers using the material properties and have been listed as well.

Table 3-1: Material properties for the SU-8, AlN and Si layers implemented in the theoretical model

	AlN [90]		Si [89]		SU-8 [99]	
Elastic Matrix in Stiffness Form ($\times 10^{11}$ Pa)	C_{11}	3.45	C_{11}	166	C_{12}	0.01257
	C_{12}	1.25	C_{12}	64	C_{44}	0.017355
	C_{13}	1.2	C_{44}	80		
	C_{33}	3.95				
	C_{44}	1.18				
	C_{66}	1.1				
Piezoelectric Matrix at Constant Strain (C/m^2)	e_{15}	-0.48				
	e_{31}	-0.58				
	e_{33}	1.55				
Permittivity Matrix at Constant Strain ($\times 10^{-11}$F/m)	ε_{11}	8	ε_{11}	10.45		
	ε_{33}	9.5	ε_{33}	10.45		
Density (kg/m^3)	3,260		2,320		1,160	
Longitudinal Wave Velocity (m/s)	10,287		8,459		2,015	
Shear Wave Velocity (m/s)	6,089		5,872		1,221	
Rayleigh Wave Velocity (m/s)	5,600		5,000		1,166	

3.11 Case A: Wave Propagation in an AlN/Si Configuration

The case considered here is a silicon substrate coated with a 1.1um thick AlN film as illustrated in Figure 3-10. This is the case when the SU-8 film is completely de-bonded from the surface of the sensor and the AlN film is a free surface. In order to plot the wave dispersion profile for this configuration the boundary conditions at the AlN/Si interface (x_3=-h) and at the free surface of the AlN film (x_3=0) need to be applied. For the AlN/Si interface the necessary boundary conditions are the continuity of the displacement u and stress components T as well as the continuity of the normal
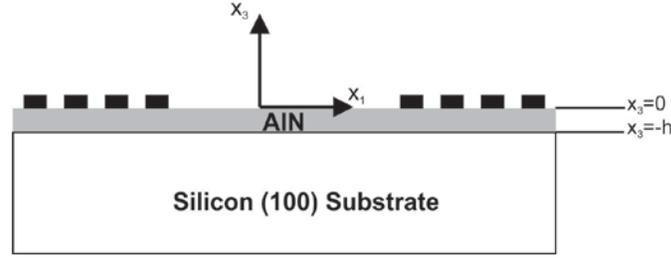
Figure 3-10: AlN coated Silicon substrate for calculating the wave dispersion profile (Case A)

component of the electrical displacement field D. At the free surface of the AlN film the boundary conditions are the vanishing of the stress components and the continuity of the normal component of the electrical displacement field. The boundary conditions for this case are listed in Table 3-2.

In order to generate the wave dispersion profile the value of the phase velocity is calculated using the theoretical approach described above. Multiple values of the normalized film thickness h_{AlN}/λ are implemented in the model to generate the dispersion profile; where h_{AlN} is the AlN film thickness (1.1µm) and λ is the acoustic wavelength. The dispersion profile is plotted in Figure 3-11.

Table 3-2: Boundary conditions for the AlN/Si configuration (Case A)

Boundary Conditions	AlN/Si
AlN Free Surface $\left(x_3 = 0\right)$	
Vanishing of the sagittal shear stress at the free surface	$T_{13} = 0$
Vanishing of the normal stress at the free surface	$T_{33} = 0$
Continuity of the normal component of the electrical displacement at the free surface	$D_3 = k\varepsilon_o\varphi$
AlN-Si Interface $\left(x_3 = -h\right)$	
Continuity of the longitudinal displacement	$u_1 = \bar{u}_1$
Continuity of the vertical particle displacement	$u_3 = \bar{u}_3$
Continuity of the normal stress	$T_{33} = \bar{T}_{33}$
Continuity of the sagittal shear stress	$T_{13} = \bar{T}_{13}$
Continuity of the electrical potential	$\varphi = \bar{\varphi}$
Continuity of the normal component of the electrical displacement at the interface	$D_3 = \bar{D}_3$

Figure 3-11: Dispersion profile for the AlN/Si Configuration (Case A)

The dispersion profile illustrates the change in Rayleigh wave velocity at various h_{AlN}/λ configurations. Initially the wave velocity is equivalent to the Rayleigh wave velocity of the silicon substrate since the wavelength is large and the wave penetrates deep inside the substrate. However, as the h_{AlN}/λ value increases the wavelength is smaller and the penetration depth of the wave decreases. The wave is then more confined near the AlN/Si interface and hence more sensitive to the AlN properties. The Rayleigh wave velocity of AlN is higher than Silicon; 5,607 and 5,000m/s, respectively; therefore the dispersion curve increases due to the increase in wave velocity. As the wavelength gets smaller the wave gets more confined in the AlN film until the AlN film acts as a half-space for the wave and the Rayleigh wave velocity approaches the velocity in an AlN half-space, which is 5,607m/s as illustrated in Figure 3-11.

3.12 Wave Propagation in an SU-8/AlN/Si Configuration (Case B)

In this configuration the SU-8 layer is assumed to be bonded to the AlN surface without any interface defects i.e. a perfect bond. This configuration consists of an 80nm thick gold film (Au) deposited on the AlN surface and the omnicoat layer is patterned on top of the Au film to enhance the adhesion of the SU-8 layer. The SU-8 layer is then deposited and patterned above the omnicoat film. When modeling this configuration the mass loading effect of the omnicoat and Au layers will
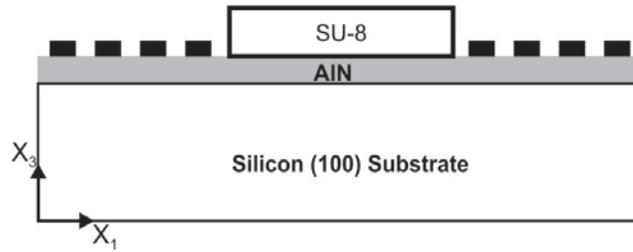
Figure 3-12: SU-8/AlN/Si sensor configuration with perfect bond at the SU-8/AlN interface (Case B)

be ignored due to their reduced thickness in comparison to the other layers. It is assumed that the SU-8 layer is patterned above the AlN film as illustrated in Figure 3-12. However, the electrical boundary condition due to the Au film will be implemented.

The boundary conditions at the SU-8/AlN interface are the continuity of the displacement and stress components on the x_1-x_3 plane. The electrical potential ϕ at the SU-8/AlN interface will be set to zero to account for the electrical effect of the Au film. The boundary conditions for this configuration are listed in Table 3-3.

Figure 3-13: Dispersion profile for the SU-8/AlN/Si configuration illustrating the first 10 modes (Case B)

Table 3-3: Boundary Conditions for the SU-8/AlN/Si Configuration (Case B)

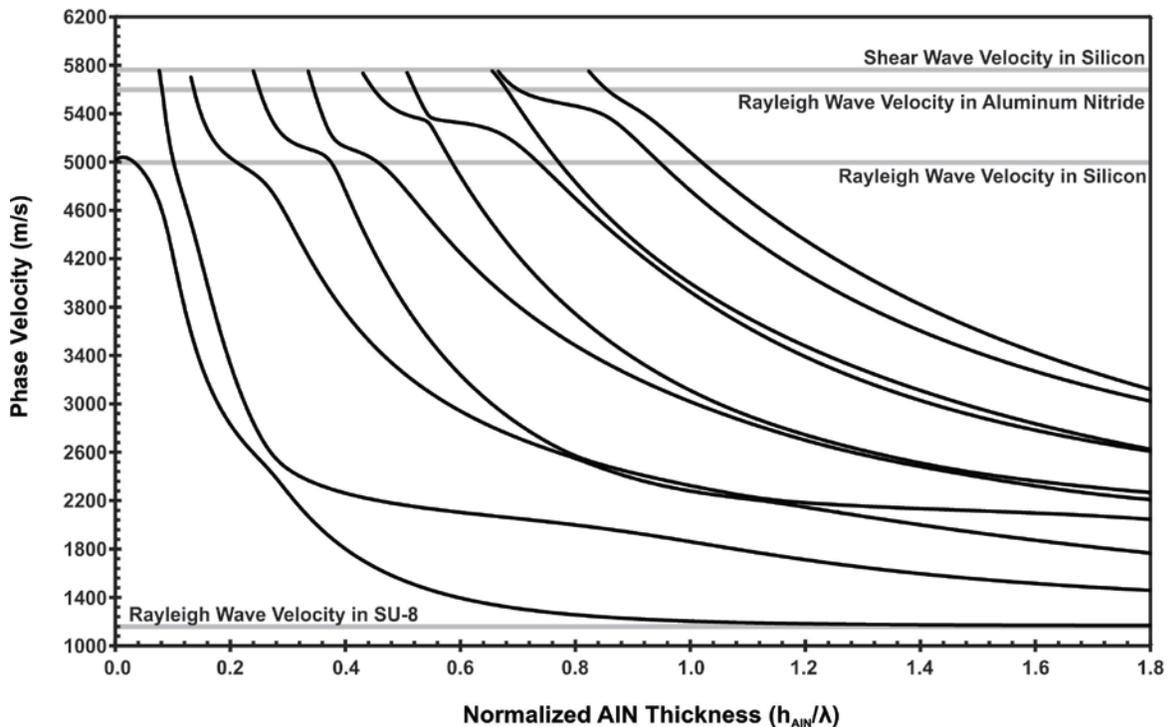| Boundary Conditions	SU-8/AlN/Si
SU-8 Free Surface $\left(x_3 = h_1\right)$	
Vanishing of the sagittal shear stress at the free surface	$\tilde{T}_{13} = 0$
Vanishing of the normal stress at the free surface	$\tilde{T}_{33} = 0$
AlN/SU-8 Interface $\left(x_3 = 0\right)$	
Continuity of the longitudinal displacement	$u_1 = \overline{u}_1$
Continuity of the vertical particle displacement	$u_3 = \overline{u}_3$
Continuity of the normal stress	$T_{33} = \overline{T}_{33}$
Continuity of the sagittal shear stress	$T_{13} = \overline{T}_{13}$
Grounding of the electrical potential	$\phi = 0$
AlN/Si Interface $\left(x_3 = -h\right)$	
Continuity of the longitudinal displacement	$\overline{u}_1 = \tilde{u}_1$
Continuity of the vertical particle displacement	$\overline{u}_3 = \tilde{u}_3$
Continuity of the normal stress	$T_{33} = \tilde{T}_{33}$
Continuity of the sagittal shear stress	$T_{13} = \tilde{T}_{13}$
Continuity of the electrical potential	$\phi = \overline{\phi}$
Continuity of the normal component of the electrical displacement at the interface	$D_3 = \overline{D}_3$

The wave dispersion profile for this configuration is shown in Figure 3-13, which illustrates the first 10 modes for the SU-8/AlN/Si configuration. The first mode starts at the Rayleigh wave velocity in silicon and then drops as the value for h_{AlN}/λ increases since the wave gets more confined in the SU-8 layer. The SU-8 layer has a lower Rayleigh wave velocity in comparison to the AlN film, which leads to a drop in the wave dispersion profile for higher values of h_{AlN}/λ. The velocity continues to drop until it reaches the Rayleigh wave velocity in the SU-8 film. The higher order modes start at the shear wave velocity of the silicon substrate and continue to drop until they reach the shear wave velocity of the SU-8 film.

3.13 Case C: Wave Propagation in SU-8/AlN/Si Configuration with Spring Boundary

In order to study the effect of different levels of SU-8 adhesion on the phase velocity the interface between the SU-8 layer and the AlN film will be modeled using a layer of distributed massless springs, which have a spring stiffness K (N/m^3). An illustration of the interface springs at the SU-8/AlN interface is shown in Figure 3-14. As the value of the spring stiffness changes different levels of adhesion can be accounted for. In the SU-8/AlN/Si configuration (case B) the adhesion of SU-8 to the AlN film is assumed to be free of defects, which is equivalent to having interface springs with infinite stiffness. However, when the SU-8 film is completely de-bonded the AlN film surface is free (case A), which is equivalent to a spring stiffness value of zero. For the intermediate cases the spring stiffness values are finite.
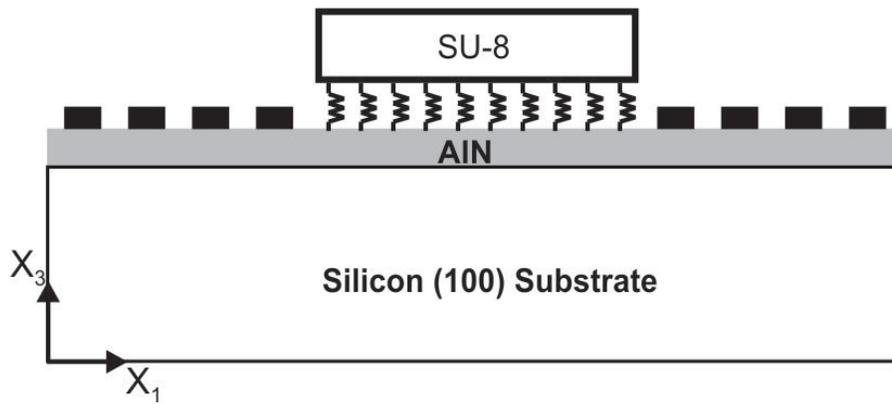
Figure 3-14: SU-8/AlN/Si sensor configuration with interface springs at the SU-8/AlN interface (Case C)

The interface spring model is commonly used to represent changes to the adhesion of bonded structures [70, 100, 101]. Due to the presence of interfacial springs the displacement field (u_1 and u_3) is discontinuous across the interface; however, the stress field is continuous. The boundary conditions for the SU-8/AlN interface with interface springs are listed in Table 3-4. The boundary conditions for all three cases of the SU-8/AlN/Si SAW sensor are listed to illustrate the changes in the boundary conditions as the sensor configuration changes.

Table 3-4: Boundary Conditions for the three configurations of the SU-8/AlN/Si SAW Sensor

	AlN[a]/Si[b] (case A)	SU-8[c]/AlN/Si (case B)	SU-8/AlN/Si (case C)
Free Surface	$T_{13} = 0$ $(x_3=0)$ $T_{33} = 0$ $(x_3=0)$ $D_3 = k\varepsilon_0^d \phi$ $(x_3=0)$	$\tilde{T}_{13} = 0$ $(x_3=h_2)$ $\tilde{T}_{33} = 0$ $(x_3=h_2)$ —	$\tilde{T}_{13} = 0$ $(x_3=h_2)$ $\tilde{T}_{33} = 0$ $(x_3=h_2)$ —
AlN/Si Interface $(x_3=-h_1)$	$u_1 = \overline{u}_1$ $u_3 = \overline{u}_3$ $T_{33} = \overline{T}_{33}$ $T_{13} = \overline{T}_{13}$ $\phi = \overline{\phi}$ $D_3 = \overline{D}_3$	$u_1 = \overline{u}_1$ $u_3 = \overline{u}_3$ $T_{33} = \overline{T}_{33}$ $T_{13} = \overline{T}_{13}$ $\phi = \overline{\phi}$ $D_3 = \overline{D}_3$	$u_1 = \overline{u}_1$ $u_3 = \overline{u}_3$ $T_{33} = \overline{T}_{33}$ $T_{13} = \overline{T}_{13}$ $\phi = \overline{\phi}$ $D_3 = \overline{D}_3$
AlN/SU-8 Interface $(x_3=0)$	— — — — —	$u_1 = \tilde{u}_1$ $u_3 = \tilde{u}_3$ $T_{33} = \tilde{T}_{33}$ $T_{13} = \tilde{T}_{13}$ $\phi = 0$	— — $T_{33} = \tilde{T}_{33} = K[u_3 - \tilde{u}_3]$ $T_{13} = \tilde{T}_{13} = K[u_1 - \tilde{u}_1]$ $\phi = 0$

Multiple wave dispersion profiles are plotted using the interface spring model to illustrate the changes that occur at different levels of adhesion by changing the stiffness value of the interface springs. Figure 3-15 illustrates the variation in the wave dispersion profile for the SU-8/AlN/Si configuration when the interface spring stiffness changes from 1×10^8 to 1×10^{10} N/m^3. At K=1×10^8 N/m^3 the wave dispersion profile matches the dispersion profile for the AlN/Si (case A) configuration as illustrated in Figure 3-15. This is because at this low value for the interface stiffness no acoustic wave propagates in the SU-8 layer and its properties do not influence the acoustic wave velocity. The wave propagates in the AlN/Si structure and the wave velocity follows the dispersion profile in Figure 3-11.
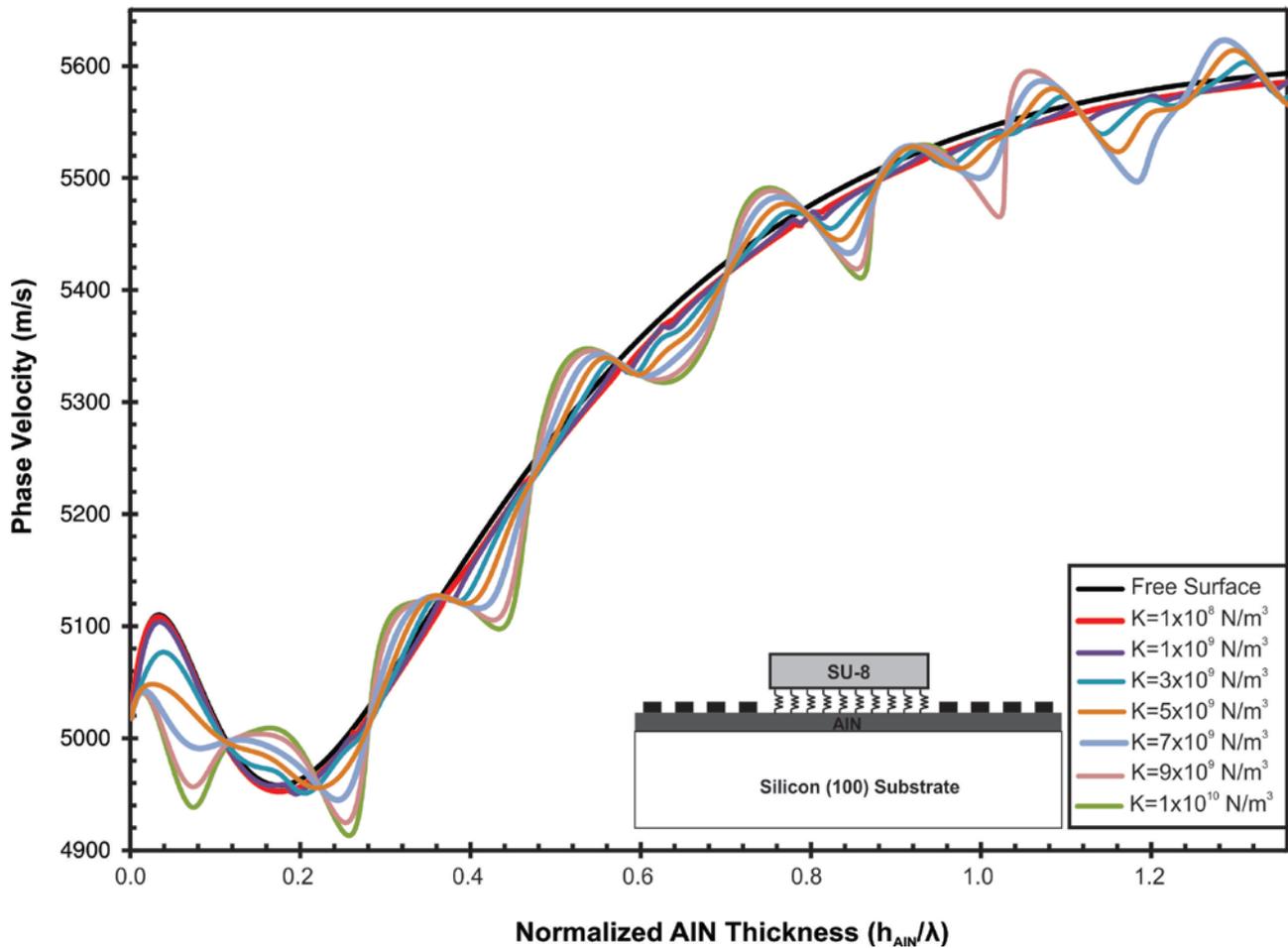
Figure 3-15: Wave dispersion profiles for the SU-8/AlN/Si configuration with interface springs and spring stiffness (K) in the range 1×10^8-1×10^{10} N/m^3

As the interface spring stiffness increases the time varying stress field in the AlN film increases, which is then transferred to the SU-8 layer leading to acoustic wave propagation in the SU-8 layer. The value of the Rayleigh wave velocity for the SU-8 layer is 1,166m/s, which is lower than AlN and silicon; 5,600 and 5,000 m/s, respectively, therefore, the wave velocity has a tendency to drop as the value for h_{AlN}/λ increases as shown in Figure 3-13. However, the Rayleigh wave velocity for the AlN film is higher than the SU-8 film and the silicon substrate, thus the wave velocity has a tendency to increase as the value for h_{AlN}/λ increases as illustrated in Figure 3-11. This variation in the Rayleigh wave velocity between the SU-8 and AlN layers at intermediate levels of adhesion for the SU-8 film leads to fluctuating dispersion profiles as illustrated in Figure 3-15. As the adhesion of the SU-8 film increases the fluctuations in the dispersion profile continue to increase until the wave dispersion profile eventually drops at K=2.6×10^{10} N/m^3 as shown in Figure 3-16. For interface
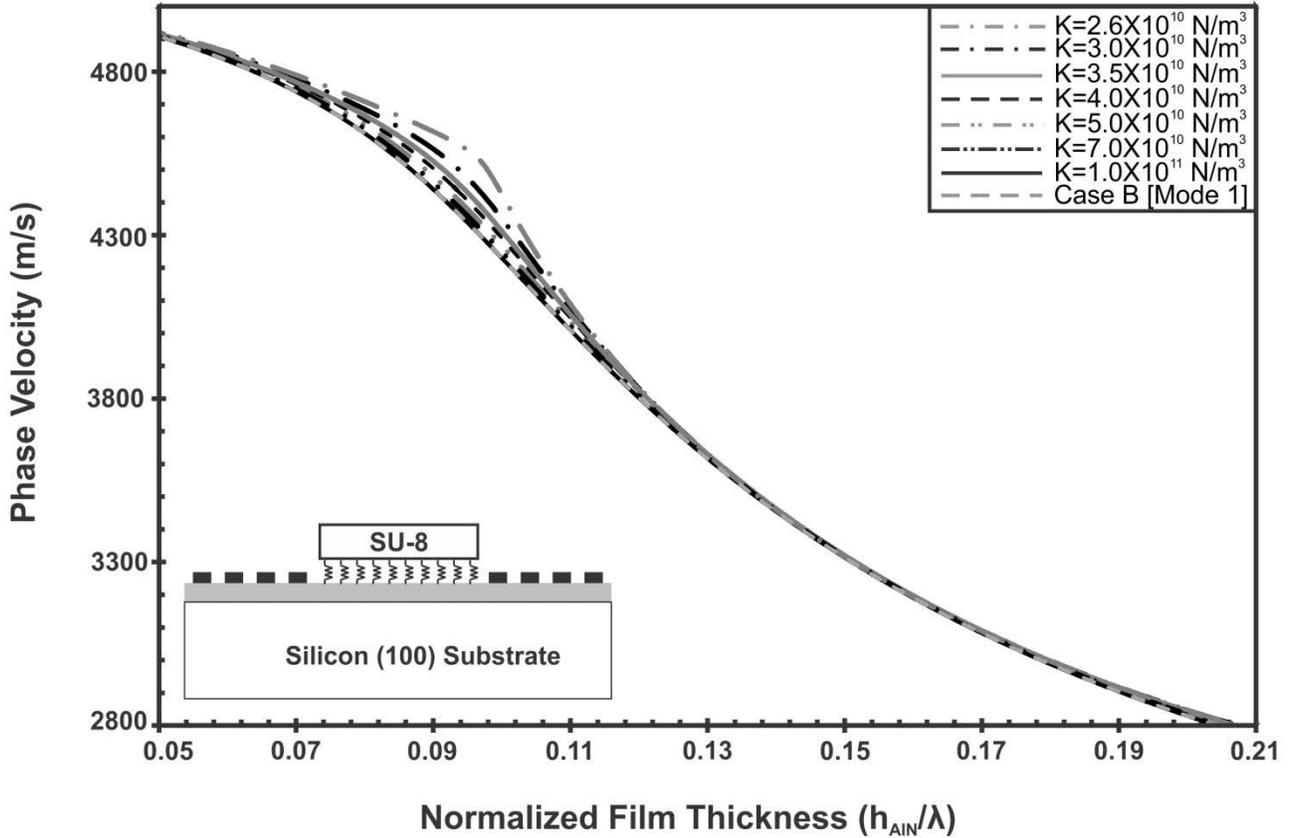
Figure 3-16: Wave dispersion profiles for the SU-8/AlN/Si configuration with interface springs and spring stiffness in the range $K=2.6 \times 10^{10} - 1 \times 10^{11}$ N/m^3

spring stiffness values higher than 2.6×10^{10} N/m^3 the wave dispersion profiles shift to lower values. The variation in the dispersion profiles occur up to $h_{AlN}/\lambda = 0.13$ as illustrated in Figure 3-16 and then the velocity values coincide for all stiffness values. At $K=1 \times 10^{11}$ N/m^3 the dispersion profile matches the dispersion profile for the SU-8/AlN/Si configuration (case B) indicating that this value for the interface stiffness corresponds to infinite stiffness, which occurs when the SU-8 is perfectly bonded to the AlN film.

The wave dispersion profiles for the different values of K re-plotted in Figure 3-17 with the contour plots of the normalized amplitude of the T_{33} stress component at the SU-8/AlN interface overlaid on the dispersion curves. The inset in Figure 3-17 illustrates the same dispersion profiles plotted with a legend to identify the different dispersion curves. In the regions where the dispersion curves drop the stress is a minimum and then starts increasing as the h_{AlN}/λ value increases due to the confinement of the wave in the SU-8 layer. The stress continues to increase as the dispersion
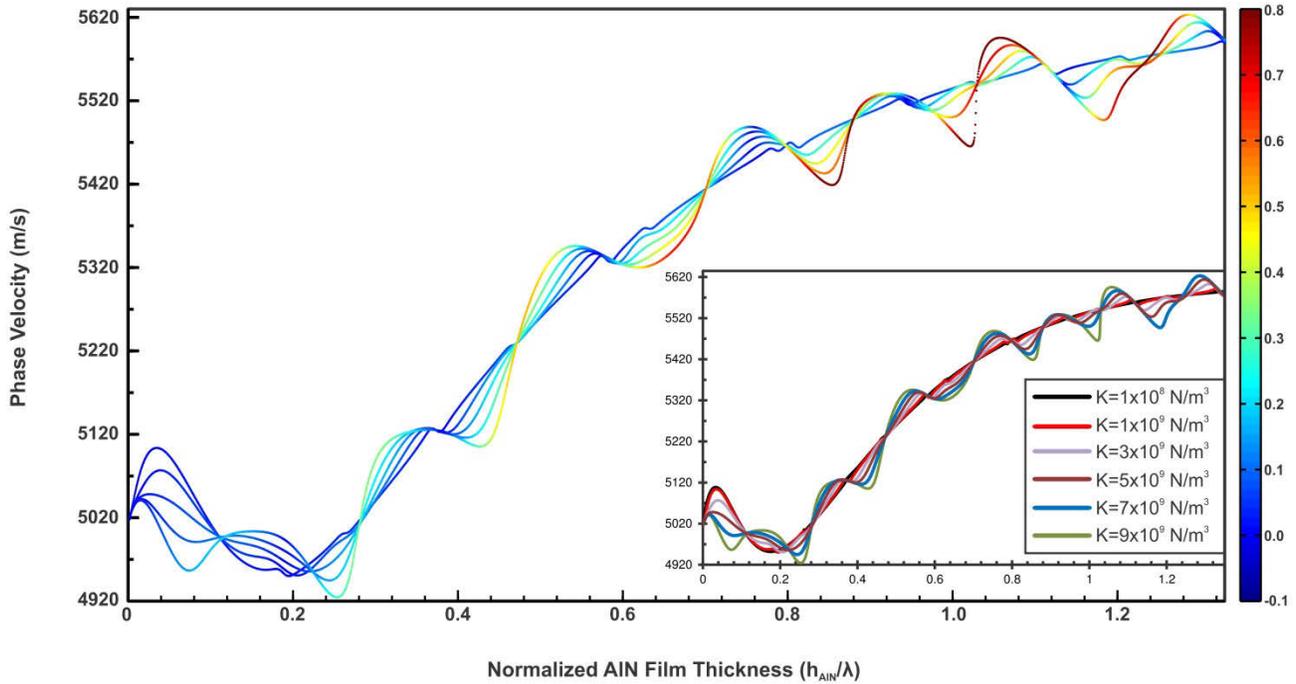
Figure 3-17: Wave dispersion profiles for the SU-8/AlN/Si configuration with spring boundary for $1x10^8 < K < 1x10^{10}$ N/m^3. The normalized amplitude of the T$_{33}$ stress component is calculated and overlaid as contour plots on the dispersion profiles.

curve shifts upwards but then begins to decrease as the velocity values continue to increase to approach the AlN/Si dispersion profile. Just before the dispersion profile starts dropping again the stress is a minimum since the wave is more confined in the AlN/Si structure and as the dispersion curve drops the stresses increase once again. Figure 3-18 illustrates the stress profiles in the SU-8 layer for different values of h_{AlN}/λ. The stresses increase as the value of h_{AlN}/λ increases up to $h_{AlN}/\lambda = 0.1245$ since the wave is more confined near the interface. However, above $h_{AlN}/\lambda = 0.1245$ the stresses at the SU-8/AlN interface (x$_3$=0) drop as illustrated but the stresses inside the SU-8 layer continue increasing as the value of h_{AlN}/λ increases until they eventually drop to zero at the free surface. The normalized stress amplitude of the T$_{33}$ component has been plotted for the AlN film in Figure 3-19 and a similar trend is observed. The stresses continue to increase at the interface and then drop above $h_{AlN}/\lambda = 0.1245$ since the weak interface cannot sustain the increased stress. However, the stresses inside the AlN film continue to increase as the value of h_{AlN}/λ increases indicating that the wave energy is concentrated inside the film away from the SU-8/AlN interface.
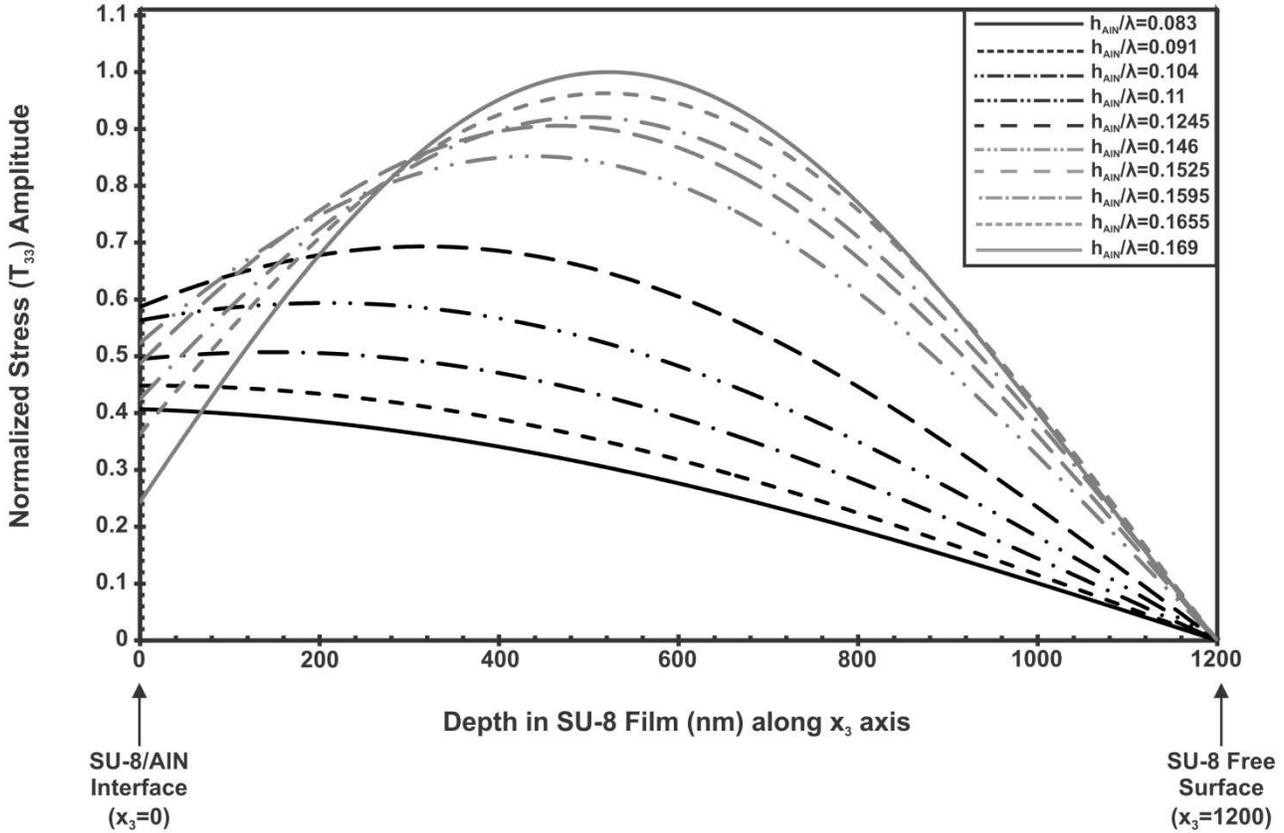
Figure 3-18: Depth profiles for the normalized amplitude of the T_{33} stress component in the SU-8 film at different values of the normalized AlN film thickness (h_{AlN}/λ)

Figure 3-20 illustrates the stress profiles within 100nm on both sides of the interface inside the SU-8 and AlN layers. These profiles illustrate the continuity of the stresses across the interface as well as the stress fluctuations in both layers for different values of h_{AlN}/λ.

The dispersion profile for the free surface case where the AlN layer is a free surface is plotted in Figure 3-21. The normalized T_{33} stress component generated in the AlN film is overlaid on the dispersion profile as illustrated. The stresses in the AlN layer continue to increases as the value of h_{AlN}/λ increases due to the increased confinement of the wave near the interface.
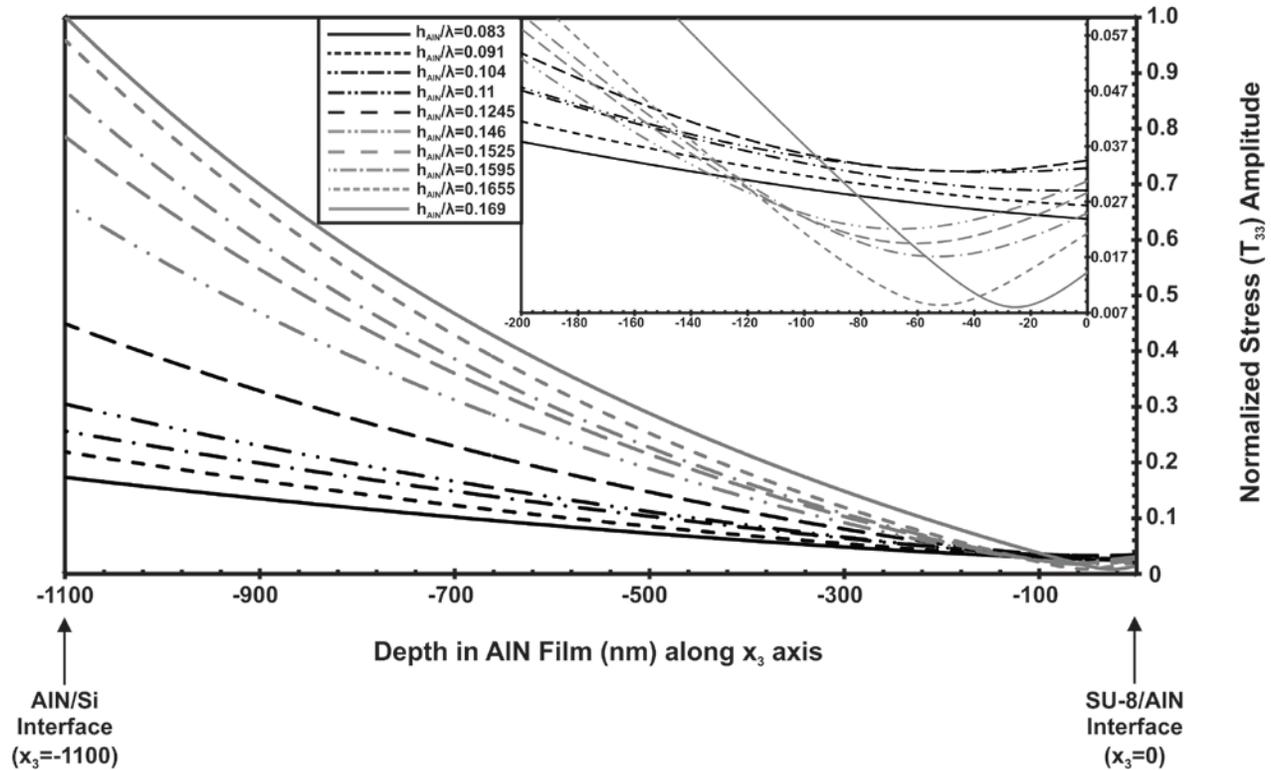
Figure 3-19: Depth profiles for the normalized amplitude of the T_{33} stress component in the AlN film at different values of the normalized film thickness (h_{AlN}/λ). The inset illustrates the stress profiles within 200nm of the SU-8/AlN interface for a better illustration of the stress fluctuations.

It is required to investigate the sensitivity of the SAW sensor configurations to select the designs with highest sensitivity. The normalized film thickness (h_{AlN}/λ) values correspond to different designs for the SAW sensor. As the value for h_{AlN}/λ increases the operating frequency of the device increases and the sensitivity also increases. As the operating frequency increases the wave is more confined near the interface and is more sensitive to the changes in adhesion of the SU-8 film. In order to examine the sensitivity of different designs for the SAW sensors the changes in the phase velocity values as the interface stiffness changes for different h_{AlN}/λ configurations are calculated and plotted in Figure 3-22.
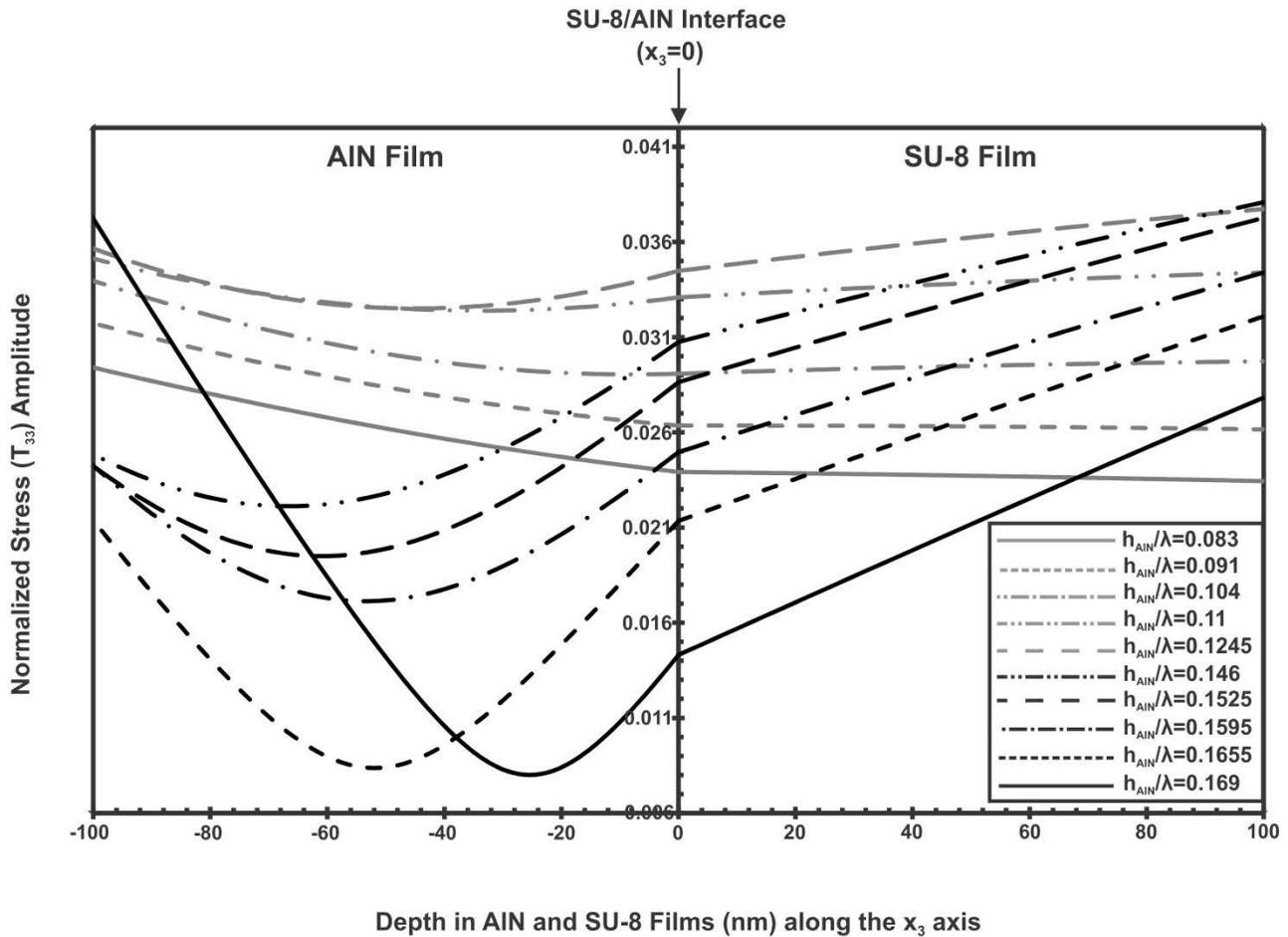

Figure 3-20: Depth profiles for the normalized amplitude of the T_{33} stress component within 100nm on bth sides of the SU-8/AlN interface at different values of the normalized film thickness (h_{AlN}/λ)

The wave dispersion profiles for different values of the interface spring stiffness in Figure 3-22 illustrate that at K=1x10^8 N/m^3 the dispersion profile matches that for the AlN/Si configuration in Case A. The variation in acoustic wave velocity values between these two cases is negligible for the different h_{AlN}/λ configurations as shown in for K=1 x10^8 N/m^3. At low values of the spring interface stiffness i.e. up to K=5 x10^8 N/m^3 the sensitivity increases as h_{AlN}/λ decreases. At K=1 x10^9 N/m^3 the trend starts reversing and from K=4 x10^9 N/m^3 to K=5 x10^{11} N/m^3 the sensitivity increases as the value for h_{AlN}/λ increases.
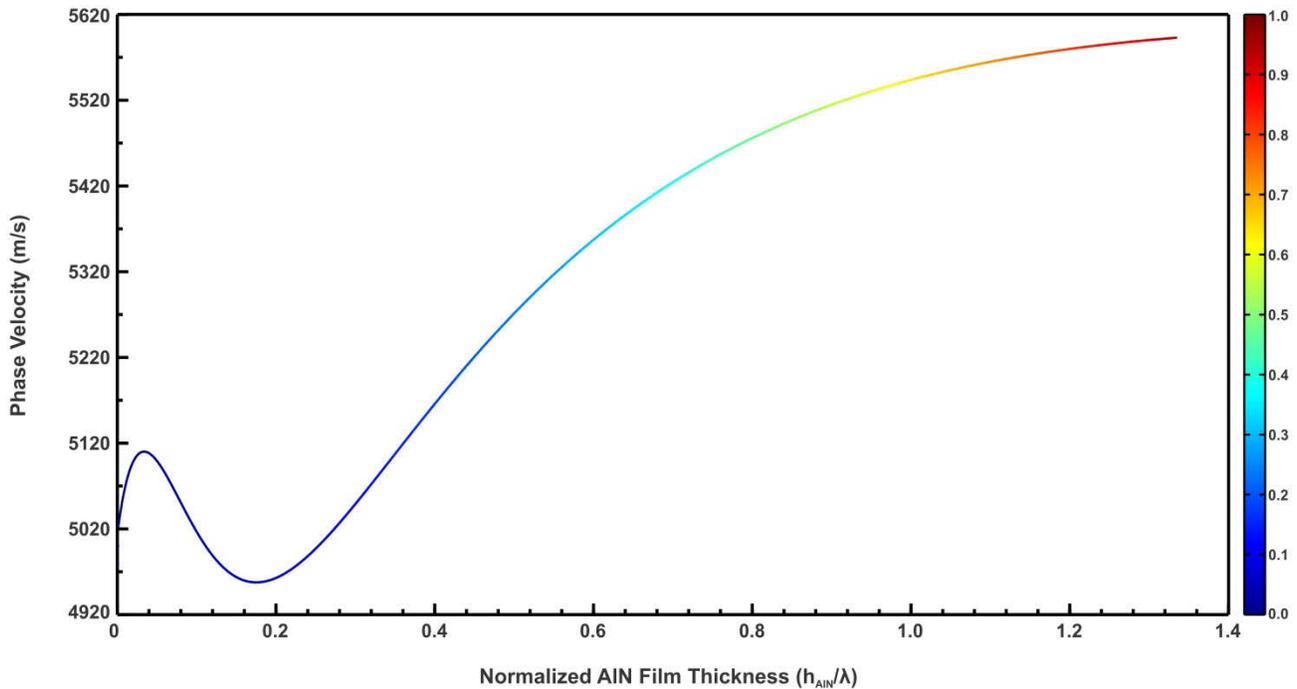
Figure 3-21: Wave dispersion profile for the AlN/Si configuration with the equivalent stress in the AlN film overlaid on the dispersion curve

This is because as the interface stiffness increases the displacement discontinuity across the interface decreases and the interfacial stresses increase. At higher h_{AlN}/λ configurations the wave is more confined near the interface and is more capable of detecting these changes with high sensitivity. The changes in wave velocity are highest at K=4 x10^9 N/m^3 for h_{AlN}/λ values greater than 0.006. This is because the increase in interface stiffness is leading to a significant drop in the wave velocity since the adhesion of the SU-8 layer is improving and this change is captured by the waves that are more concentrated near the SU-8/AlN interface. This effect is represented by a drop in the dispersion profile in Figure 3-15 at K=4 x10^9N/m^3. The second peak occurs at K=2.6 x10^{10} N/m^3 because the dispersion profiles drop as the interface stiffness increases until it eventually matches Case B as illustrated in Figure 3-16. The changes to the acoustic wave velocity beyond K=2.6 x10^{10} N/m^3 are within 0.1%, which is represented by the small shifts occurring in the dispersion profiles in Figure 3-16. The change in wave velocity in Figure 3-22 is plotted for spring stiffness values up to K=5 x10^{11} N/m^3 to illustrate that any further increase beyond K=1 x10^{11} N/m^3 would lead to a negligible change in wave velocity since at K=1 x10^{11} N/m^3 the dispersion profile matches Case B as illustrated in Figure 3-16.
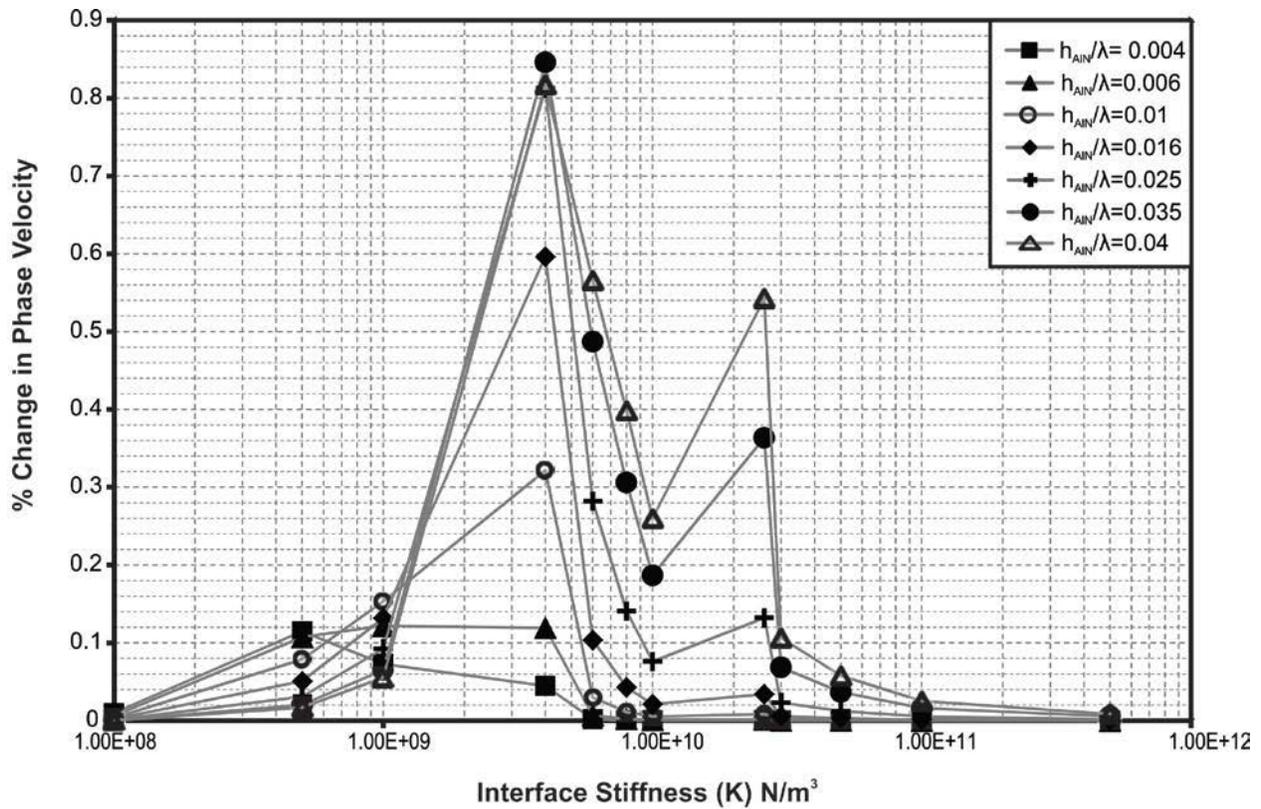
Figure 3-22: Changes in wave velocity for the SU-8/AlN/Si SAW sensor at multiple values of the normalized film thickness (h_{AlN}/λ) due to the change in interface spring stiffness (K)

3.14 Conclusions

This chapter presented the theoretical background for understanding wave propagation characteristics in infinite media. The slowness curves were plotted for isotropic, anisotropic and piezoelectric media to illustrate the variation of the wave velocties for different crystal structures. The derivation of the Rayleigh wave solution was also illustrated and the displacements solutions in an isotropic half-space were also plotted. Dispersion curves illustrating the change in SAW velocity for different configurations of the AlN/Si structure were plotted. The interface spring model was introduced to demonstrate the use of interface springs with finite rigidity to represent different adhesion levels of the SU-8 thin film. Due to the intermediate levels of adhesion of the SU-8 film the dispersion curves exhibited a fluctuating pattern. The stress in the SU-8 and AlN films was evaluated to demonstrate that the fluctuations in SAW velocity are primarily due to the fluctuating stress field at the SU-8/AlN interface. Finally, the sensitivity of different h_{AlN}/λ configurations was investigated and the results illustrated an increased sensitivity as the value of h_{AlN}/λ increases. Four configurations of the SAW sensors with high sensitivity will be selected for fabrication.

CHAPTER 4.   MICROFABRICATION OF THE SU-8/ALN/SI SURFACE ACOUSTIC WAVE SENSOR[2]

4.1 Overview

This chapter illustrates the process developed for fabrication of the SU-8/AlN/Si SAW sensor. The SAW sensor utilized in this study is developed at the micro and nanofabrication facility at the University of Alberta "Nanofab". One of the main objectives of this study is to investigate the change in sensor sensitivity in detecting the change in adhesion of the SU-8 layer; therefore, four SAW sensor designs were fabricated and tested. The four SAW sensors operate at four different center frequencies ranging from 84-208MHz. For each design of the four SAW sensors two configurations are developed to create two adhesion states for the SU-8 film. The first configuration consists of patterning the SU-8 layer on top of the AlN/Si SAW sensor and a thin gold film is patterned below the SU-8 layer and on top of the AlN film. In the second configuration the gold film will be coated with a layer of omnicoat and the SU-8 film will be patterned on top of it. The frequency response from the two configurations will be used to calculate the frequency and velocity shifts. The four SAW sensor designs will be fabricated on the same substrate, adjacent to each other in order to minimize the effect of variations in the microfabrication processes on the frequency response of the SAW sensors. The process flow for fabricating the sensors will be presented and the processes involved will be discussed in detail. The challenges faced at multiple stages will also be presented as well as the characterization techniques adopted to evaluate the recipes for the process flow.

4.2 Material Selection

SU-8 is a widely used structural material for MEMS applications. In this study its adhesion on the surface of the AlN/Si SAW sensor is modified to investigate the effect of different adhesion states on the acoustic wave propagation velocity. An introduction to the chemical structure and

---

[2] Someof the material in this chapter has been published by El Gowini and Moussa.[102]

properties of SU-8, its applications in MEMS devices and its adhesion to metallic layers will be presented.

The SAW sensor utilizes a piezoelectric Aluminum Nitride film for the electrical excitation of acoustic waves. The deposition step of the AlN film is the most challenging step in the process for fabricating the SAW sensor. A discussion of the reactive sputtering technique, which will be used to deposit AlN thin films, will be presented. The characterization of the AlN crystal structure using XRD will also be discussed and the XRD plot of the AlN film deposited will be presented.

4.2.1 *SU-8 Properties and Processing Techniques*

4.2.1.1 SU-8 Chemical Structure and Material Properties

A photoresist is a material that undergoes physical and chemical change after irradiation with an energy source and the unchanged regions can be removed by dissolving in a solvent. Photoresists can be classified in to two major groups; positive and negative. A positive photoresist becomes soluble in a solvent upon irradiation; meanwhile a negative photoresist becomes insoluble after irradiation. SU-8 is an epoxy based negative photoresist material, which consists of glycidyl ether derivative of Bisphenol A novolac (also known as EPON® resin SU-8 and manufactured by Shell Chemicals) and photoinitiator (triaryl sulfonium salt) dissolved in a cyclopentanone solvent (CP) solvent. Each monomer unit consists of 8 epoxy groups, hence its commercial name SU-8.

SU-8 was developed by IBM in 1989 to be used as a resist material in deep UV lithography for semiconductor applications [103]. However, its applications have been extended to x-ray and e-beam lithography. SU-8 possesses desirable properties that led to its current widespread use in patterning high aspect ratio structures for MEMS applications. Its low molecular weight ~7,000 allows it to be soluble in a wide range of organic solvents such as propylene glycol methyl ether acetate (PGMEA), cyclopentanone (CP) and methyl iso-butyl ketone (MIBK) and form highly concentrated solutions that contain 72-85% solids by weight. This facilitates the formation of very thick layers in a single spinning cycle. In addition, SU-8 has very low optical absorption in the near –UV range i.e. for wavelengths >350nm [104], which allows the patterning of very thick layers. If a photoresist has high optical absorption it would be very difficult to pattern HAR structures even with high doses of UV exposure, however, with SU-8 it is possible to pattern HAR structures with aspect ratios up to 20 [105, 106]. The high functionality of the SU-8 photoresist leads to a high degree of cross-linking

during polymerization, which allows it to be chemically and thermally stable and leads to improved aspect ratio and side-wall profile. SU-8 can be used as a masking layer in prolonged plasma etching processes [104]. Table 4-1 lists some of the useful properties for SU-8.

Table 4-1: Material Properties of SU-8

Young's Modulus E (postbake temp. 95ºC)	4.02 GPa	[99]
Density ρ	1,160 kg/m^3	[99]
Poisson Ratio v	0.42	[99]
Glass Temperature T_g (fully crosslinked)	>200 ºC	[107]
Degradation Temperature T_d (fully crosslinked)	380 ºC	[107]
Thermal Expansion Coefficient α (postbake temp. 95ºC)	52±5.1 ppm/K	[108]
Polymer Shrinkage	7.5%	[108]

SU-8 layer thicknesses up to 700μm have been achieved using a single spin cycle [109]. Multiple spin coating cycles of SU-8 can be implemented to achieve ultra-thick SU-8 layers in the range of 1.0-1.5mm [110]. Thicknesses up to 3mm have also been achieved via casting techniques [106]. SU-8 has a wide range of desirable properties that led to its widespread use in MEMS applications other than a photoresist material. These include optical waveguides [111] and acoustic waveguide applications in love wave sensors [112]. It is used as a structural material in energy harvesters [113] and graphene based resonators [114]. In addition, SU-8 has also been widely used in microfluidic applications as a mold for fabricating PDMS micro-channels [115] or as a candidate material for microfluidic channels [116].

4.2.1.2 SU-8 Processing

In this study SU-8 is applied to the substrate via spin coating and the desired SU-8 film thickness is 1.5μm. A soft baking step on a hot plate follows the spin coating cycle, which is necessary to drive off the solvent. The SU-8 film is then exposed to UV light at wavelengths >365nm. Due to exposure the photoinitiator (triaryl sulfonium salt) decomposes to generate a strong acid (hexafluoroantimonic acid), the term photoacid generater (PAG) is used interchangeably with photoinitiator. The acid diffuses to the SU-8 monomers and opens the epoxy rings to initiate polymerization. Cross linking takes place when an epoxy group reacts with another. Due to the high

functionality of the SU-8 a dense cross-linked network develops. A postexposure bake (PEB) step at elevated temperatures is required in order to accelerate the cross-linking reactions. The PEB promotes the diffusion of the acid and increases the mobility of the SU-8 monomers, which improves the cross-linking. The unexposed regions will undergo no cross-linking and will dissolve
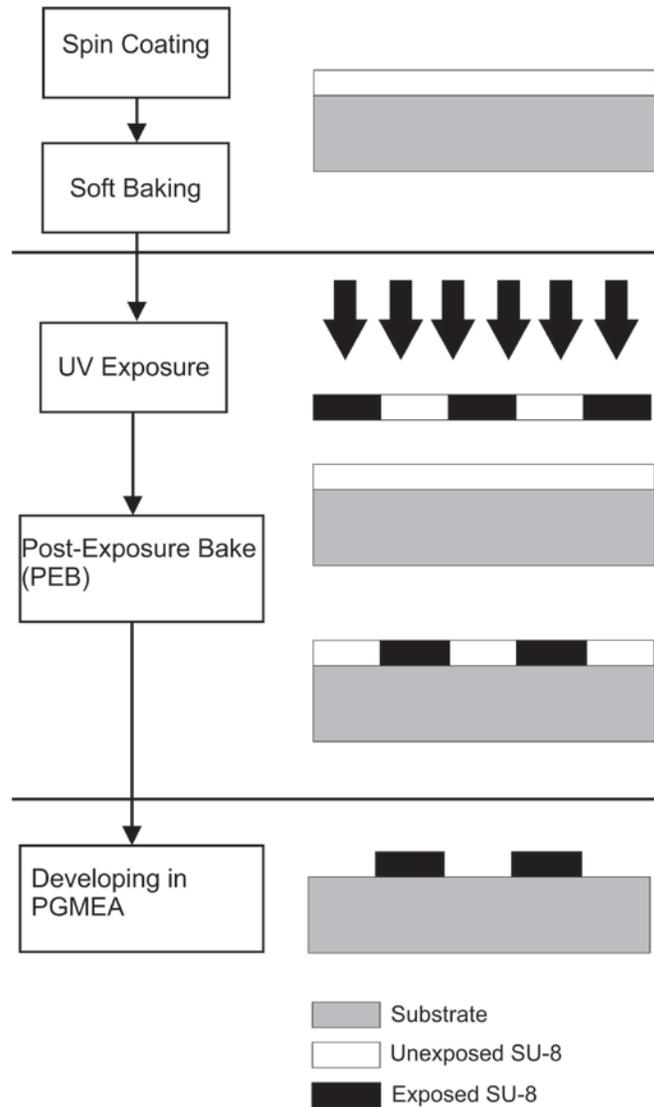

Figure 4-1: SU-8 Patterning Process Flow

upon inserting the substrate in propylene glycol methyl ether acetate (PGMEA) developer leaving a negative image of the photomask. Figure 4-1 illustrates the process flow for pattering SU-8 films.

4.2.1.3 SU-8 Adhesion to Metallic Layers

The wide range of SU-8 applications led to significant efforts to investigate its adhesion to metallic layers. Various studies have investigated the adhesion strength of SU-8 to some of the commonly used metallic layers in microelectronic applications [117-120]. Dai *et al.* [117] measured the adhesion strength of SU-8 to Titanium, Copper, Gold, Nickel and Chromium layers using the pull test. A detailed analysis of the different levels of adhesion strengths was provided in relation to the atomic structures and electron configurations of the metallic layers and SU-8, which are listed in Table 4-2. According to the results of Dai *et al.* [117] Titanium was found to have the highest adhesion strength to SU-8 as illustrated in Table 4-2. This is because Ti has the lowest electronegativity, least outer layer electrons and largest atomic volume. These properties imply that Ti has a higher tendency to lose electrons to the Oxygen atoms in the SU-8 molecule and can form the strongest bond. Gold was found to have intermediate adhesion strength to SU-8 in comparison to the five metallic layers investigated. Although Au has a large atomic volume, which could imply that it can easily lose its electrons to the Oxygen atoms in the SU-8 molecule, it possesses the highest electronegativity. A high value for electronegativity implies that the atom draws the electrons much closer to its nucleus and possess a higher negative charge, therefore, making it difficult to lose its electrons. In addition, Au has the lowest surface energy in comparison to the other metals in Table 4-2, which deteriorates its adhesion to the SU-8 layer.

Table 4-2: Atomic structure and electron configuration of different metallic layers [117]

Metal	Ti	Cr	Ni	Cu	Au
Atomic Numbers	22	24	28	29	79
Ground State Electron Configuration	$[Ar]3d^2 4s^2$	$[Ar]3d^5 4s^1$	$[Ar]3d^8 4s^2$	$[Ar]3d^{10} 4s^1$	$[Xe]4f^1 5d^{10} 6s^1$
Electronegativity (Pauling Scale)	1.54	1.66	1.91	1.9	2.54
Atomic Volume ($cm^3 mol^{-1}$)	10.6	7.29	6.64	7.11	10.22
Surface Energy ($J m^{-2}$)	2.6	2.1	2.5	1.9	1.6
Adhesion Strength ($x10^4$ Pa)	7.783	7.679	4.486	4.697	7.099

Adhesion promoters have been used to improve the adhesion of SU-8 to metallic layers. Omnicoat is an adhesion promoter composed of 70-90% cyclopentanone and 10-20% Propylene Glycol Methyl Ether (PGME). Omnicoat^{TM} (MicroChem, MA) is a commonly used adhesion promoter that is used to improve the adhesion of SU-8 to metallic layers and has been widely used to improve the adhesion of SU-8 to Au [118, 119, 121, 122]. Nordstrom *et al.* [118] and Barber *et al.*

[119] investigated the change in adhesion strength of SU-8 layers on Au films using the pull test. Both studies illustrated a significant increase in the adhesion strength of SU-8 using Omnicoat. Omnicoat has a low molecular weight and increases the wettability of the metallic layers, which leads to an improved adhesion to the SU-8 layer.

In this study two cases that represent two different adhesion states for the SU-8 will be generated and the SAW sensor will be used to detect the change in SU-8 adhesion between these two cases.
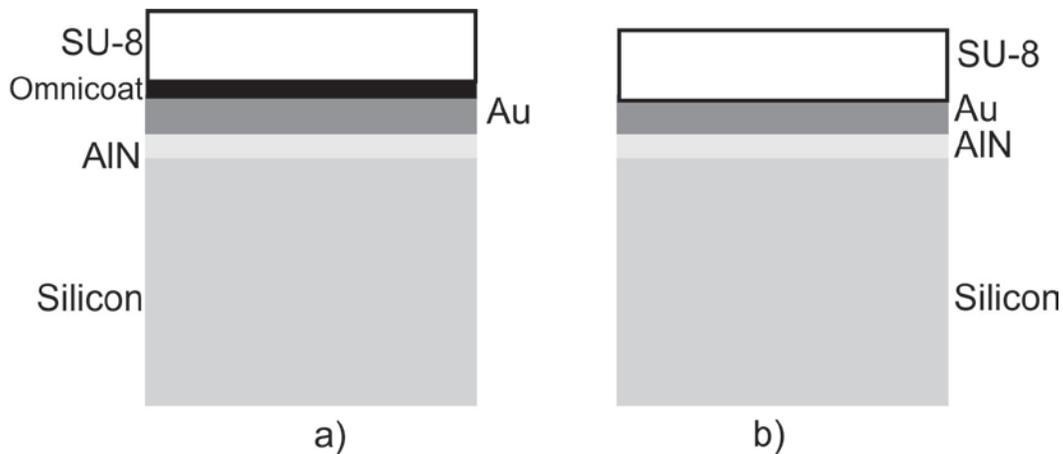
Figure 4-2: The two configurations for SU-8 adhesion that will be tested using the SAW sensors

The first case which is illustrated in Figure 4-2a, a thin Au film is patterned on the surface of the AlN film, followed by an Omnicoat layer and finally the SU-8 layer is patterned on top. The second case which is shown in Figure 4-2b shows that the SU-8 layer is patterned directly above the Au film without the use of an Omnicoat layer. It is expected that due to the Omnicoat layer the adhesion of the SU-8 layer will improve.

4.2.2   *Aluminum Nitride Properties and Processing Techniques*

4.2.2.1 Aluminum Nitride Properties

Aluminum Nitride (AlN) is a group III-V semiconductor along with GaAs, GaN and InP. It possesses a hexagonal wurtzite crystal structure, which is the thermodynamically stable structure at room temperature, with lattice constants $a_0=3.11\text{Å}$ and $c_0=4.98\text{Å}$ [123]. The wurtzite crystal structure of AlN consists of two interpenetrating hexagonal closed pack sub-lattices; each consists of only Nitrogen atoms or Aluminum atoms. Each Nitrogen atom is bonded to four Aluminum atoms

forming a tetrahedron as illustrated in Figure 4-3 and each Aluminum atom is bonded to four Nitrogen atoms in a similar manner forming an antiparallel tetrahedron. Three of the Al-N bonds will be referred to as a B_1 bond type with a bond length of 1.885Å and the fourth Al-N bond in the c-axis direction will be referred to as a B_2 bond type and has a bond length of 1.917Å as in Figure 4-3 [123]. The ionic character of the B_2 bond is higher than that of the B_1 bond but its bond energy is lower .

There are two centers of opposite charges in the AlN crystal structure along the (002) direction. The first charge center has Al^{3+} at its center and the second has N^{3-} at its center. The opposing polarities of the charge centers lead to a permanent dipole between them. In the case of an applied electric field the dipoles align in the direction of the field and an overall electrical voltage exists across the AlN crystal. This is the converse piezoelectric effect. An applied stress will also lead to an overall potential difference across the crystal, which is called the direct piezoelectric effect.
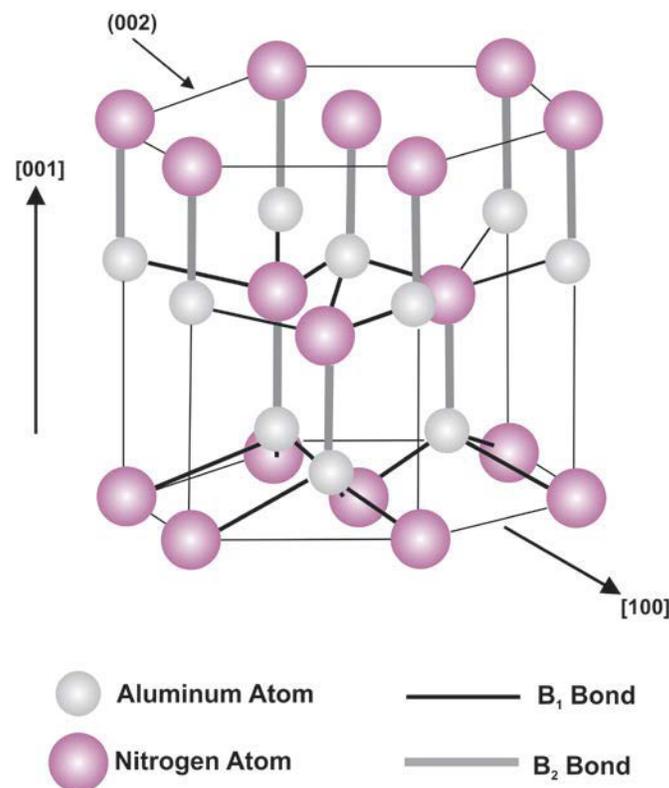

Figure 4-3: Hexagonal crystal structure of Aluminum Nitride

AlN possesses a wide range of desirable properties that led to its use in numerous applications. AlN has a wide bandgap, very high melting point, chemical resistance, low coefficient of thermal

expansion and excellent thermal conductivity. Some of the material properties of AlN are listed in Table 4-3.

Table 4-3: Properties of Aluminum Nitride

Melting Point (ºC)	[124]	>2,000
Thermal Conductivity (W/cm·K)	[125]	2.85
Electrical Resistivity (Ω·cm)	[124]	10^{11}-10^{13}
Bandgap (eV)	[125]	6.2
Index of Refraction	[125]	2.08
Thermal Expansion (1/ºC)	[125]	α_c=4.2 x10^{-6}
Breakdown Potential (kV/mm)	[126]	14

Aluminum Nitride is widely used as a piezoelectric layer in acoustic device applications, this is due to its excellent piezoelectric properties and especially its high acoustic wave velocity, which leads to high frequency acoustic wave devices. The material properties of AlN are listed below [90].

Table 4-4: Material Properties for Aluminum Nitride

Density (kg/m³)	3,260
Stiffness Constants (N/m²)	$[c]=\begin{bmatrix} 345 & 125 & 120 & 0 & 0 & 0 \\ 125 & 345 & 120 & 0 & 0 & 0 \\ 120 & 120 & 395 & 0 & 0 & 0 \\ 0 & 0 & 0 & 118 & 0 & 0 \\ 0 & 0 & 0 & 0 & 118 & 0 \\ 0 & 0 & 0 & 0 & 0 & 110 \end{bmatrix} x10^9$
Piezoelectric Stress Constants (C/m²)	$[e]=\begin{bmatrix} 0 & 0 & 0 & 0 & -0.48 & 0 \\ 0 & 0 & 0 & -0.48 & 0 & 0 \\ -0.58 & -0.58 & 1.55 & 0 & 0 & 0 \end{bmatrix}$
Electrical Permittivity Matrix (F/m)	$[\varepsilon]=\begin{bmatrix} 8.0 & 0 & 0 \\ 0 & 8.0 & 0 \\ 0 & 0 & 9.5 \end{bmatrix} x10^{-11}$

4.2.3 *Aluminum Nitride Deposition Techniques*

Aluminum Nitride possesses several desirable properties and has been used in numerous applications. Numerous techniques have been developed to deposit AlN thin films. These techniques include Molecular Beam Epitaxy (MBE) [127], Metal Organic Chemical Vapor Deposition (MOCVD) [128], Electron Cyclotron Resonance Dual Ion Beam Sputtering [129], Pulsed laser ablation [130] and Reactive Magnetron Sputtering (DC or RF) [131]. However, reactive sputtering is a widely used technique because of its process simplicity, low cost, low deposition temperature and the ability to deposited highly oriented AlN films in the [002] direction [132-134]. In this study reactive magnetron sputtering is used for the deposition of the AlN films to fabricate the SAW sensors. Details of the sputtering process will be explained and the parameters used in the deposition will be presented.

4.2.4 *Sputtering Deposition*

Sputtering is the process of ejecting atoms from the surface of a target material when more energetic particles bombard the surface. The transfer of momentum from the incident particles to the target surface leads to a cascade of collisions within the target as illustrated in Figure 4-4. Particles that have gained sufficient energy to overcome the binding forces of the target material are ejected (sputtered) from the target and condense on the substrate surface. The particles emitted from the target surface are atoms, ions, electrons, photons, molecules and secondary electrons [134]. The sputtering process described relies primarily on the transfer of momentum; therefore it is referred to as Physical Sputtering. Almost all elements in the periodic table have been deposited as thin films via physical sputtering [134].
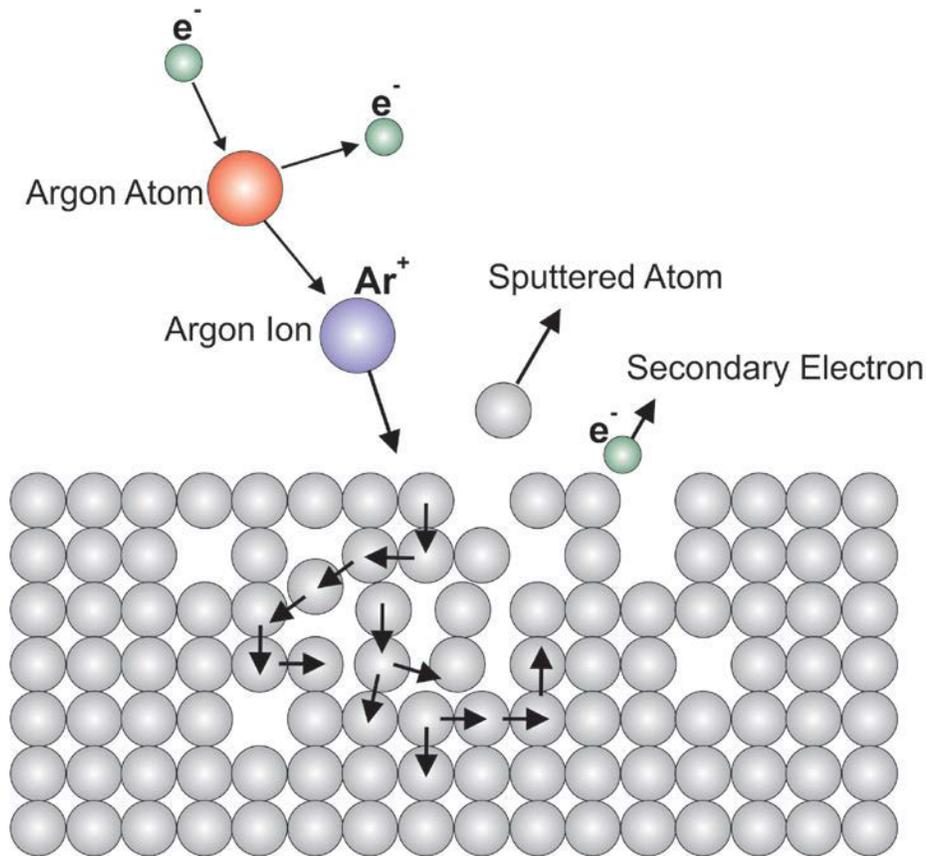
Figure 4-4: Schematic illustration of the sputtering process

In the sputtering chamber a high voltage is applied between two electrodes in a vacuum environment to initiate plasma. The gas pressure in the chamber needs to be in the range of a few mTorr to maintain the plasma. Adjusting the gas pressure in the chamber accelerates the electrons to energies that are capable of ionizing the neutral gas atoms by the electron-atom collisions as illustrated in Figure 4-4. Argon is the most commonly used gas for sputtering due to its low cost, it is chemically inert and its atomic mass is close to many of the most commonly used metals such as Titanium, Copper and Gold [135]. At low pressure few collisions take place, which cannot sustain the plasma. The ionized atoms are attracted towards the negative potential at the cathode, where the target material is placed. The impinging ions on the target surface eject atoms of the target material (sputtered atoms) and secondary electrons. The sputtered atoms deposit on the substrate surface to form thin films and the secondary electrons ejected from the target surface are necessary for maintaining the plasma.

Multiple sputtering configurations exist such as AC sputtering, Radio Frequency (RF) sputtering, Direct Current (DC) magnetron sputtering, Pulsed Power magnetron sputtering and Ion and Plasma beam sputtering. However, magnetron sputtering systems have gained significant development over the last decade and are the most commonly used systems for depositing thin metal films [134, 136]. This is primarily due to the high quality of the deposited films in comparison to thin films deposited by other physical vapor deposition techniques. The main advantage of magnetron sputtering is that a dense plasma can be developed near the cathode. This allows the accelerated ions to strike the target surface without losing their energy in collisions with other species.
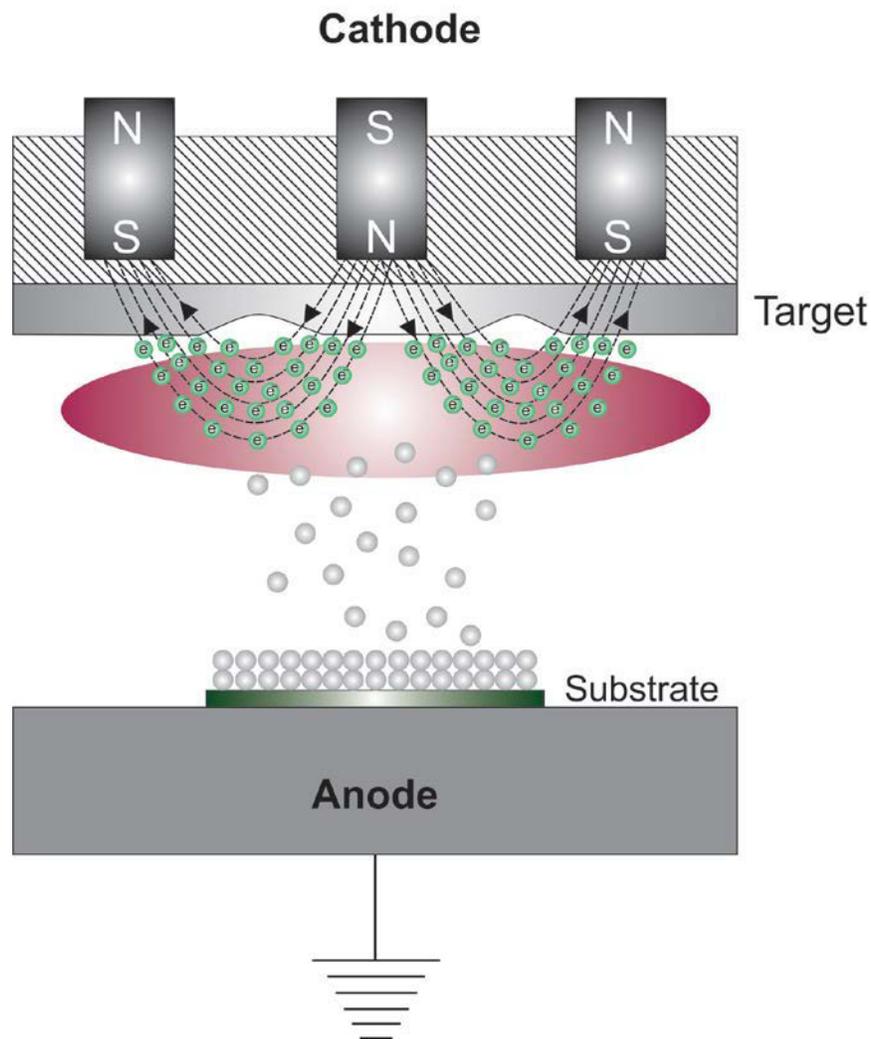
Figure 4-5: Magnetron sputtering system

In a magnetron sputtering system the cathode utilizes permanent magnets to create a magnetic field that helps maintaining the electrons near the target surface. The resulting magnetic field **B**

points in the radial direction along the target surface and acts normal to the electric field **E**. The electrons are trapped near the target surface by the Lorentz force resulting from the electromagnetic field. The electrons spiral around the magnetic field lines and circulate the target surface forming a closed loop with a drift velocity normal to the **E** X **B** plane. Maintaining the electrons near the target surface increases the number of atoms ionized by the accelerating electrons, which increases the density of the plasma and substantially improves the deposition rate [136]. The magnetic field on the target surface is non-uniform, which leads to a non-uniform plasma and hence non-uniform sputtering from the target surface [137]. The density of the plasma is highest where the magnetic field is strongest. The region where the sputtering rate is highest is represented by an eroded circular path, referred to as racetrack, on the target surface as illustrated in Figure 4-5.

For the sputtering of Aluminum Nitride reactive sputtering needs to be used. Reactive sputtering is a process that involves sputtering a metal, alloy or compound in a reactive gas mixture where a reactive gas such as nitrogen or oxygen is introduced in the chamber with Argon. The reactive gas molecules react with the sputtered atoms to form a compound film on the substrate surface. When the concentration of the reactive gas is low the target is mostly metallic and the films deposited on the substrate surface are mostly metallic. This is the metallic mode of reactive sputtering. However, as the concentration of the reactive gas increases the species react with the target material and the substrate surface to form a compound layer. This is known as Target Poisoning and significantly deteriorates the deposition rate.

The insulating layer formed on the target surface is charged by the positive charges accelerating towards the target surface. An electric field builds up in the insulating layer, which reduces the effect of the overall electric field in the sputtering chamber. In the hypothetical case where the insulating layer on the target surface can withstand infinite electric field strength the potential difference across the insulating layer would reach the power supply voltage. There will be no potential difference to accelerate the ions or electrons in the plasma, which would eventually cease to exist and the sputtering process will reach a complete stop. However, the electric field strength for the thin insulating layer on the target surface varies from 1-10MV/cm before electrical breakdown [138]. The electric breakdown of this thin film results in arcing, where particles are ejected from the target surface. The ejected particles can reach the substrate surface and deteriorate structure and composition of the deposited film. Arcing can be avoided by utilizing a pulsed DC power supply.

This power supply reverses the polarity of the cathode and applies a positive pulse to attract electrons towards the target surface and neutralize the accumulated positive charge. The frequency of the pulsed power supply systems is 10-200kHz [136]. Utilizing pulsed DC power supplies increases the deposition rate, reduces arcing and improves film quality.

4.3 Microfabrication of the Surface Acoustic Wave (SAW) Sensors

The process flow for fabricating the Surface Acoustic Wave (SAW) sensors that will be tested in this study is presented in this section. The process is carried out at the University of Alberta's Micro and Nanofabrication facility (Nanofab). In this study four designs of SAW sensors will be fabricated, which operate in the frequency range 84-208MHz. For each design two device configurations will be fabricated; the first configuration has Omnicoat patterned on the gold film prior to spinning the SU-8 layer and in the second configuration the SU-8 layer is patterned on top of the gold film without the omnicoat layer. Both configurations are illustrated in Figure 4-6.
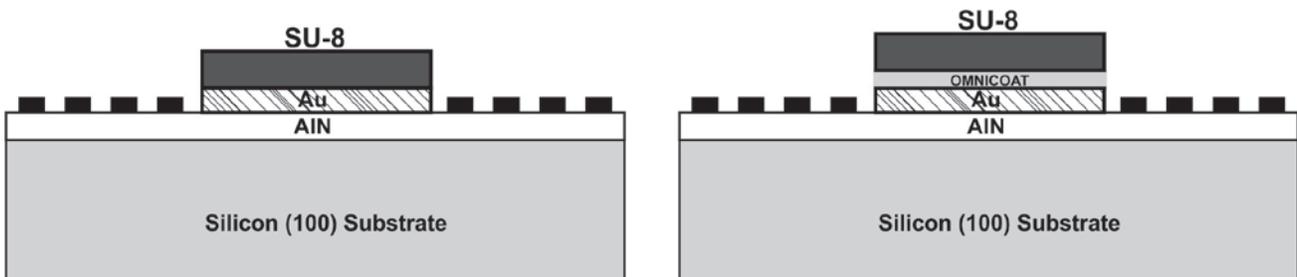
Figure 4-6: Two device configurations for the SAW sensor designs

The process flow for fabricating the SAW sensors is illustrated in Figure 4-7. The details of each process utilized in the fabrication will be described and the process parameters will be presented.
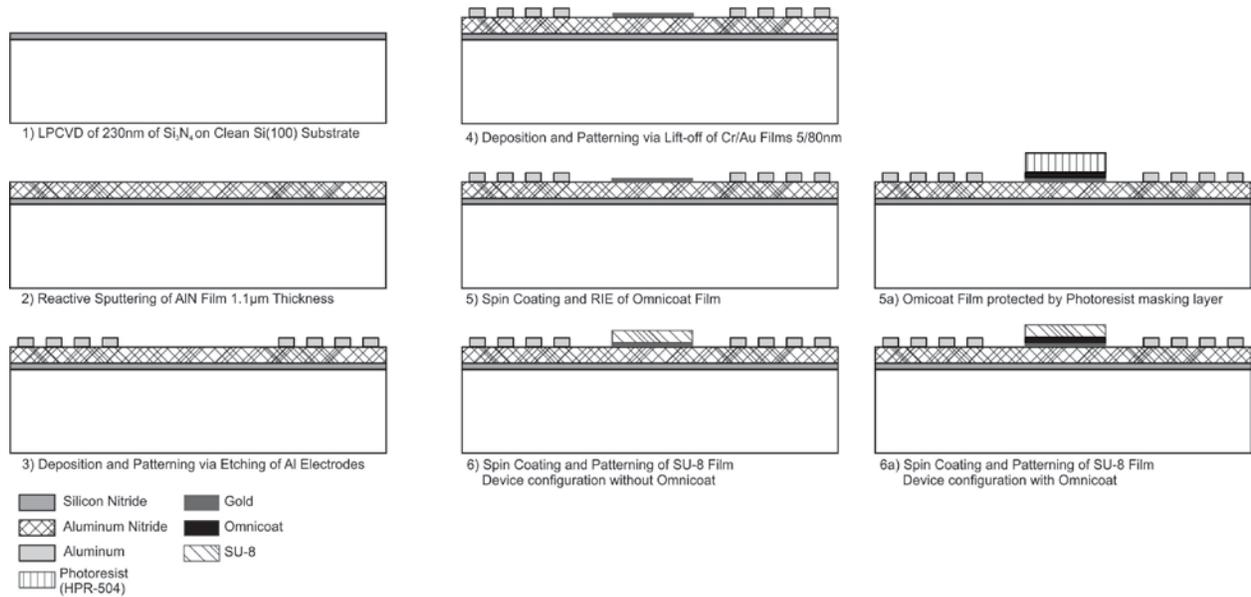
Figure 4-7: Process flow for fabricating the SAW sensors

1. The substrate used is a (100) single-sided polished silicon wafer with a 100mm diameter and 525±25μm thickness. The first step in the process flow is to clean the silicon wafer. The wafer is initially cleaned in a solution of sulphuric acid and hydrogen peroxide, commonly referred to as Piranha, to remove organic contaminants. The sulphuric acid and hydrogen peroxide are mixed in a ratio of (3 H_2SO_4 : 1 H_2O_2) by volume. Upon mixing a severe exothermic reaction takes place and the temperature of the solution rises above 100°C. The wafer is carefully immersed in the piranha solution for 15min and then rinsed with DI water and dried.

2. This step involves depositing a silicon nitride film (Si_3N_4), which acts as an insulating layer. The silicon nitride film is deposited using Low Pressure Chemical Vapor Deposition (LPCVD). The wafer is placed in the LPCVD reactor and gaseous species are introduced at high temperature; 700-800°C. The gaseous species are thermal dichlorosilane and ammonia, which react with the substrate surface i.e. chemisorption to form the nitride layer. The gaseous by-products flow out of the reacting chamber. The chemical reaction for depositing a silicon nitride layer on a silicon wafer is [139]:

$$3SiH_2Cl_{2(g)} + 4NH_{3(g)} \rightarrow Si_3N_{4(s)} + 6HCl_{(g)} + 6H_{2(g)}$$
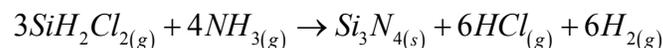
The thickness of the silicon nitride film deposited in this step is 230nm.

3. Aluminum Nitride (AlN) thin film with a crystal structure oriented along the [002] direction is deposited in this step via reactive magnetron sputtering. It is essential to deposit the AlN thin film with a high degree of orientation along the [002] direction to ensure the film adopts the piezoelectric property. The sputtering system used utilizes two pulsed DC power supplies and two 3'' diameter x 0.25'' thick, high purity (99.9995%) Al targets from Kurt J. Lesker Canada Inc. Two targets are used to increase the deposition rate. The sputtering system utilized in this process is illustrated in Figure 4-8.
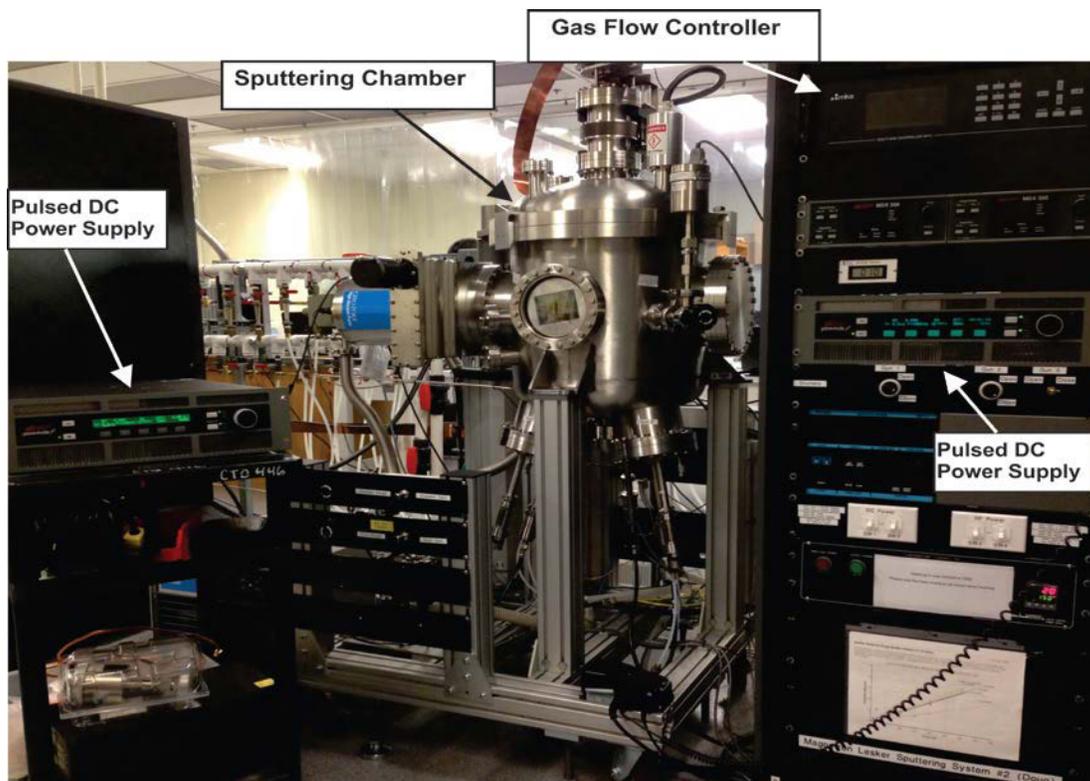
Figure 4-8: Sputtering system for depositing Aluminum Nitride films

The silicon wafer is initially loaded in the sputtering chamber as well as the two Aluminum targets as illustrated in Figure 4-9. The sputtering chamber is then locked and the pressure is lowered to reach high vacuum i.e. pump-down. The base pressure in the chamber reaches 2.3×10^{-7} Torr. Argon gas is then introduced in the chamber at a flow rate of 50sccm and the pressure in the chamber is set to 7mTorr.
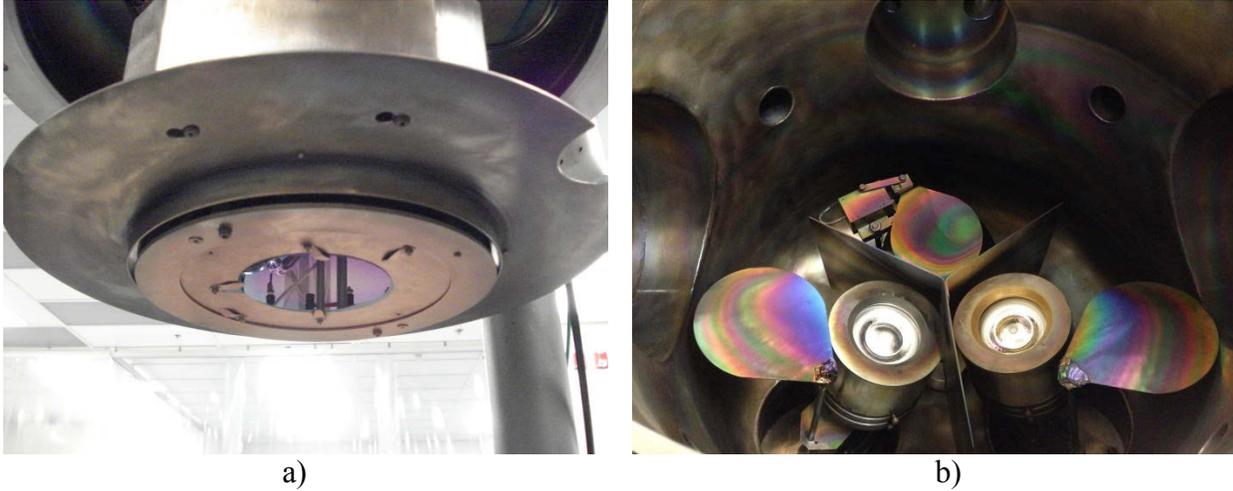
Figure 4-9: a) Loading the silicon substrate. b) Loading the Aluminum targets.

Both power supplies are switched on to initiate the plasma and set to a power level of 300W, a frequency of 150 KHz and a time step of 0.5µs. These conditions are maintained for 10min to condition the target i.e. remove the oxide layer on the surface of the aluminum target. Nitrogen gas is then introduced at a flow rate of 20sccm, the Argon gas flow rate is set to 8.57sccm and the pressure in the chamber is set to 4mTorr. These are the sputtering parameters and so the shutters on the targets are opened and the deposition begins as illustrated in Figure 4-10. The deposition rate in these conditions has an average value of 6nm/min and the desired film thickness is 1.1µm.

Figure 4-10: Argon/Nitrogen plasma during Aluminum Nitride deposition

4. A 210nm Aluminum film is then deposited above the AlN layer via DC magnetron sputtering. The sputtering time is 17min. This Al film is used for generating the input and output electrodes on top of the AlN film.

5. An optical lithography step follows the Al deposition step to generate the electrode pattern. A photoresist layer is spin coated on the substrate for patterning. Initially, 10mL of HPR 504 photoresist are poured on the substrate, a spread cycle follows for 10 seconds at 500rpm and then a spin cycle takes place for 40 seconds at 4,000rpm. After spinning the photoresist the wafer is placed on a hot plate for soft-baking for 90 seconds at 115ºC. This step is necessary to drive-off the solvent. The wafer is then re-hydrated and left to cool for 15min prior to exposure. The mask with the electrode patterns is placed on the mask aligner and the substrate is placed on the mask aligner chuck in preparation for exposure. The HPR 504 photoresist is exposed using a mercury *i-line* lamp at 365nm wavelength with an intensity of 76.4mW/cm^2 for 2.2 seconds. The exposed wafer is then placed in a Microposit 354

developer (an aqueous alkaline solution) for 25 seconds to remove the exposed photoresist regions. The wafer is then sprayed with DI water and dried with nitrogen.

6. The wafer is then placed in an Aluminum etchant to pattern the electrodes. The etchant used is phosphorous-acetic-nitric acid. The wafer is placed in the Al etchant for 8min and subjected to gentle agitation. The electrode patterns are inspected using a microscope to ensure all patterns are properly etched and there are no residual Aluminum traces. The wafer is then sprayed with Acetone to strip the photoresist layer followed by IPA and then cleaned with DI water and dried using nitrogen.

7. This step involves depositing the gold film above the AlN layer between the input and output aluminum electrodes. A mask is developed for patterning the gold films on the surface of the sensors. An optical lithography step is first required to pattern a photoresist layer prior to film deposition. This will open windows for depositing the gold films along the propagation paths on the surface of the sensors.

    a. In this step a positive tone photoresist (AZ5214) is spin coated on the wafer. 10mL of AZ5214 are poured on the wafer followed by a spread step at 500rpm for 10 seconds. A spin step then takes place for 40 seconds at 4,000rpm. The wafer is then placed on a hotplate for soft baking at 90°C for 50 seconds. The wafer is then left to cool and re-hydrate for 15min prior to exposure. The wafer is then exposed using a mercury *i-line* lamp at 365nm wavelength with an intensity of 76.4mW/cm^2 for 7 seconds. After exposure the wafer is placed in a Microposit MF-319 developer for 60 seconds to remove the exposed regions. The wafer is then sprayed with DI water and dried with nitrogen.

    b. The wafer is the placed in a DC magnetron sputtering chamber for gold deposition. A thin chromium layer is deposited prior to gold deposition. The chromium layer acts as an adhesion layer for the gold film. The deposition time for the chromium film is 2 minutes, the sputtering power is set to 75 watts and the deposition rate in these conditions is 5nm/min. The expected film thickness is 10nm. Upon completing the chromium deposition the gold film deposition is initiated. The sputtering power is set to 80 watts and the deposition time is 7 minutes. The average thickness of the chromium/gold films is 90nm.

c. The wafer is then immersed in an acetone bath with ultrasonic agitation to lift-off the excess AZ5214 photoresist and gold. The lift-off time is 13 minutes.

8. After successfully patterning the gold films the next step involves creating two configurations for each design. This is done by patterning omnicoat on half of the sensors. The sensors are fabricated on the wafer such that for each design a sensor with omnicoat is fabricated adjacent to a sensor without omnicoat as illustrated in Figure 4-7. A mask is developed to selectively pattern omnicoat on some of the sensors. This step is divided into three sub-steps:

a. Omnicoat is first spin coated on the whole wafer. 5mL of omnicoat are poured on the wafer. A spread cycle takes place at 500rpm for 5 seconds at a ramp rate of 100rpm/s followed by a spin cycle at 3,000rpm for 30 seconds and a ramp of 300rpm/s. The wafer is then placed on a hot plate and soft baked at 200ºC for 1 minute and then left to cool to room temperature for 15 minutes. The coating and baking steps are repeated 2 additional times to spin a total of 3 layers of omnicoat on the wafer.

b. HPR 504 photoresist is spin coated on the wafer and patterned to protect the omnicoat layers that should not be etched. The spinning, exposure and developing conditions for HPR504 in this step are the same as those described in step 5 above. This procedure results in sensors with a layer of HPR504 photoresist patterned on top of the omnicoat layers and sensors that have the omnicoat layer exposed as illustrated in Figure 4-7.

c. The wafer is then placed in a Reactive Ion Etch (RIE) system to etch the exposed omnicoat via oxygen plasma. The power of the system is set to 100 watts, the oxygen flow rate is set to 35sccm, the pressure in the chamber is set to 190mTorr and the etching time is 10 seconds. After completing the omnicoat etching the wafer is sprayed with acetone followed by IPA to remove the HPR 504 photoresist and then rinsed with DI water and dried with nitrogen. Two configurations of the SAW sensors are developed at this stage, one configuration has omnicoat patterned on top of the gold film and the second configuration does not.

9. This step involves spinning and patterning the SU-8 layer on the sensors. SU-8 2002 is used for this purpose. 5ml of SU-8 are poured on the wafer and then spread at 500rpm for 5 seconds with a ramp rate of 100rpm/s. A spin cycle follows the spread cycle at 5,000rpm for

30 seconds with a ramp rate of 500rpm/s. A two stage soft bake step takes place at 65ºC for 1 minute followed by 95ºC for 2 minutes. The wafer is then exposed to UV light using a mercury *i-line* lamp at 365nm wavelength with an intensity of 76.4mW/cm^2 for 5 seconds. A post exposure bake takes place at 65ºC for 5 minutes followed by 15 minutes at 95ºC. The wafer is the left to cool for 15 minutes. The SU-8 is then developed for 30 seconds in propylene-glycol-monomethyl-ether-acetate (PGMEA) to generate the desired film patterns. The thickness of the film stack (Au/Omnicoat/SU-8) on the surface of the sensor is measured using an Alpha-Step Profilometer (KLA-Tencor, CA, United States) and is found to have an average value of 1.3μm.

An image of a processed wafer is illustrated in Figure 4-11, which shows the SAW sensors that will be tested. The next step involves dicing the wafer to produce individual sensors for packaging and finally testing.
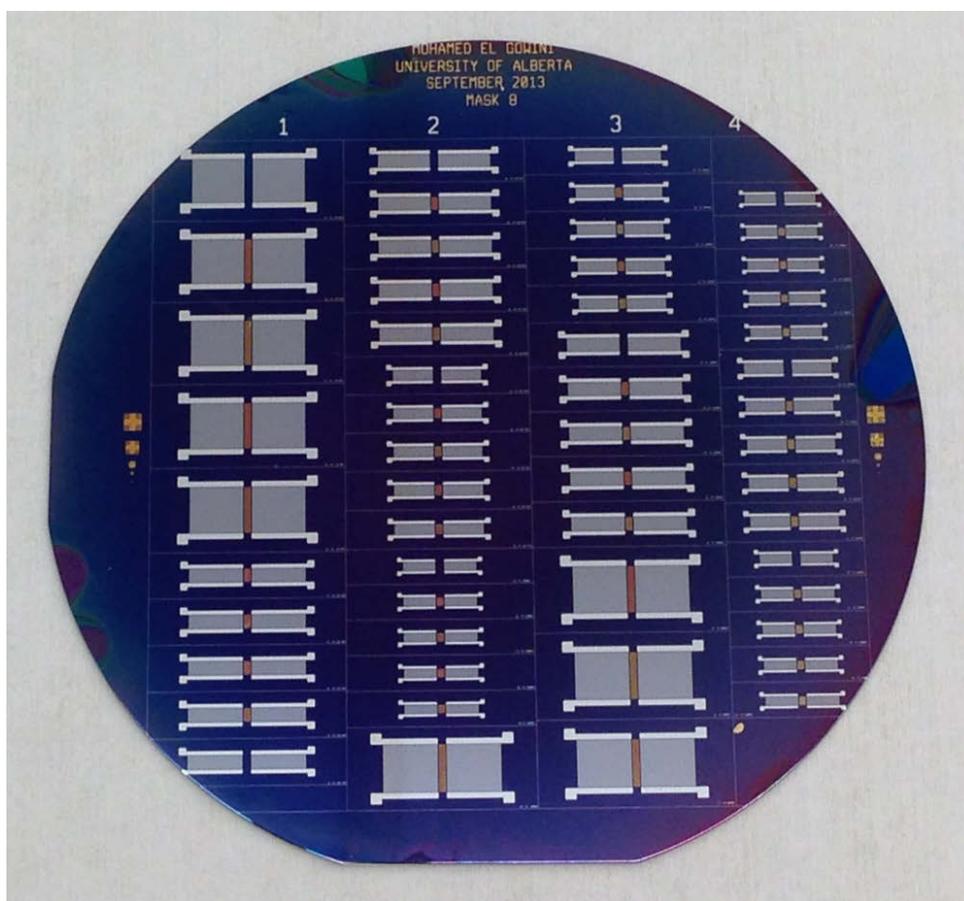
Figure 4-11: Fully processed wafer illustrating the Surface Acoustic Wave sensors

10. The wafer is diced using an automatic dicing saw DAD321 (Disco Corporation, Tokyo, Japan). Prior to dicing the wafer is coated with a layer of HPR-504 photoresist to protect the sensors from the debris that results during the dicing process. The photoresist is spin coated and soft baked using the parameters described in step 5. The wafer is then left to cool for 15 minutes prior to dicing. Dicing tape is used to attach the wafer to a thin metal frame. The metal frame and the wafer are placed on the chuck of the dicing machine and fixed in place using vacuum. The dicing parameters are then inserted to initiate the dicing process. The work thickness is set to 0.5mm, which is the thickness of the silicon substrate, the blade height is set to 0.05mm and the feed speed is between 10-20mm/s. Aluminum cutting lines with 50µm widths are patterned on the substrate during fabrication as illustrated in Figure 4-11 to provide guidance during the dicing process and define the boundaries of the sensors. After successfully completing the dicing process the sensors can be removed and packaged individually. Figure 4-12 illustrates an individual sensor for each of the four sensor designs prior to packaging.
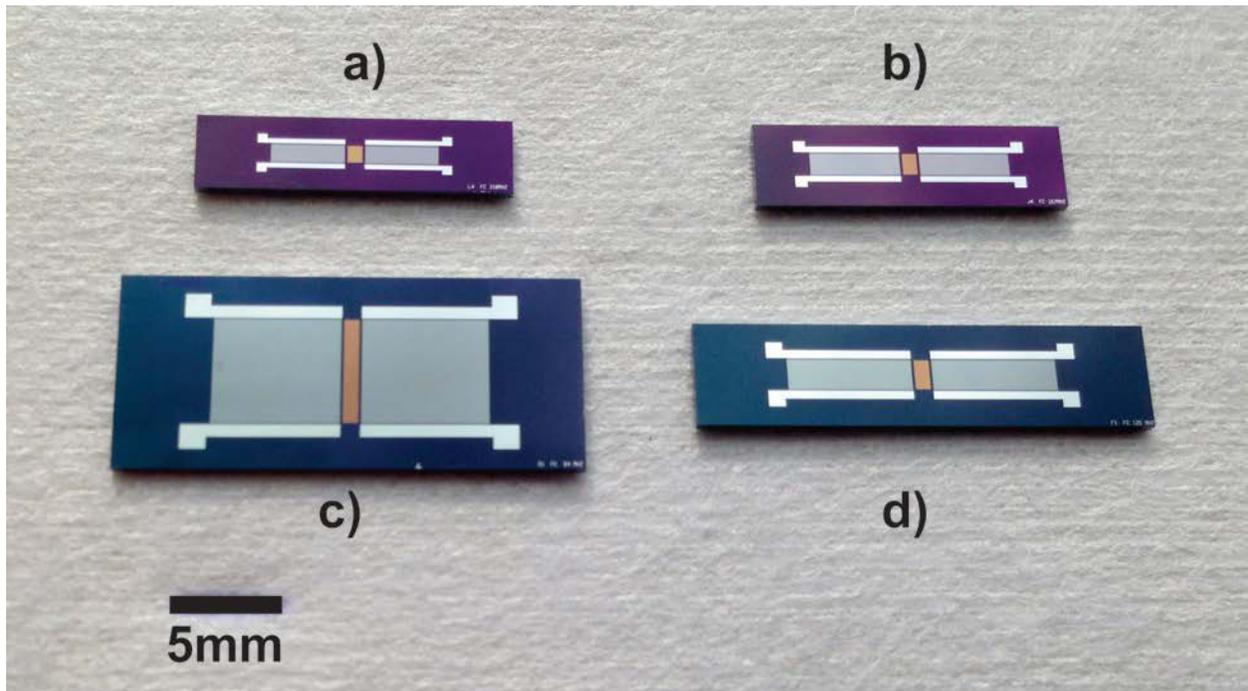
Figure 4-12: Four designs of SAW sensors operating in the frequency range 84-208MHz

4.4 Characterization of Aluminum Nitride Thin Films

The Aluminum Nitride (AlN) film samples deposited by reactive sputtering in the microfabrication phase are characterized to investigate their crystal structure. The deposition parameters for the reactive sputtering phase are optimized to deposit AlN films that possess c-axis orientation where the (0002) plane is parallel to the substrate surface. This orientation enhances the piezoelectric property of the AlN samples, which is necessary for electrical actuation and reception of acoustic waves. The crystal structures of the AlN samples are investigated using the X-Ray diffraction system available at the University of Alberta's micro and nanofabrication facility "Nanofab".

4.4.1 *Basics of X-Ray Diffraction (XRD)*

In an x-ray diffraction system x-rays are generated by accelerating electrons towards an anode, which is made of a high purity metal target. Commonly used metals include Copper, Cobalt and Molybdenum. The interaction between the metal target and the electron leads to the generation of x-rays. In this study a Copper anode is used to generate x-rays (Cu Kα radiation), which irradiate the lattice planes of the thin film sample. The x-rays are scattered by the atoms at the lattice planes since the inter-planar distance is the same length scale as the wavelength of the x-rays; therefore the lattice structure acts as a diffraction grating for the photons. The intensity of the scattered beams is maximized when the condition given by the Bragg equation is satisfied. The Bragg equation is given by [140]:

$$2d_{hkl} \sin \vartheta = n\lambda \qquad \qquad (4\text{-}1)$$

where d_{hkl} is the distance between two adjacent planes, ϑ is the angle between the incident/ scattered beam and the sample surface, λ is the wavelength and n is a constant. The condition given by the Bragg equation is geometrically illustrated in Figure 4-13.
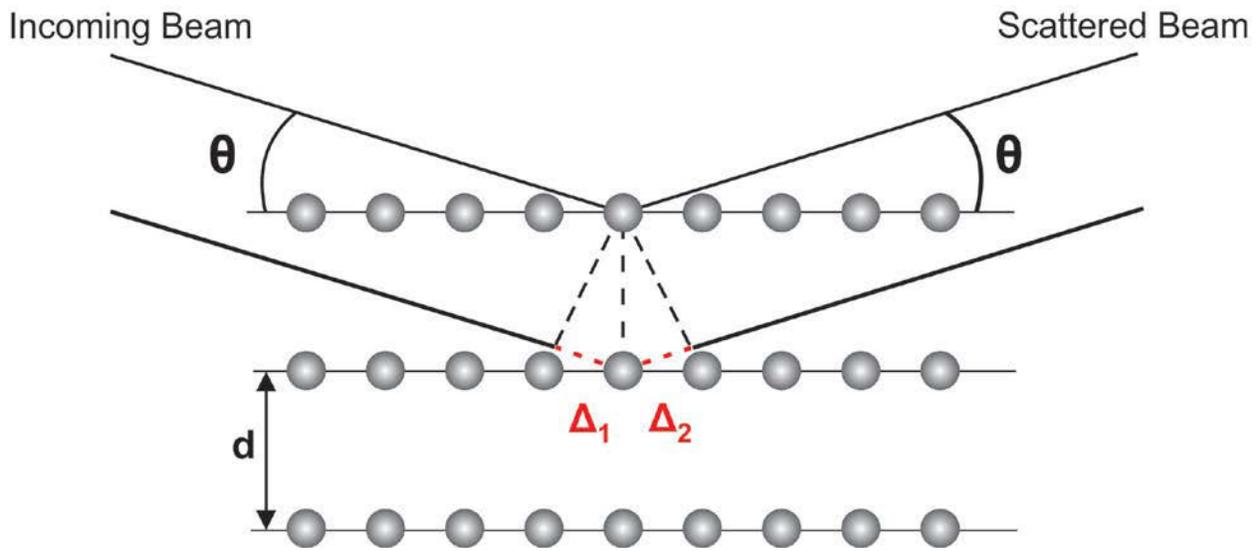
Figure 4-13: Geometric illustration of the Bragg equation

An incoming x-ray beam at an angle ϑ irradiates the lattice planes of a thin film sample, which are separated by the inter-planar distance d. The phase shift between the scattered beams from the first and second lattice planes in Figure 4-13 consists of $\Delta_1 + \Delta_2$. By simple geometric calculations it can be found that the phase shift is equivalent to:

$$\Delta_1 + \Delta_2 = 2d \sin \vartheta \tag{4-2}$$

The highest intensity of the scattered beams is achieved when the phase shift between the scattered beams is an integer multiple of the wavelength $(n\lambda)$, which gives the Bragg equation (4-1). When conducting an XRD scan the sample is placed at the center of the instrument and the incoming x-ray beam irradiates the sample surface at an angle ϑ. The detector monitors the scattered beam at the same angle ϑ of the incoming beam. The scan angle ϑ is varied throughout the measurement to generate a profile of the intensities at a wide range of angles. This provides a more detailed understanding of the microstructure of the sample. Figure 4-14 provides an illustration of a typical arrangement during an XRD scan. Although during an XRD scan the angles of the source and detector are equivalent; the angle of the scattered beam is commonly calculated with respect to the extension of the incoming beam and is equivalent to 2ϑ as illustrated in Figure 4-14. This type of measurement is referred to as a $\vartheta / 2\vartheta$ scan.
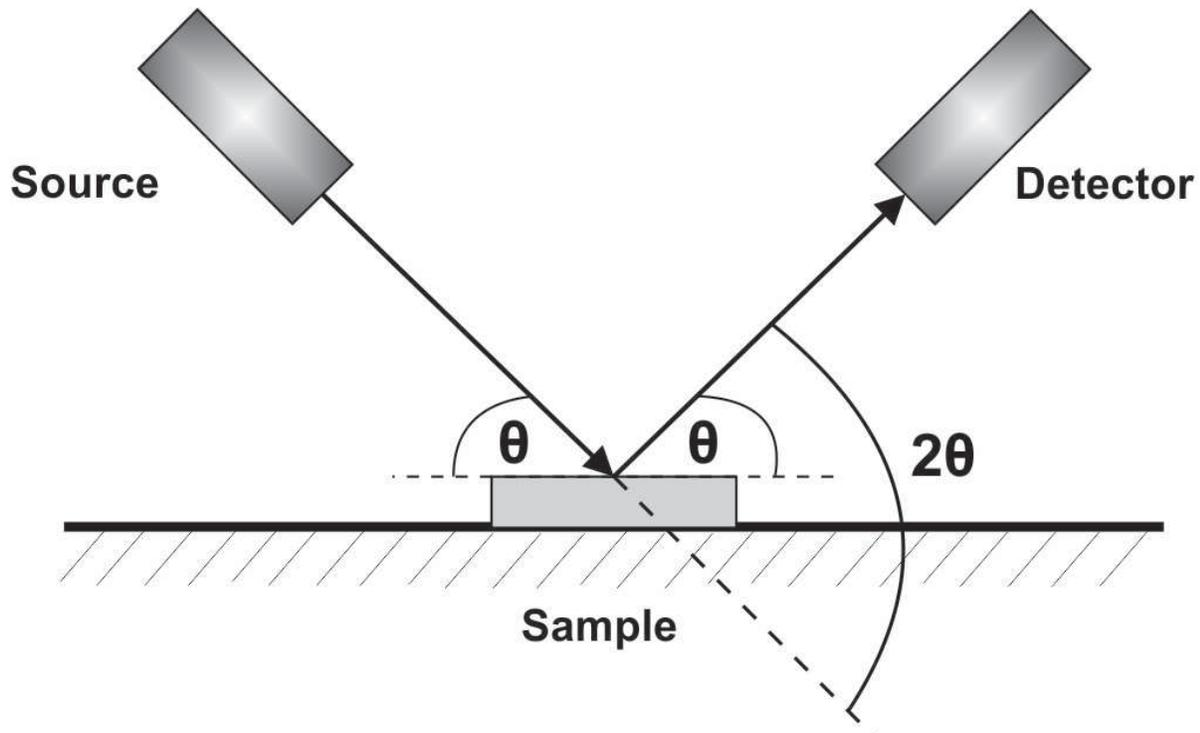
Figure 4-14: Illustration of the $\vartheta / 2\vartheta$ scan for an XRD system

4.4.2 *X-Ray Diffraction of AlN Film Samples*

The inter-planar distance d_{hkl} separating the lattice planes can be calculated for the different crystal systems. The value of the inter-planar distance is dependent on the geometry of the unit cell and the Miller indices (hkl) for the given plane. For the AlN Hexagonal structure the inter-planar distance d_{hkl} is related to the Miller indices and the unit cell parameters (a,c) by [140]:

$$\frac{1}{d_{hkl}^2} = \frac{4}{3}\frac{h^2 + hk + k^2}{a^2} + \frac{l^2}{c^2} \tag{4-3}$$

The lattice constants for AlN are $a = 0.3128\ nm$ and $c = 0.4974\ nm$ [141] and the required orientation is (002). Substituting these values in equation (4-3) the inter-planar distance d_{002} for AlN is 0.2487nm. The angle corresponding to the XRD peak of the (002) plane of AlN can be determined by inserting the value of the inter-planar distance d_{002} in to the Bragg equation (4-1) and using the value of the wavelength for $Cu\ k_{\alpha}$ radiation; 0.154nm[141], which results in a value of $2\vartheta = 36°$. An XRD plot for an AlN film sample deposited by reactive sputtering for the SAW sensors fabricated in
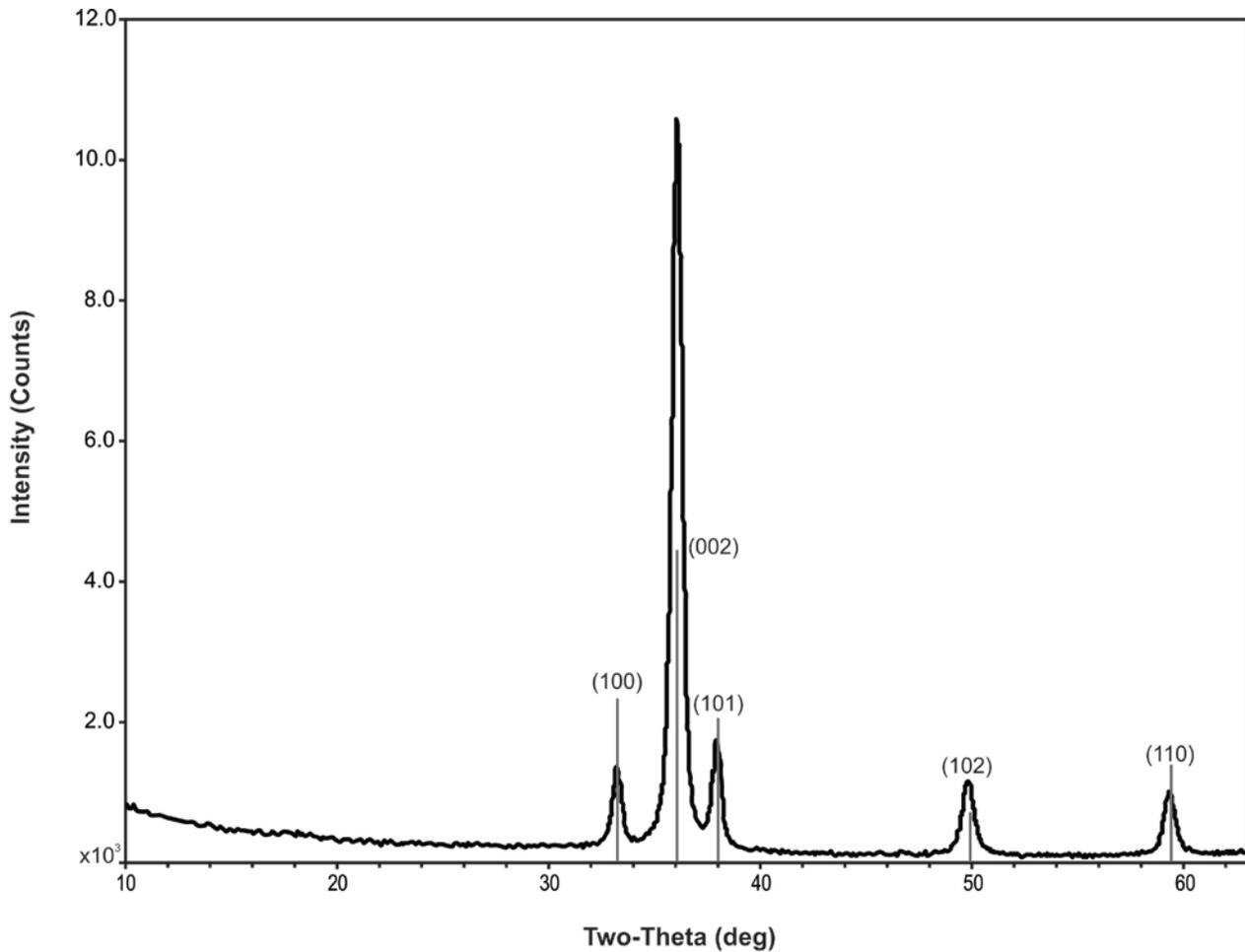
Figure 4-15: XRD plot for an AlN thin film sample deposited by reactive sputtering

this study is shown in Figure 4-15. The figure illustrates a major peak at $2\vartheta = 36°$, which is characteristic of the (002) plane and indicates a high degree of orientation of the film sample.

4.5 Packaging of Surface Acoustic Wave Sensors

The diced sensors are then packaged to allow measurement of their frequency responses. The sensors are attached to custom design Printed Circuit Boards (PCB) using double-sided adhesive tape (3M, MN, United States). The sensors are then wire bonded to the PCBs using a 747677E wire bonder (West·Bond Inc., CA, United States). Four gold wires with 25μm diameter are used to connect the four Aluminum contact pads (2 for input electrodes and 2 for output electrodes) of the SAW sensors to the PCB using ball/wedge bonding. Each PCB has a SMA connector on each end to allow connection to external measurement equipment. Figure 4-16 illustrates the packaged sensor as
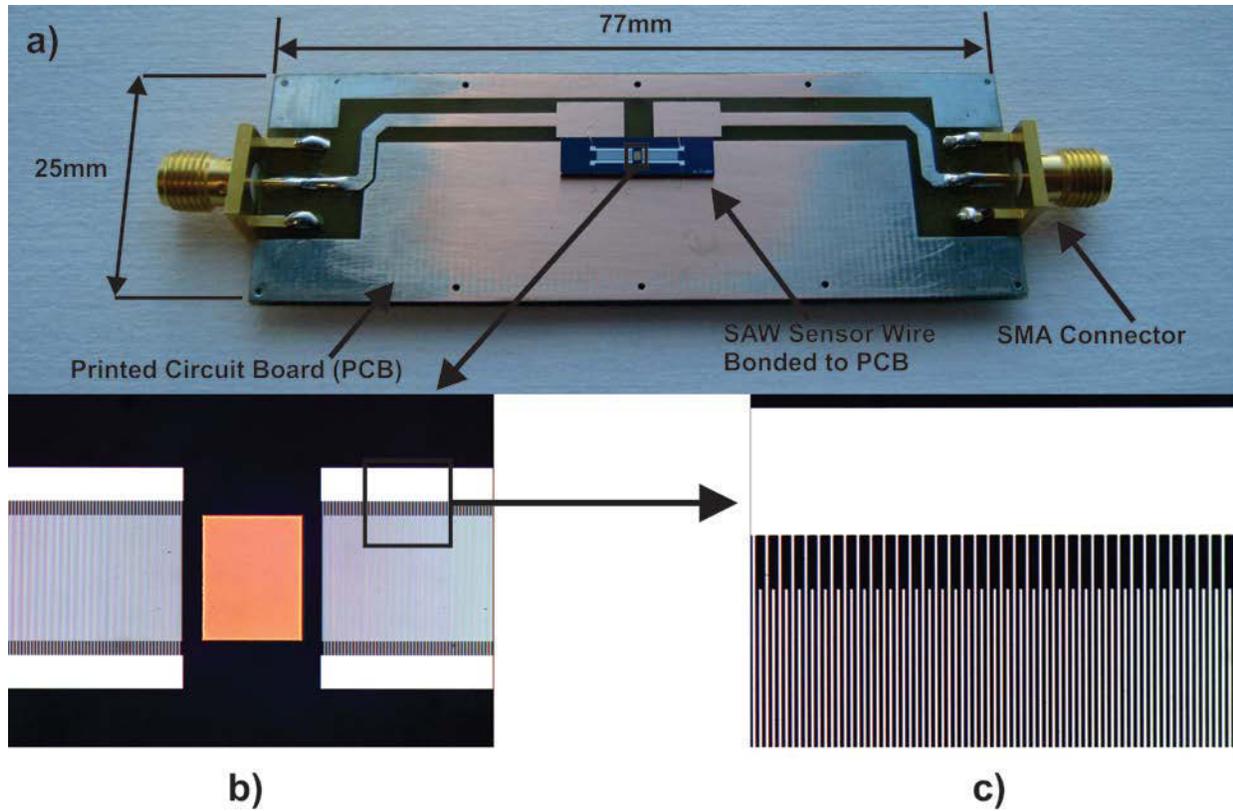
Figure 4-16: a) Surface Acoustic Wave Sensor wire bonded to PCB. b) Gold/Omnicoat/SU-8 film stack patterned between the input and output electrodes. c) An illustration of the sensor electrodes.

well as the film stack patterned along the wave propagation path and the sensor electrodes used for generating and receiving acoustic waves.

4.6 Conclusions

This chapter introduced the chemical composition/crystal structure, processing techniques and material properties of SU-8 and Aluminum Nitride. The adhesion of SU-8 to different metallic layers was discussed with respect to the atomic structure of the different metals. The microfabrication process for developing the SU-8/AlN/Si SAW was presented in detail. The reactive sputtering process for depositing thin AlN film samples was presented and the effects of the sputtering parameters on the film properties were also discussed. Characterization of the crystal structure of the AlN film using XRD was described and an illustration of the XRD plot for the AlN film samples was shown. Finally, the fabricated sensors were packaged on printed circuit boards using wire bonding to allow connection to the vector network analyzer for frequency response measurements.

CHAPTER 5.   EXPERIMENTAL METHODS AND ELECTRICAL CHARACTERIZATION OF SURFACE ACOUSTIC WAVE SENSORS

5.1 Overview

This chapter presents the layout of the Surface Acoustic Wave (SAW) devices used for testing, which is the Delay Line configuration. An explanation of the inter-digital electrodes used for the generation and reception of acoustic waves is also provided. The representation of the SAW device as a two-port network will be used to demonstrate the importance of measuring the scattering parameters (S-Parameters). The experimental set-up used in this study for frequency response measurements will be presented as well as the architecture of the Vector Network Analyzer (VNA). In addition, the different types of errors that exist in the VNA will be discussed as well as the error correction procedure to eliminate these errors from the frequency response measurements. The scattering parameter measurements of an AlN/Si SAW device using the VNA will be presented. Finally, the time gating procedure to eliminate some of the second order effects from the frequency response measurements will be applied to the AlN/Si SAW device measurements.

5.2 Operating Principle of SAW Sensors

The configuration of surface acoustic wave devices used in this study is the Delay line configuration. In this configuration two sets of inter-digital electrodes (IDT) are patterned on the surface of the sensor and separated by a distance along the wave propagation path. The IDT electrodes are electrode fingers with alternating polarities on the surface of the device. A layout of the IDT electrodes patterned on the surface of a SAW device is illustrated in Figure 5-1.
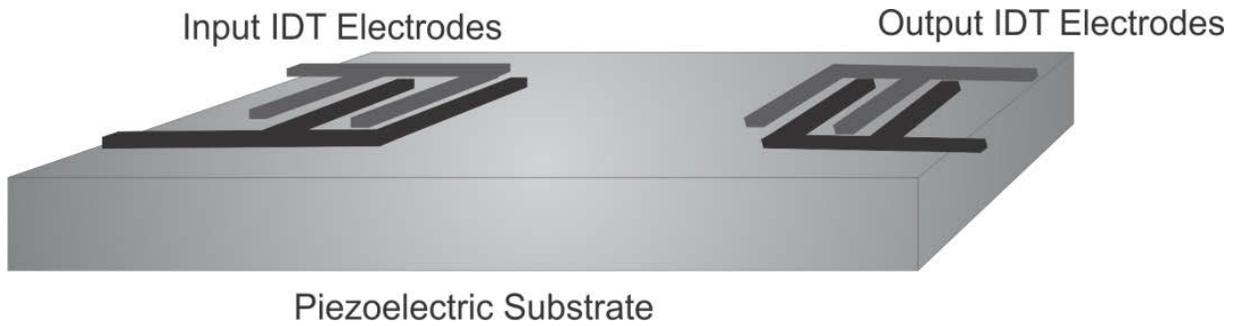
Figure 5-1: Layout of a SAW Device with IDT electrodes arranged in delay line configuration

The Delta Function Model will be adopted to present an understanding of the operation of the SAW device [142]. This is a one-dimensional model that solves for the relative insertion loss since it does not take into consideration the impedance of the SAW device and does not account for the second order effects that occur during the operation of a SAW device. However, it still provides very good understanding of the operating principle of the SAW device.
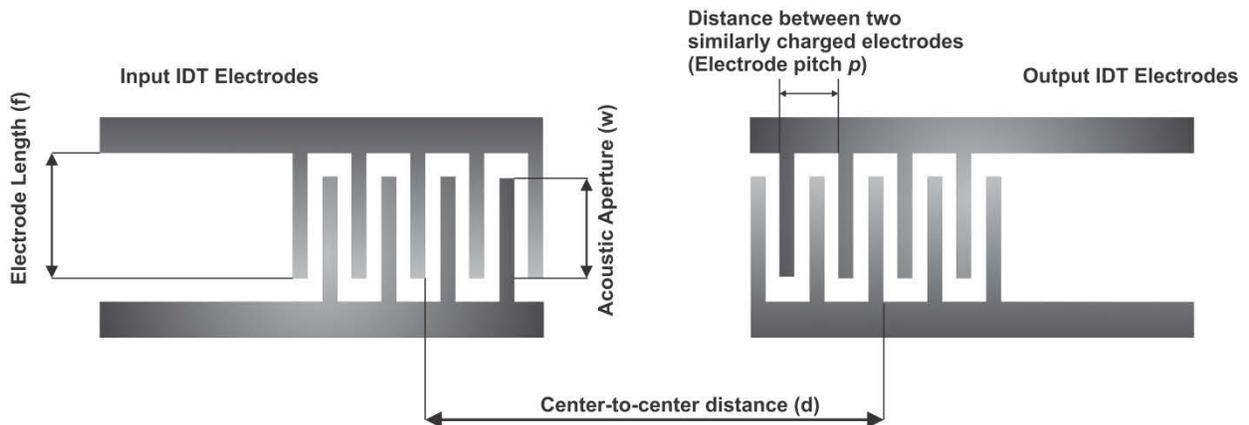
Figure 5-2: Parameters of IDT electrodes

When an AC voltage signal is applied to the input IDT charges accumulate at the surface of the substrate below the electrodes. Due to the alternating polarity of the electrodes and the attraction between opposite charges the highest concentration of charges occurs near the edges of each electrode and decay towards its' center [143]. The resulting electric field distribution between the adjacent electrodes is complex; however, the Delta Function model approximates this complex electric field distribution as a discrete number of delta function sources normal to the substrate surface [142]. The electric field intensity at each electrode finger is E_y, which is proportional to the applied voltage. Figure 5-3 illustrates the representation of the electric field distribution as delta

function sources normal to the electrode surface in an IDT. Summation of the delta sources can be used to simulate the resultant electric field intensity of one IDT. The overall response function of the SAW device is obtained by including the response functions of both IDTs. The transfer function of a SAW device using the delta function model will be obtained and the frequency response will be plotted.
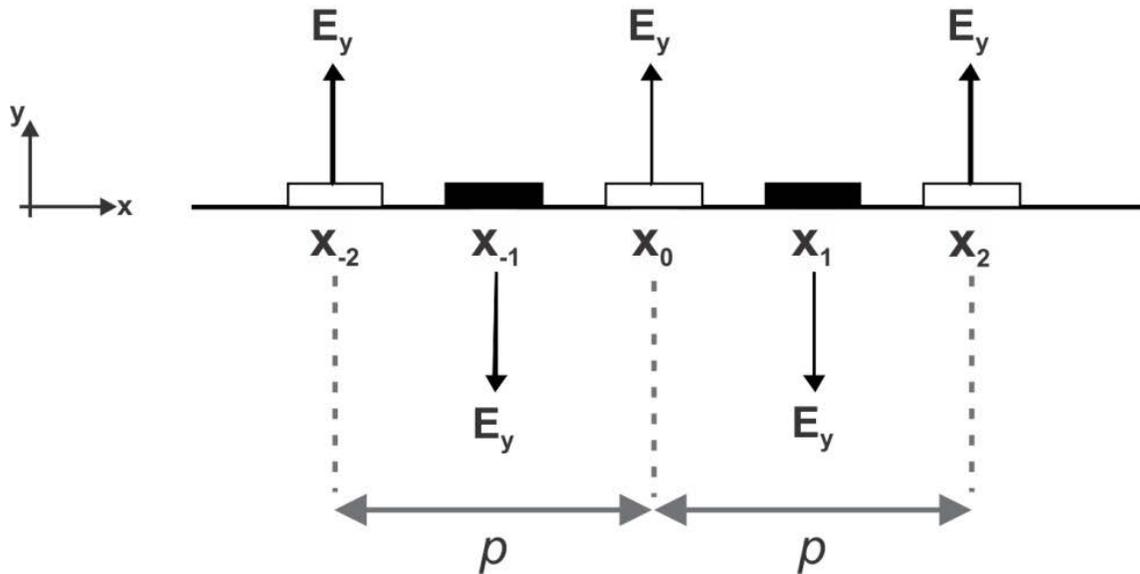
Figure 5-3: Illustration of the delta sources at the centers of the electrodes of an IDT with electric field intensity E_y

A reference point needs to be selected along the IDT for summing the delta sources. This point will be assigned x_0 and will be chosen at the center of the IDT as illustrated in Figure 5-3. The amplitudes of the delta sources are constant; however, their individual phase angles differ according to their distance x_n from the reference point x_0. The phase shift terms e^{-jkx_n} will be utilized in the calculations. The distance between two similarly charged electrodes is p as illustrated in Figure 5-3. Since the delta function model generates the relative insertion loss the amplitudes of the delta sources can be normalized to $|E_y| = 1$ [142]. By summing the delta sources to the reference point, the following frequency response function can be generated

$$H_1(f) = \sum_{n=-(N-1)/2}^{(N-1)/2} (-1)^n e^{-jkx_n} \tag{5-1}$$

---

where $(-1)^n$ refers to the alternating electrode polarity and N refers to the number of electrode fingers. In summing the delta sources the distance of each electrode to the reference point x_0 is x_n, which is a multiple of $p/2$. When $p = m\lambda$ where m is an odd integer the elements of the summation add constructively. This is an important design condition for SAW devices. In order to excite a specific frequency f with the SAW device the distances between the electrodes need to be spaced such that the condition $p = m\lambda$ is satisfied. The waves whose wavelength satisfy this condition will add constructively at the IDT electrodes and will be excited with the highest efficiency, however, when the wavelength does not satisfy this condition the waves add destructively.

Using Euler's formula the expression for the frequency response function can be expanded in terms of trigonometric functions. For the configuration considered in Figure 5-3 the reference point x_0 is at the center of the IDT with equal numbers of electrodes on both sides. This facilitates the use of trigonometric identities to cancel out the imaginary terms $\left(j \sin \left(\beta x_n \right) \right)$. To determine the frequency response of an IDT near a center frequency f_0 the frequency can be expressed as $f = \left[\left(f - f_0 \right) + f_0 \right]$. The response function of the IDT can now be expressed as [142]:

$$H_1(f) = 1 + 2\cos\left(\pi \frac{f - f_0}{f_0} \right) + 2\cos\left(2\pi \frac{f - f_0}{f_0} \right) + \ldots + 2\cos\left(N_p \pi \frac{f - f_0}{f_0} \right) \tag{5-2}$$

where N_p is the number of electrode pairs of an IDT. Near the center frequency f_0 the expression for the frequency response function given in equation (5-2) can be expressed as [142]:

$$\left| H_1(f) \right| \simeq N \left| \frac{\sin\left[N_p \pi \left(f - f_0 \right) / f_0 \right]}{N_p \pi \left(f - f_0 \right) / f_0} \right| \tag{5-3}$$

This represents the response of one IDT; however when the input and output IDT's are included the overall frequency response function will be expressed as

$$H(f) = H_1(f) \cdot H_2(f) e^{-jkd} \tag{5-4}$$

where d is the center-to-center distance between the mid-sections of the input and output IDT's. Figure 5-4 illustrates the response function of two IDTs with 20 electrode pairs, whose center-to-center distance is 1mm and their operating frequency is 100MHz.
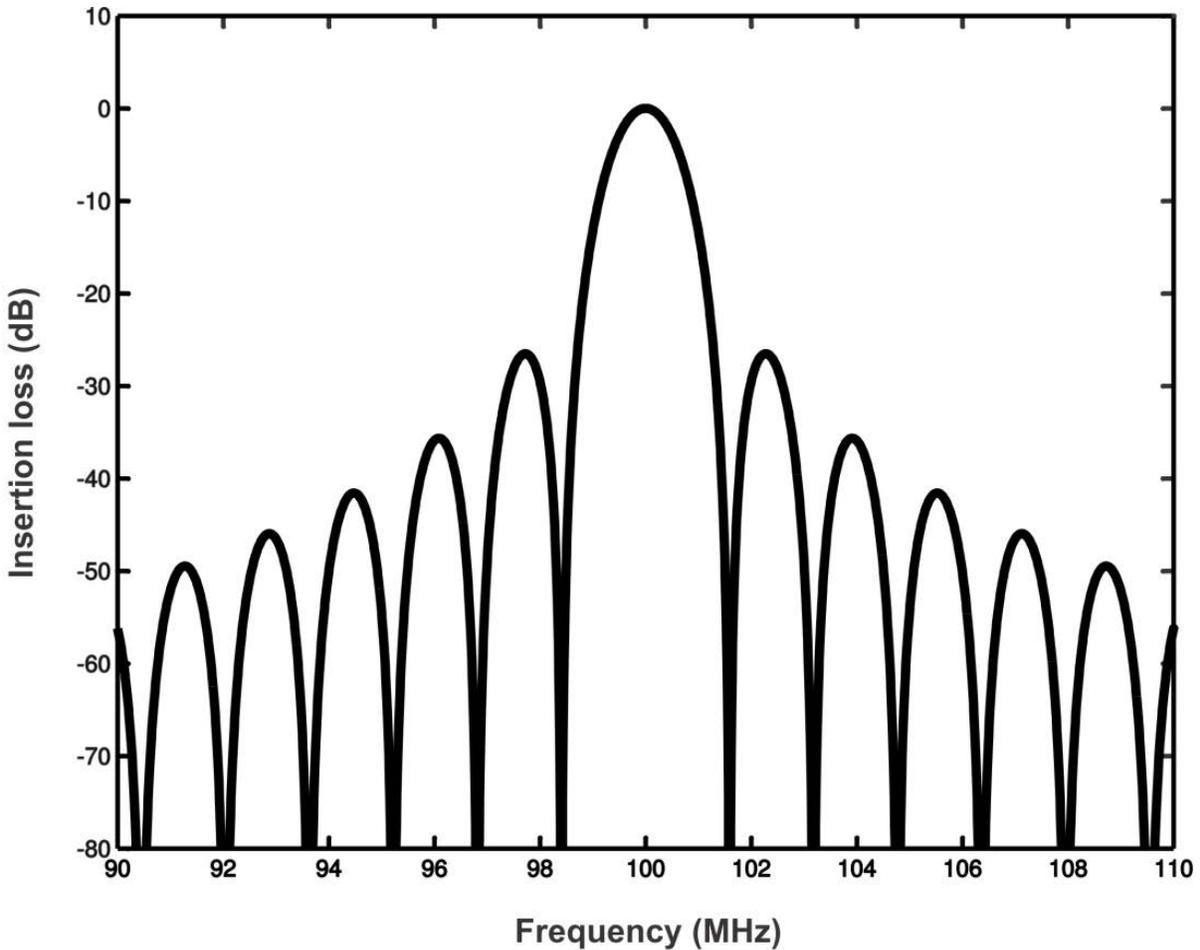
Figure 5-4: Frequency Response of two IDTs operating at 100MHz using the Delta Function model

5.3 Vector Network Analyzer (VNA)

A Network Analyzer is an instrument used for measuring the characteristics of electrical networks in the frequency range of 3KHz - 300GHz. Today, most network analyzers measure the Scattering parameters (S-parameters) of electrical networks, which illustrate the reflection and transmission characteristics. An electrical network can have any number of ports N i.e. terminals that allow connecting to external circuitry, and accordingly will have N^2 S-parameters that describe the transmission and reflection characteristics of the network. In this study an Agilent 8753ES two port vector network analyzer, which is illustrated in Figure 5-5 is used to measure the scattering parameters of the SAW sensors. The architecture of the VNA will be presented as well as the measurement errors that can occur and the calibration of the VNA to eliminate those errors.
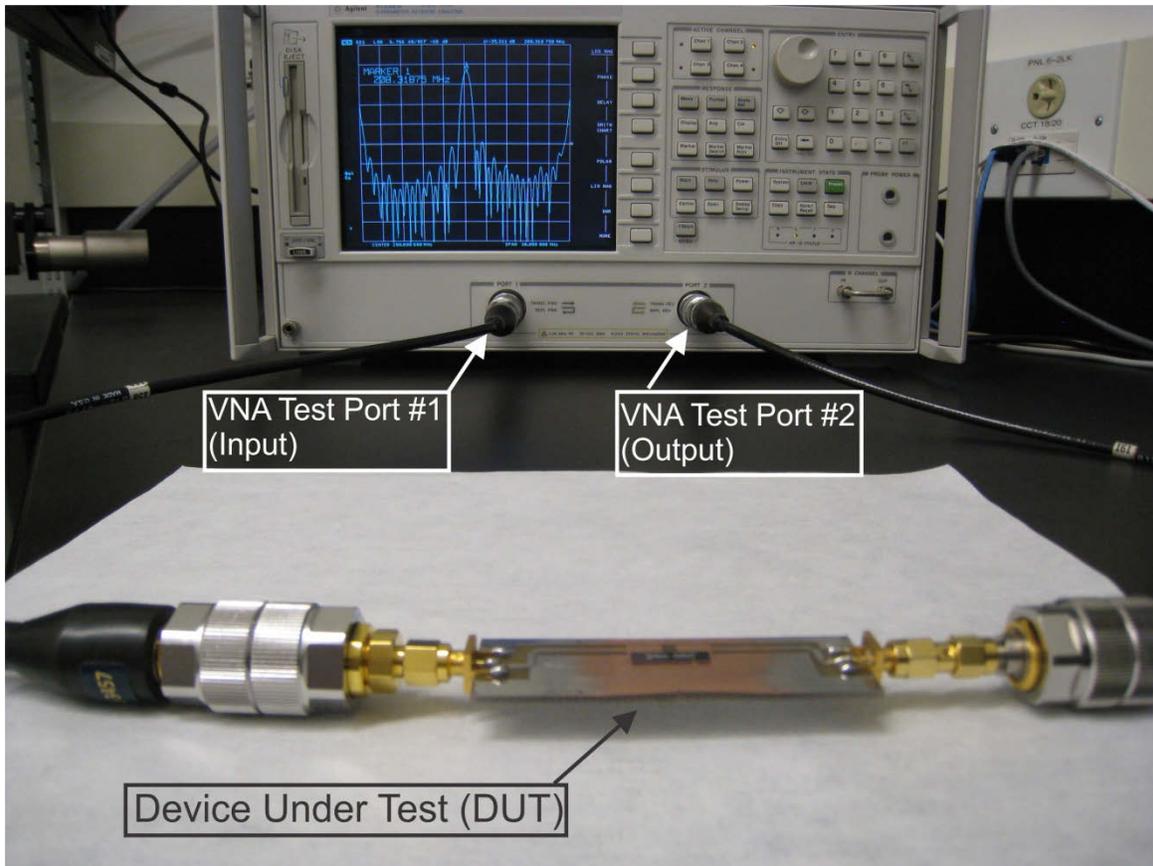
Figure 5-5: Vector Network Analyzer used in this study to measure the scattering parameters of the SAW sensors

5.3.1 *Network Analyzer Architecture*

Network analyzers can be scalar (measures magnitude only) or vector (measures magnitude and phase). Scalar network analyzers are simpler and cheaper to use, however, vector network analyzers (VNA) offer better error correction and have more complex measurement capabilities. In this section the main components of the VNA will be presented. The main components are; signal generator, test set, receivers and processor and display units for calculating and viewing the results.

5.3.1.1 Signal Generator

The signal generator provides the test signal or the stimulus needed for the response measurement. The signal generator can either sweep the frequency of the source or sweep its power.

5.3.1.2 Test Set

In old models test sets were external hardware, however, in the recent VNA's the test sets are integrated within the network analyzer. A VNA's test set includes the signal separation unit. The signal separation unit has two main functions; the first is to measure the incident signal for reference, which is done using directional couplers. The second function is to separate the incident and reflected signals at the input of the device under test (DUT). Test sets have two configurations transmission/reflection T/R or full S-parameter.

VNAs have at least two receivers as illustrated in Figure 5-6 including the reference receiver labeled **R**, which is used for measuring the incident signal magnitude and phase. There is usually one receiver for each test port. In T/R test sets the **A** receiver has a directional coupler to measure the reflected signal at port 1. The transmitted signal amplitude and phase are measured using the **B** receiver at port 2. T/R test sets measure only in the forward directions since RF power is generated at port 1 only, while port 2 is always connected to a receiver. In order to measure the reverse parameters the DUT needs to be disconnected and reversed.

In the VNA used in this study and recent models that have a full S-parameter test set there is an embedded switch that allows for measuring the forward and reverse parameters of the DUT since RF power can be generated at any test port. Therefore it has two receivers in addition to the reference receiver **R** and each port has a directional coupler that measures the magnitude and phase of the reflected signal as shown in Figure 5-6.

5.3.1.3 Processor/Display

The processor and display are used for calculating the displaying the DUT characteristics in the different formats such as smith chart, log formats and polar plots.
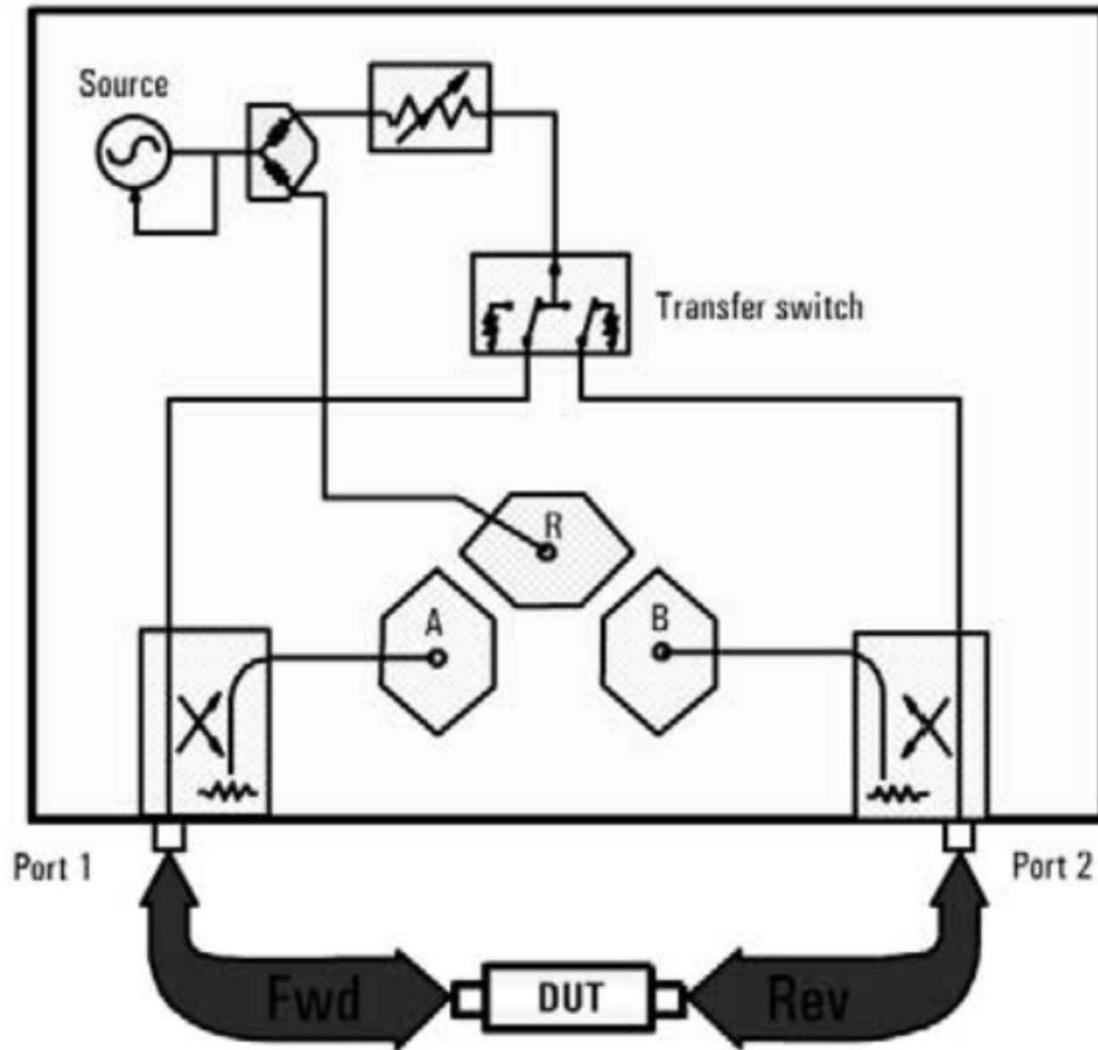
Figure 5-6: Block diagram showing the S-Parameter test set [144]

5.3.2 *Scattering Parameters (S-Parameters)*

Scattering parameters are complex vector quantities used to characterize electrical networks in high frequency applications where the use of conventional measurement techniques for voltages and currents are unfeasible. Scattering refers to the interaction of the voltages and currents with a discontinuity in the transmission line. S-parameters facilitate the characterization of networks from the input and output signals without having to deal with their internal structures.

The interdigital transducers on the surface of the SAW device can be can be represented by a two port network as illustrated in Figure 5-7 and are connected to the two test ports of the VNA. The travelling wave components a_1, b_1, a_2 and b_2 represent the incident wave on port 1, reflected wave at port 1, incident wave on port 2 and reflected wave on port 2; respectively. The wave flowing away from port 2, b_2, consists partly of the wave a_2 reflected at port 2 and partly of the incident wave on port 1, a_1. The wave b_1 consists partly of the reflected portion of the incident wave on port 1, a_1, and the transmitted portion of the incident wave on port 2, a_2.
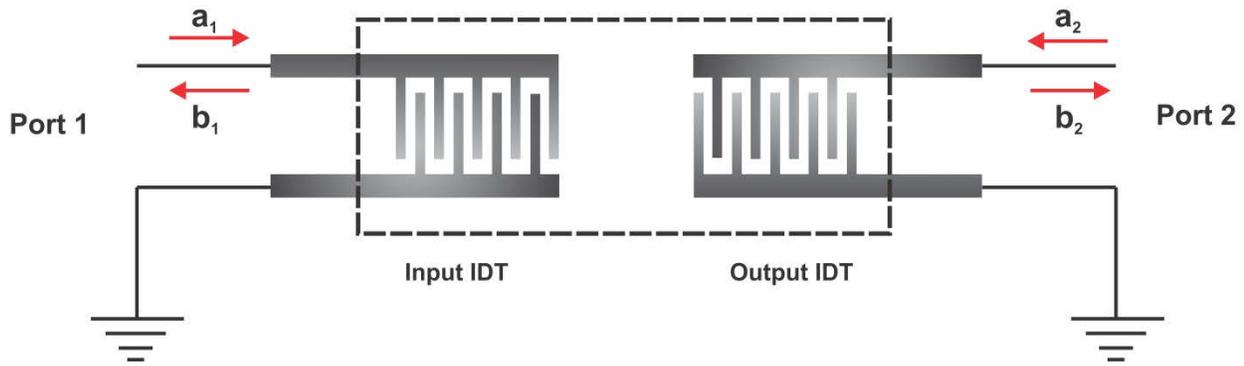
Figure 5-7: IDTs of the SAW device represented as a two port network

The waves b_1 and b_2 can be expressed in terms of the waves a_1 and a_2 using scattering parameters as given by;

$$b_1 = S_{11} a_1 + S_{12} a_2$$
$$b_2 = S_{21} a_1 + S_{22} a_2$$

(5-5)

which can be expressed in matrix form as

$$\begin{bmatrix} b_1 \\ b_2 \end{bmatrix} = \begin{bmatrix} S_{11} & S_{12} \\ S_{21} & S_{22} \end{bmatrix} \begin{bmatrix} a_1 \\ a_2 \end{bmatrix}$$

(5-6)

where the parameter S_{xy} relates the output at port X being measured due to the input port Y where the wave is incident. The S-parameters can be expressed as:

$$S_{11} = \left. \frac{b_1}{a_1} \right|_{a_2=0} \quad ; \quad S_{12} = \left. \frac{b_1}{a_2} \right|_{a_1=0}$$

$$S_{21} = \left. \frac{b_2}{a_1} \right|_{a_2=0} \quad ; \quad S_{22} = \left. \frac{b_2}{a_2} \right|_{a_1=0}$$

(5-7)

S_{11}: forward reflection coefficient. S_{22}: reverse reflection coefficient.

S_{21}: forward transmission coefficient. S_{12}: reverse transmission coefficient.

The SAW sensors used in this study consist of two sets of interdigital electrodes (IDTs) patterned on the surface of the SAW device. The two sets of IDTs are symmetric and identical; therefore the forward and reverse S-parameters are equivalent and the S-parameter matrix is symmetric.

5.3.3 *Measurement Error Modeling*

There are three basic types of measurement errors in a vector network analyzer; systematic, random and drift errors, which are explained below:

Systematic Errors: these errors are due to imperfections in the network analyzer and the test set-up (cables and adapters) and they are repeatable and time-invariant. Therefore, these errors can be characterized during the calibration process and mathematically removed during measurements.

Random Errors: these are random errors that vary in time and therefore cannot be removed by calibration. The main sources of random errors are instrument noise.

Drift Errors: these refer to the variation in the system performance over time. The main cause of drift errors is temperature variation and can be removed by further calibration. The rate at which drift errors affect the instrument depends on the user's test environment. Maintaining a stable test environment can greatly minimize the effect of drift errors.

There are six types of systematic measurement errors, which can be divided into three groups:

Signal Leakage errors: directivity and cross-talk

Signal Reflections: source and load match

Frequency response of receivers: reflection and transmission tracking

Table 5-1 Systematic error terms in the forward and reverse directions

EDF	Forward Directivity	EDR	Reverse Directivity
ESF	Forward Source Match	ESR	Reverse Source Match
ERF	Forward Reflection Tracking	ERR	Reverse Reflection Tracking
ELF	Forward Load Match	ELR	Reverse Load Match
ETF	Forward Transmission Tracking	ETR	Reverse Transmission Tracking
EXF	Forward Crosstalk	EXR	Reverse Crosstalk

5.3.3.1 Frequency Response Tracking Errors

These errors result from the difference between the frequency response from the measurement channel and the frequency response from the reference channel. In the full two-port, two-path error model this leads to four error terms: forward reflection (ERF) and reverse transmission (ETR) at port 1 and forward transmission (ETF) and reverse reflection (ERR) at port 2. These errors affect both reflection and transmission measurements.

5.3.3.2 Directivity

A small amount of the power transmitted to the DUT will appear in the coupled arm causing an error in the reflected signal. This signal is below another signal travelling from the DUT by an amount equal to the directivity. Directivity error could be the main reason there is a large ripple pattern in the measurements of the return loss. There are two directivity error terms; forward directivity (EDF) and reverse directivity (EDR).

5.3.3.3 Source Match

This error is due to the mismatch between the source test port and the system characteristic impedance. This mismatch leads to reflected signals being re-reflected from the DUT. Source match errors are most significant in devices with large reflection coefficients. There are two source match errors; forward source match (ESF) and reverse source match (ESR).

5.3.3.4 Load Match

This error is due to the mismatch between the load test port and the system characteristic impedance. This mismatch leads to reflected signals being re-reflected from the DUT, which causes reflection and transmission measurement errors especially in devices with high reflection coefficients. There are two load match errors; forward load match (ELF) and reverse load match (ELR).

5.3.3.5 Cross-Talk/Isolation

This refers to the signal leakage between the test ports of the network analyzer when no device is present. There are two isolation error terms; forward cross talk (EXF) and reverse cross talk (EXR).

The full two-port calibration model includes six measurement errors in the *forward* and *reverse* direction, thus leading to twelve error terms, which are listed in Table 5-1. There are two types of

error correction techniques, which are *response correction* and *vector correction*. Response correction is simple to perform, however it does not account for all twelve error terms, it accounts only for the tracking terms.

5.3.4 *Vector Error Correction*

In vector error correction the magnitude and phase responses of known calibration standards are carried out and then the effect of these errors are removed from subsequent measurements. This calibration technique accounts for all twelve measurement errors. One-port calibration can be used for reflection measurements and can remove three error terms (directivity, source match and reflection tracking). In order to remove the remaining errors transmission and reflection measurements need to be carried out on bot h ports. Two-port calibration requires twelve measurements of four known standards (Short-Open-Load-Through i.e. SOLT). A detailed discussion of the different error terms and how the error correction procedure takes palce, can be found in Appendix B.

5.4 SAW Device Frequency Response Measurements

In this section the measurement of the S-parameters for an AlN/Si SAW device operating at 208MHz using the 8753ES vector network analyzer will be demonstrated. The measurement procedure illustrated in this secion will be used when measuring the frequency response of the SAW sensors to determine the effect of changing the adhesion of the SU-8 film on the SAW sensor frequency response.

In order to carry out frequency response measurements using a vector network analyzer the input/output IDT electrodes of the SAW device should be connected to the VNA's input and output ports as illustrated in Figure 5-5. An APC-7 to SMA adapter is connected to the SMA connecters on both sides of the PCB. The APC-7 adapters are connected to the Agilent 11857D test port cables thus connecting to the two ports of the vector network analyzer. The vector network analyzer (VNA) applies a frequency sweep to the SAW device and the frequency response is displayed on the VNA monitor. The VNA is connected to a computer using an Agilent 82357B USB/GPIB cable and the frequency response is displayed on t he PC monitor via Agilent Intuilink software. A schematic illustration of the electrical set-up used for measuring the frequency response of the SAW sensors is shown in Figure 5-8 and the actual set-up is shown in Figure 5-9 .
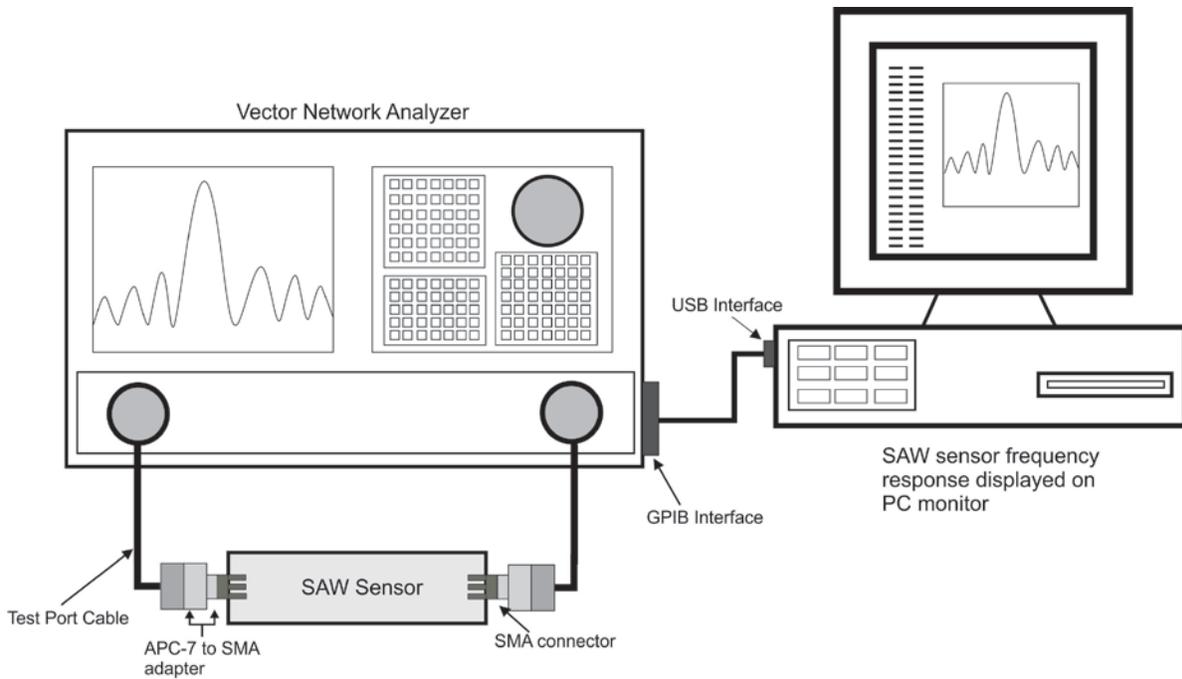
Figure 5-8: Schematic illustration of the experimental set-up adopted in this study to measure the frequency response of the SAW sensors
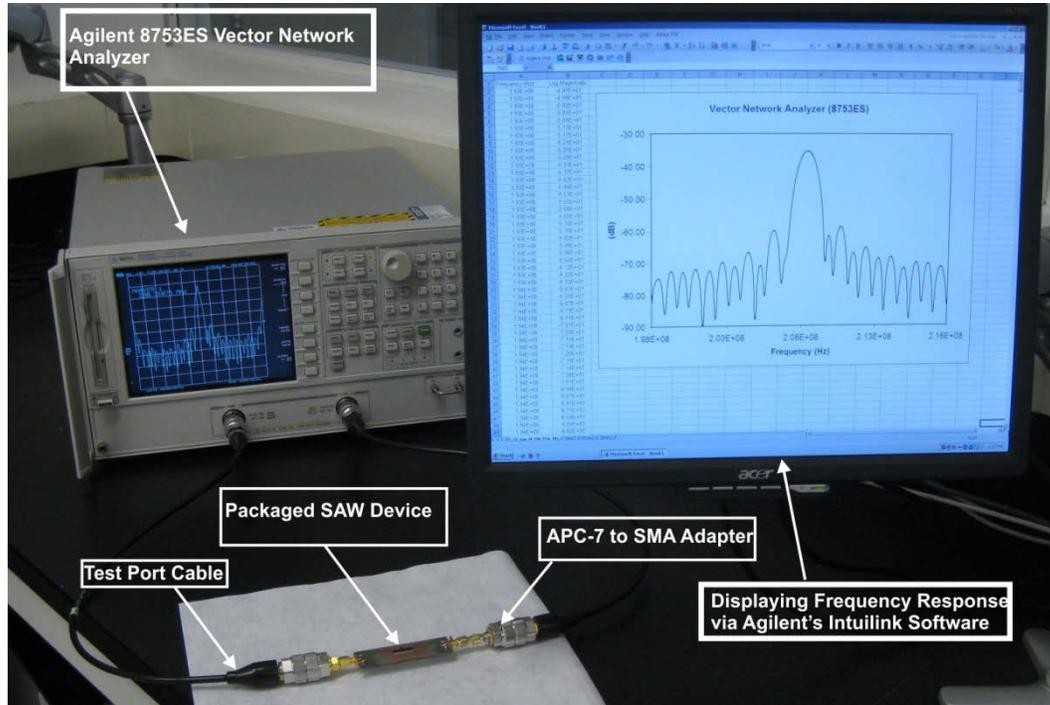
Figure 5-9: Frequency response measurement of the AlN/Si SAW device using an 8753ES vector network analyzer

A VNA applies a frequency sweep in the range of 198-228MHz to the SAW device and the power of the applied signal is set to -10dBm. The S-parameters of the SAW device are recorded and are plotted below.

5.4.1 *Reflection Coefficients (S₁₁ and S₂₂)*

The reflection coefficients for the AlN/Si SAW device have been measured using the VNA and the plots are shown in Figure 5-10 and Figure 5-11. The input and output IDT's of the SAW device are symmetric; therefore the forward and backward reflection coefficients are identical.
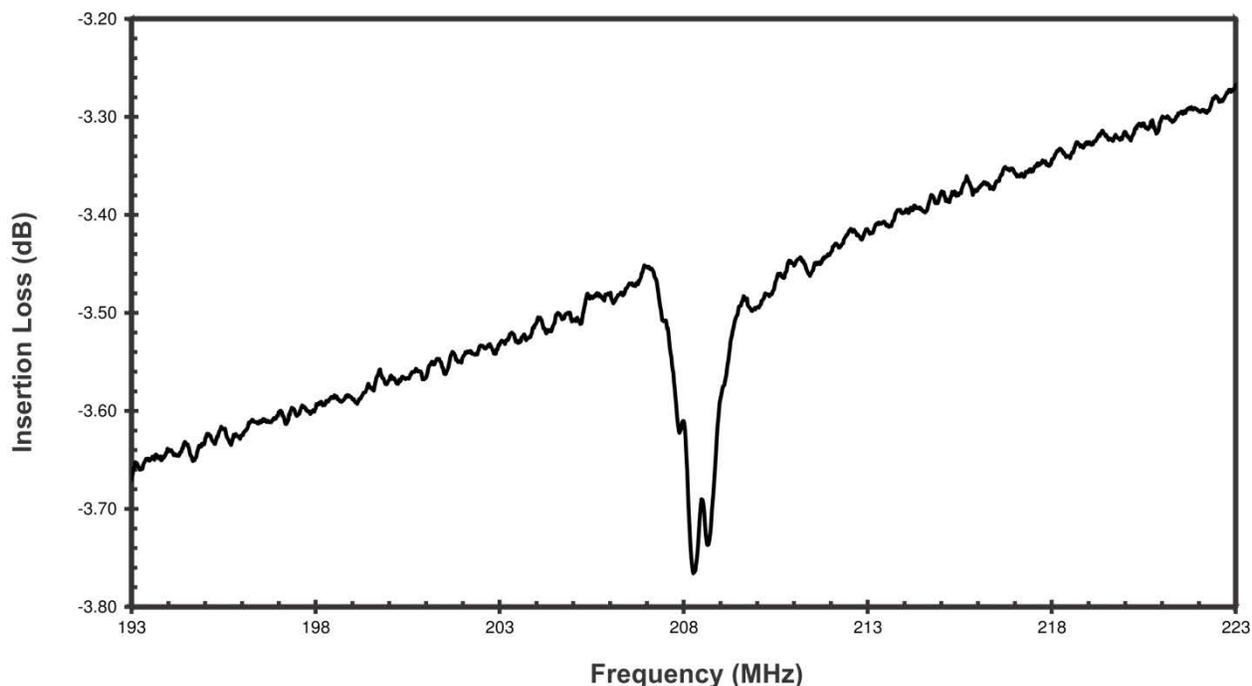
Figure 5-10: Forward reflection coefficient (S$_{11}$) for the AlN/Si SAW device

The frequency plots for both figures illustrate a major drop at 208MHz, which is the operating frequency of the SAW device. When the impedance of the SAW device is designed to have a value close to the source impedance at its operating frequency, the reflection coefficient will be a minimum at this frequency since most of the signal power will not be reflected. However, the impedance value at frequencies different from the center frequency will lead to signal reflection due to the impedance mismatch and the reflection coefficient will increase. In this study impedance matching was not carried out; however, drops at the center frequencies are observed in the reflection coefficient plots.
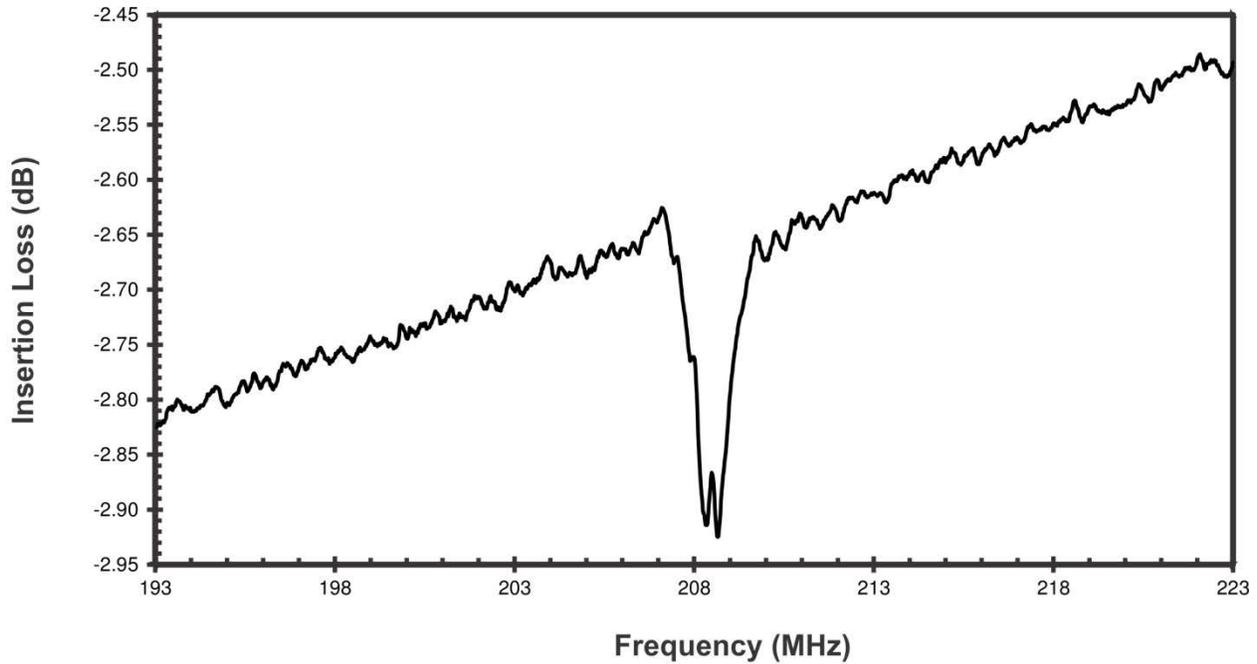
Figure 5-11: Reverse reflection coefficient (S_{22}) for the AlN/Si SAW Device

5.4.2   *Transmission Coefficients (S_{12} and S_{21})*

The transmission coefficients of the SAW device are plotted in Figure 5-12 and Figure 5-13. Both plots are identical due to the symmetry of IDT's. The plots of the transmission coefficients illustrate a peak at 208MHz, which is the center frequency of the SAW device. At this frequency the wavelength of the SAW wave is equivalent to the electrode pitch *p*. This allows the waves to add constructively at the IDT's and are transmitted with highest efficiency, which corresponds to a peak at that frequency as illustrated in the transmission coefficient plots. However, frequencies different from the center frequency add destructively at the IDTs and are displayed as peaks with lower amplitude than the center frequency peak.
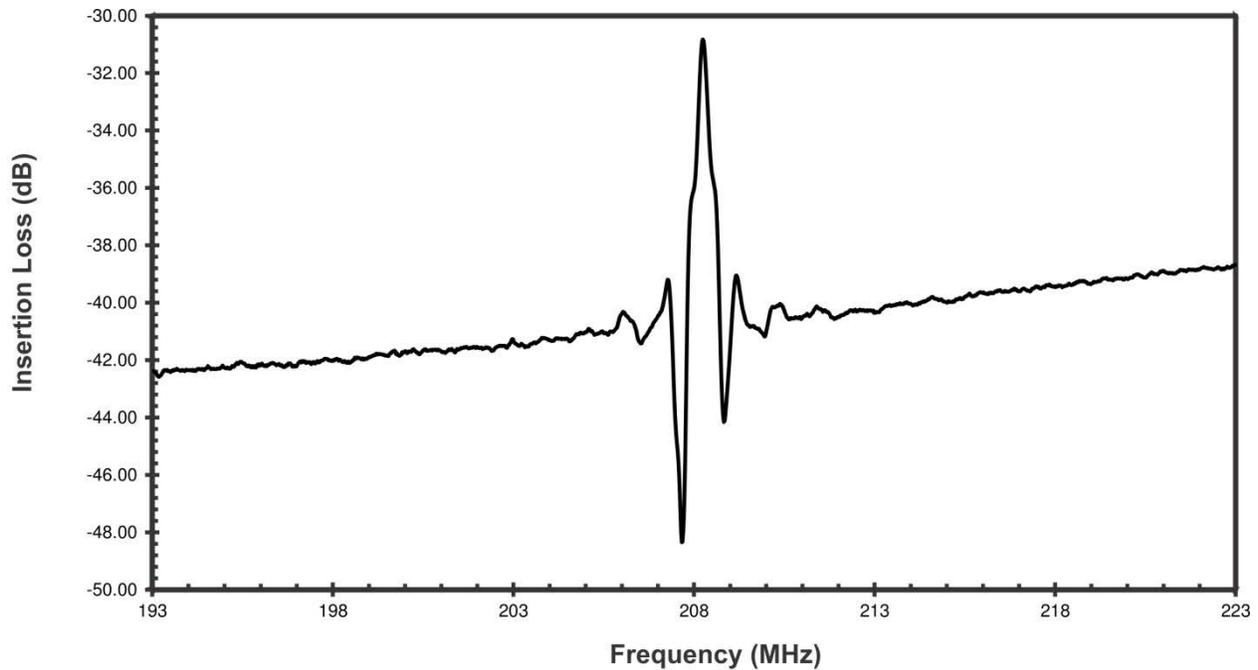
Figure 5-12: Forward transmission coefficient (S_{21}) for the AlN/Si SAW device

The peaks of the center frequencies are highest as illustrated in Figure 5-12 and Figure 5-13. These amplitudes can be significantly higher by eliminating the second order effects that occur in the frequency response measurement and deteriorate the response of the SAW device.
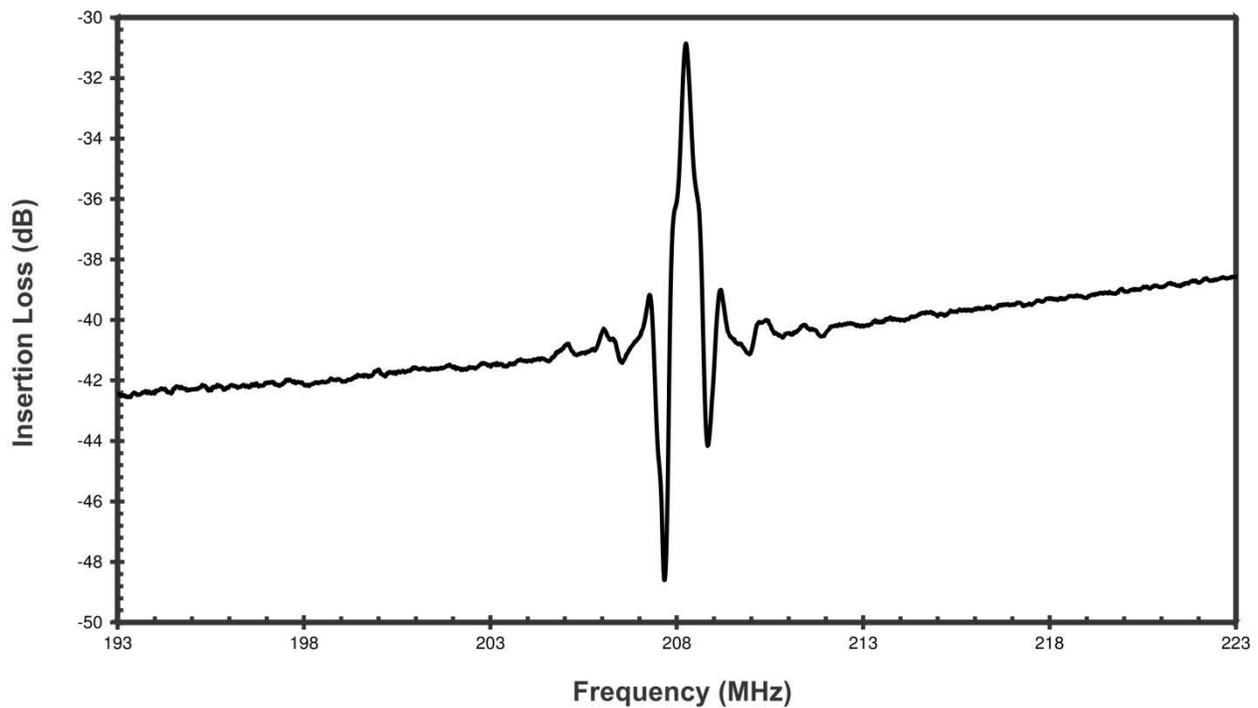
Figure 5-13: Reverse transmission coefficient (S_{12}) for the AlN/Si SAW device

5.4.2.1 Triple Transit Echo

Triple transit echo is one of the common second order effects that deteriorate the SAW device response [142, 145]. This effect arises due to the multiple reflections of the bi-directional IDTs of the SAW device. When an electrical signal is applied to the IDTs SAW waves of equal magnitude are generated in both directions as illustrated in Figure 5-14.
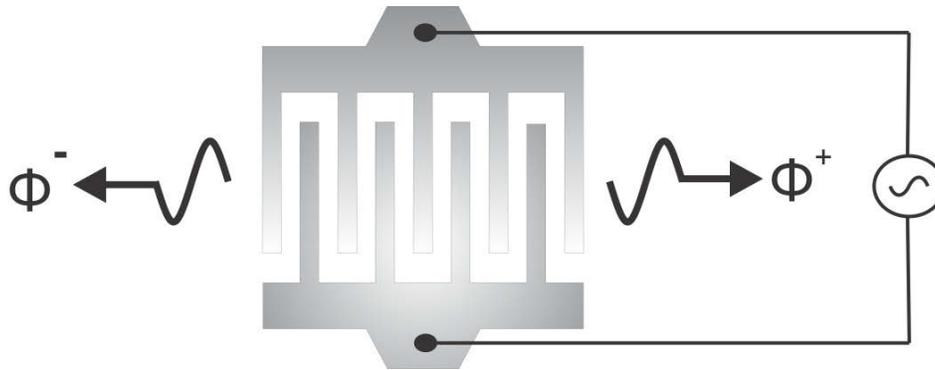
Figure 5-14: Waves emanating from both directions of a bidirectional IDT

In the case of two IDTs on the surface of the SAW device when the transmitted signal from the input IDT reaches the output IDT half of this signal is reflected back towards the input IDT. This signal leads to the generation of waves in the forward and backward directions; therefore half of this signal causes wave propagation again towards the output IDT. The triple transit echo effect is illustrated in Figure 5-15.
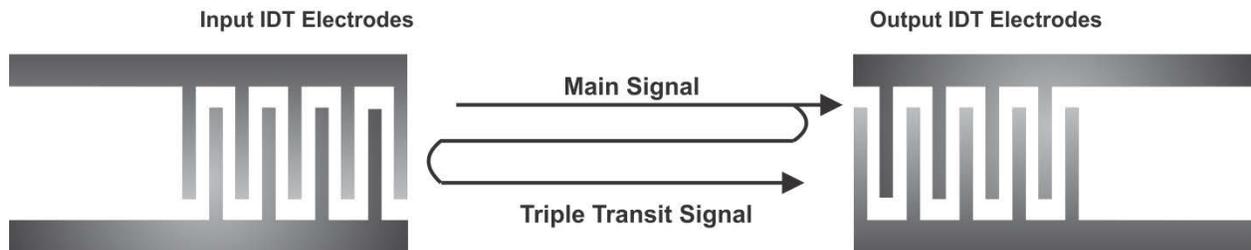
Figure 5-15: Triple Transit echo in SAW device

5.4.2.2 Electromagnetic feedthrough (EMF)

This refers to the coupling that occurs between the input and output IDTs of the SAW device, which leads to electromagnetic wave propagation. This is a common effect in SAW devices [142, 146]. If significant electromagnetic feedthrough occurs the signal will be completely leaked and no SAW wave propagation will take place. Some of the common ways of suppressing EMF is though

using highly resistive silicon and/or using insulating layers such as silicon nitride or silicon oxide [147]. In this study a 230nm layer of Silicon Nitride is deposited on the silicon substrate prior to depositing the AlN film to minimize the EMF. However, some coupling takes place between the input and output IDTs, which needs to be eliminated from the SAW device frequency response.

5.4.2.3 Time Domain Analysis (Time Gating)

The triple transit echo and the electromagnetic feedthrough can be eliminated from the response signal using time gating [148, 149]. The frequency response is converted from the frequency domain to the time domain via inverse Fourier transform. This can be done using a built-in feature in the vector network analyzer since the VNA used in this study has time domain analysis capability. When the signal is displayed in the time domain the responses due to EMF, the main signal response and triple transit echo can be seen separated in time as illustrated in Figure 5-16. Each of these three signals will have a different velocity. The electromagnetic feedthrough appears as the first signal since electromagnetic wave velocity is significantly higher than the acoustic wave velocity. The second signal that appears is the main SAW wave signal and its peak occurs at 918.75ns. The triple transit signal appears after the main SAW signal and its peak occurs at 3,123.75ns. The time required for the peak of the triple transit signal to appear is approximately three times the time required for the peak of the main signal. This is because the triple transit signal travels three times the distance traveled by the main signal as illustrated in Figure 5-15.
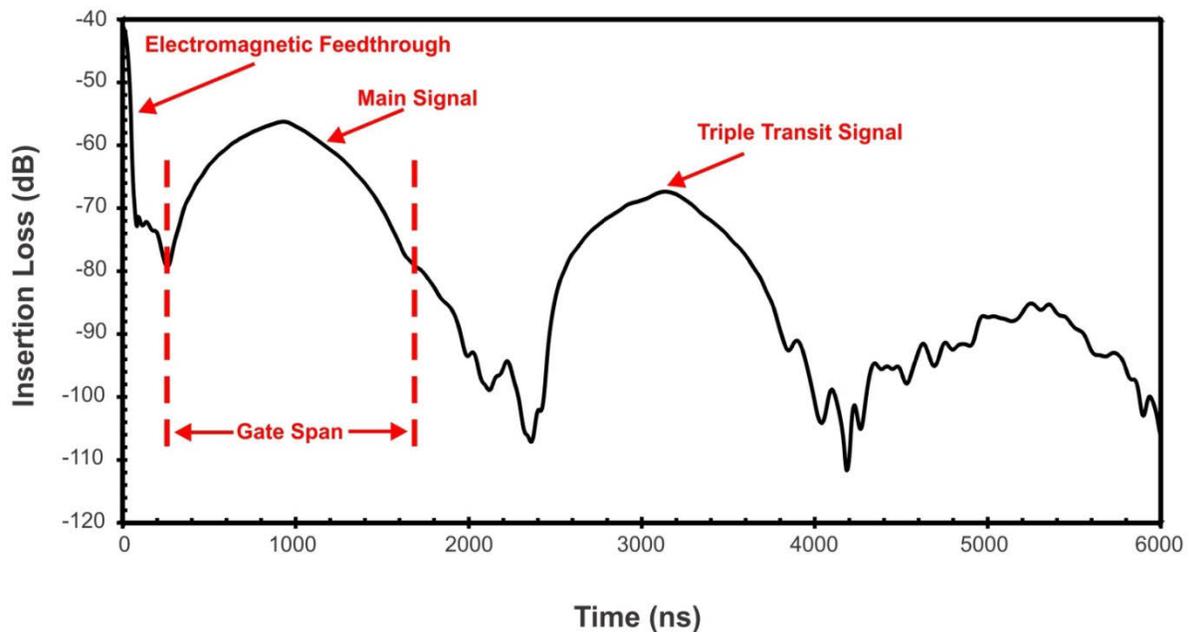
Figure 5-16: S$_{21}$ parameter of an AlN/Si SAW device plotted in the time domain

The time gating function needs to be applied to eliminate the electromagnetic feedthrough and the triple transit signal. The center of the gate function is specified to be 918.75ns, which is at the peak of the main SAW signal as shown in Figure 5-16 and the span of the gate is set to 1.28µs. Everything beyond the gate span will be set to zero by the time gating function and only the main signal will remain. The result of applying the time gating function to the signal in Figure 5-16 is illustrated in Figure 5-17.
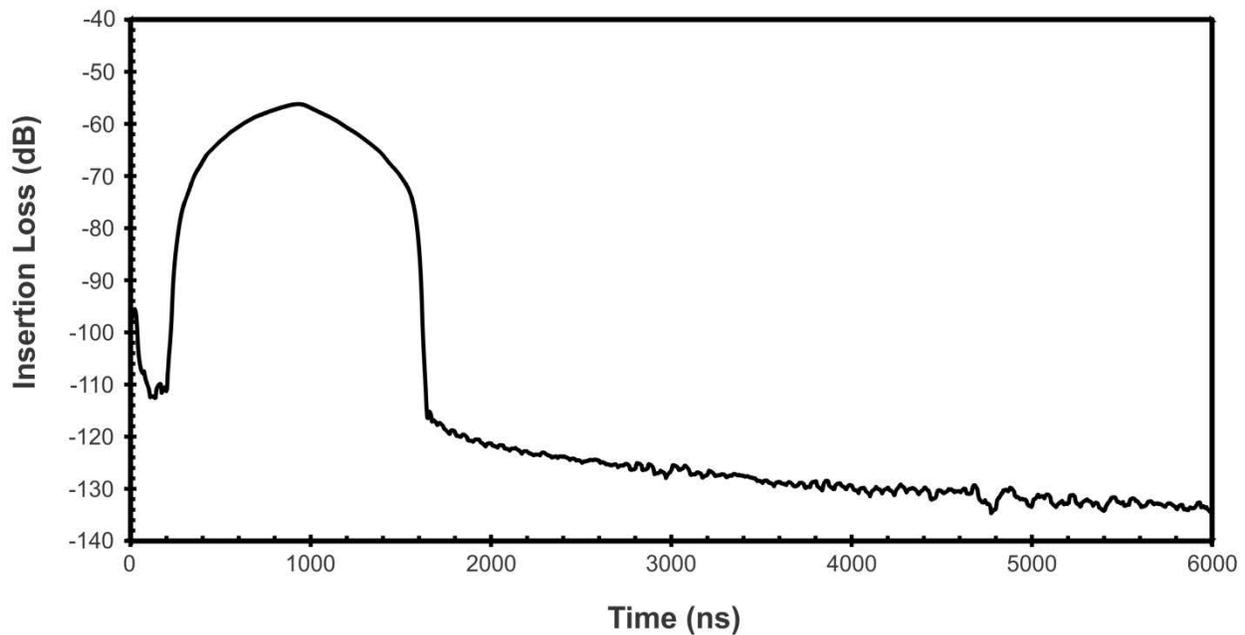
Figure 5-17: S$_{21}$ parameter of AlN/Si SAW device in the time domain after removing the electromagnetic feedthrough and triple transit signal by time gating

The electromagnetic feedthrough and triple transit signal have been successfully removed and only the main signal is kept. By converting the time gated signal in Figure 5-17 to the frequency domain the frequency response of the AlN/Si SAW device can be clearly seen. The time gated signal in the time domain is converted back to the frequency domain via Fourier transform. The final S$_{21}$ plot for the AlN/Si SAW device is illustrated in Figure 5-18. The same approach has been applied to the S$_{12}$ parameter plot in Figure 5-13. The time domain signal is plotted in Figure 5-19 and the time domain signal after time gating is plotted in Figure 5-20 and the final S$_{12}$ parameter plot is illustrated in Figure 5-21.
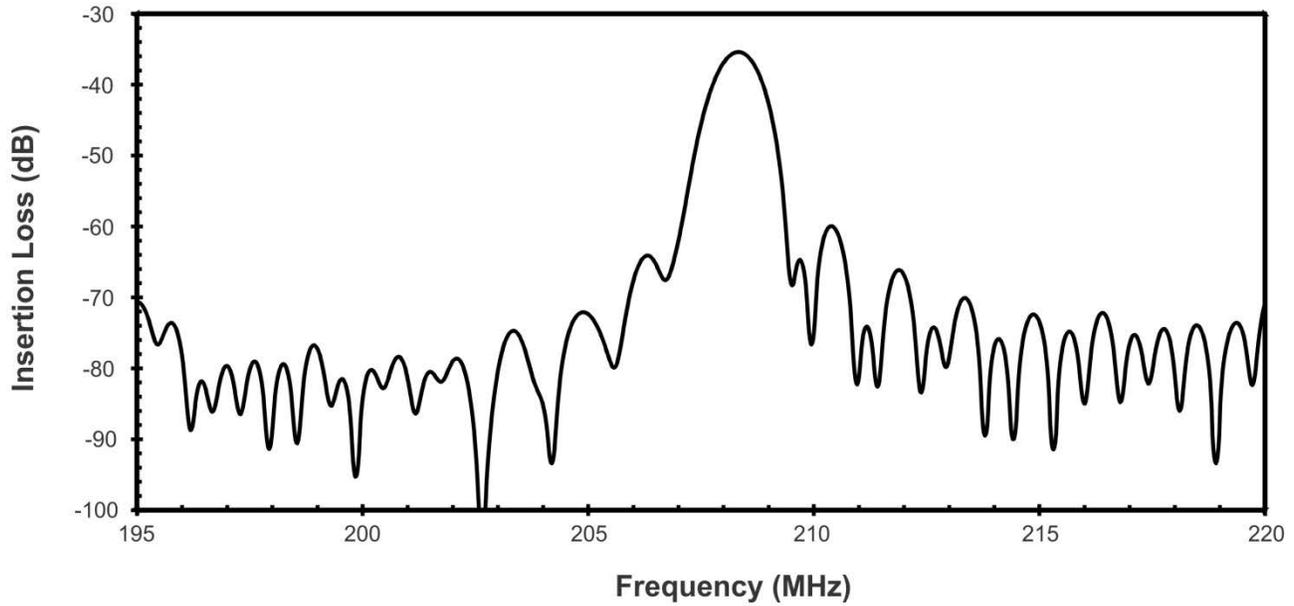
Figure 5-18: S_{21} parameter of the AlN/Si SAW device plotted in the frequency domain after eliminating the electromagnetic feedthrough and triple transit signal by time gating
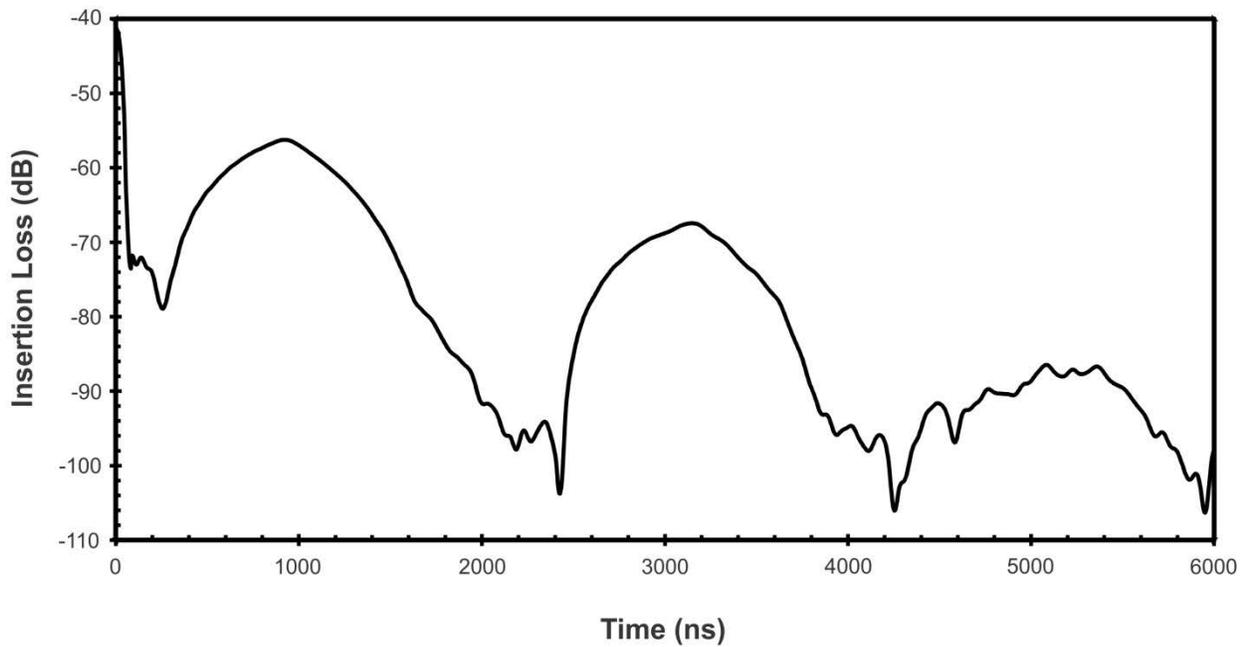
Figure 5-19: S_{12} parameter of AlN/Si SAW device plotted in the time domain
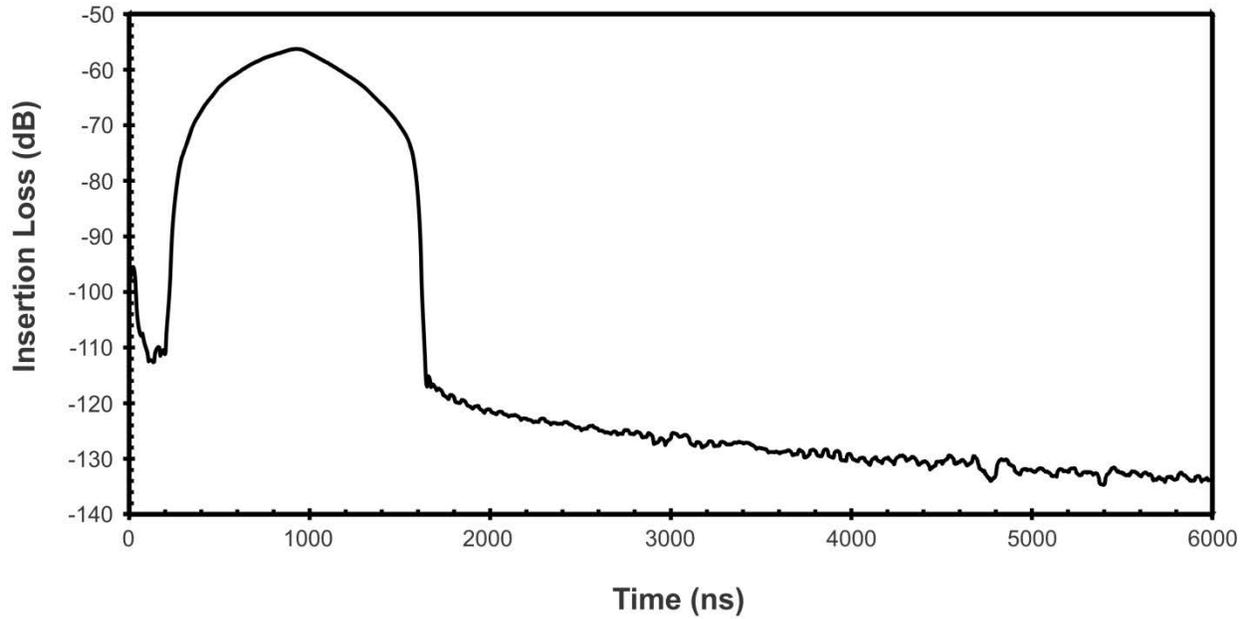
Figure 5-20: S_{12} parameter of AlN/Si SAW device in the time domain after removing the electromagnetic feedthrough and triple transit signal by time gating
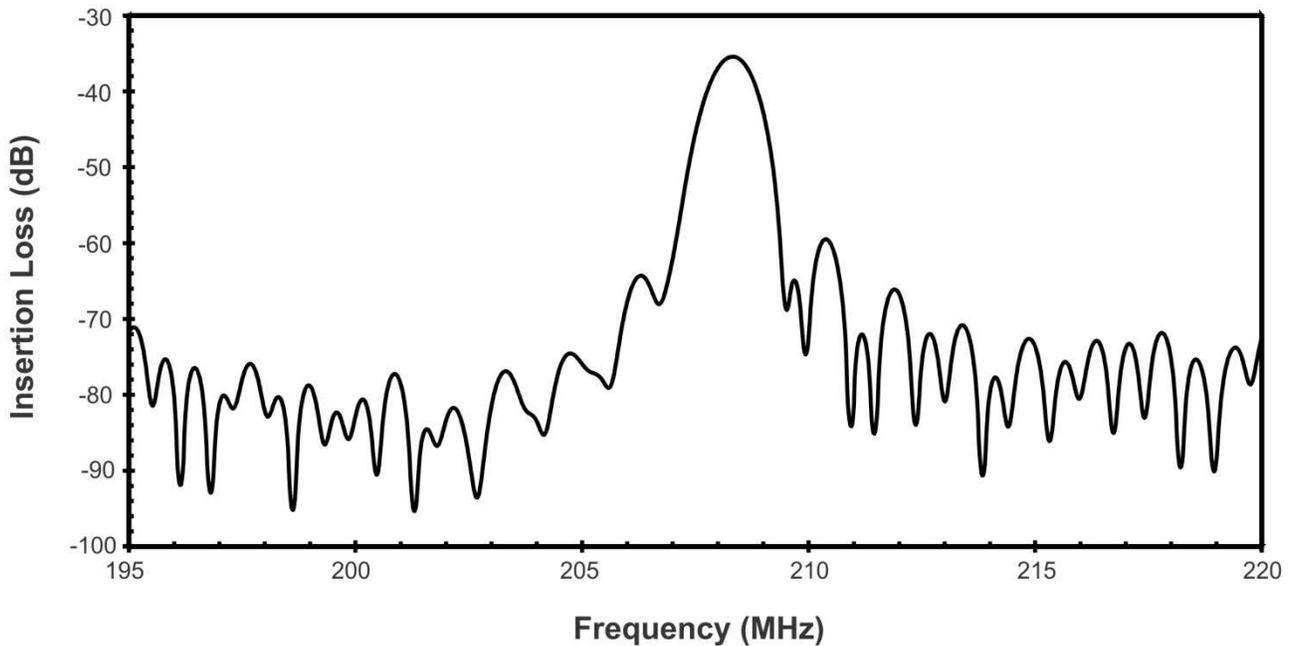
Figure 5-21: S_{12} parameter of the AlN/Si SAW device plotted in the frequency domain after eliminating the electromagnetic feedthrough and triple transit signal by time gating

5.5 Conclusions

This chapter discussed the operating principle of surface acoustic wave devices with delay line configuration and the electric field distribution due to the inter-digital transducers. The architecture and operating principle of the vector network analyzer were also presented. Some of the common errors that affect frequency response measurements using a v ector network analyzer were also introduced as well as the calibration technique to eliminate those errors. The electrical set-up for measuring the scattering parameters of the SAW sensors was illustrated and the measurement of a SAW device was carried out. Second order effects such as electromagnetic feedthrough and triple transit effect, which deteriorate the frequency response of the SAW device, were illustrated. The time gating technique for eliminating these effects was applied to the measured SAW device and the improvements to the S-parameters of the SAW device response were illustrated. The electrical setup and measurement procedures introduced in this chapter will be applied to the SU-8/AlN/Si SAW sensors in the next chapter to measure their frequency responses.

CHAPTER 6.   FREQUENCY RESPONSE MEASUREMENTS OF SU-8/ALN/SI SAW SENSORS FOR SU-8 ADHESION EVALUATION[3]

6.1 Overview

This chapter illustrates the testing of the SU-8/AlN/Si SAW sensors to evaluate the adhesion of the SU-8 thin film. Four SAW sensor designs operating in the frequency range of 84-208MHz will be tested. For each design two device configurations will be implemented one of the device configurations has an SU-8 patterned above a thin gold film on the surface of the AlN/Si SAW sensor and in the second configuration an omnicoat layer is patterned on top of the gold film prior to SU-8 patterning. The frequency response for both configurations will be measured and the frequency shifts will be calculated. It is expected that the frequency shift will increase as the operating frequency of the sensor increases due to the increased sensitivity. Using the center frequency values the SAW phase velocity values will be calculated to determine the velocity shifts resulting from the change in adhesion of the SU-8 layer. Since one of the device configurations has a thin omnicoat layer to improve the adhesion of SU-8, the mass loading effect due to the omnicoat layer will be evaluated and its effect on the overall frequency and velocity shifts will be eliminated. This allows the exact evaluation of the frequency and velocity shifts due to the change in adhesion of the SU-8 layer. Finally, the theoretical model will be used to find the equivalent interface spring stiffness values that correspond to the SU-8/Au/AlN/Si configuration with and without omnicoat by curve fitting the dispersion curves to the experimental wave velocity values.

6.2 Testing methodology

The testing approach utilized in this study involves developing two device configurations of the four SAW sensor designs operating in the frequency range of 84-208MHz. In the first configuration the SU-8 layer is patterned on the surface of the AlN/Si SAW sensor on top of a gold film. In the

---

[3] Some of the materials in this chapter has been submitted for publication [86] and other parts of this chapter have been published by Elgowini and Moussa [102]

second configuration the gold film is coated with an omnicoat layer prior to SU-8 patterning. The frequency responses from both device configurations will be measured and the shift in the center frequency value will be evaluated for each of the four SAW sensor designs. The two device configurations with and without omnicoat are illustrated in Figure 6-1.
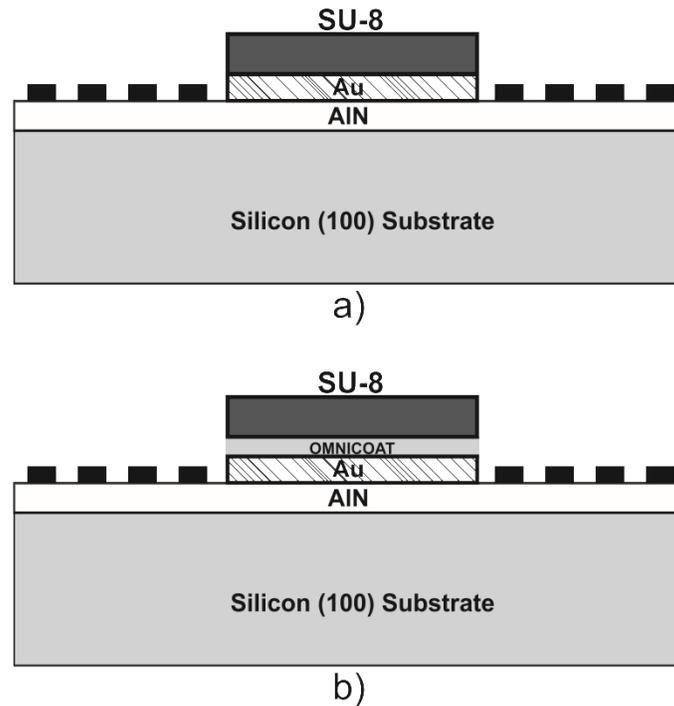
Figure 6-1: Two configurations for the SU-8/AlN/Si SAW sensors used for evaluating the adhesion of the SU-8 film. a) SU-8/AlN/Si SAW sensor configuration without omnicoat. b) SU-8/AlN/Si SAW sensor configuration with omnicoat.

The SAW phase velocity values v will be evaluated from the center frequency values f using $v = f \cdot \lambda$, where λ is the acoustic wavelength. The change in wave velocity due to the change in adhesion of the SU-8 film can be evaluated using this approach for each of the four SAW sensor designs. For each design two device configurations are utilized to measure the change in frequency and velocity due to the change in adhesion of the SU-8 layer using omnicoat. The mass loading effect of omnicoat needs to be evaluated to ensure the shift in SAW sensor response is due to the change in adhesion of the SU-8 film and not due to the presence of omnicoat in one of the device configurations. Another set of SAW sensors will be developed without the SU-8 layer. There will be two device configurations of the SAW sensors, one with omnicoat patterned on top of the gold film on the surface of the AlN/Si sensor and in the second configuration the gold film will be patterned

on the surface of the AlN/Si SAW sensor without the omnicoat layer. These SAW sensors are fabricated using the process flow illustrated in the microfabrication chapter Figure 4-7 except for the last step that involves patterning the SU-8 layer.
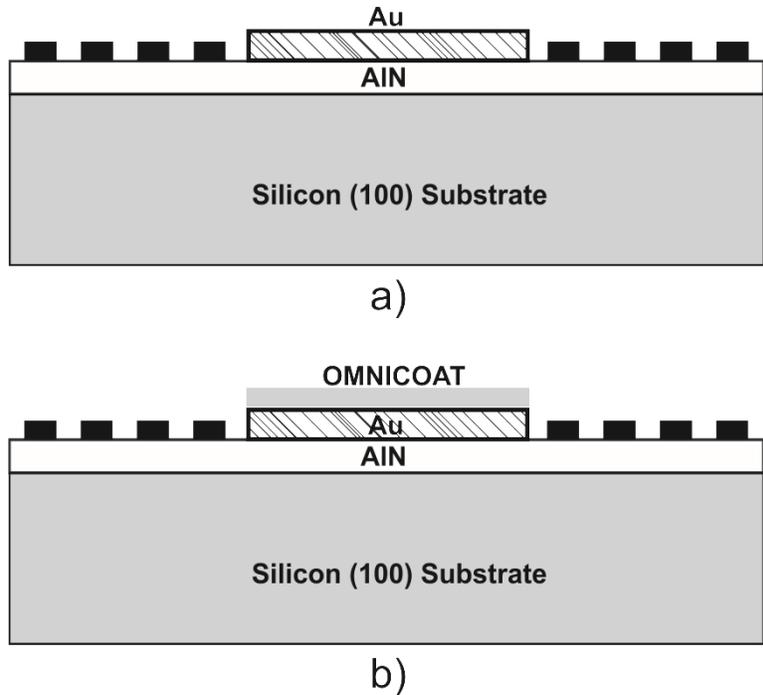
Figure 6-2: Two SAW sensor configurations without SU-8 to evaluate the mass loading effect due to omnicoat. a) Au/AlN/Si SAW sensor. b) Omnicoat/Au/AlN/Si SAW sensor.

The frequency response measurements of the four sensor designs will be measured using the vector network analyzer and the frequency shift between the two configurations in Figure 6-2 will be measured and the velocity shift will also be calculated. The frequency and velocity shifts due to the mass loading effect of omnicoat will be subtracted from the frequency and velocity shifts due to the change in adhesion of the SU-8 layer. The parameters of the four SAW sensor designs that will be used in this study to evaluate the adhesion of the SU-8 layer as well as the mass loading effect of omnicoat are listed in Table 6-1. A schematic illustration of the SAW sensor parameters were shown in the previous chapter in Figure 5-2.

Table 6-1: Parameters of the SAW sensors used in this study

Design Parameters	Design 1	Design 2	Design 3	Design 4
Operating frequency (MHz)	84	125	167	208
Wavelength (λ) (μm)	60	40	30	24
Number of electrode pairs	100	150	150	150
Electrode length (f) (μm)	5,363	1,595	1,230	1,012
Acoustic aperture (w) (xλ)	90	40	41	42
Center-to-Center distance (d) (μm)	6,985	6,990	5,492	4,594
Normalized Film Thickness (h_{AlN}/λ)	0.01833	0.0275	0.03667	0.04583

6.3 Frequency response measurements for the SU-8/AlN/Si SAW sensors

The scattering parameters of the SU-8/AlN/Si SAW sensors are carried out using the vector network analyzer as described in the previous chapter. The S-parameters are measured for both configurations of the four SAW sensor designs. In this section the four scattering parameters will be plotted for two of the SU-8/AlN/Si SAW sensors for illustration and just the S_{21} parameter plot for the remaining sensors. The S_{21} parameter is used to determine the center frequency of the SAW sensor and in the calculation of the phase velocity. The scattering parameter plots for the rest of the SU-8/AlN/Si SAW sensors can be found in Appendix B. The S-parameters of a SU-8/AlN/Si SAW sensor with an omnicoat layer operating at 167MHz are plotted in Figure 6-3 to Figure 6-6. The time domain response of the S_{21} parameter is plotted in Figure 6-7, which illustrates the electromagnetic feedthrough, the main SAW response and the triple transit echo separated in time. The time gated response is illustrated in Figure 6-8 and the final S_{21} parameter plot in the frequency domain is plotted in Figure 6-9. Similar plots are obtained for a SU-8/AlN/Si SAW sensor without an omnicoat layer operating at 167MHz, which are illustrated in Figure 6-10 through Figure 6-16. Figure 6-17 through Figure 6-19 illustrate the S_{21} parameter plots of the remaining three SU-8/AlN/Si SAW sensor designs with an omnicoat layer operating in the frequency range of 84-208MHz. Figure 6-20 through Figure 6-22 also illustrate the S_{21} parameter plots for the three remaining SU-8/AlN/Si SAW sensor designs without an omnicoat layer operating in the frequency range of 84-208MHz.
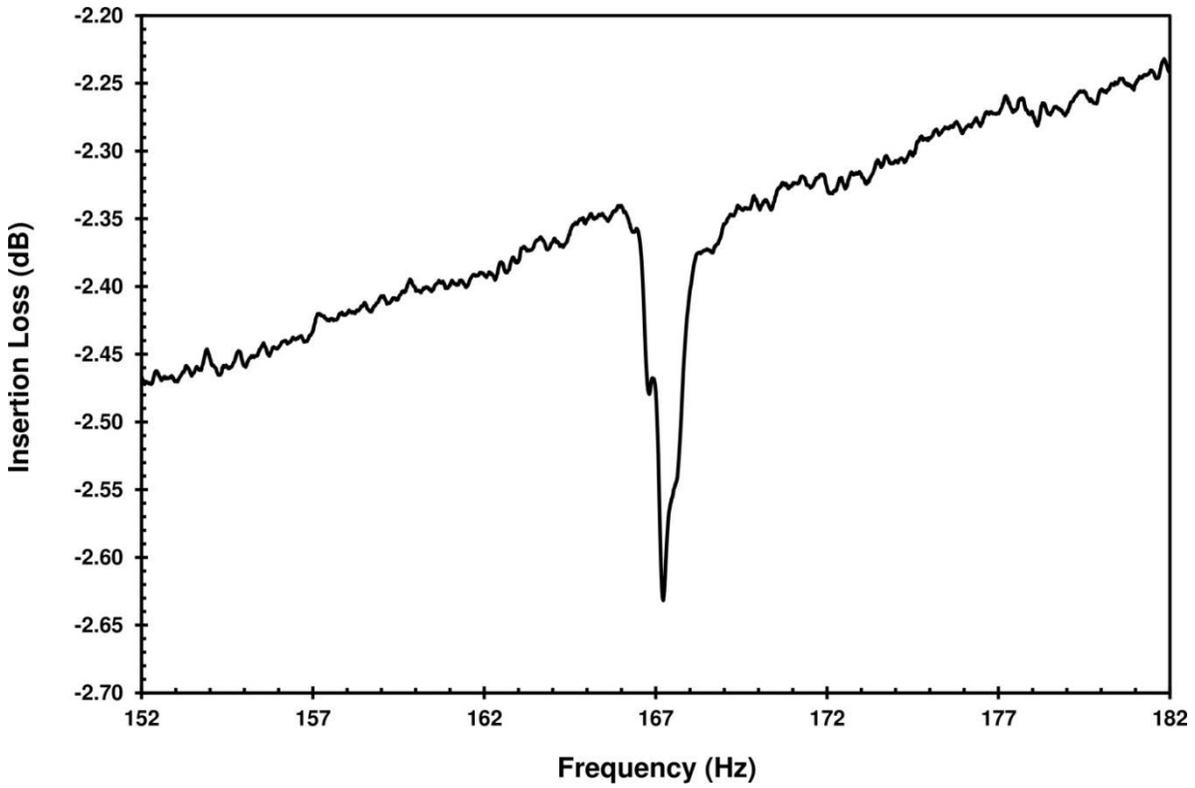
Figure 6-3: S_{11} parameter plot for the SU-8/AlN/Si SAW sensor with omnicoat operating at 167MHz
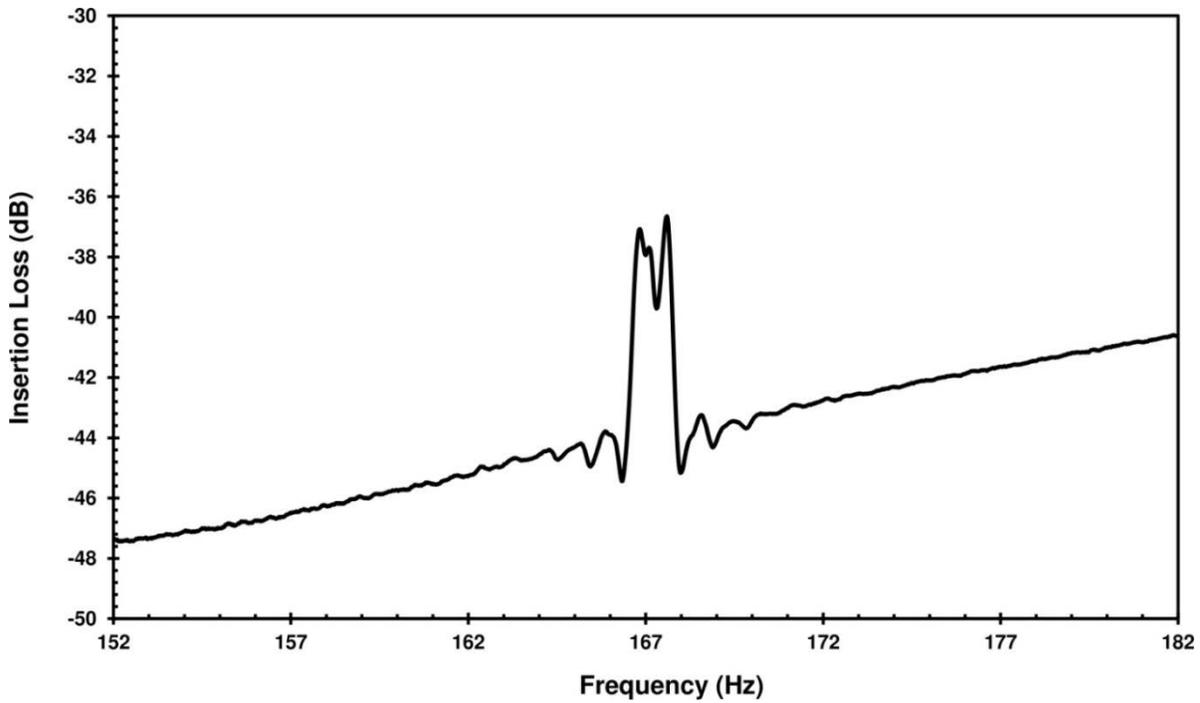
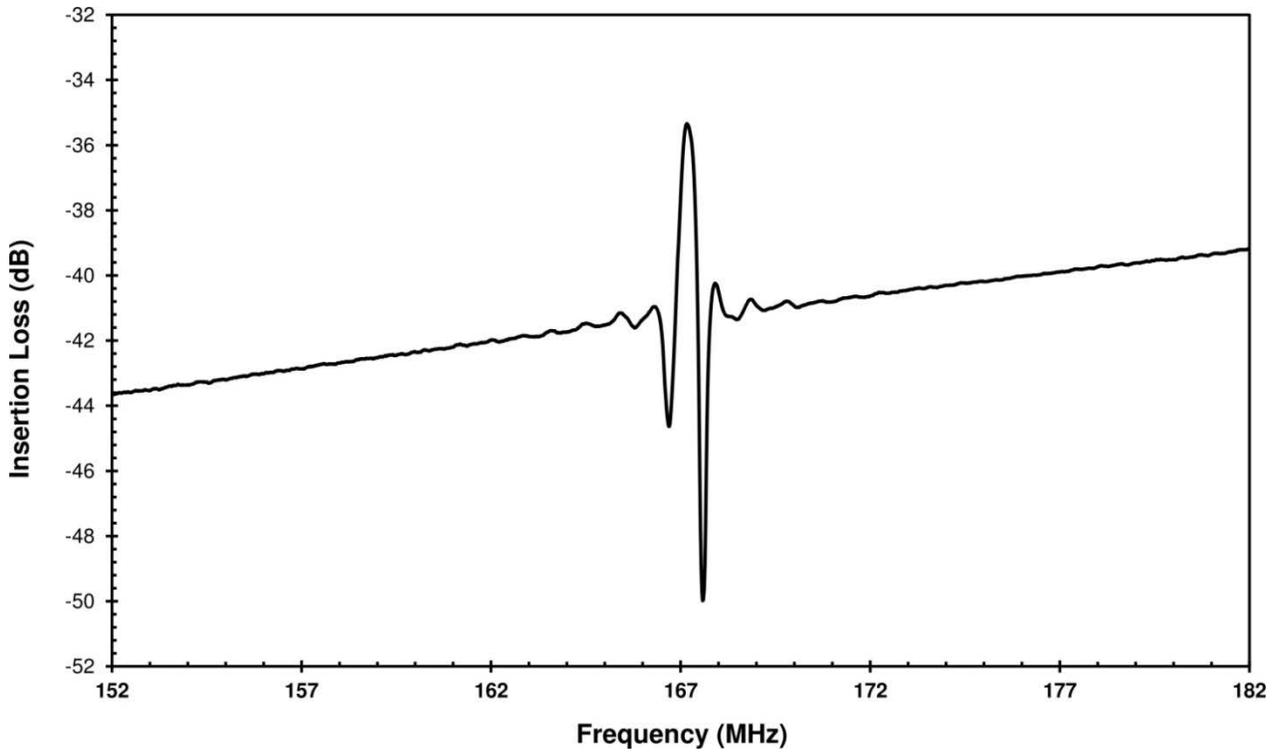**Figure 6-4: S_{21} parameter plot for the SU-8/AlN/Si SAW sensor with omnicoat operating at 167MHz**
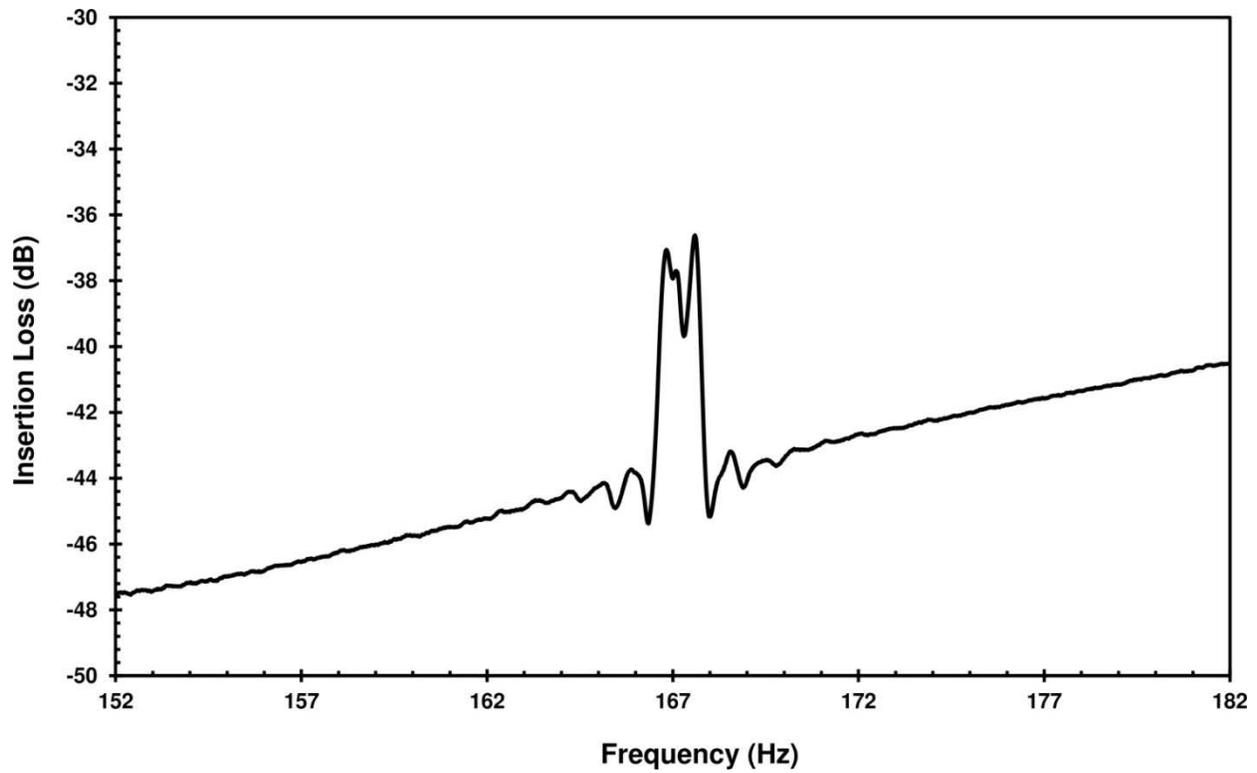
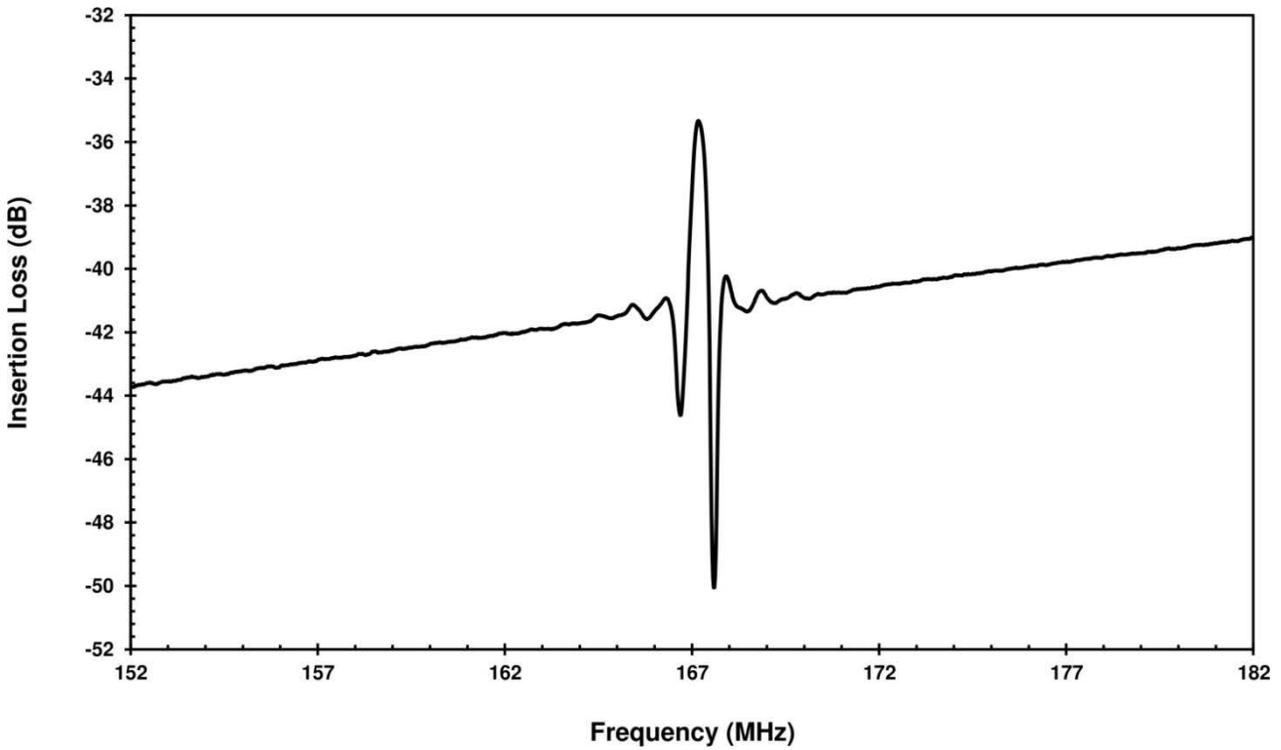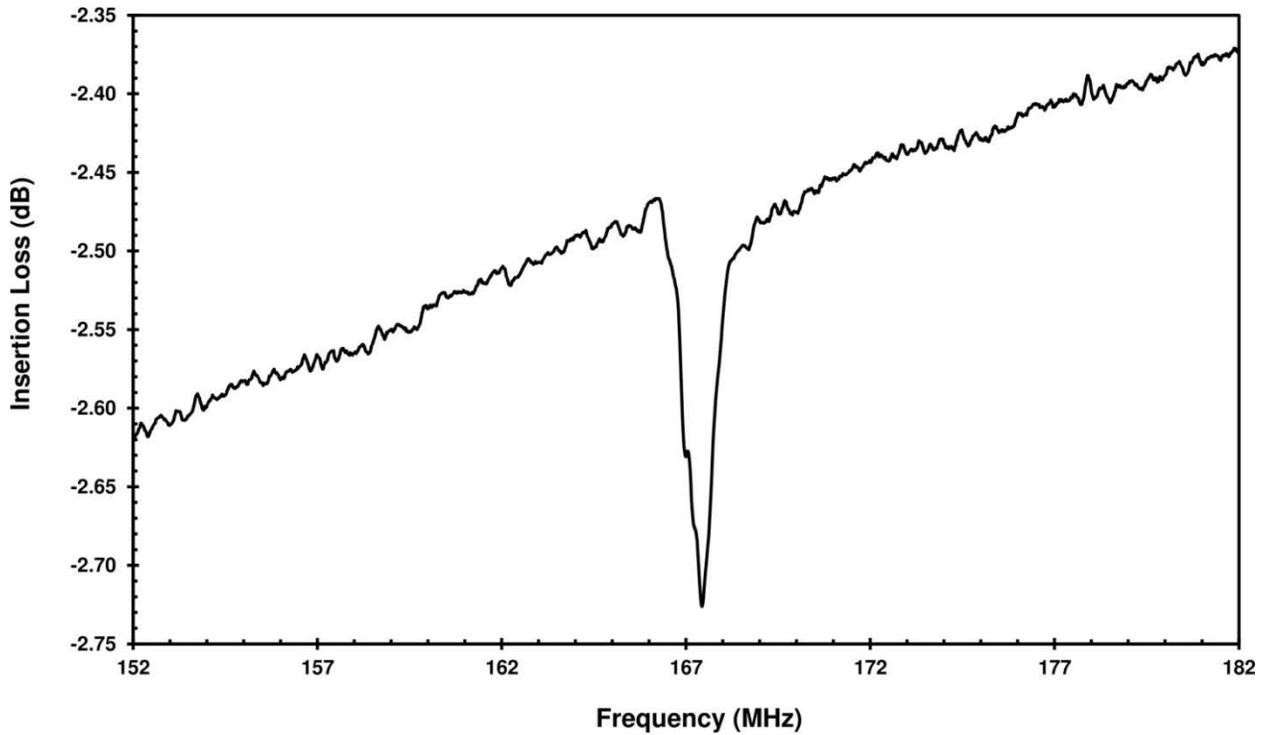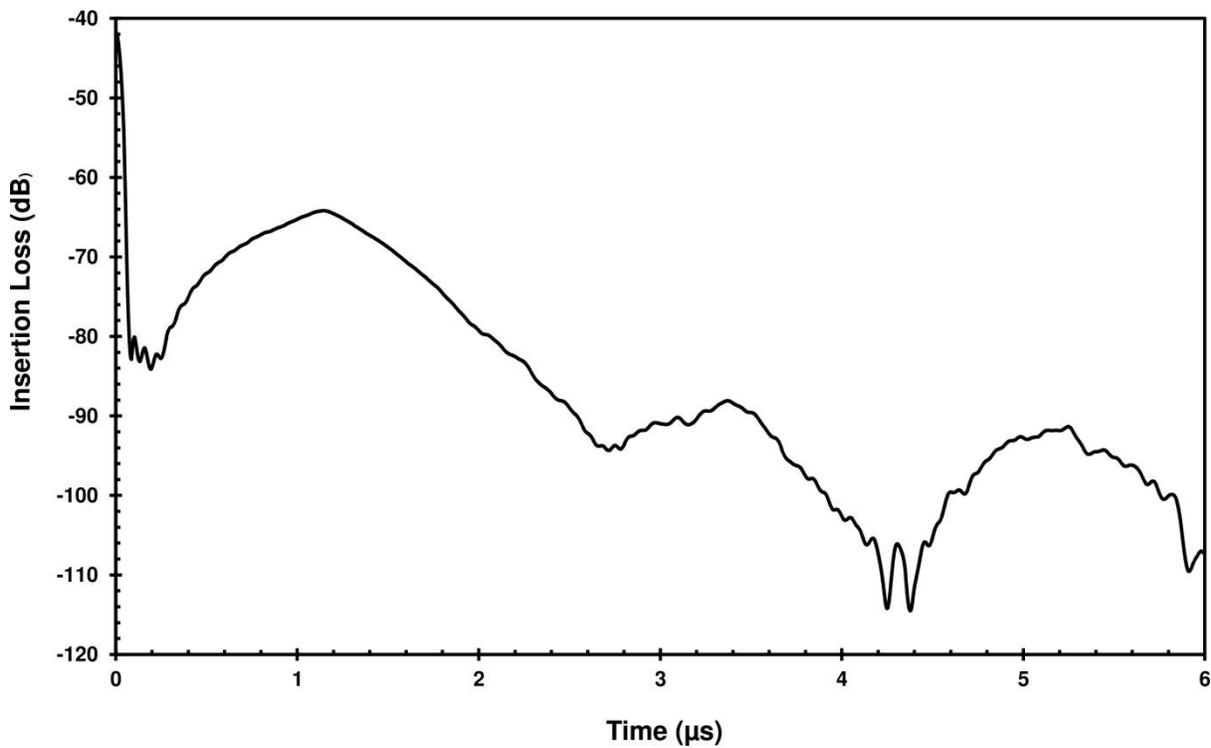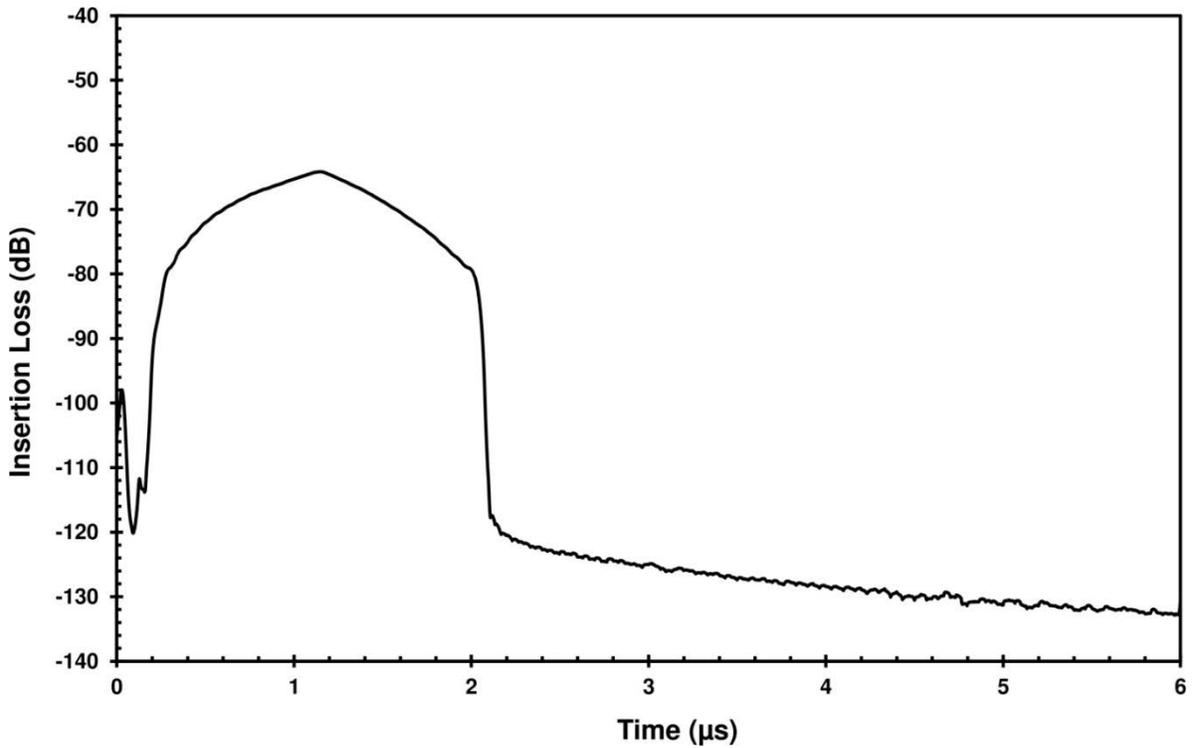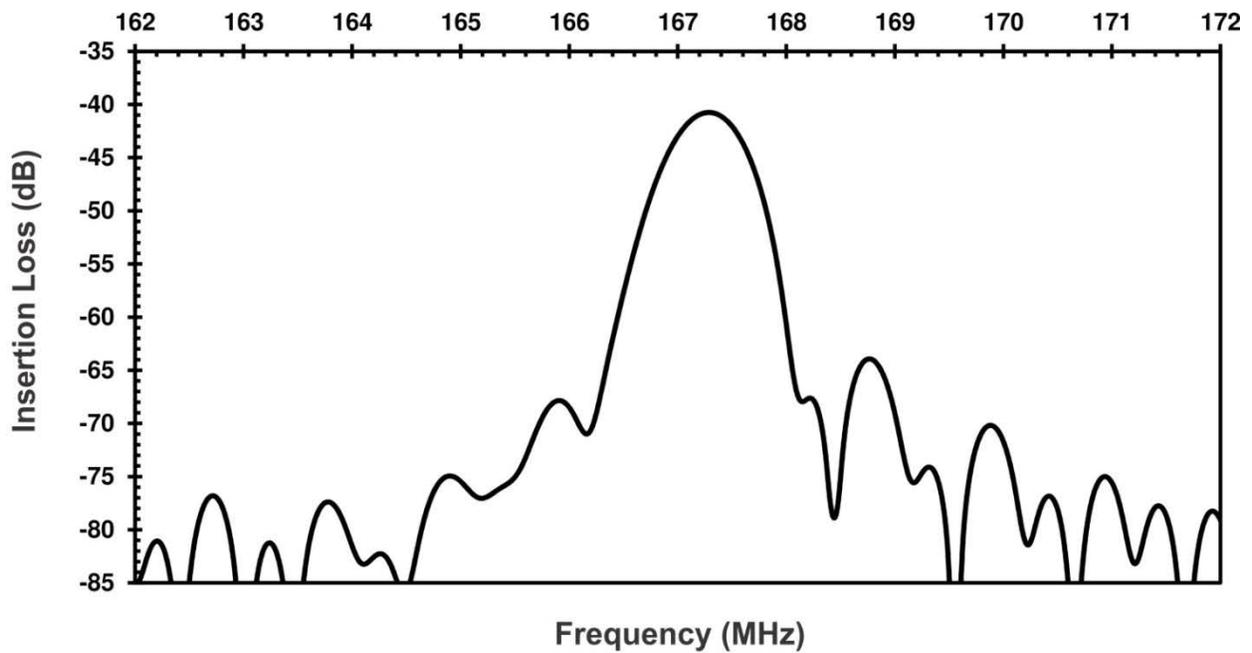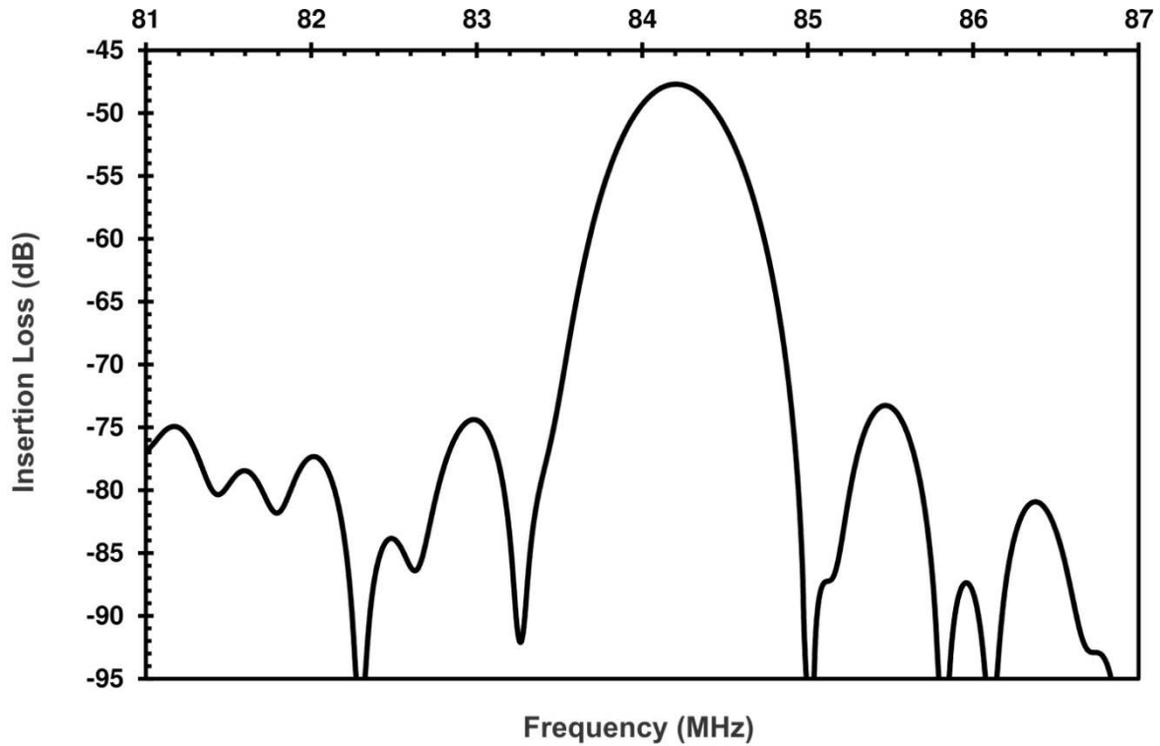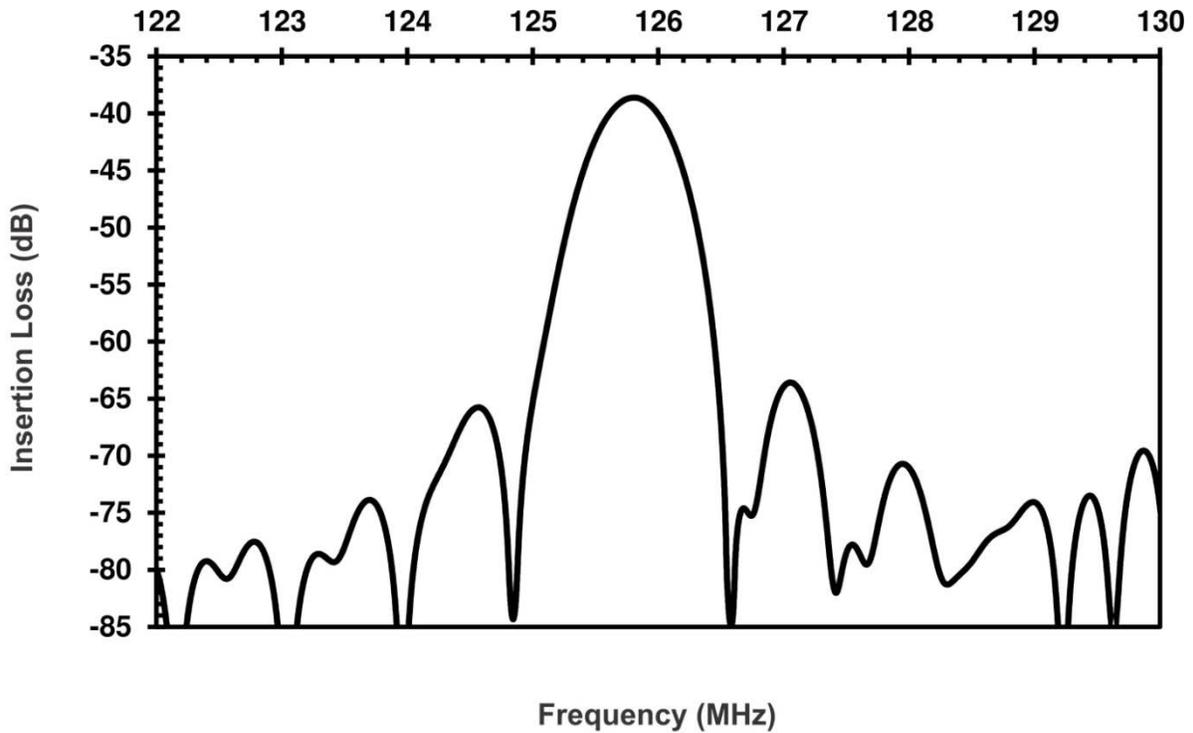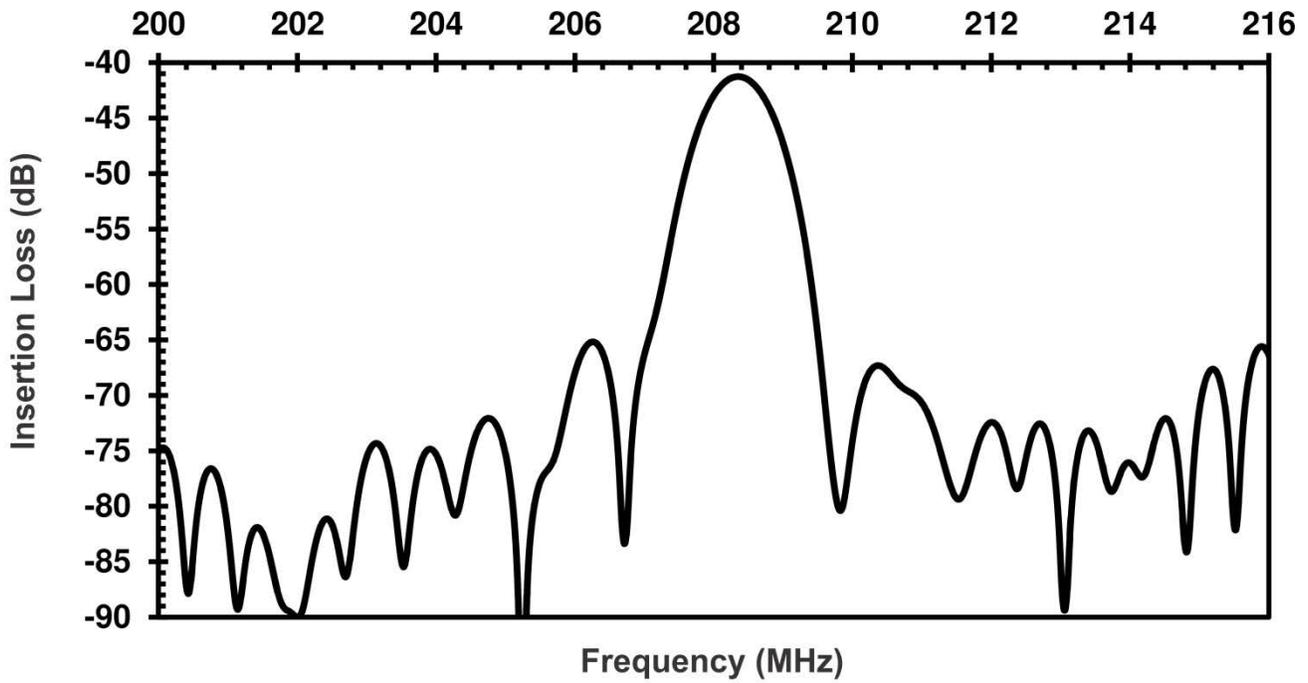**Figure 6-5: S$_{12}$ parameter plot for the SU-8/AlN/Si SAW sensor with omnicoat operating at 167MHz**
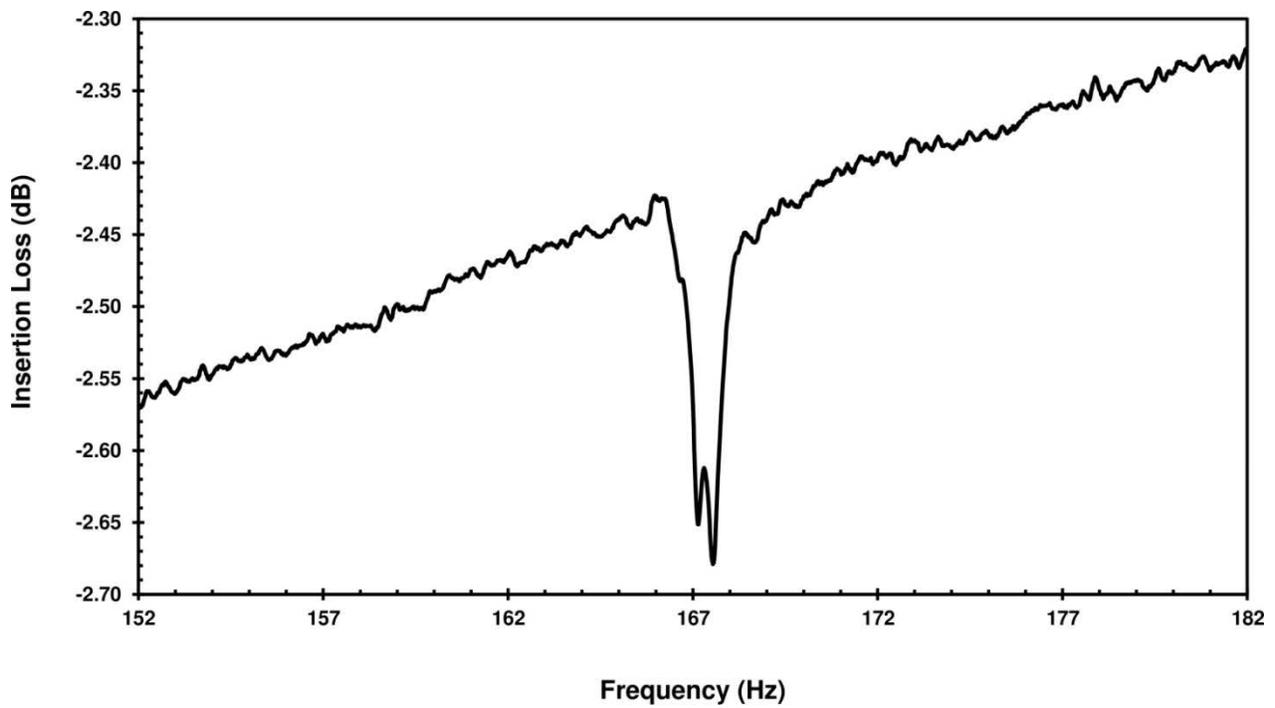
Figure 6-6: S$_{22}$ parameter plot for the SU-8/AlN/Si SAW sensor with omnicoat operating at 167MHz
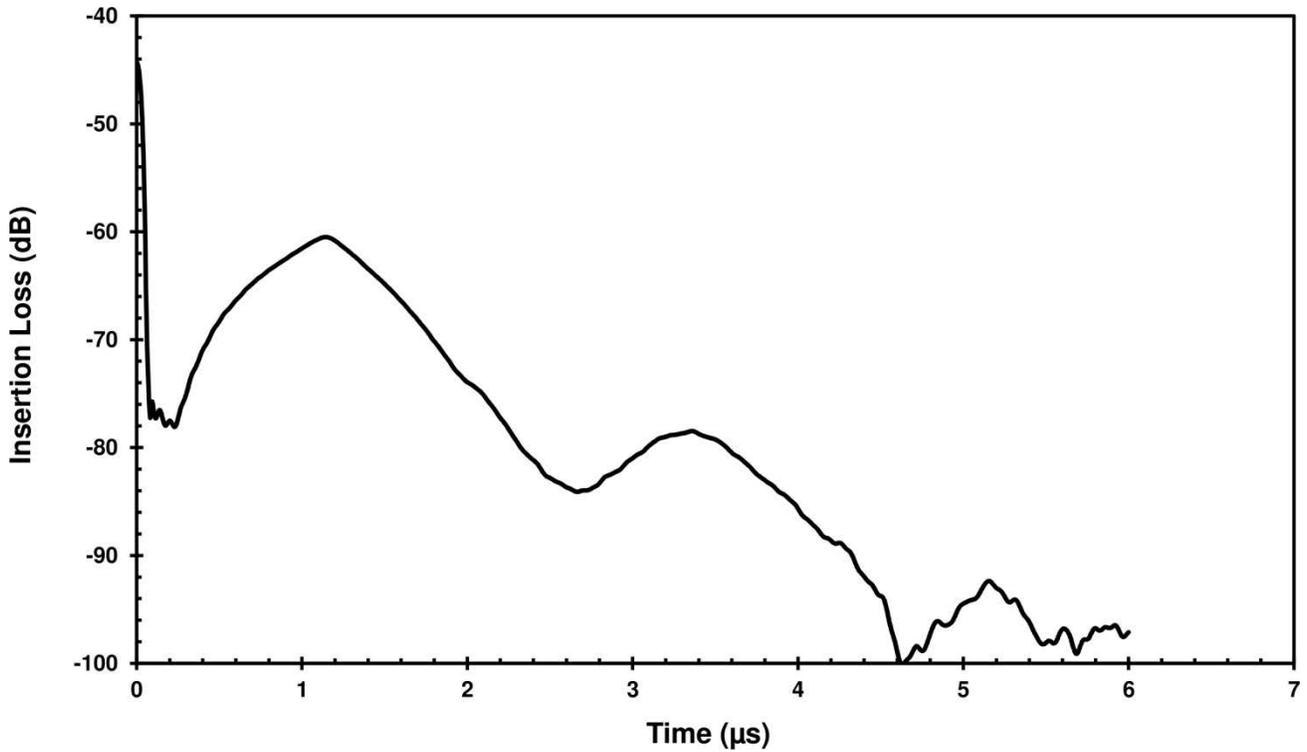
Figure 6-7: Time domain response of the S_{21} parameter plot for the SU-8/AlN/Si SAW sensor with omnicoat operating at 167MHz
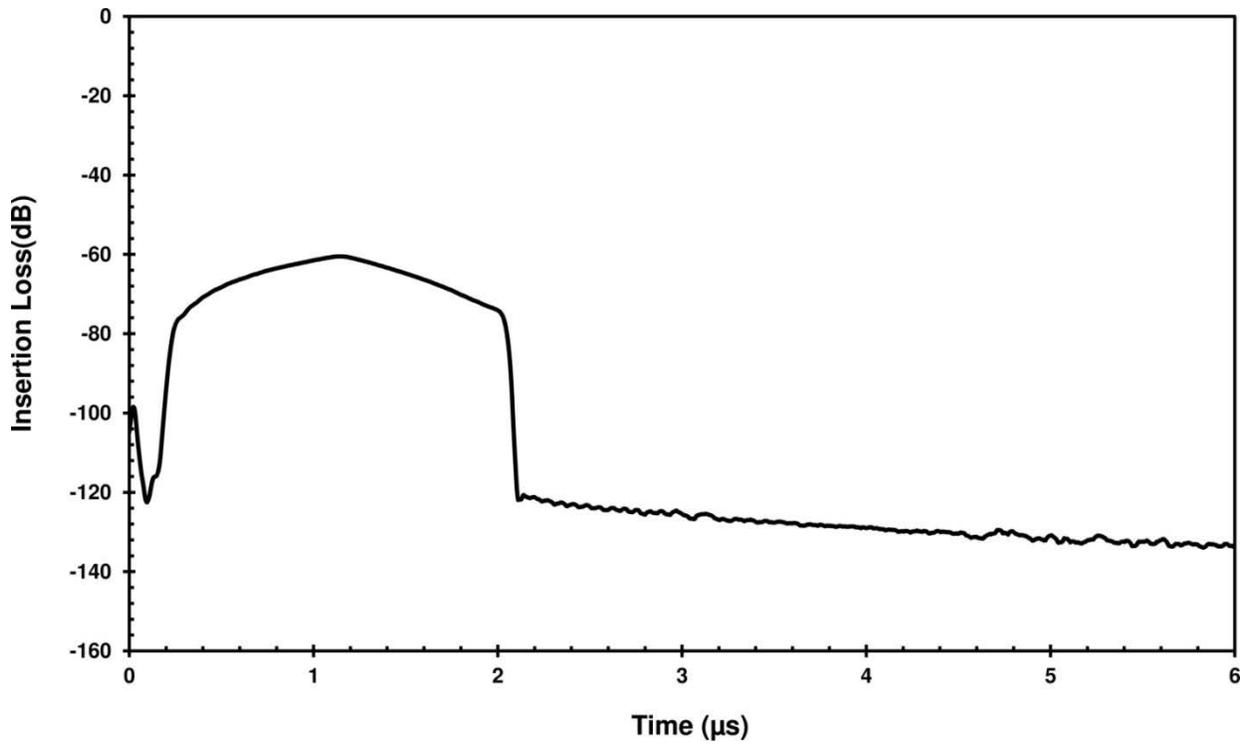
Figure 6-8: Time domain response after applying the time gating function for the S_{21} parameter of the SU-8/AlN/Si SAW sensor with omnicoat operating at 167MHz
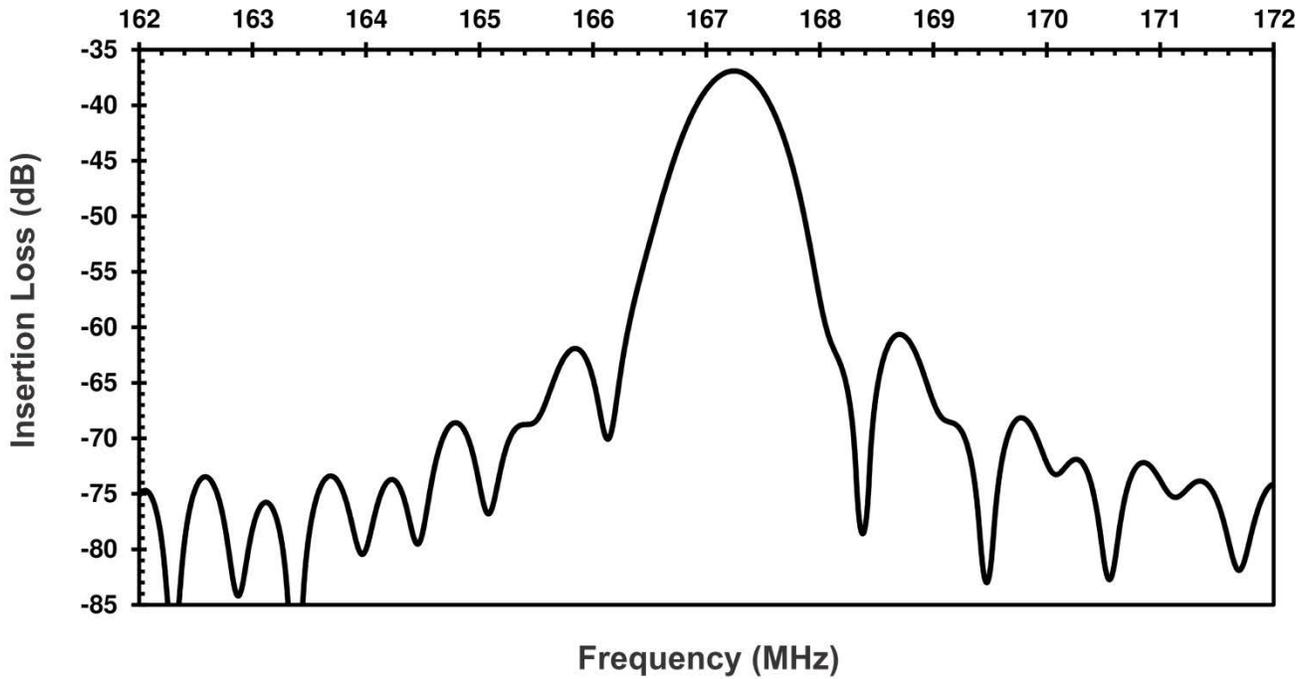
Figure 6-9: S_{21} parameter plot with time gating for the SU-8/AlN/Si SAW sensor with Omnicoat operating at 167MHz
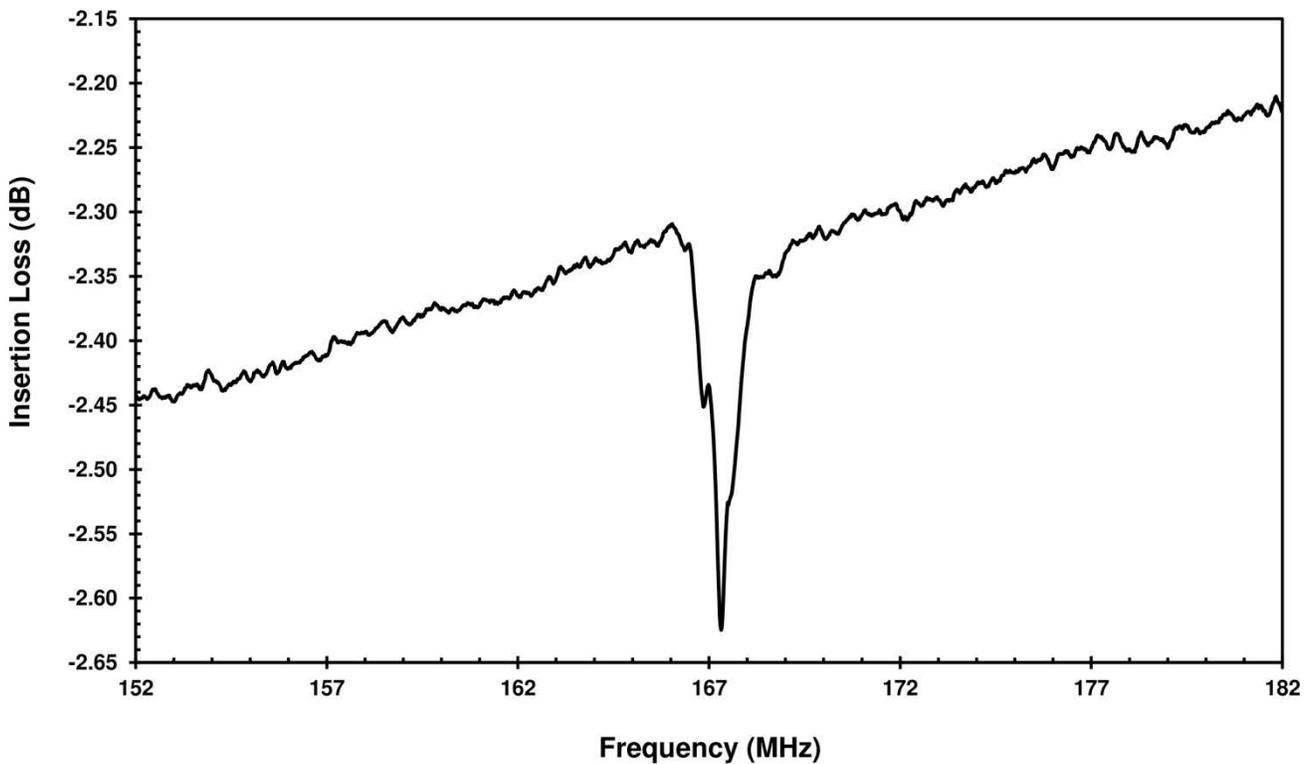
Figure 6-10: S_{11} parameter plot for the SU-8/AlN/Si SAW sensor without omnicoat operating at 167MHz

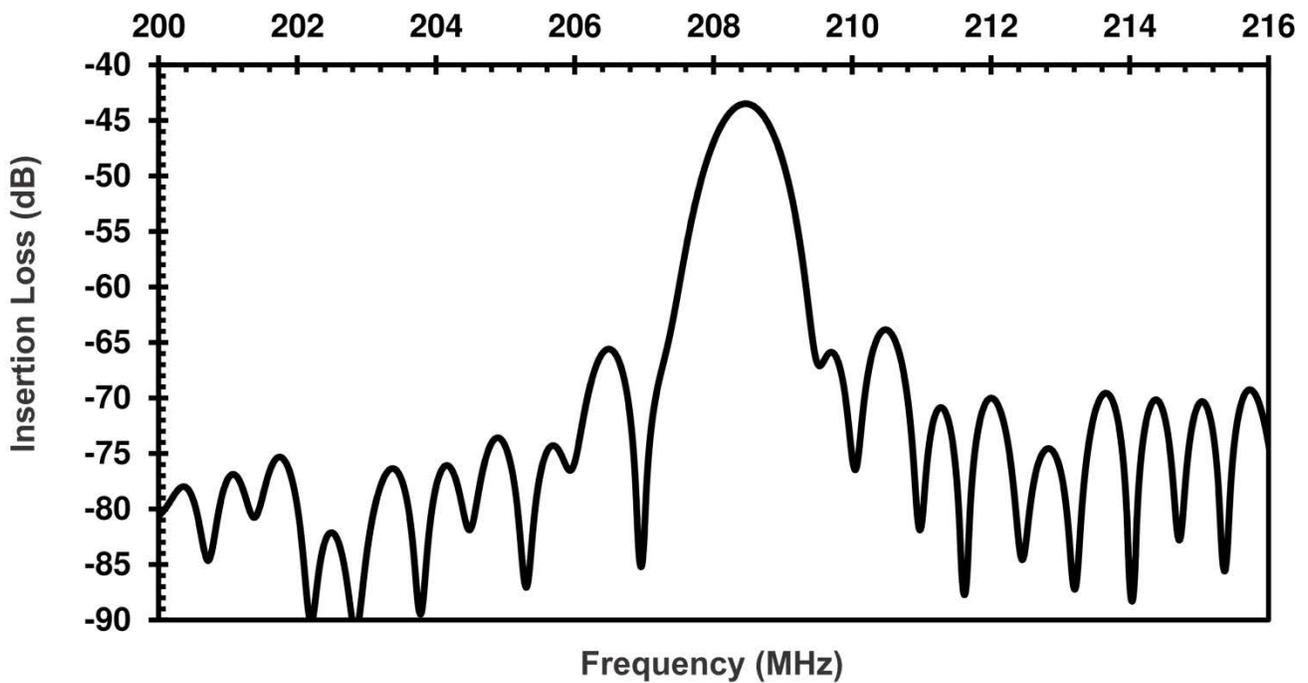**Figure 6-11: S_{12} parameter plot for the SU-8/AlN/Si SAW sensor without omnicoat operating at 167MHz**

Figure 6-12: S_{21} parameter plot for the SU-8/AlN/Si SAW sensor without omnicoat operating at 167MHz

Figure 6-13: S$_{22}$ parameter plot for the SU-8/AlN/Si SAW sensor without omnicoat operating at 167MHz

Figure 6-14: Time domain response of the S$_{21}$ parameter plot for the SU-8/AlN/Si SAW sensor without omnicoat operating at 167MHz

Figure 6-15: Time domain response after applying the time gating function for the S_{21} parameter of the SU-8/AlN/Si SAW sensor without omnicoat operating at 167MHz

Figure 6-16: S_{21} parameter plot with time gating for the SU-8/AlN/Si SAW sensor without Omnicoat operating at 167MHz

Figure 6-17: S_{21} parameter plot for the SU-8/AlN/Si SAW sensor with Omnicoat operating at 84MHz

Figure 6-18: S_{21} parameter plot for the SU-8/AlN/Si SAW sensor with Omnicoat operating at 125MHz

Figure 6-19: S$_{21}$ parameter plot for the SU-8/AlN/Si SAW sensor with Omnicoat operating at 208MHz
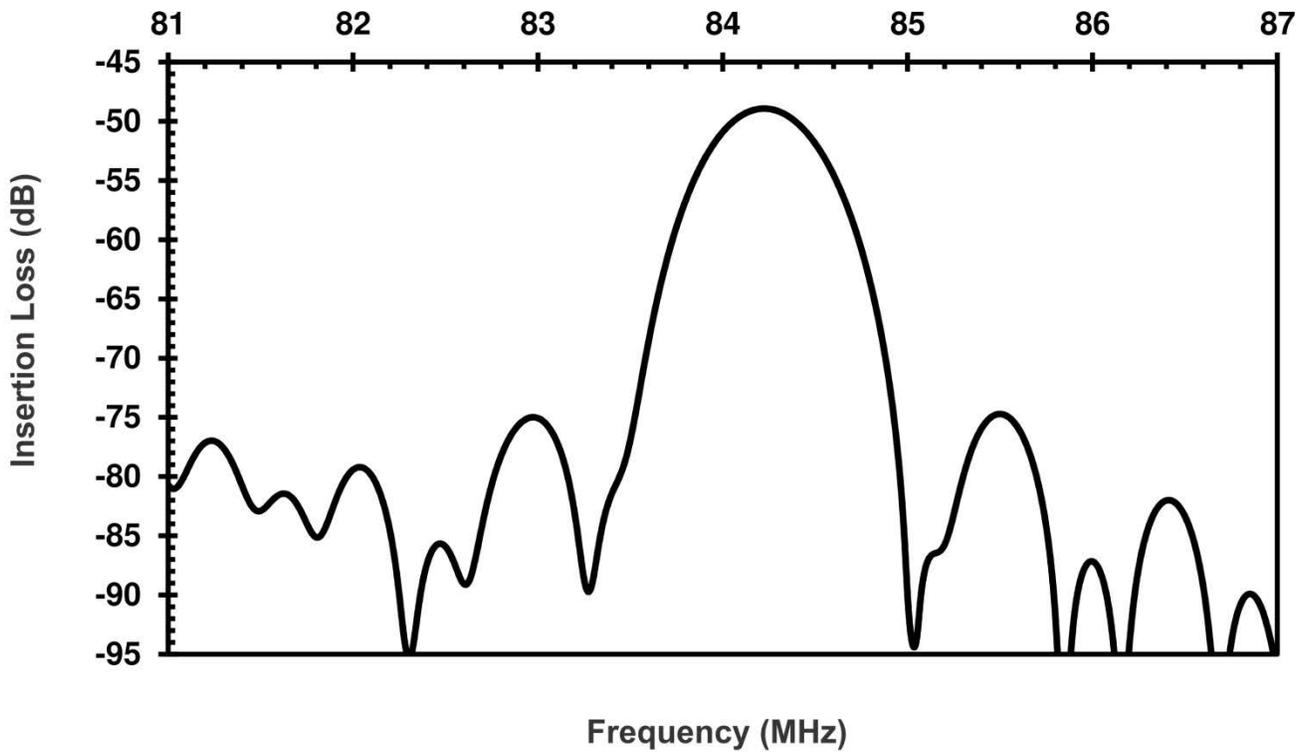
Figure 6-20: S$_{21}$ parameter plot for the SU-8/AlN/Si SAW sensor without Omnicoat operating at 84MHz
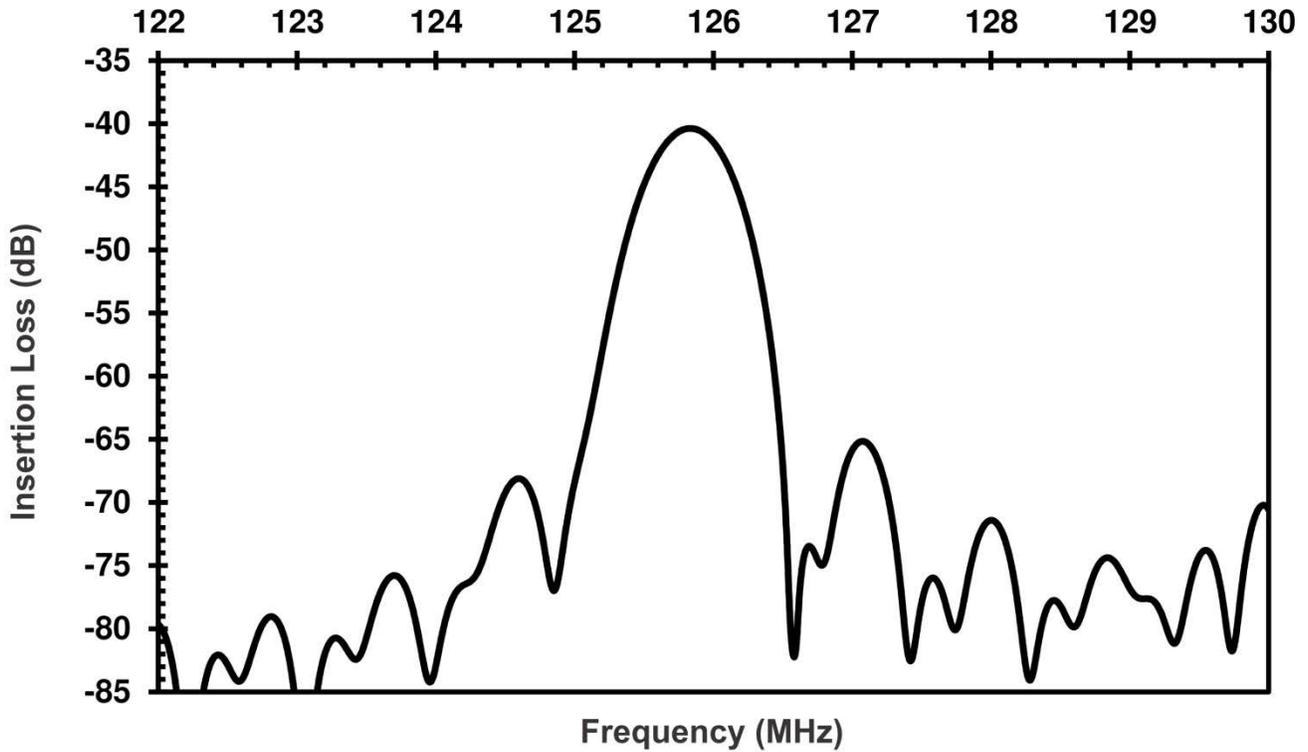
Figure 6-21: S_{21} parameter plot for the SU-8/AlN/Si SAW sensor without Omnicoat operating at 125MHz

Figure 6-22: S_{21} parameter plot for the SU-8/AlN/Si SAW sensor without Omnicoat operating at 208MHz
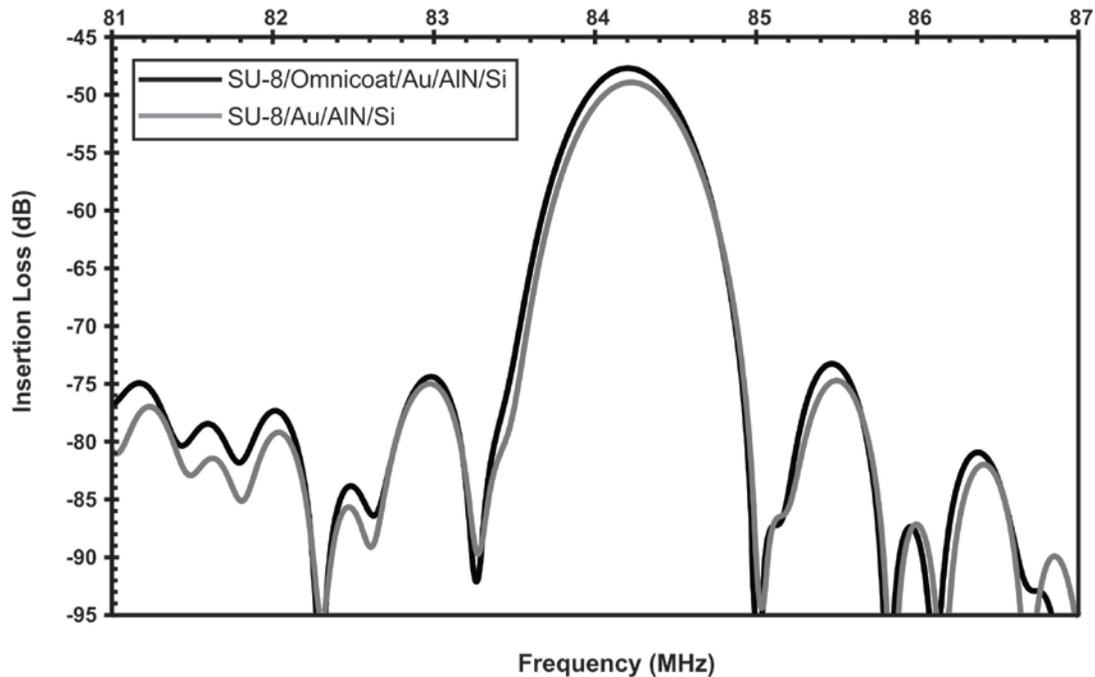
Figure 6-23: Frequency response plots of the two SU-8/AlN/Si SAW sensors operating at 84MHz with and without omnicoat

In order to illustrate the shift in the frequency response of the SU-8/AlN/Si SAW sensors with and without omnicoat the frequency responses from both configurations are plotted together in Figure 6-23 through Figure 6-26 for each of the four SAW sensor designs. The main peaks of the frequency response curves for the SU-8/AlN/Si (without Omnicoat) sensors at the four operating frequencies shift to higher center frequency values as illustrated in Figure 6-23 to Figure 6-26. It is also illustrated that the shifts increase as the operating frequency of the sensors increases, which is due to the increased sensitivity of the SAW sensors. For each of the four operating frequencies of the SAW sensor designs three pairs of sensors are fabricated and their frequency responses are measured. A total of 24 SAW sensors have been measured and the frequency shifts due to the change in adhesion of SU-8 have been calculated. The SAW phase velocity values are calculated from the center frequency values for each of the four SAW sensor designs. The average of the center frequency and phase velocity values are listed in Table 6-2 for both configurations of each of the four SAW sensor designs. The frequency shift and velocity shift values have been calculated and listed as well. The center frequency values illustrate that for the SAW sensor configurations without omnicoat the frequency shifts to higher values as illustrated in Table 6-2. The frequency shift values also increase as the operating frequency of the SAW sensor increases. The calculated velocity values also show an upward shift for the sensor configurations without omnicoat.
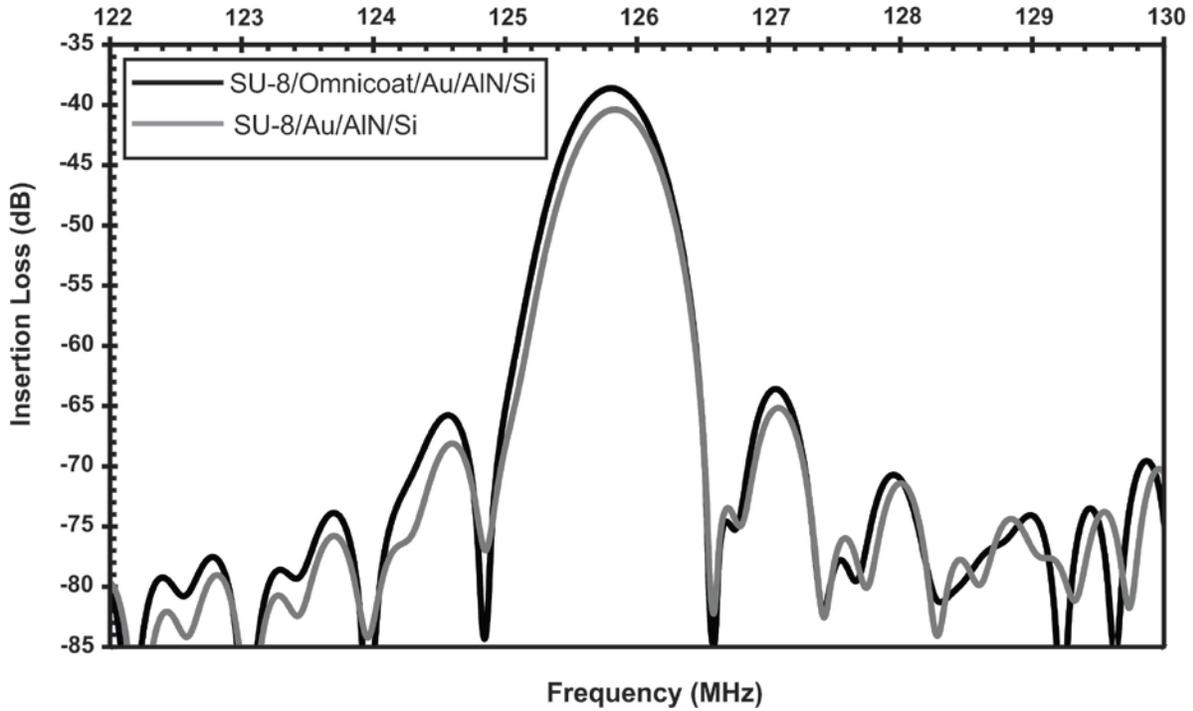
Figure 6-24: Frequency response plots of the two SU-8/AlN/Si SAW sensors operating at 125MHz with and without omnicoat
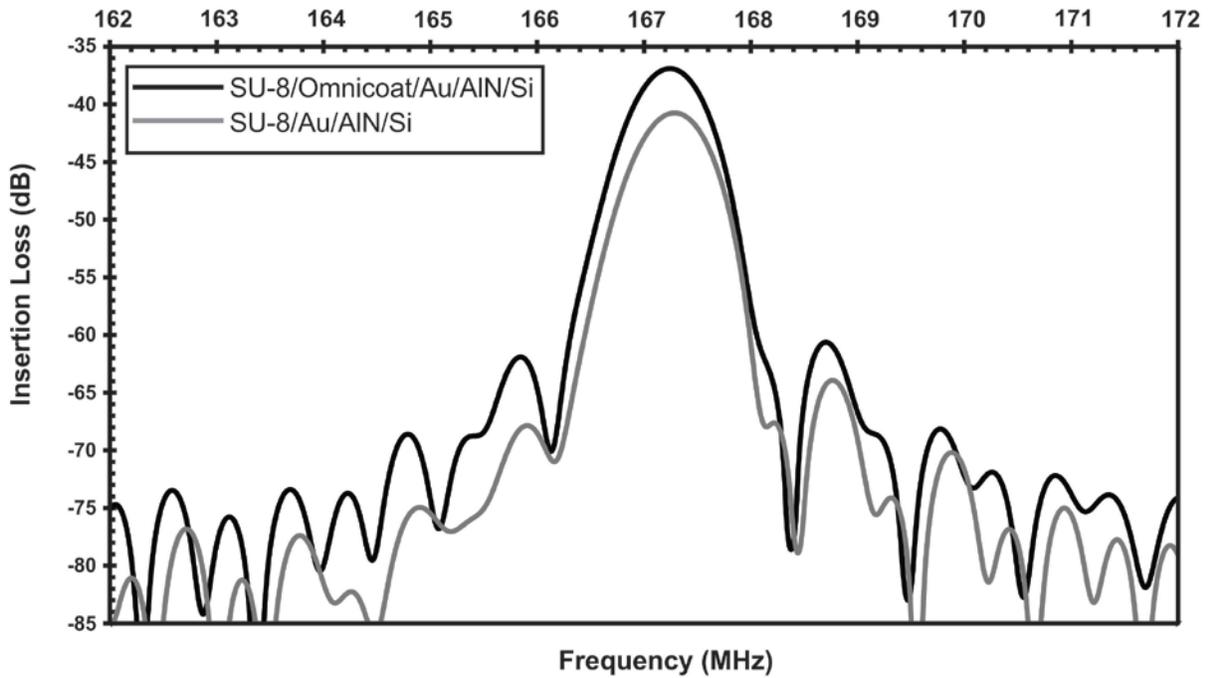

Figure 6-25: Frequency response plots of the two SU-8/AlN/Si SAW sensors operating at 167MHz with and without omnicoat
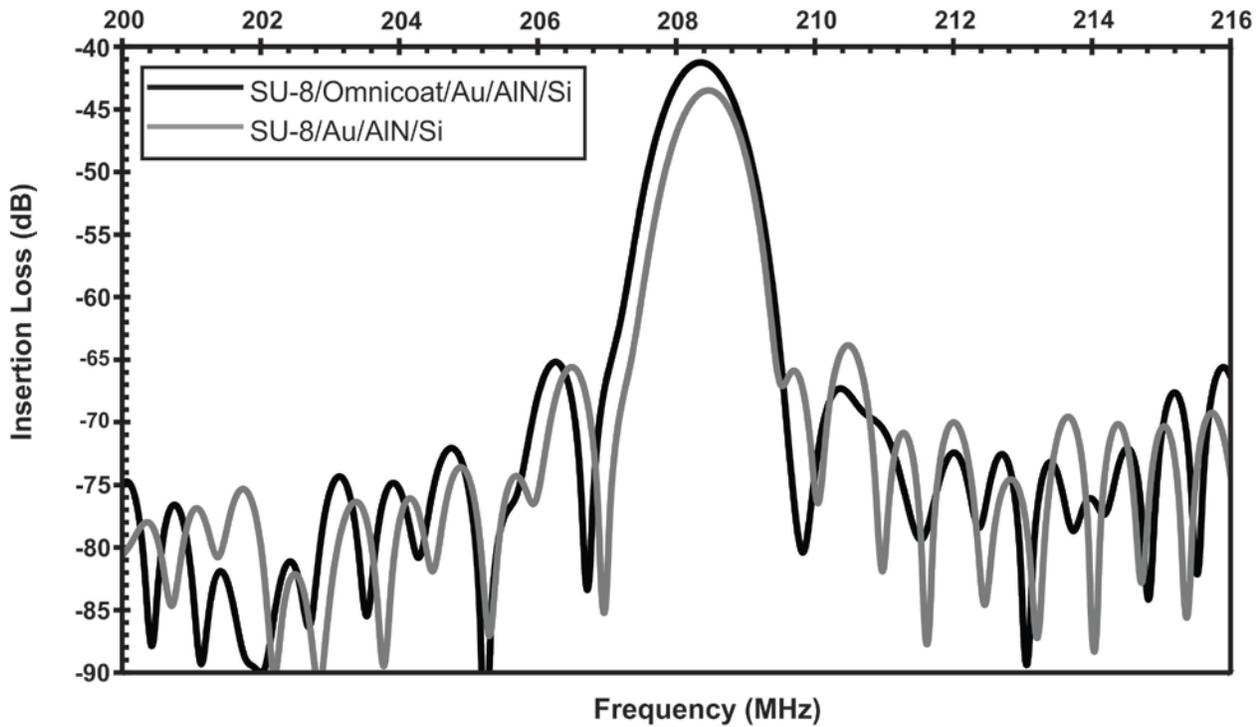
Figure 6-26 Frequency response plots of the two SU-8/AlN/Si SAW sensors operating at 208MHz with and without omnicoat

Figure 6-27 illustrates the average frequency shifts due to the change in adhesion of the SU-8 film from the two sensor configurations used in this study i.e. SU-8/Omnicoat/Au/AlN/Si and SU-8 /Au/AlN/Si at the four operating frequencies in the range of 84-208MHz. The frequency shift values range from 13.3 - 96.22kHz as illustrated in Table 6-2. Figure 6-27 illustrates that the frequency shift increases as the operating frequency of the sensor increases. The average frequency shift values are plotted with the standard deviations. The phase velocity values are calculated from the center frequencies of the four SAW sensor designs for both configurations i.e. with and without omnicoat.

Table 6-2: Frequency response data from the four designs of the SAW sensors due to changing the adhesion of the SU-8 film

Freq. (MHz)	Frequency (MHz)		Freq. Shift (kHz)	Phase Velocity (m/s)		Velocity Shift (m/s)
	SU-8/OC/Au/AlN/Si	SU-8/Au/AlN/Si		SU-8/OC/Au/AlN/Si	SU-8/Au/AlN/Si	
84	84.225	84.238	13.326	5,053.50	5,054.30	0.8
125	125.881	125.912	30.817	5,035.23	5,036.47	1.233
167	167.161	167.213	52.061	5,014.83	5,016.39	1.5625
208	208.279	208.375	96.22	4,998.69	5,001.00	2.31

The velocity values are plotted in Figure 6-28. The plot illustrates that the velocity shifts to higher values for the sensors without omnicoat i.e. when the SU-8 layer is patterned directly above the gold film on the surface of the AlN/Si SAW sensor. This agrees with the increase in center frequencies of the SAW sensors for the devices without omnicoat. The frequency and velocity shift values are plotted together in Figure 6-29. This figure illustrates the increase in the frequency and velocity shift values of the SAW sensors as the operating frequency increases.

The two configurations of the SAW sensors (SU-8/Omnicoat/Au/AlN/Si and SU-8 /Au/AlN/Si) are fabricated on the same substrate and the only difference between them is the presence of the omnicoat layer in one of them. The changes in the frequency and velocity shift values are due to the change in adhesion of the SU-8 layer through omnicoat. However, the mass the stiffness properties of the omnicoat layer can also lead to a change in frequency and velocity due since its present in one of device configuration and not the other. Therefore, it is necessary to evaluate the effect of the presence of an omnicoat layer on the SAW sensor response and eliminate this effect from the frequency and velocity shift values in Table 6-2.
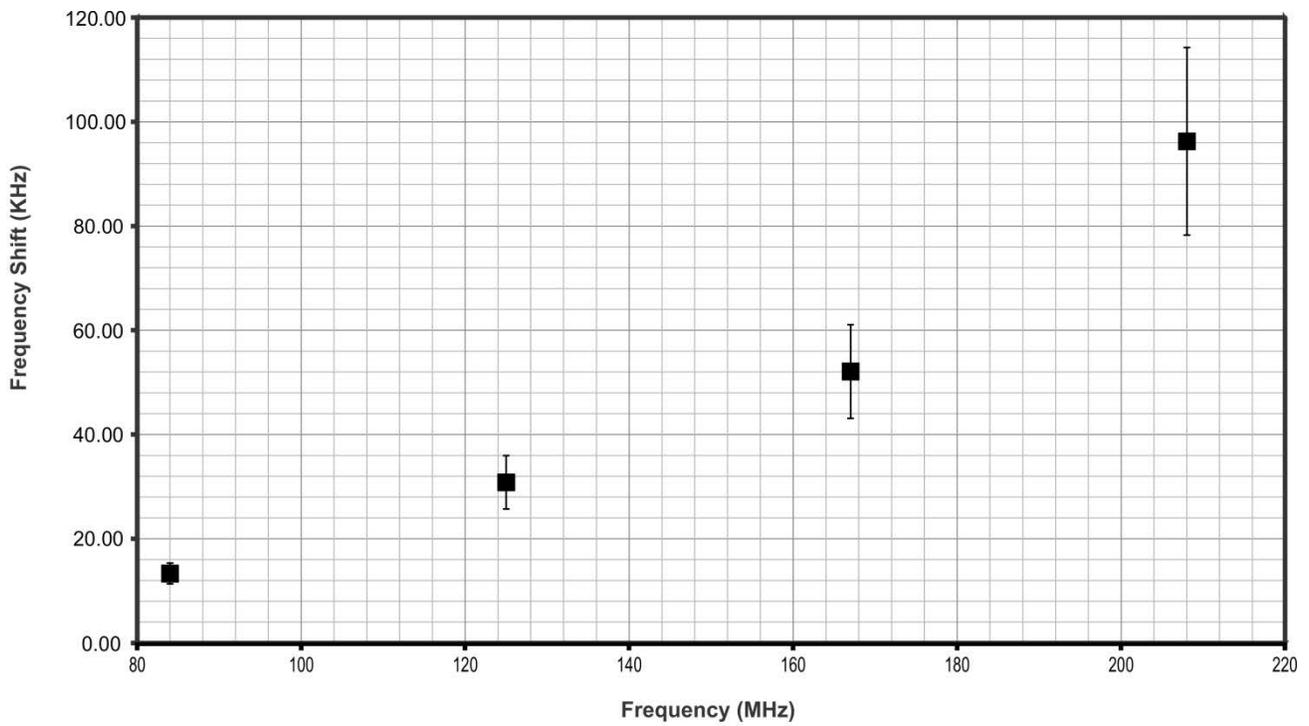
Figure 6-27: Frequency shift between the SU-8/Omnicoat/Au/AlN/Si and SU-8/Au/AlN/Si SAW sensors for the four SAW sensor designs
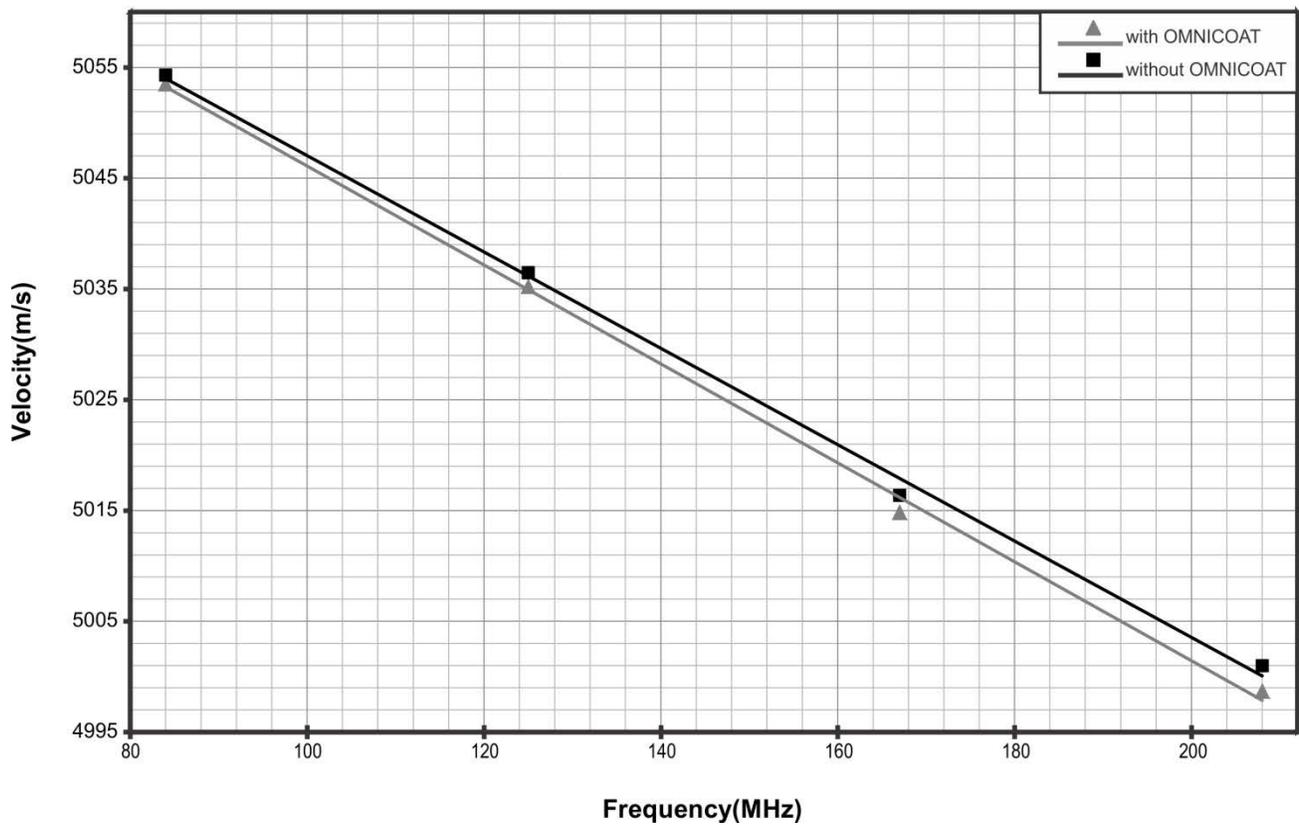
Figure 6-28: Phase velocities calculated using the center frequency values from both sensor configurations (SU-8/Omnicoat/Au/AlN/Si and SU-8/Au/AlN/Si) for the four SAW sensor designs
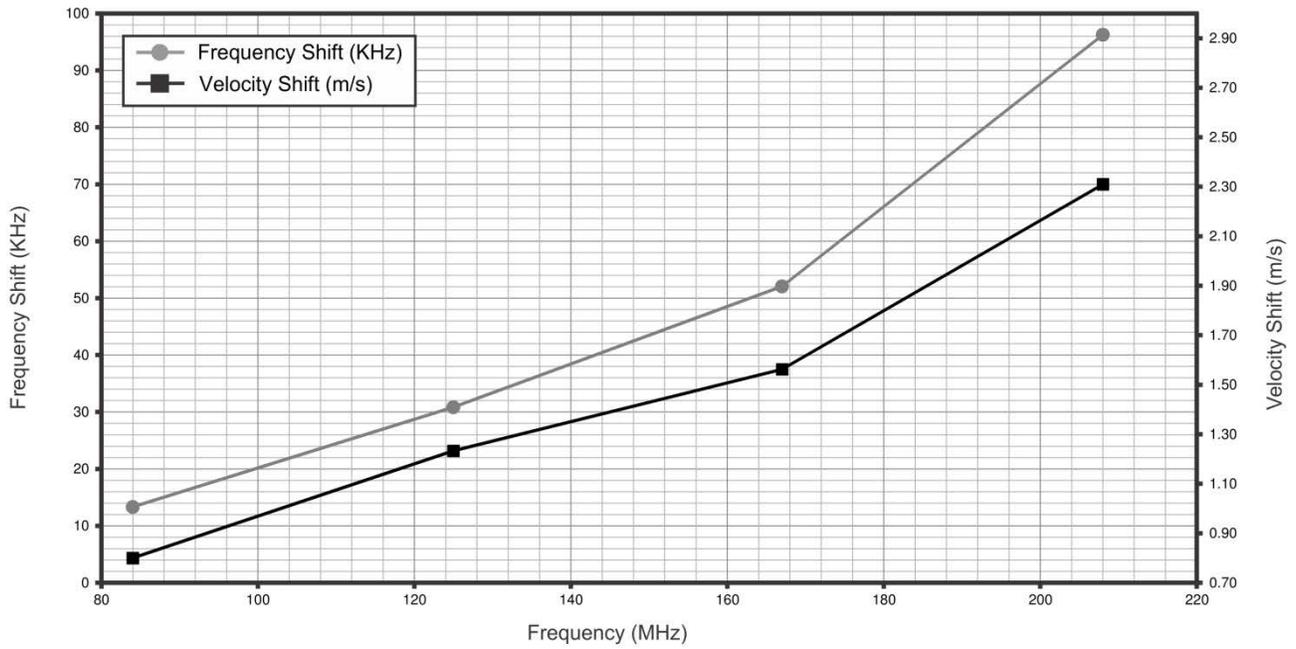
Figure 6-29: Frequency and velocity shift values from both sensor configurations i.e. SU-8/Omnicoat/Au/AlN/Si and SU-8/Au/AlN/Si at each of the four design frequencies

6.4 Frequency response measurements to evaluate the mass loading effect of omnicoat

The mass loading effect of omnicoat will be evaluated for the four SAW sensor designs operating in the frequency range of 84-208MHz using the device configurations in Figure 6-2. Both configurations do not have a SU-8 film patterned on the surface of the SAW sensor to eliminate the effect of SU-8 adhesion from the frequency shifts. The frequency plots for the four SAW sensors are illustrated in Figure 6-30 to Figure 6-33. Each plot shows two frequency response measurements for the sensors with and without omnicoat. Frequency response measurements are carried out for a total of 24 sensors to calculate the frequency shift due to the mass loading effect of omnicoat. For each of the four design frequencies three pairs of sensors are measured and the average frequency shift is calculated. The average values for the center frequencies and the frequency shift values are listed in Table 6-3. The results illustrate that the frequency shifts to a higher value for the sensors without omnicoat. For the sensors operating at 84 MHz the frequency shift between the sensors with and without omnicoat is 7.5 kHz. This value increases for the sensors operating at 126 MHz to 16.7 kHz, for the sensors operating at 167 MHz the frequency shift is 22.5 KHz and for the 208 MHz sensors the frequency shift is 29.58 kHz. The frequency shift increases as the operating frequency of the sensor increases due to the higher sensitivity. The SAW phase velocity values are calculated from the center frequency data and are plotted in Figure 6-35 and listed in Table 6-3.

Table 6-3: Frequency and velocity data from the four SAW sensor designs investigating the mass loading effect of omnicoat

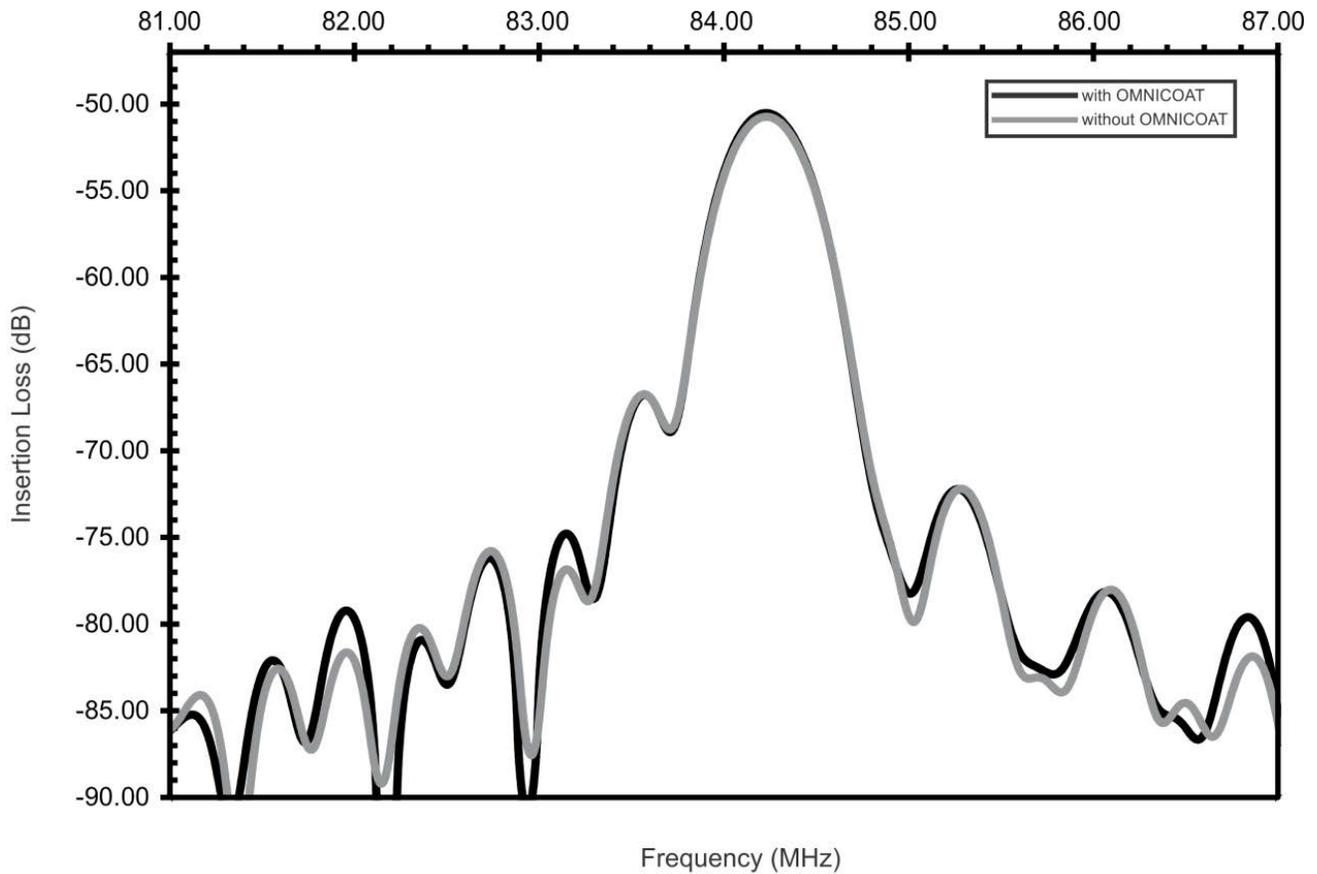| Frequency (MHz)	Wavelength (um)	Frequency Response			Velocity Values		
		OC/Au/AlN/Si	Au/AlN/Si	Freq.Shift (kHz)	OC/Au/AlN/Si	Au/AlN/Si	Velocity Shift (m/s)
84	60	84,236,250	84,243,750	7.50	5,054.18	5,054.63	0.45
125	40	125,825,000	125,841,666.67	16.67	5,033.00	5,033.67	0.67
167	30	167,062,500	167,085,000	22.50	5,011.88	5,012.55	0.67
208	24	208,005,000	208,034,583.33	29.58	4,992.12	4,992.83	0.71

Figure 6-30: Frequency response plots for the SAW sensors with and without omnicoat operating at 84MHz to determine the mass loading effect of omnicoat. Both sensors do not have an SU-8 layer.

The plot illustrates that the velocity shifts to a higher value for the SAW sensors without omnicoat. This trend continues for the four design frequencies. The velocity shift values are calculated and found to be within 0.45-0.71m/s for the four sensor designs. The velocity shift values are plotted in Figure 6-36 and illustrate that at 84MHz the velocity shift is 0.45m/s, which increases to 0.67m/s for the sensors operating at 125MHz and 167MHz. This jump illustrates the low sensitivity of the sensors operating at 84MHz to the omnicoat layer. At 208MHz the velocity shift increases to 0.71m/s. The frequency shift and velocity shift data due to the effect of omnicoat are listed in Table 6-3.
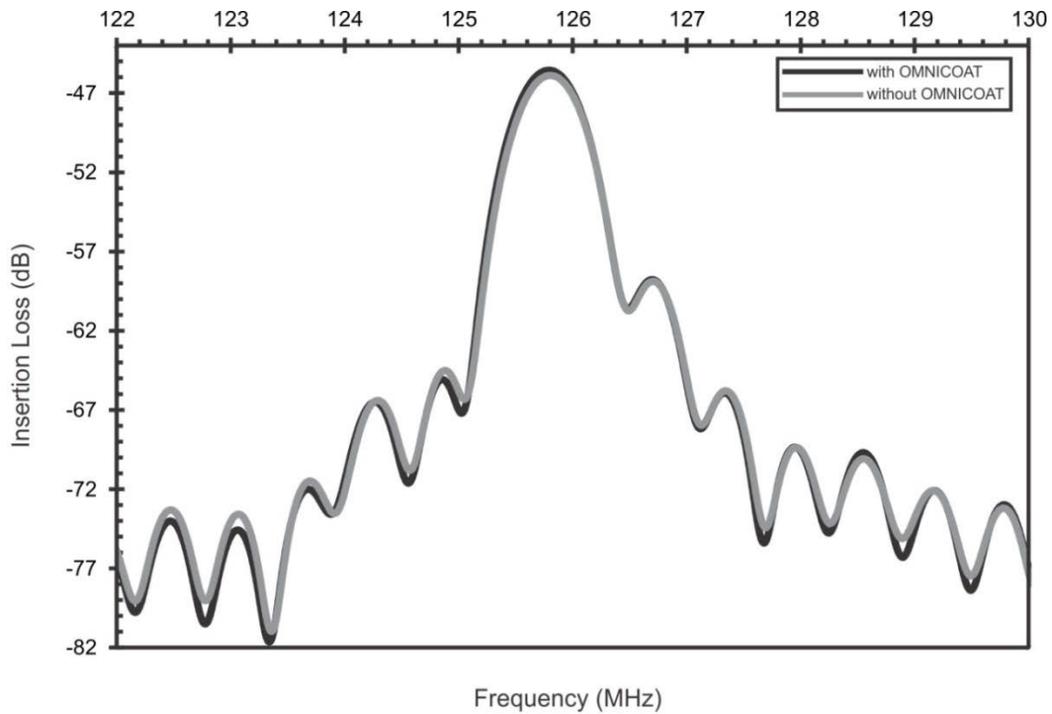
Figure 6-31: Frequency response plots for the SAW sensors with and without omnicoat operating at 125MHz to determine the mass loading effect of omnicoat. Both sensors do not have an SU-8 layer.
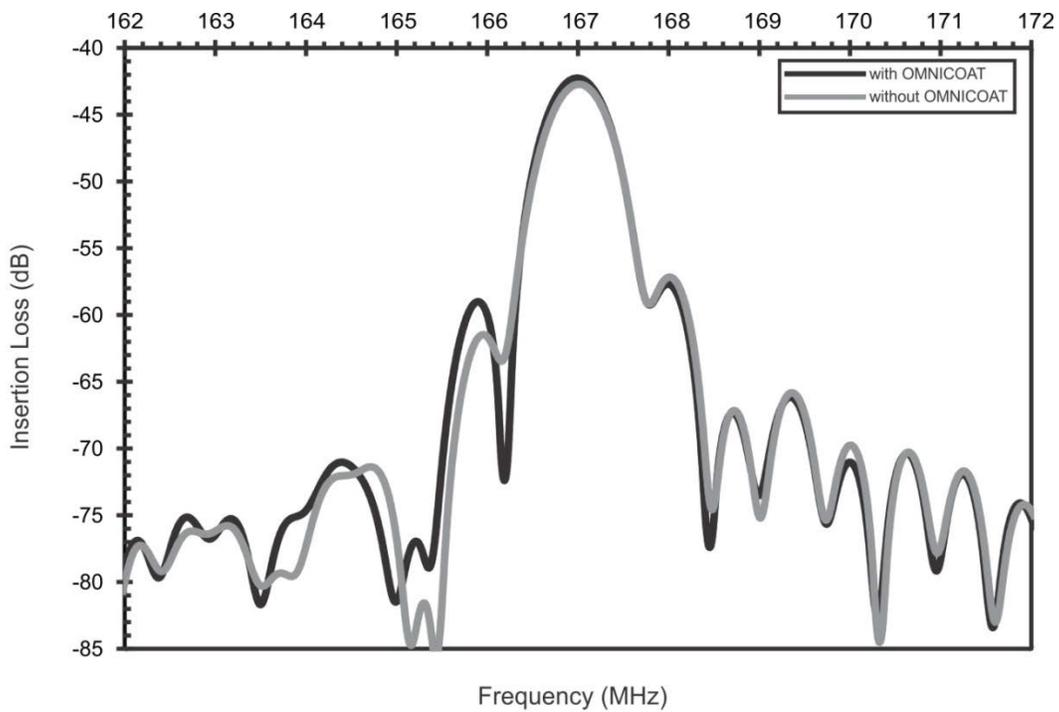
Figure 6-32: Frequency response plots for the SAW sensors with and without omnicoat operating at 167MHz to determine the mass loading effect of omnicoat. Both sensors do not have an SU-8 layer.
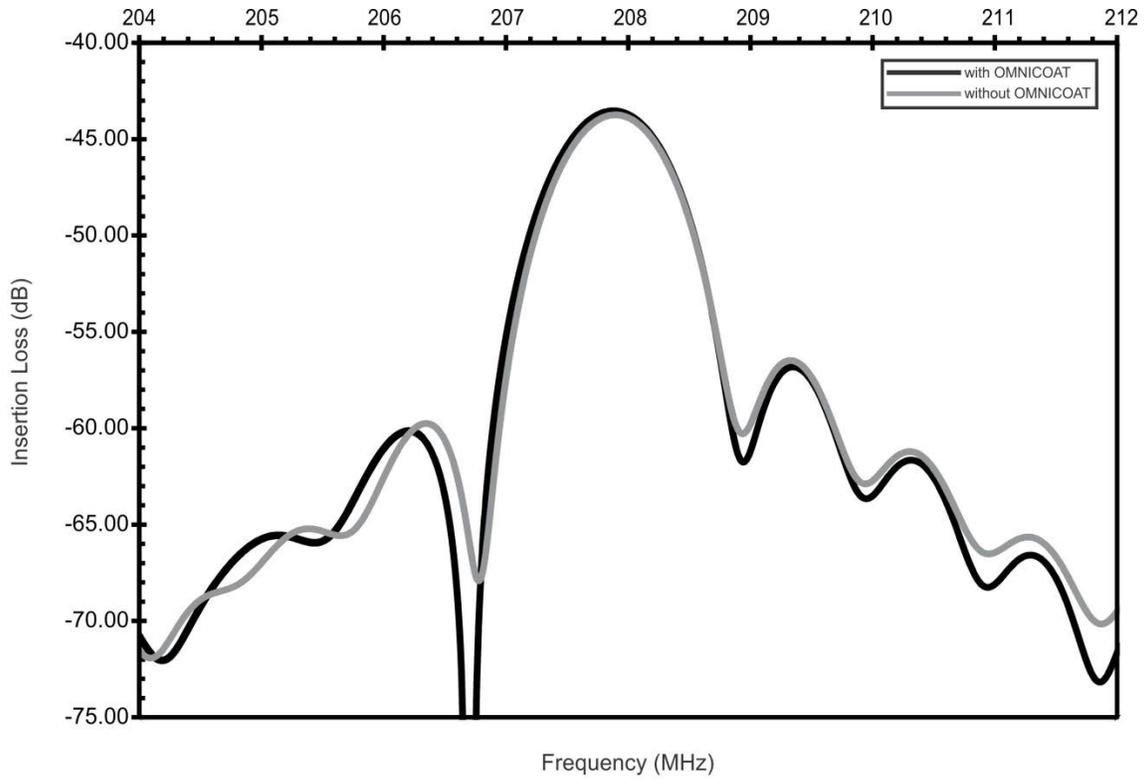
Figure 6-33: Frequency response plots for the SAW sensors with and without omnicoat operating at 208MHz to determine the mass loading effect of omnicoat. Both sensors do not have an SU-8 layer.
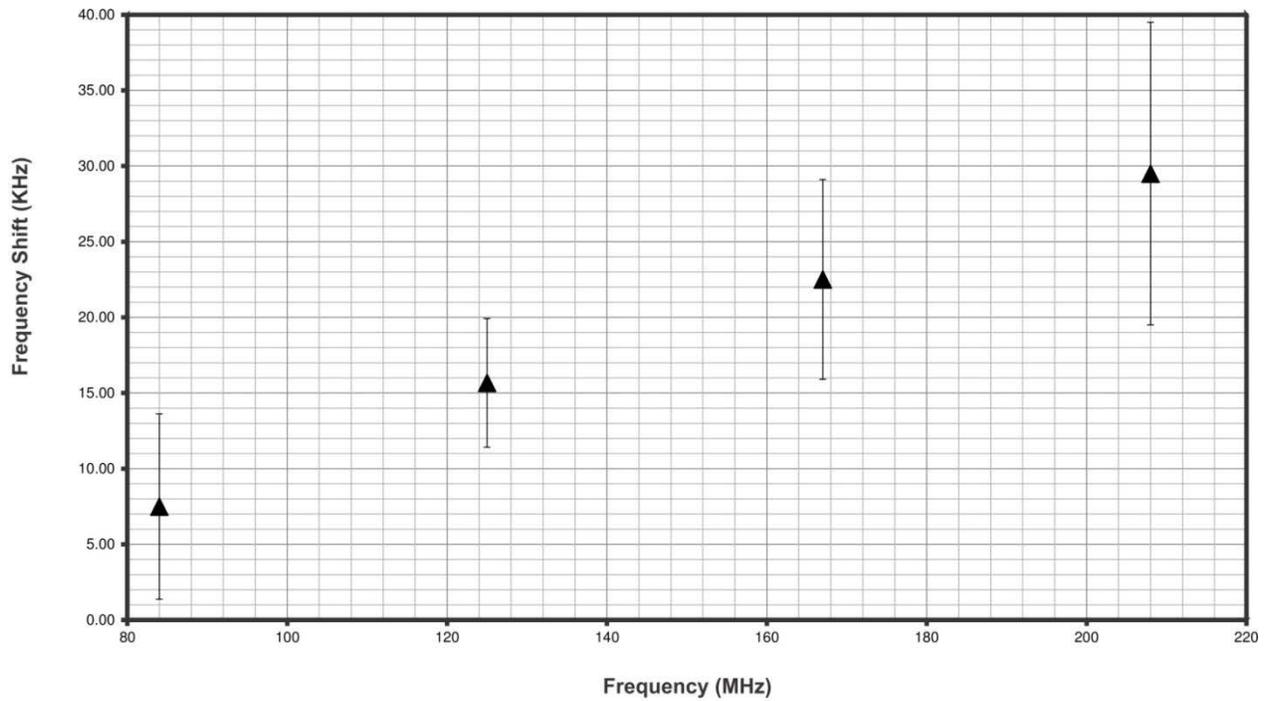
Figure 6-34: Frequency shift due to the mass loading effect of omnicoat
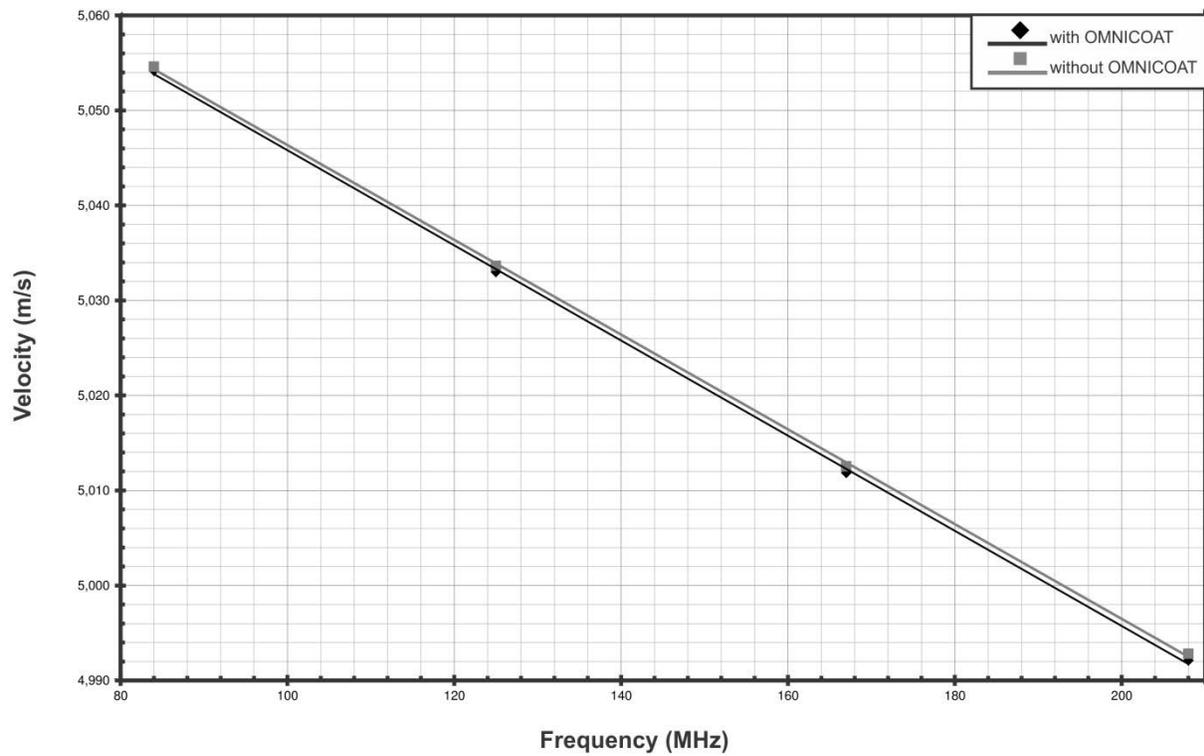
Figure 6-35: Velocity values for the SAW sensors used in investigating the mass loading effect of omnicoat
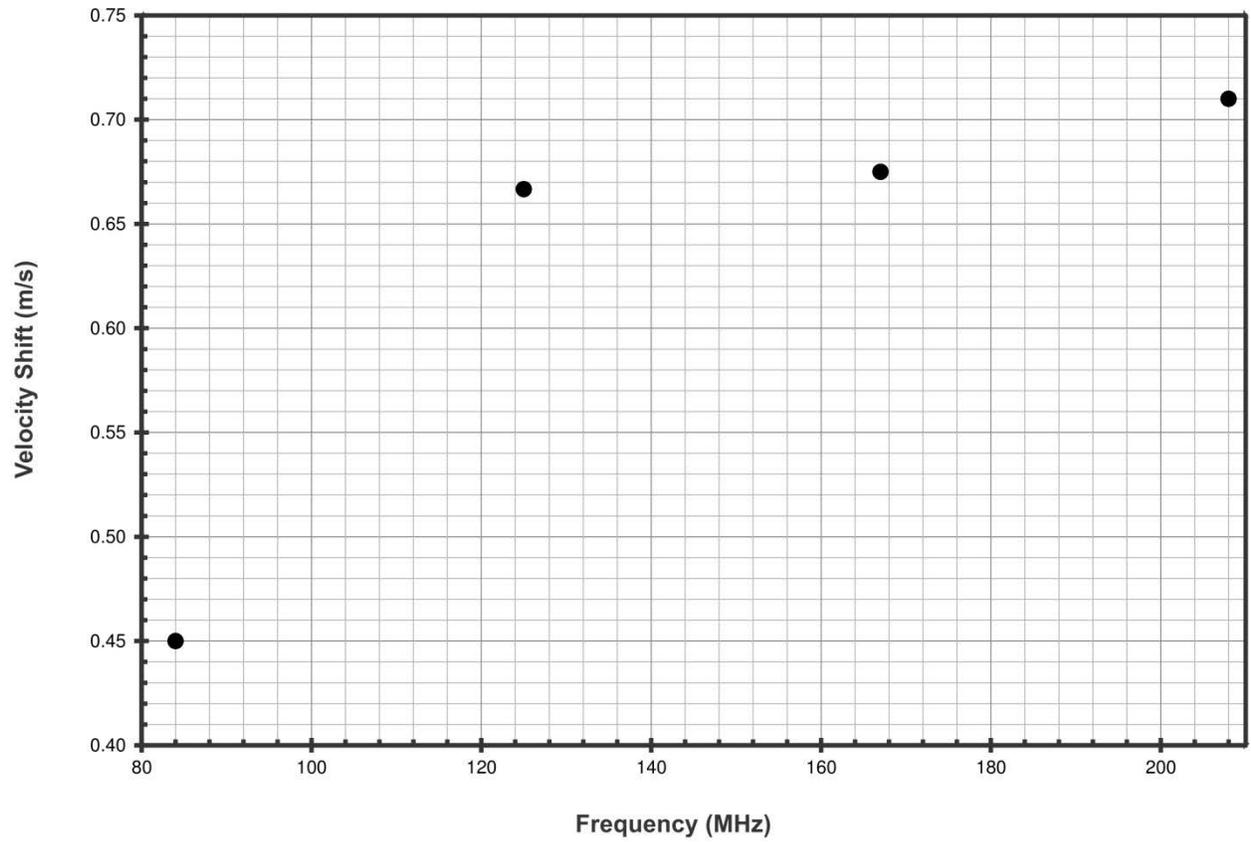
Figure 6-36: Velocity shift due to the mass loading effect of omnicoat

Table 6-4: Frequency data for the SAW sensors due to the change in adhesion of the SU-8 film and the mass loading effect of omnicoat and the final frequency shift data due to the change in SU-8 adhesion

Freq. (MHz)	Frequency (MHz)		Freq. Shift (kHz)	Frequency (MHz)		Freq. Shift (kHz)	*Final Freq Shift (kHz)*
	SU-8/OC/Au /AlN/Si	SU-8 /Au/AlN/Si		OC/Au/AlN/Si	Au/AlN/Si		
84	84.225	84.238	13.326	84,236,250	84,243,750	7.50	*5.826*
125	125.881	125.912	30.817	125,825,000	125,841,666.67	16.67	*14.147*
167	167.161	167.213	52.061	167,062,500	167,085,000	22.50	*29.561*
208	208.279	208.375	96.25	208,005,000	208,034,583.33	29.58	*66.67*

6.5 Evaluating frequency and velocity shifts due to the change in adhesion of the SU-8 film

The two device configurations illustrated in Figure 6-1 are used to measure the frequency and velocity shift values in the presence and absence of omnicoat as an adhesion promoter to the SU-8 film patterned on the surface of the sensor. The frequency and velocity shift values due to the change in adhesion did not account for the mass loading effect of omnicoat. Table 6-3 illustrated that the presence of an omnicoat layer on the surface of the sensor shifts the center frequency and velocity values of the SAW sensors. The shift due to the omnicoat layer needs to be eliminated from the frequency and velocity data from the SU-8/AlN/Si SAW sensors, which are listed in Table 6-2. Table 6-4 lists the frequency data from the sensors investigating the change in SU-8 adhesion and the sensors investigating the effect of omnicoat. Figure 6-37 illustrates the frequency shift values due to the change in adhesion of the SU-8 layer plotted with the frequency shift values due to the mass loading effect of omnicoat. The frequency shift values for the sensors due to the change in SU-8 adhesion are much higher than the values due to the mass loading effect of omnicoat. The frequency shift due to the effect of omnicoat has a minimum value of 7.5kHz and a maximum value of 29.58kHz; however, due to the change in SU-8 adhesion the frequency shift for the sensors operating at 84MHz is 13.33kHz and continues to increase until it reaches 96.25kHz for the sensors operating at 208MHz. These results demonstrate that the effect of the change in SU-8 adhesion is the dominating parameter that leads to a shift in the frequency response curves for the four SAW sensor designs. The frequency shift due to the mass loading effect of omnicoat is subtracted from the overall frequency shift data. The final frequency shift data are also listed in Table 6-4, which corresponds to the change in adhesion of the SU-8 film. The frequency shift values due to the change in SU-8 adhesion are found to be within the range of 5.83 - 66.67kHz for the four SAW sensor designs and the frequency shift value increases with the sensor operating frequency.
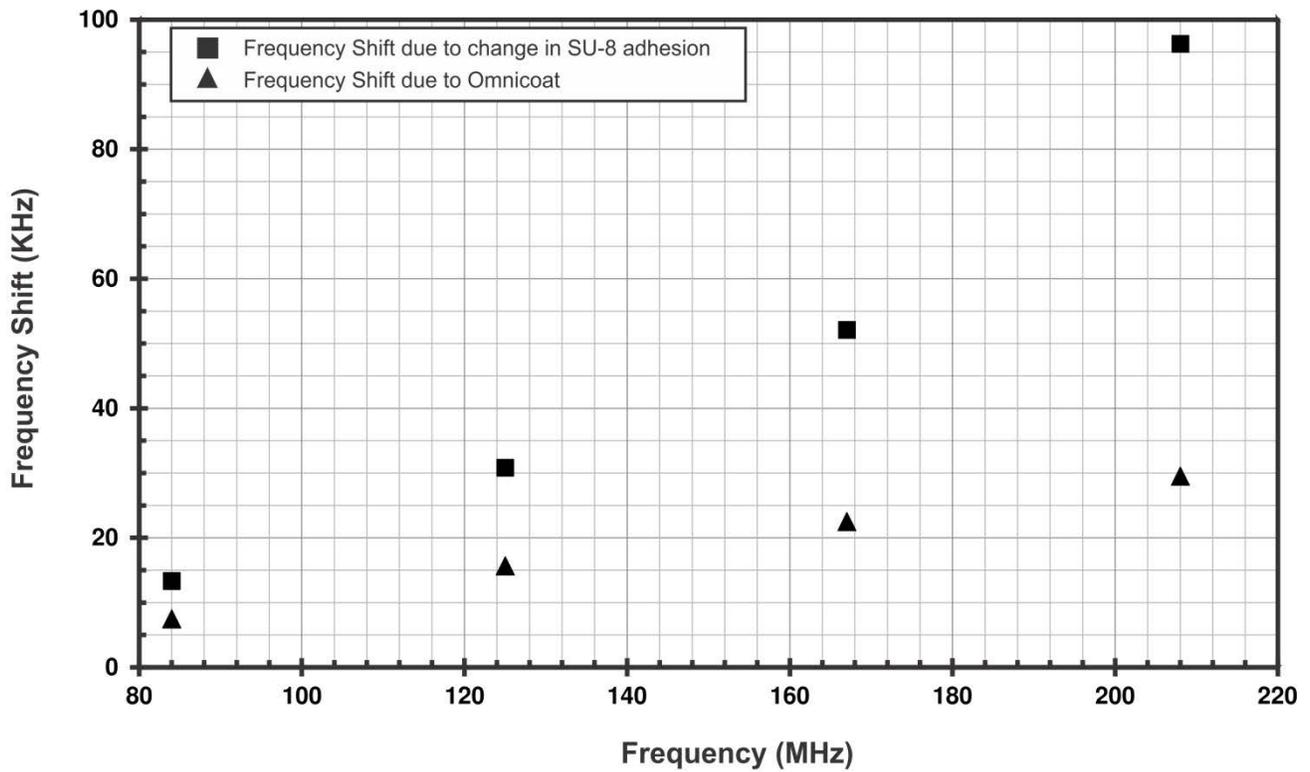
Figure 6-37: Frequency shift values due to the change in adhesion of the SU-8 thin film and the mass loading effect of omnicoat
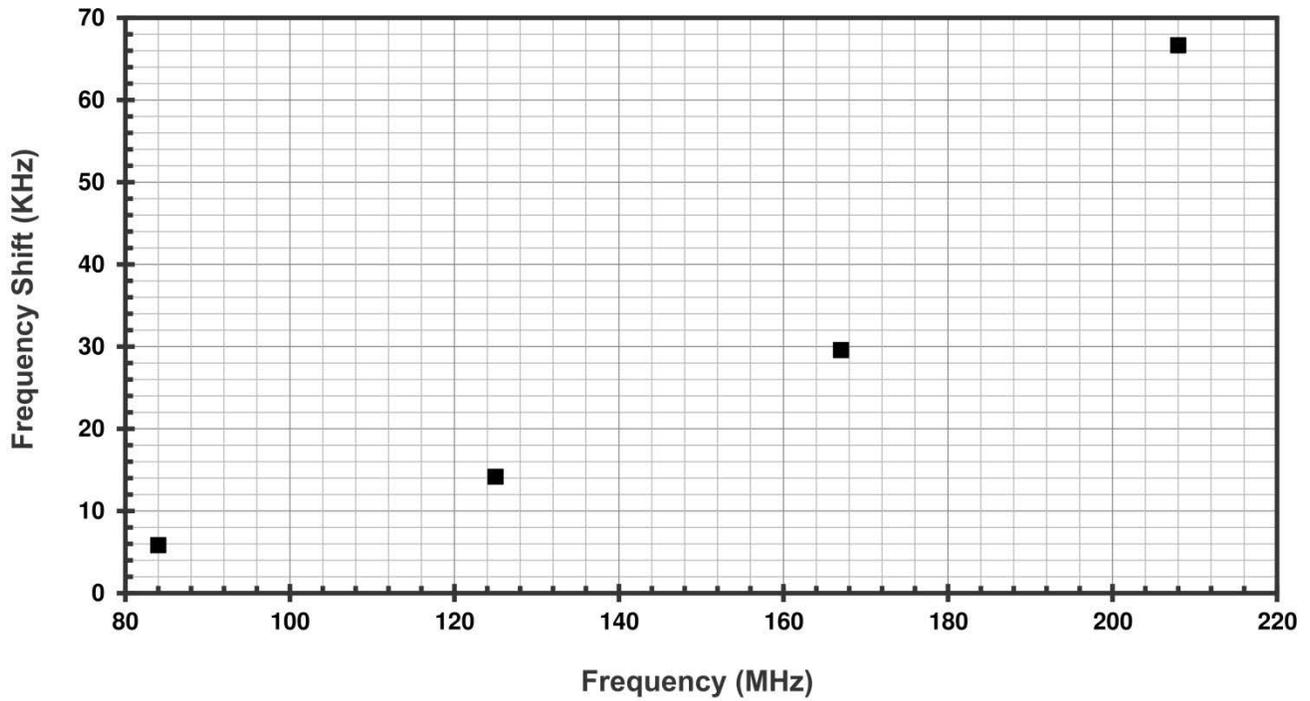
Figure 6-38: Final frequency shift of the SU-8/AlN/Si SAW sensors operating in the frequency range of 84-208MHz due to the change in SU-8 adhesion

Table 6-5: Phase velocity data for the SAW sensors due to the change in adhesion of the SU-8 film and the mass loading effect of omnicoat and the final velocity shift data due to the change in SU-8 adhesion

Freq. (MHz)	Phase Velocity (m/s)		Velocity Shift (m/s)	Phase Velocity (m/s)		Velocity Shift (m/s)	*Final Velocity Shift (m/s)*
	SU-8/OC/Au /AlN/Si	SU-8 /Au/AlN/Si		OC/Au/AlN/Si	Au/AlN/Si		
84	5,053.50	5,054.30	0.8	5,054.18	5,054.63	0.45	*0.35*
125	5,035.23	5,036.47	1.233	5,033.00	5,033.67	0.67	*0.5667*
167	5,014.83	5,016.39	1.5625	5,011.88	5,012.55	0.67	*0.8925*
208	4,998.69	5,001.00	2.31	4,992.12	4,992.83	0.71	*1.6*

The phase velocity data for the sensors investigating the change in SU-8 adhesion and the mass loading effect of omnicoat are calculated and listed in Table 6-5 and plotted in Figure 6-39. The velocity shift plot illustrates that the change in wave velocity due to the adhesion of the SU-8 film is significantly higher than the velocity shift due to the mass loading effect of omnicoat. In addition, the shifts increase with the operating frequency of the sensor due to the higher sensitivity. As the phase velocity values in Table 6-5 illustrate, the mass loading effect of omnicoat leads to a reduction in phase velocity. In addition, the changes in the velocity values of the SU-8/AlN/Si SAW sensors indicate that the sensors with omnicoat recorded a l ower phase velocity value. Therefore, the omnicoat layer leads to a reduction in the wave velocity due to its mass loading effect and also when it is used as an adhesion promoter for the SU-8 layer. The final velocity shift due to the change in adhesion of the SU-8 layer is determined by subtracting the velocity shift due to the mass loading effect of omnicoat from the values of the phase velocity shifts due to the change in adhesion of the SU-8 layer. The final phase velocity shift values range from 0.35-1.6m/s for the four SAW sensor designs. These values are listed in Table 6-5 and plotted in Figure 6-40 and illustrate an increasing trend with the sensor frequency. The phase velocity values for the SU-8/Omnicoat/AlN/Si SAW sensors, which are listed in Table 6-5 include the mass loading effect of omnicoat. In order to determine the exact velocity values due to the change in adhesion of the SU-8 layer the velocity shift values listed in Table 6-3 are added to the velocity values of the SU-8/OC/Au/AlN/Si SAW sensors. This is because the velocity values of the SU-8/OC/Au/AlN/Si SAW sensors include the mass loading effect of omnicoat. The final velocity values for the SU-8/AlN/Si SAW sensors due to the change in adhesion of the SU-8 film using omnicoat are plotted in Figure 6-41. The results illustrate that the velocity shifts upwards for the SU-8/AlN/Si SAW sensors without omnicoat. In the absence of omnicoat the adhesion of the SU-8 film on the surface of the SAW sensor is less rigid; therefore,

the wave energy transmitted across the interface to the SU-8 layer drops and the wave is more concentrated in the AlN/Si structure [150, 151]. On the other hand, when omnicoat is used the adhesion of the SU-8 film on the surface of the AlN/Si SAW is more rigid, therefore the wave energy transmitted across the interface to the SU-8 film increases. This leads to an overall drop in the SAW phase velocity since the SU-8 layer has a lower Rayleigh wave velocity in comparison to AlN; 1,166 and 5,600m/s, respectively. The frequency shifts due to the change in adhesion of the SU-8 film plotted in Figure 6-38 occur as a result of the change in wave energy transmitted across the SU-8/AlN interface as well.

The theoretical model is used to plot the equivalent stress and displacement fields generated in the SU-8 layer for different values of the interface spring stiffness at h_{AlN}/λ =0.04583. Figure 6-42 illustrates the contour plot of the equivalent stress generated in the SU-8 layer for different values of the interface spring stiffness. The contour plots illustrate that the magnitude of the stress field increases as the value of the interface spring stiffness increases. In addition, the maximum stress occurs at x_3=0, which corresponds to the SU-8/AlN interface and decreases along the depth of the SU-8 layer. The stress magnitude drops to zero at x_3=1.2μm since this is the free surface of the SU-8 films. At K=$3x10^9$ N/m^3 the maximum stress generated in the SU-8 layer is 16kPa and increases to 50kPa at K=$9x10^9$ N/m^3. The increased stresses generated in the SU-8 layer at higher interface stiffness values illustrate the increased rigidity of the SU-8/AlN interface and the improved transfer of the wave energy to the SU-8 film. Figure 6-43 illustrates contour plots of the equivalent displacements generated in the SU-8 layer. The plots illustrate the increased displacement amplitude generated in the SU-8 as the interface spring stiffness value increases. The displacements increase from $10x10^{-12}$ m at K=$3x10^9$ N/m^3 to $2.5x10^{-11}$ m at K=$9x10^9$ N/m^3. These results illustrate the increased confinement of the wave in the SU-8 film as the interface rigidity improves, which strengthens the influence of the SU-8 material properties on the overall SAW phase velocity. The SAW phase velocity drops as the adhesion of the SU-8 film on the surface of the AlN/Si SAW sensor improves since the Rayleigh wave velocity in the SU-8 layer is much lower than in AlN; 1,166m/s and 5,600m/s, respectively.
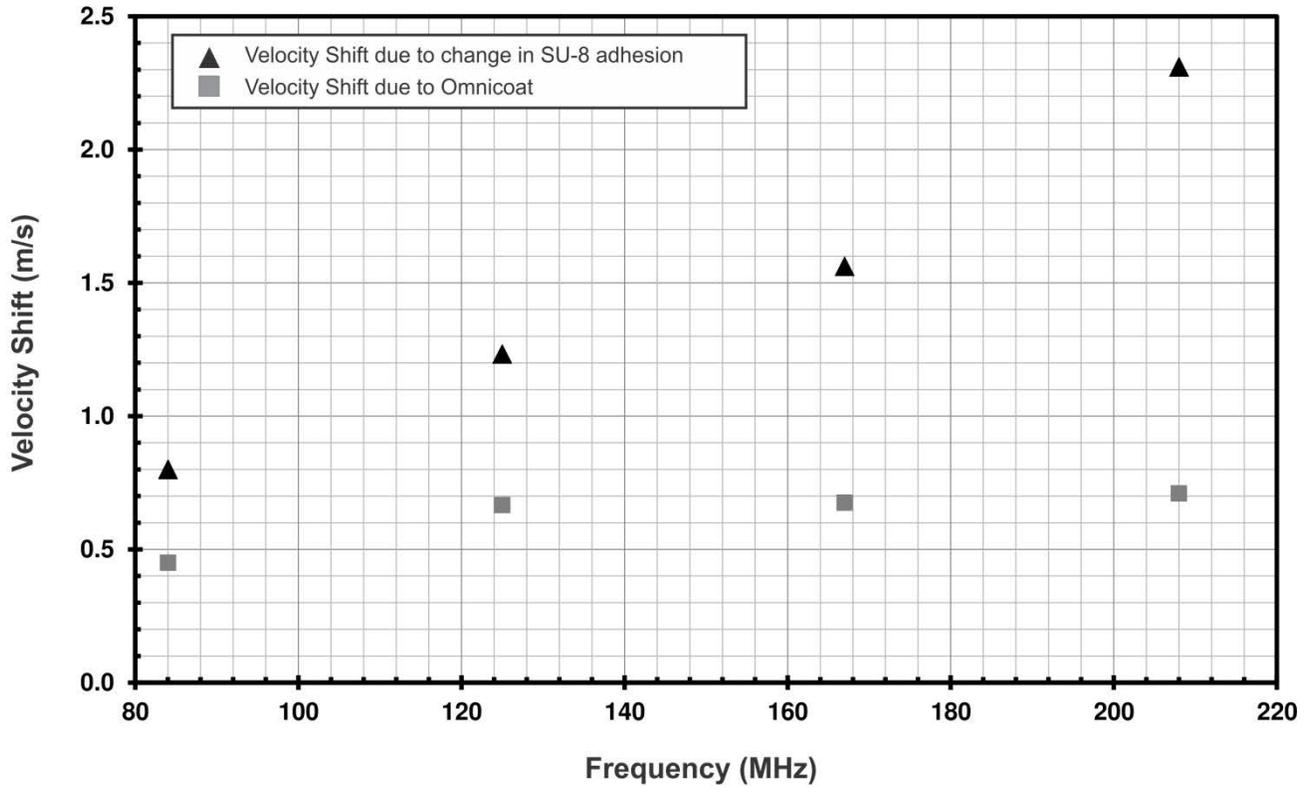
Figure 6-39: Phase velocity shifts due to the change in adhesion of the SU-8 layer and due to the mass loading effect of omnicoat
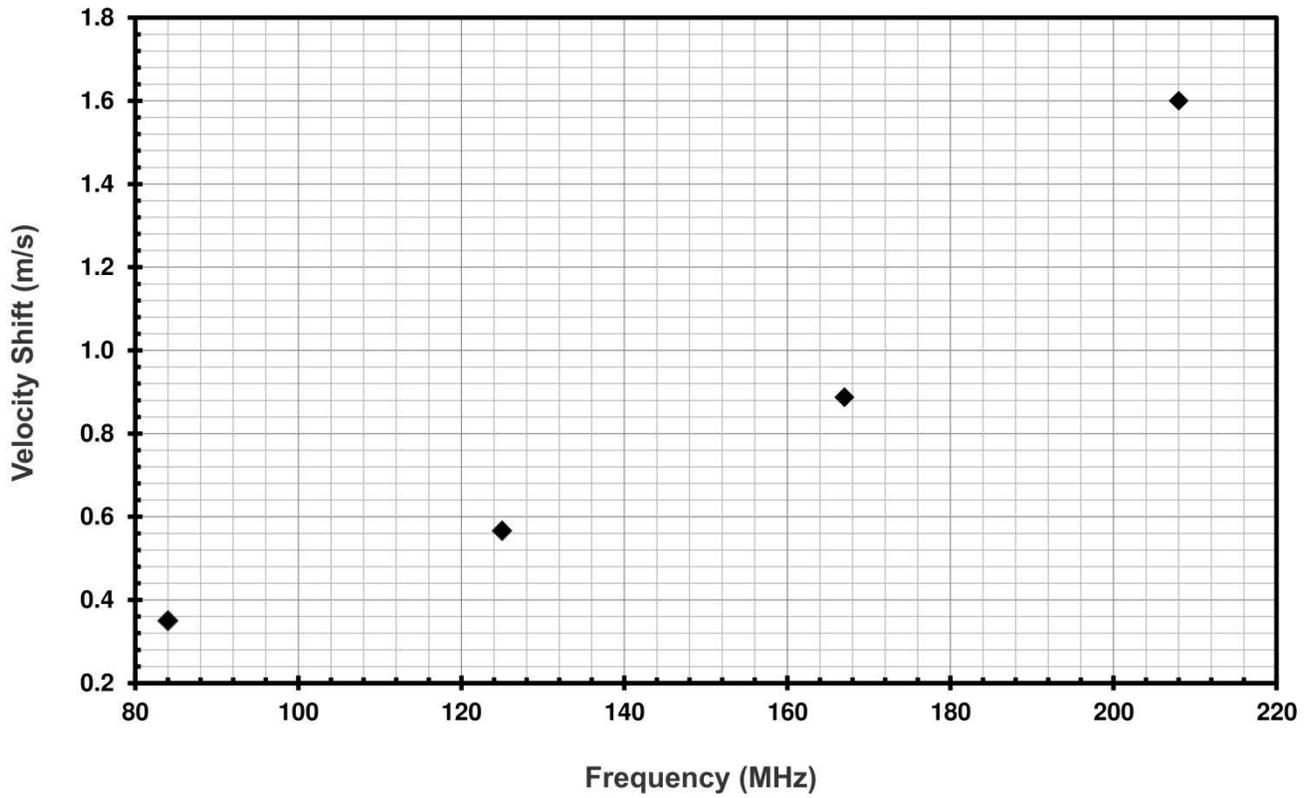
Figure 6-40: Final velocity shift of the SU-8/AlN/Si SAW sensors operating in the frequency range of 84-208MHz due to the change in SU-8 adhesion
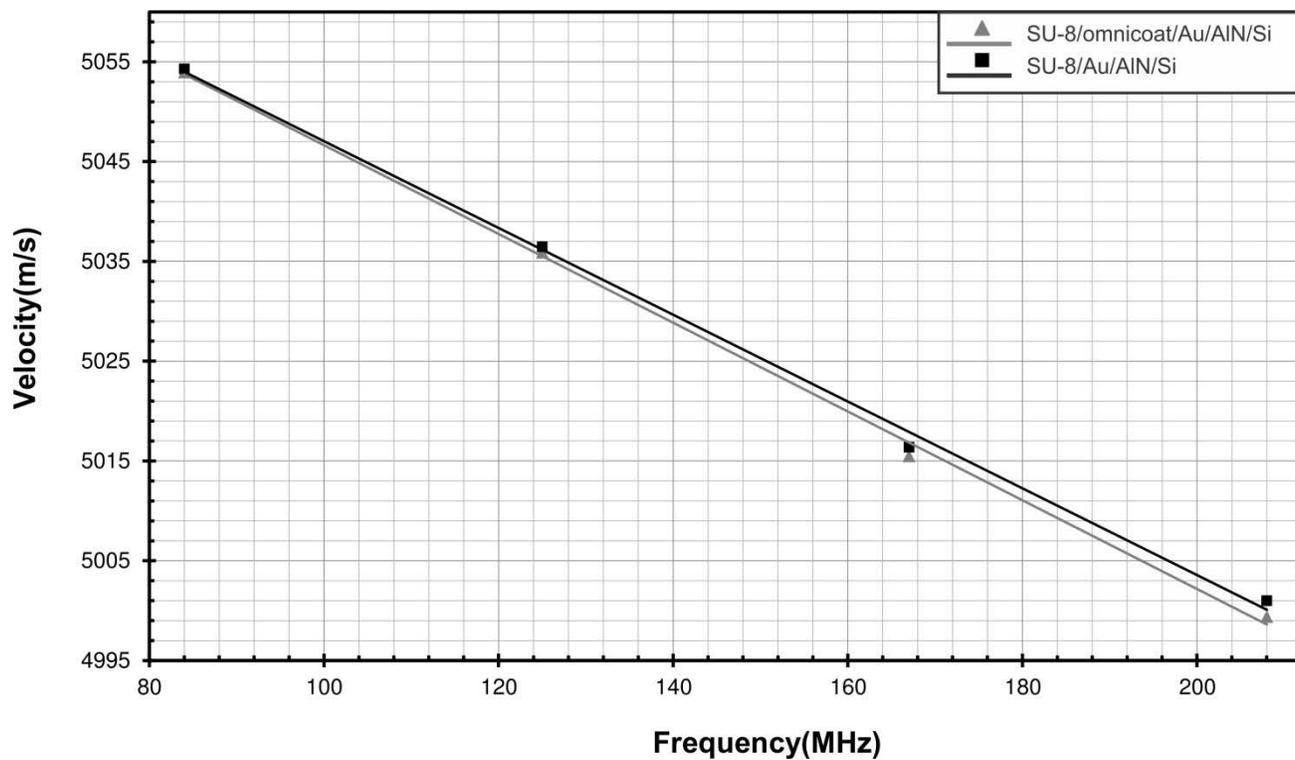
Figure 6-41: Final velocities for the SU-8/AlN/Si SAW sensor configurations in the presence and absence of omnicoat after eliminating the mass loading effect of omnicoat
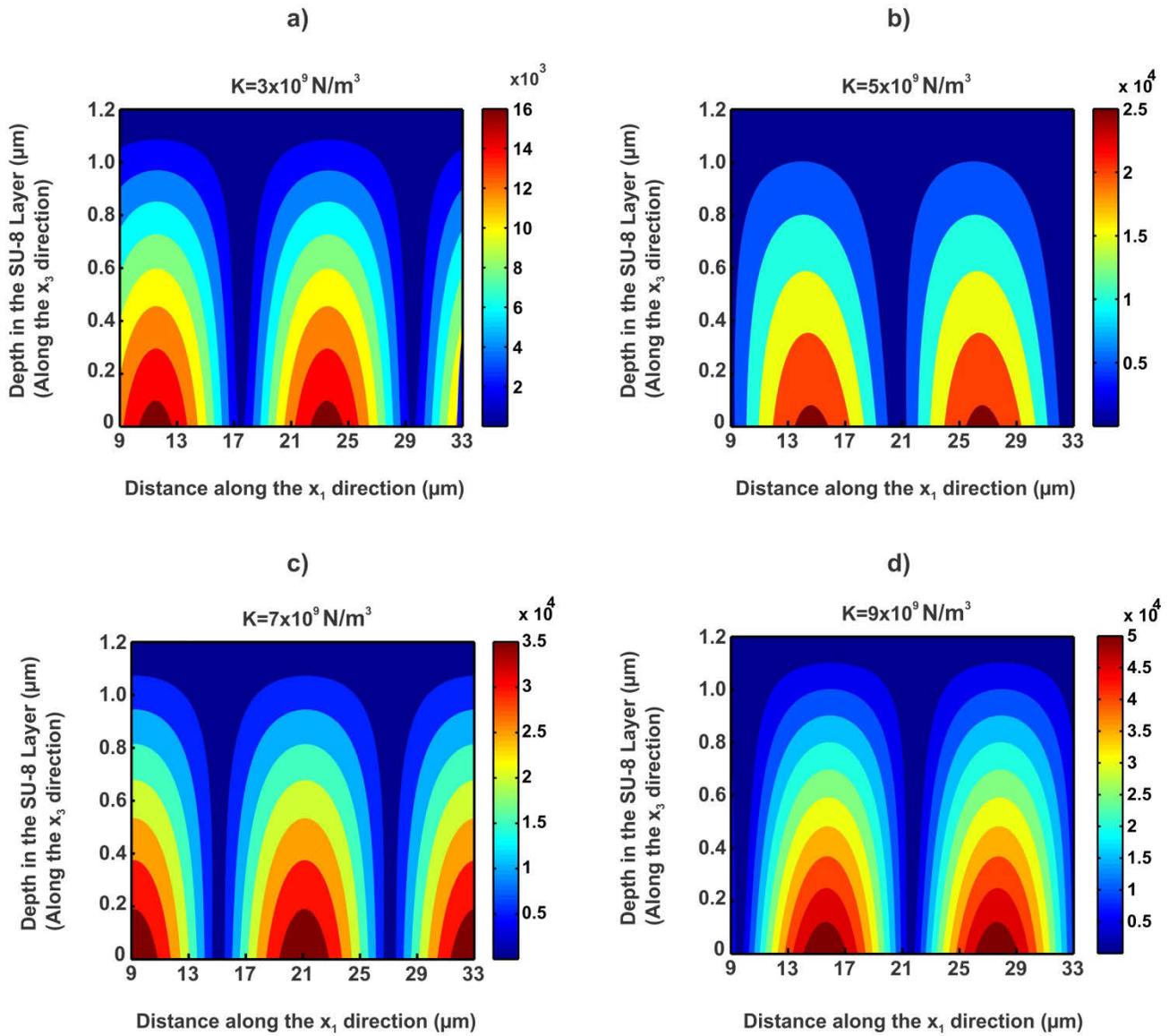
Figure 6-42: Contour plots for the equivalent stress in the SU-8 layer at different values of the interface spring stiffness (K) for h_{AlN}/λ = 0.04583
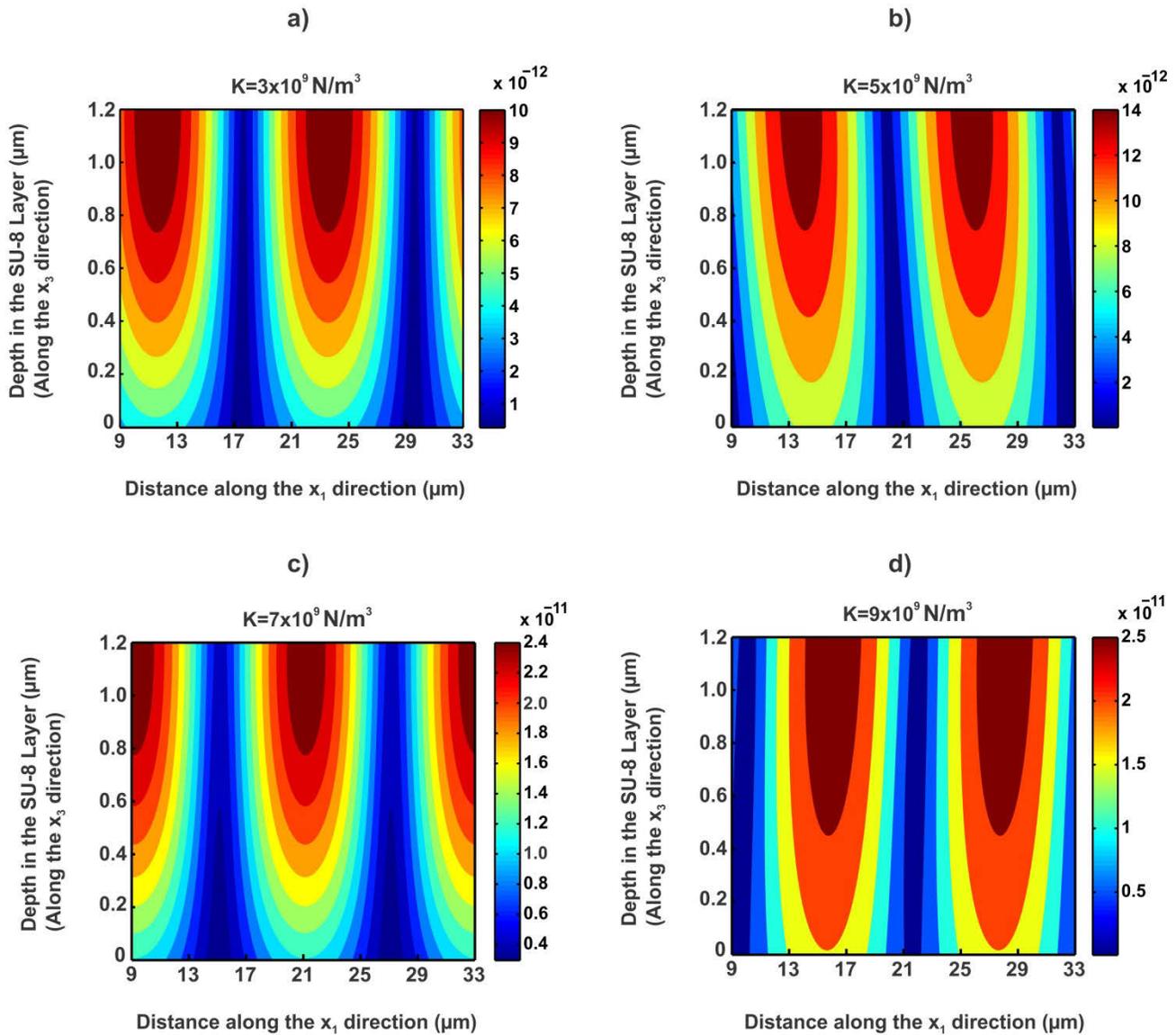
Figure 6-43: Contour plots for the equivalent displacement in the SU-8 layer at different values of the interface spring stiffness (K) for $h_{AlN}/\lambda = 0.04583$

6.6 Evaluating the adhesion of the SU-8 film

The experimental results illustrating the increase in wave velocity in the absence of omnicoat agrees with the results from the theoretical model for the range of h_{AlN}/λ used in this study (0.01833-0.04583), which also indicated an upward shift in the phase velocity as the value of the interface spring stiffness decreases as illustrated in chpater 3 Figure 3-15 and Figure 3-16. The theoretical model illustrated the shift in the wave dispersion profile for different values of the interface spring stiffness. This model can be used with the experimental velocity values to find the equivalent interface spring stiffness values that correspond to the two cases investigated in this study, which are SU-8/Omnicoat/Au/AlN/Si and SU-8/Au/AlN/Si. By using a least square fitting function the dispersion profiles that best match the phase velocity values for SU-8/Omnicoat/Au/AlN/Si and SU-8/Au/AlN/Si can be found. The interface spring stiffness values are iterated in the range of $1 \times 10^8 -$ 1×10^{11} N/m^3 for h_{AlN}/λ in the range of 0.01833 to 0.04583 to find the phase velocity values that match the experimental phase velocities for both cases. Figure 6-44 illustrates the phase velocity values for the SU-8/Au/AlN/Si and SU-8/Omnicoat/Au/AlN/Si configurations and the fitted dispersion curves. The equivalent interface spring stiffness values for these two cases are found to be 7.9492$\times 10^9$ N/m^3 and 8.0992$\times 10^9$ N/m^3, respectively. The results illustrate an excellent agreement between the fitted dispersion curves and the experimental phase velocity values. The highest deviation is 0.265% and occurs at $h_{AlN}/\lambda = 0.01833$, however, as the value of h_{AlN}/λ increases the sensitivity of the SAW wave increases since the wave energy is concentrated near the interface and is more sensitive to the SU-8 adhesion properties; therefore, showing a higher agreement with the fitted dispersion curves. The equivalent interface stiffness for the SU-8/Omnicoat/Au/AlN/Si configuration is higher than the stiffness value for SU-8/Au/AlN/Si. This result demonstrates the improved adhesion of SU-8 due to omnicoat, which leads to a higher interface spring stiffness value. The shift in phase velocity between the dispersion profiles for K = 7.9492$\times 10^9$ N/m^3 and K = 8.0992 $\times 10^9$ N/m^3 is calculated and plotted on the secondary axis in Figure 6-44 along with the shifts calculated from the experimental velocity values. The results also show an excellent agreement between the theoretical velocity shifts and the experimental values.
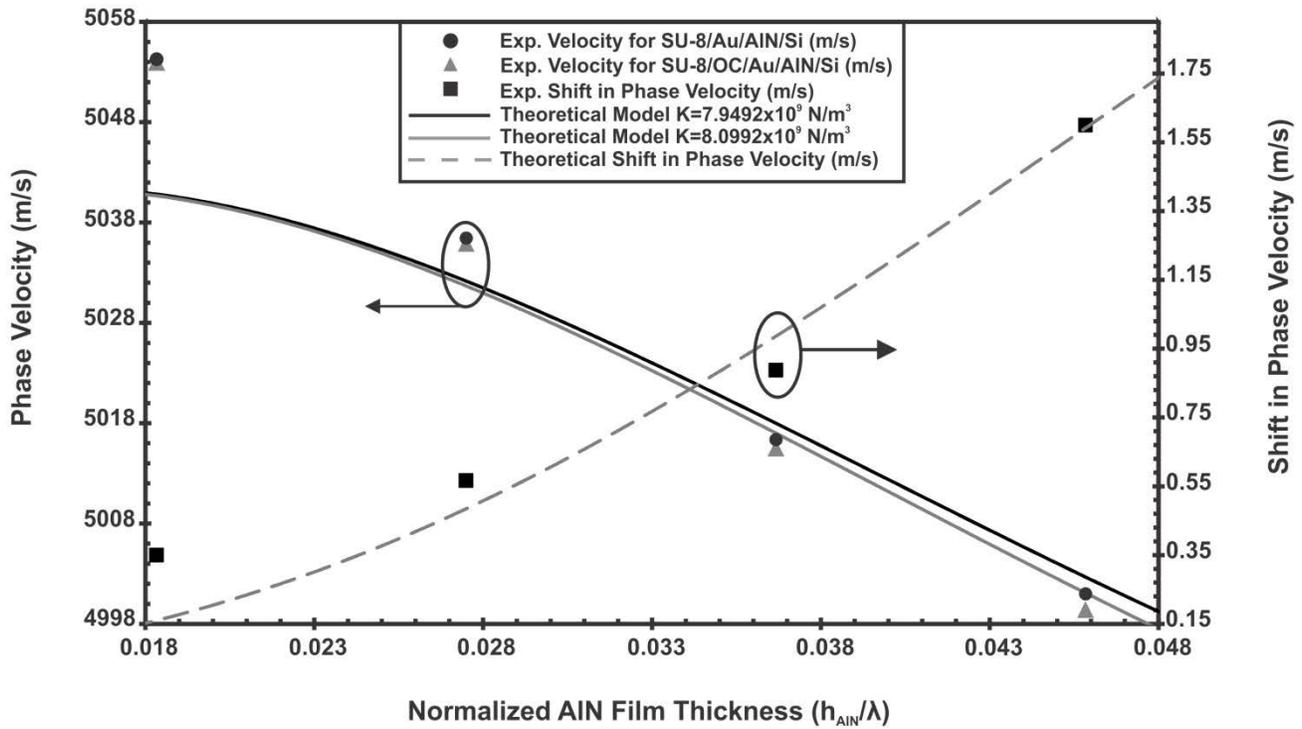
Figure 6-44: Velocity values for the four designs of SAW sensors; with and without the use of omnicoat and the dispersion curves obtained by curve fitting the theoretical velocity values to the experimental data points. On the secondary axis the shift in phase velocity obtained from the experimental data points are plotted with the theoretical shift in phase velocity.

6.7 Conclusions

This chapter illustrated the testing of four SU-8/AlN/Si SAW sensors operating in the frequency range of 84-208 MHz to determine the effect of changing the adhesion of the SU-8 film using an omnicoat layer on the sensors' frequency responses. The results illustrated that the frequency shifts to a higher value without the omnicoat layer since the wave is more concentrated in the AlN/Si structure. The wave velocities are calculated from frequencies and were shown to shift to a higher value without the omnicoat layer. The shifts in the frequency and velocity values increase as the operating frequencies of the sensor increase due to the improved sensitivity. Since two configurations of the four SAW sensor designs were tested and one included an omnicoat layer but the other did not the mass loading effect of omnicoat had to be evaluated. Another set of SAW sensors without SU-8 were also tested. The results illustrated that the presence of an omnicoat layer on the surface of the gold film leads to a drop in the SAW velocity for the four SAW sensor designs. This shift was subtracted from the overall frequency and velocity shifts due to the change in SU-8 adhesion. In addition, the final wave velocities due to the change in SU-8 adhesion were determined and were used to find the interface spring stiffness values that correspond to the two cases of SU-8 adhesion i.e. SU-8/Omnicoat/Au/AlN/Si and SU-8/Au/AlN/Si. The interface spring stiffness value for the SU-8/Omnicoat/Au/AlN/Si configuration was higher, this result was expected due to the improved adhesion of the SU-8 film using omnicoat.

CHAPTER 7. CONCLUSIONS AND FUTURE WORK

7.1 Research Contributions

This research investigated the use of an AlN/Si SAW sensor for evaluating the adhesion of SU-8 thin films. This hypothesis was first theoretically investigated and proven to be successful and four SAW sensor designs with high sensitivities were then selected for development. A microfabrication process was successfully developed to fabricate the SAW sensors. The fabricated SAW sensors were then packaged and tested. Frequency response measurements of two SAW sensor configurations for each of the four SAW sensor designs were measured. The frequency response measurements were used to calculate the SAW wave velocities. The velocity values were fitted with the theoretical dispersion curves to evaluate the adhesion of SU-8 thin films with and without Omnicoat. This presents a general overview of the adopted methodology in this research study. However, the following are the major contributions of this research:

1. A theoretical model for calculating the wave dispersion profile for the SU-8/AlN/Si configuration was developed. The spring boundary model was used to represent different levels of SU-8 adhesion by representing the SU-8/AlN interface using a layer of massless springs with interface stiffness $K(N/m^3)$. The change in the wave dispersion profile due to the change in the interface spring stiffness value was evaluated. The model illustrates that as the adhesion of the SU-8 film on the surface of the sensor deteriorates the SAW phase velocity shifts to a higher value. Finally, the stress and displacement fields generated in the SU-8 film at different adhesion levels are calculated and plotted.

2. The sensitivities of different SU-8/AlN/Si configurations were investigated using the theoretical model and the results indicated the increased sensitivity as the value of the normalized film thickness parameter (h_{AlN}/λ) increases. This is because the value of h_{AlN}/λ increases the wave penetration depth decreases, hence the wave is more concentrated near the interface and more sensitive to the changes in the SU-8 adhesion. By investigating the sensitivities of the different configurations four SAW sensor designs

were selected for fabrication at the University of Alberta micro-and nanofabrication facility. The four SAW sensor designs operated in the frequency range of 84-208MHz.

3. A process flow for the SU-8/AlN/Si SAW sensor was successfully developed at the University of Alberta micro-and nanofabrication facility. Using this recipe four SAW sensor designs operating in the frequency range of 84-208MHz were fabricated. For each design two configurations were developed. One of the configurations had an omnicaot layer patterned above the thin gold film on the surface of the sensor, prior to patterning the SU-8 layer. In the other configuration the SU-8 film was patterned directly above the thin gold film. The fabricated sensors were successfully packaged using wire bonding prior to testing.

4. The packaged sensors were successfully tested using a vector network analyzer to determine their scattering parameters. The frequency responses from both configurations of each sensor design were compared and the shifts in the center frequency values were evaluated. The center frequency values were used to calculate the SAW wave velocities for each of the four SAW sensor designs. The effect of having an omnicoat layer in one of the sensor configurations was evaluated. The effect of omnicoat on the frequency and velocity shifts was found to be less the effect of changing the adhesion of the SU-8 layer. The frequency and velocity shifts due to the mass loading effect were subtracted from the overall shifts. Therefore, the frequency and velocity shifts due to the change in adhesion of the SU-8 film were successfully determined.

5. The SAW velocities were curve fitted with the wave dispersion curves calculated for different values of the interface spring stiffnesses. The interface spring stiffness values whose dispersion curves were fitted to the SAW phase velocity values were found to be 7.9492×10^9 N/m^3 and 8.0992×10^9 N/m^3 for the SAW sensors without omnicoat and with omnicoat, respectively. These results illustrated that for the sensors without omnicoat the equivalent interface spring stiffness value was lower than for the sensors with an omnicoat layer. This is the expected result since omnicoat is an adhesion promoter widely used to increase the adhesion of the SU-8 to gold.

7.2 Future Work

This research successfully demonstrated the evaluation of SU-8 adhesion using an AlN/Si SAW sensor theoretically and experimentally. However, there still exists a few areas that require further development and more testing needs to be carried out to improve the possibilities of this non-destructive MEMS based sensing approach:

1. In this study the adhesion of SU-8 thin films was investigated using the SAW sensor both theoretically and experimentally. The theoretical model illustrated that adding a SU-8 film on the surface of the SAW sensor leads to a drop in the wave dispersion profile due to the lower Rayleigh wave velocity of SU-8 in comparison to the AlN and Si. At intermediate adhesion levels of the SU-8 film the dispersion curves fluctuated as was shown. However, another interesting case that should be investigated using the AlN/Si SAW sensor is a thin film that has a higher Rayleigh wave velocity in comparison to AlN and Si. There are numerous metallic films that have higher Rayleigh wave velocities and are widely used in thin film structures and components. Therefore, investigating the effect of changing the adhesion of these metallic films on the wave dispersion profile would certainly be very useful and would extend the applications of the proposed SAW sensor in adhesion characterization.

2. The applications of the proposed sensing methodology in thin film applications and structures were highlighted throughout. However, there are also numerous potential applications of the proposed sensing methodology as embedded sensors. In order to investigate the possibility of embedding the proposed SAW sensor for adhesion characterization the thickness of the adhering film needs to be increased. In this study the thickness of the SU-8 layer was fixed at 1.2μm. This thickness was less than the wavelengths of the four SAW sensor designs. However, the thickness needs to be increased such that it's higher than the acoustic wavelength. In this case the adhering medium would correspond to a half-space and the SAW wave would become a Stoneley wave. This changes the characteristics of the acoustic wave and the boundary conditions of the problem. But it needs to be investigated to increase the potential applications of this MEMS based sensing technology.

3. The acoustic wavelength is significantly affected by the thickness of the adhering film. During the testing phase of this study the thickness of the SU-8 layer in the initial samples was ranging from 1.6 μm -1.9μm. It was found that at this thickness range the sensor operating at 208MHz was incapable of monitoring the change in adhesion of the SU-8 film since the wave attenuation was significant. Therefore, the maximum thickness of the adhering layer should be determined if the SAW sensor will be used to investigate the adhesion of other thin film materials.

4. In this study the thickness of the AlN film was 1.1μm this was the maximum thickness that could be achieved using the available resources at the University of Alberta micro- and Nanofabrication facility. If higher thicknesses can be deposited this would lead to SAW sensors operating at higher frequencies with much higher sensitivities. This could be highly useful in monitoring the adhesion of very thin films since at higher frequencies the SAW waves are more concentrated near the interface and hence can detect the changes in properties of thin films with very high sensitivity.

5. Two configurations of the four SAW sensor designs were investigated in this study. One of the configurations had an omnicoat layer patterned below the SU-8 film and the other did not. They represented two levels of adhesion of the SU-8 film. It is highly encouraged to investigate more intermediate levels of adhesion of the adhering layer. This will provide more in depth information on the sensitivity of the SAW sensors in detecting changes in adhesion and could lead to improvements in the SAW sensor design.

BIBLIOGRAPHY

[1] M. Zhong, C. Zhang, J. Luo, and X. Lu, "The protective properties of ultra-thin diamond like carbon films for high density magnetic storage devices," *Applied Surface Science,* vol. 256, pp. 322-328, 2009.

[2] C. P. O. Treutler, "Industrial use of plasma-deposited coatings for components of automotive fuel injection systems," *Surface and Coatings Technology,* vol. 200, pp. 1969-1975, 2005.

[3] F. H. Sun, M. Zhang, M. Chen, and H. S. Shen, "Improvement of adhesive strength and surface roughness of diamond films on co-cemented tungsten carbide tools," *Diamond and Related Materials,* vol. 12, pp. 711-718, 2003.

[4] E. Uhlmann and J. Koeing, "Analysis of the manufacturing chain of CVD diamond coated shaft type cutting tools," *Production Engineering,* vol. 4, pp. 211-220, 2010.

[5] S. Niyomsoan, W. Grant, D. L. Olson, and B. Mishra, "Variation of color in titanium and zirconium nitride decorative thin films " *Thin Solid Films,* vol. 415, pp. 187-194, 2002.

[6] W. Luo, Q. Fu, D. Zhou, J. Deng, H. Liu, and G. Yan, "A surface acoustic wave H2S gas sensor employing nanocrystalline SnO2 thin film," *Sensors and Actuators B: Chemical* vol. 176, pp. 746-752, 2013.

[7] O. Pabst, J. Perelaer, E. Beckert, U. S. Schubert, R. Eberhardt, and A. Tunnermann, "All Ink-Jet Printed Polymer Actuators: Characterization and Applications for Micropumps in Lab-On-a-Chip Systems," *Organic Electronics,* vol. 14, pp. 3423-3429, 2013.

[8] M. Patrascu, J. Gonzalo-Ruiz, M. Goedbloed, S. H. Brongersma, and M. Crego-Calama, "Flexible, electrostatic microfluidic actuators based on thin film fabrication," *Sensors and Actuators A: Physical,* vol. 186, pp. 249-256, 2012.

[9] R. Daniel, K. J. Martinschitz, J. Keckes, and C. Mitterer, "The Origin of Stresses in Magnetron Sputtered Thin Films with Zone T Structures," *Acta Materialia,* vol. 58, pp. 2621-2633, 2010.

[10] A. Moridi, H. Ruan, L. C. Zhang, and M. Liu, "Residual stresses in thin film systems: effects of lattice mismatch, thermal mismatch and interface dislocations," *International Journal of Solid and Structures,* vol. 50, pp. 3562-3569, 2013.

[11] J. A. Thornton and D. W. Hoffman, "Stress-related effects in thin films," *Thin Solid Films,* vol. 171, pp. 5-31, 1989.

[12] Y.-C. Huang, S.-Y. Chang, and C.-H. Chang, "Effect of Residual Stresses on Mechanical Properties and Interface Adhesion Strength of SiN Thin Films " *Thin Solid Films* vol. 517, pp. 4857-4861, 2009.

[13] A. Lee, B. M. Clemens, and W. D. Nix, "Stress induced delamination methods for the study of adhesion on Pt thin films to Si," *Acta Materialia,* vol. 52, pp. 2081-2093, 2004.

[14] T. Kitamura, H. Hirakata, and T. Itsuji, "Effect of residual stress on delamination from interface edge between nano-films," *Engineering Fracture Mechanics,* vol. 70, pp. 2089-2101, 2003.

[15] S. R. Dupont, E. Voroshazi, P. Heremans, and R. H. Dauskardt, "The effect of anneal, solar irradiation and humidity on the adhesion/cohesion properties of P3HT:PCBM based inverted

polymer solar cells," in *38th IEEE Photovoltaic Specialists Conference*, Austin, TX, USA, 2012.

[16] A. Kamer, K. Larson-Smith, L. S. C. Pingree, and R. H. Duskardt, "Adhesion and degradation of hard coatings on poly(methyl methacrylate) substrates," *Thin Solid Films,* vol. 519, pp. 1907-1913, 2011.

[17] E. C. Benzel, M. Kayanja, A. Fleischman, and S. Roy, "Spine Biomechanics: Fundamentals and Future," *Clinical Neurosurgery,* vol. 53, pp. 98-105, 2006.

[18] L. A. Ferrera, A. J. Fleischman, D. Togawa, T. W. Bauer, E. C. Benzel, and S. Roy, "An in-vivo biocompatibility assessment of MEMS materials for spinal fusion monitoring," *Biomedical Microdevices,* vol. 5, pp. 297-302, 2003.

[19] F. Alfaro, "A multi axial bioImplantable MEMS array bone stress sensor," 19, Robotics Institute, Carnegie Mellon University, USA, 2009.

[20] M. C. Hsieh, Y. K. Fang, M.-S. Ju, G.-S. Chen, J.-J. Ho, C. H. Yang*, et al.*, "A contact-type piezoresistive micro-shear stress sensor for above-knee prosthesis application," *Journal of Microelectromechanical Systems,* vol. 10, pp. 121-127, 2001.

[21] A. R. Baker, L. R. F. Rose, and R. Jones, *Advances in the bonded composite repair of metallic aircraft structure*. United Kingdom: Elsevier 2002.

[22] W. Baker, I. McKenzie, and R. Jones, "Development of life extension strategies for Australian military aircraft, using structural health monitoring of composite repairs and joints," *Composite Structures,* vol. 66, pp. 133-143, 2004.

[23] H. C. H. Li, F. Beck, O. Dupouy, I. Herszberg, P. R. Stoddart, C. E. Davis*, et al.*, "Strain-based health assessment of bonded composite repairs," *Composite Structures,* vol. 76, pp. 234-242, 2006.

[24] Z. Chaudhry, F. Lalande, A. Ganino, C. Rogers, and J. Chung, "Monitoring the integrity of composite patch structural repair via piezoelectric actuators/sensors," in *Proceedings of the 36th AIAA/ASME/ASCE/AHS/ASC Structures, Structural Dynamics, and Materials Conference and AIAA/ASME Adaptive Structures Forum. Part 4 (of 5)*, New Orleans, USA, 1995, pp. 2243-2248.

[25] G. D. Davis, "Electrochemical impedance evaluation of aluminum/boron–epoxy composite bonds," *Journal of Adhesion Science and Technology,* vol. 19, pp. 1397-1408, 2005.

[26] A. Baldan, "Adhesively-bonded joints and repairs in metallic alloys, polymers and composite materials: Adhesives, adhesion theories and surface pretreatment," *Journal of Materials Science,* vol. 39, pp. 1-49, 2004.

[27] L. Goglio and M. Rossetto, "Ultrasonic testing of adhesive bonds of thin metal sheets," *NDT&E International,* vol. 32, pp. 323-331, 1999.

[28] S. A. Titov, R. G. Maev, and A. N. Bogachenkov, "Pulse-echo NDT of adhesively bonded joints in automotive assemblies," *Ultrasonics,* vol. 48, pp. 537-546, 2008.

[29] R. S. Dwyer-Joyce, B. W. Drinkwater, and A. M. Quinn, "The Use of Ultrasound in the Investigation of Rough Surface Interfaces " *Transactions of ASME. Journal of Tribology,* vol. 123, pp. 8-16, 2001.

[30] P. Cawley, T. P. Pialucha, and B. D. Zeller, "The characterization of oxide layers in adhesive joints using ultrasonic reflection measurements " *Proceedings of the royal society of london A,* vol. 452, pp. 1903-1926, 1996.

[31] A. Pilarski and J. L. Rose, "Ultrasonic oblique incidence for improved sensitivity in interface weakness determination," *NDT International,* vol. 21, pp. 241-246, 1988.

[32]   J. M. Allin, P. Cawley, and M. J. S. Lowe, "Adhesive bond de tection of automotive components using first mode ultrasonic measurements " *NDT&E International,* vol. 36, pp. 503-514, 2003.

[33]   Q. Shen, M. Omar, and S. Dongri, "Ultrasonic NDE Techniques for Impact Damage Inspection on C FRP Laminates," *Journal of Materials Science Research,* vol. 1, pp. 2 -16, 2012.

[34]   R. L. V. Kumar, M. R. Bhat, and C. R. L. Murthy, "Some studies on e valuation of degradation in composite adhesive joints using ultrasonic techniques," *Ultrasonics,* vol. 53, pp. 1150-1162, 2013.

[35]   L. A. Denisova, R. G. Maev, V. K. Leontjev, A. F. Denisov, G. G. Grayson, F. S. Rusanov*, et al.*, "A study of the adhesion between dental cement and dentin using a nondestructive acoustic microscopy approach," *Dental Materials,* vol. 25, pp. 557-565, 2009.

[36]   T. Nam, T. Lee, C. Kim, K.-Y. Jhang, and N. Kim, "Harmonic generation of an obliquely incident ultrasonic wave in solid-solid contact interfaces," *Ultrasonics* vol. 52, pp. 778 -783, 2012.

[37]   B. W. Drinkwater, R. S. Dwyer-Joyce, and P. Cawley, "A study of the transmission of ultrasound across solid-rubber interfaces," *Journal of the Acoustical Society of America,* vol. 101, pp. 970-981, 1997.

[38]   Z. Su and L. Ye, *Identification of damage using lamb waves* vol. 48: Springer-Verlag, 2009.

[39]   Z. Su, L. Ye, and Y. Lu, "Guided Lamb waves for identification of damage in composite structures: a review," *Journal of Sound and Vibration* vol. 295, pp. 753-780, 2006.

[40]   F. L. di Scalea, M. Bonomo, and D. Tuzzeo, "Ultrasonic guided wave inspection of bonded lap joints: Noncontact method and photoelastic visualization " *Research in Nondestructive Evaluation* vol. 13, pp. 153-171, 2001.

[41]   S. Huo, "Estimation of Adhesive Bond Strength in Laminated Safety Glass using Guided Mechanical Waves " PhD, Systems Engineering University of Illinois at Urbana-Champaign, USA, 2008.

[42]   D. Cerniglia, A. Pantano, and N. Montinaro, "3D simulations and experiments of guided wave propagation in adhesively bonded multi-layered structures " *NDT&E International,* vol. 43, pp. 527-535, 2010.

[43]   D. M. Benson, P. Karpur, T. E. Matikas, and T. Kundu, "Experimental Generation of Lamb Wave Dispersion using Fourrier Analysis of Leaky Modes," *Review of Progress in Quantitative Nondestructive Evaluation,* vol. 14, pp. 187-194, 1998.

[44]   B. A. Auld, *Acoustic Fields and waves in solids* vol. 2: John Wiley & Sons Inc., 1973.

[45]   D. E. Chimenti and R. W. Martin, "Nondestructive evaluation of composite laminates by leaky lamb waves " *Ultrasonics,* vol. 29, pp. 13-21, 1991.

[46]   A. K. Mal, P.-C. Xu, and Y. Bar-Cohen, "Leaky Lamb Wavess for the ultrasonic nondestructive evaluation of adhesive bonds " *Journal of Engineering Materials and Technology,* vol. 112, pp. 255-259, 1990.

[47]   M. J. S. Lowe and P. Cawley, "The applicability of plate wave techniques for the inspection of adhesive and diffusion bonded joints " *Journal of Nondestructive Evaluation* vol. 13, pp. 185-200, 1994.

[48]   P. C. Xu, K. E. Lindenschmidt, and S. A. Meguid, "A new high-frequency analysis of coatings using leaky Lamb waves," *Journal of the Acoustical Society of America,* vol. 94, pp. 2954-2962, 1993.

[49]   V. K. Kinra, P. T. Jaminet, C. Zhu, and V. R. Iyer, "Simultaneous measurement of the acoustical properties of a t hin-layered medium: The inverse problem," *Journal of the Acoustical Society of America,* vol. 95, pp. 3059-3074, 1994.

[50]   M. R. Karim, A. K. Mal, and Y. Bar-Cohen, "Inversion of leaky lamb wave data by simplex algorithm," *Journal of the Acoustical Society of America,* vol. 88, pp. 482-491, 1990.

[51]   Y. Bar-Cohen and A. K. Mal, "Characterization of adhesive bonding using leaky lamb waves," *Review of Progress in Quantitative Nondestructive Evaluation,* vol. 9, pp. 1271 - 1277, 1990.

[52]   P. B. Nagy and L. Adler, "Nondestructive evaluation of adhesive joints by guided waves " *Journal of Applied Physics,* vol. 66, pp. 4658-4663, 1989.

[53]   S. I. Rokhlin, M. Hefets, and M. Rosen, "An ultrasonic interface wave method for predicting the strength of adhesive bonds " *Journal of Applied Physics* vol. 52, pp. 2847-2851, 1981.

[54]   Z. G. Chen, Y. T. Hu, and J. S. Yang, "Shear horizontal piezoelectric waves in a piezoceramic plate imperfectly bonded to two piezoceramic half-spaces," *Journal of Mechanics* vol. 24, pp. 229-239, 2008.

[55]   M. D. Gardner, "Ultrasonic guided wave nondestructive evaluation using generalized anisotropic interface waves " Ph.D., Pennsylvania State University, USA, 2014.

[56]   Q. B. Han, M. L. Qian, and H. Wang, "Investigation of solid/solid interface waves with laser ultrasonics " *Ultrasonics* vol. 44, pp. e1323-e1327, 2006.

[57]   R. O. Claus and R. A. Kline, "Adhesive bonding interrogation using stoneley wave methods," *Journal of Applied Physics,* vol. 50, pp. 8066-8069, 1979.

[58]   F. N. Nguyen and J. C. Berg, "Use of an Optical-Mechanical Test Combined with Acoustic-Emission Techqnies to Study Adhesion in Filled Polymeric Composites," *The Journal of Adhesion,* vol. 81, pp. 823-841, 2005.

[59]   C. B. Scruby, "An Introduction to Acoustic Emission " *Journal of Physics E: Scientific Instruments,* vol. 20, pp. 946-953, 1987.

[60]   H. Ollendorf and D. Schneider, "A Comparative Study of Adhesion Test Methods for Hard Coatings," *Surface Coatings & Technology,* vol. 113, pp. 86-102, 1999.

[61]   M. Shiwa, E. R. Weppelmann, A. Bendeli, M. V. Swain, D. Munz, and T. Kishi, "Acoustic emission and precision force-displacement observations of sperical indentations into TiN films on silicon," *Surface and Coatings Technology,* vol. 68-69, pp. 598-602, 1994.

[62]   M. V. Swain and M. Wittling, "Comparison of acoustic emissions from pointed and spherical indentattion of TiN films on s ilicon and sapphire," *Surface and Coatings Technology,* vol. 76-77, pp. 528-533, 1995.

[63]   D. Croccolo and R. Cuppini, "A methodology to estimate the adhesive bonding defects and the final releasing moments in conical joints based on t he acoustic emissions technique," *International Journal of Adhesion & Adhesives,* vol. 26, pp. 490-497, 2006.

[64]   D. Croccolo and R. Cuppini, "Adhesive defect density estimation applying the acoustic emission technique " *International Journal of Adhesion & Adhesives,* vol. 29, pp. 234 -239, 2009.

[65]   J. J. Schubbe and S. Mall, "Investigation of a cracked thick aluminum panel repaired with bonded composite patch," *Engineering Fracture Mechanics* vol. 63, pp. 305-323, 1999.

[66]   Y. He, M. Pan, F. Luo, and G. Tian, "Pulsed eddy current imaging and frequency spectrum analysis for hidden defect nondestructive testing and evaluation " *NDT&E International* vol. 44, pp. 344-352, 2011.

[67]   J. W. Allin, "Disbond detection in adhesive joints using low-frequency ultrasound," PhD, Mechanical Engineering Imperial College London, United Kingdom, 2005.

[68]   A. W. Stevenson, T. E. Gureyev, D. Paganin, S. W. Wilkins, T. Weitkamp, A. Snigirev, *et al.*, "Phase-Contrast X-Ray imaging with synchrotron radiation for materials science applications," *Nuclear Instruments and Methods in Physics Research B,* vol. 199, pp. 427 - 435, 2003.

[69]   G. C. DeNolf, L. Haack, J. Holubka, A. Straccia, K. Blohowiak, C. Broadbent, *et al.*, "Axisymmetric Peel Test for Adhesion Measurement of Polymer Coatings " *Journal of Polymer Science Part B: Polymer Physics,* vol. 50, pp. 1706-1712, 2012.

[70]   J. Du, B. R. Tittmann, and H. S. Ju, "Evaluation of Thin Film Adhesion to Substrates by Means of Surface Acoustic Wave Dispersion," *Thin Solid Films* vol. 518, pp. 5786-5795, 2010.

[71]   C. Tsou, C. Hsu, and W. Fang, "Interfaces Friction Effect of Sliding Contact on Nanoindentation Test," *Sensors and Actuators A: Physical,* vol. 117, pp. 309-316, 2005.

[72]   P. Tran, S. S. Kandula, P. H. Geubelle, and N. R. Sottos, "Comparison of Dynamic and Quasi-Static Measurements of Thin Film Adhesion " *Journal of Physics D: Applied Physics* vol. 44, p. 034006, 2011.

[73]   M. Berdova, J. Lyytinen, K. Grigoras, A. Baby, L. Kilpi, H. Ronkainen, *et al.*, "Characterization of Thin Film Adhesion by MEMS Shaft-Loading Blister Testing " *Journal of Vacuum Science and Technology A,* vol. 31, p. 031102, 2013.

[74]   P. Richard, G. Gremaud, and A. Kulik, "Thin Film Adhesion Investigation with the Acoustic Microscope," presented at the Proceedings of IEEE Ultrasonics Symposium, Cannes, France, 1994.

[75]   R. P. Birringer, P. J. Chidester, and R. H. Dauskardt, "High Yield Four-Point Bend Thin Film Adhesion Testing Techniques " *Engineering Fracture Mechanics* vol. 78, pp. 2390-2398, 2011.

[76]   L. Sun, J. He, H. Kong, F. Yue, P. Yang, and J. Chu, "Structure, Composition, and Optical Properties of Cu2ZnSnS4 Thin Films Deposited by Pulsed Laser Deposition Method," *Solar Energy Materials & Solar Cells* vol. 95, pp. 2907-2913, 2011.

[77]   S. M. Xia, L. Ponson, G. Ravichandran, and K. Bhattacharya, "Adhesion of Heterogenous Thin Films - I: Elastic Heterogeneity," *Journal of Mechanics and Physics of Solids* vol. 61, pp. 838-851, 2013.

[78]   I. Alig, S. Tadjbach, P. Kruger, H. Oehler, and D. Lellinger, "Characterization of coating systems by scanning acoustic microscopy: Debonding, blistering and surface topology," *Progress in Organic Coatings* vol. 64, pp. 112-119, 2009.

[79]   R. D. Weglein and A. K. Mal, "A study of layer adhesion by acoustic microscopy " presented at the IEEE Ultrasonics Symposium Denver, USA, 1987.

[80]   K. Kosbi, T. Blum, U. Scheer, and S. Boseck, "Evaluation of imperfect gold/glass interaces using scanning acoustic microscope," in *Acousto-Optics and Applications III*, Gdansk-Jurata, Poland, 1998, pp. 314-319.

[81]   S. Parthasarathi, B. R. Tittmann, and M. Nishida, "Characterization of film interface integrity through scanning acoustic microscopy " *Surface Coatings & Technology* vol. 105, pp. 1-7, 1998.

[82]   M. Berdova, J. Lyytinen, K. Grigoras, A. Baby, L. Kilpi, H. Ronkainen, *et al.*, "Characterization of Thin Film Adhesion by MEMS Shaft-Loading Blister Testing " *Journal of Vacuum Science & Technology A,* vol. 31, p. 031102, 2013.

[83] J. Lyytinen, M. Berdova, S. Franssila, and J. Koskinen, "Adhesion Testing of Atomic Layer Deposited TiO$_2$ on Glass Substrate by the Use of Embedded SiO$_2$ Microspheres " *Journal of Vacuum Science & Technology A,* vol. 32, p. 01A102(pp.5), 2014.

[84] G. T. Ostrowicki and S. K. Sitaraman, "Magnetically Actuated Peel Test For Thin Films," *Thin Solid Films,* vol. 520, pp. 3987-3993, 2012.

[85] K. Matoy, T. Detzel, M. Muller, C. Motz, and G. Dehm, "Interface Fracture Properties of Thin Films Studied by Using the Micro-Cantilever Deflection Technique," *Surface Coatings & Technology,* vol. 204, pp. 878-881, 2009.

[86] M. M. EL Gowini and W. A. Moussa, "Investigating the change in surface acoustic wave velocity due to the change in adhesion of a SU-8 thin film using a SU-8/AlN/Si SAW sensor," *International Journal of Adhesion & Adhesives,* 2015. (submitted)

[87] M. M. EL Gowini and W. A. Moussa, "Theoretical and experimental investigation on the use of a s urface acoustic wave sensor for SU-8 thin-film adhesion characterization," *IEEE Sensors,* vol. 15, pp. 4667-4676, 2015.

[88] E. Dieulesaint and D. Royer, *Elastic Waves In Solids: Applications to Signal Processing* Great Britain: John Wiley & Sons, 1980.

[89] M. J. Madou, *Fundamentals of Microfabrication*. Boca Raton, Florida: CRC Press, 1997.

[90] K. Tsubouchi and N. Mikoshiba, "Zero Temperature Coefficient SAW Devices on A lN Epitaxial Films," *IEEE Transactions on Soni cs and Ultrasonics* vol. SU-32, pp. 634 -644, 1985.

[91] L. Rayleigh, "On Waves Propagated Along the Plane Surface of an Elastic Solid," *Proceedings of the London Mathematical Society,* vol. 17, 1885.

[92] A. E. H. Love, *Some Problems of Geodynamics*. Cambridge: Cambridge University Press, 1911.

[93] W. G. Cady, *Piezoelectricity; An Introduction to the Theory and Application of Electromechanical Phenomena in Crystals*: McGraw-Hill book company, inc, 1946.

[94] B. A. Auld, *Acoustic Fields and Waves in Solids* vol. vol. 1: John Wiley & Sons, 1973.

[95] T. Ikeda, *Fundamentals of Piezoelectricity*: Oxford University Press, 1990.

[96] G. W. Farnell and E. L. Adler, *Physical Acoustics: Principles and M ethods: Elastic Wave Propagation in Thin Layers* vol. 9: Academic Press, 1972.

[97] J.-M. Baik and R. B. Thompson, "Ultrasonic Scattering from Imperfect Interfaces: A Quasi Stais Model," *Journal of Nondestructive Evaluation,* vol. 4, pp. 177-196, 1984.

[98] H. Tada, P. Paris, and G. Irwin, *The Stress Analysis of Cracks Handbook*: ASME Press, 1973.

[99] I. Roch, P. Bidaud, D. Collard, and L. Buchaillot, "Fabrication and Characterization of an SU-8 Gripper Actuated by a Shape Memory Alloy Thin Film " *Journal of Micromechanics and Microengineering* vol. 13, pp. 330-336, 2003.

[100] J. H. Cantrell, "Determination of absolute bond strength from hydroxyl groups at oxidized aluminum-epoxy interfaces by angle beam ultrasonic spectroscopy," *Journal of Applied Physics,* vol. 96, pp. 3775-3781, 2004.

[101] S. Parthasarathi, B. R. Tittmann, and R. J. Ianno, "Quantitative Acoustic Microscopy for Characterization of the Interface Strength of Diamond Like Carbon Films " *Thin Solid Films* vol. 300, pp. 42-50, 1997.

[102] M. M. EL Gowini and W. A. Moussa, "Evaluating the adhesion of SU-8 thin fims using an AlN/Si surface acoustic wave sensor," *Journal of Micromechanics and M icroengineering,* vol. 25, p. 035031, 2015.

[103] J. M. Shaw, J. D. Gelrome, N. C. LaBianca, W. E. Conley, and S. J. Holmes, "Negative Photoresists for Optical Lithography," *IBM Journal of Research and Development* vol. 1-2, pp. 81-94, 1997.

[104] K. Y. Lee, N. C. LaBianca, S. A. Rishton, S. Zolgharnain, J. D. Gelrome, J. Shaw, *et al.*, "Micromachining Applications of a High Resolution Ultrathick Photoresist," *Journal of Vacuum Science & Technology B,* vol. 13, pp. 3012-3016, 1995.

[105] S. Keller, G. Blagoi, M. Lillemose, D. Haefliger, and A. Boisen, "Processing of Thin SU-8 Films," *Journal of Micromechanics and Microengineering,* vol. 18, p. 125020(10pp), 2008.

[106] C. Becnel, Y. Desta, and K. Kelly, "Ultra Deep X-Ray Lithography of Densely packed SU-8 Features: I. An SU-8 Casting Procedure to Obtain Uniform Solvent Content with Accompanying Experimental Results," *Journal of Micromechanics & Microengineering* vol. 15, pp. 1242-1248, 2005.

[107] R. Feng and R. J. Farris, "Influence of Processing Conditions on the Thermal and Mechanical Properties of SU8 Negative Photoresist Coatings," *Micromechanics & Microengineering* vol. 13, pp. 80-88, 2003.

[108] W. H. Teh, U. Durig, U. Drechsler, C. G. Smith, and H.-J. Guntherodt, "Effect of Low Numerical-Aperture Femtosecond Two-Photon Absorption on (SU-8) Resist for Ultrahigh-Aspect-Ratio Microstereolithography," *Journal of Applied Physics,* vol. 97, p. 054907, 2005.

[109] M. Despont, H. Lorenz, N. Fahrni, J. Brugger, P. Renaud, and P. Vettiger, "High-spect-Ratio Ultrathick Negative-Tone Near-UV Photoresist for MEMS Applications " presented at the IEEE 10th Annual International Workshop on Micro Electro Mechanical Systems, 1997.

[110] C.-H. Lin, G.-B. Lee, B.-W. Chang, and G.-L. Chang, "A New Fabrication Process for Ultra-Thick Microfluidic Microstructures Utilizing SU-8 Photoresist," *Journal of Micromechanics & Microengineering* vol. 12, pp. 590-597, 2002.

[111] R. Bharadwaj, R. Tripathi, A. Prabhakar, and S. Mukherji, "S-shaped SU-8 optical waveguide immobilized with gold nanoparticles for trace detection of explosives," presented at the Fourth Asia Pacific Optical Sensors Conference, Wuhan, China, 2013.

[112] J. Liu, L. Wang, Y. Lu, and S. He, "Properties of Love Waves in a Piezoelectric Layered Structure with a Viscoelastic Guiding Layer " *Smart Materials and Structures* vol. 22, p. 125034(8pp), 2013.

[113] N. E. DuToit, B. L. Wardle, and S.-G. Kim, "Design considerations for MEMS-scale piezoelectric mechanical vibration energy harvesters," presented at the Symposium on Ferroelectricity and Piezoelectricity, IMRC 2004, Cancun, Mexico, August 22 - 26 2004

[114] S. Lee, C. Chen, V. V. Deshpande, G.-H. Lee, I. lee, M. Lekas, *et al.*, "Electrically Integrated SU-8 Clamped Graphene Resonators," *Applied Physics Letters,* vol. 102, p. 153101, 2013.

[115] B.-H. Jo, L. M. Van Lerberghe, K. M. Motsegood, and D. J. Beebe, "Three-Dimensional Micro-Channel Fabrication in Polydimethylsiloxane (PDMS) Elastomer," *Journal of Micromechanical Systems,* vol. 9, pp. 76-81, 2000.

[116] Y. Moser, R. Forti, S. Jiguet, T. Lehnert, and M. A. M. Gijs, "Suspended SU-8 structures for monolithic microfluidic channels," *Microfluidics and Nanofluidics,* vol. 10, pp. 219 -224, 2011.

[117] W. Dai, K. Lian, and W. Wang, "A Quantitative Study on the Adhesion Property of Cured SU-8 on Various Metallic Surfaces," *Microsystem Technologies,* vol. 11, pp. 526-534, 2005.

[118] M. Nordstrom, A. Johansson, E. S. Nogueron, B. Clausen, M. Calleja, and A. Boisen, "Investigation of the Bond Strength between the Photo-sensitive Polymer SU-8 and Gold," *Microelectronic Engineering,* vol. 78-79, pp. 152-157, 2005.

[119] R. L. Barber, M. K. Ghantasala, R. Divan, D. C. Mancini, and E. C. Harvey, "Study of Stress and Adhesion Strength in SU-8 Resist Layers on S ilicon Substrate with Different Seed Layers " *Journal of Micro/Nanolithography, MEMS, and MOEMS,* vol. 6, p. 033006(pp.9), 2007.

[120] K.-Y. Hwang, C.-S. Park, J.-H. Kim, K.-Y. Suh, E.-C. Cho, and N. Huh, "The Effects of Adhesion Energy on the Fabrication of High-Aspect-Ratio SU-8 Microstructures " *Journal of Micromechanics & Microengineering* vol. 20, p. 117001(7pp), 2010.

[121] B. P. Corgier and D. Juncker, "Polymeric Microfabricated Electrochemical Nanoprobe with Adressable Electrodes," *Sensors and Actuators B: Chemical,* vol. 157, pp. 691-696, 2011.

[122] A. del Campo and C. Greiner, "SU-8: A Photoresist for High-Aspect-Ratio and 3D Submicron Lithography," *Journal of Micromechanics and M icroengineering* vol. 17, pp. R81-R95, 2007.

[123] R. Rodriguez-Clement, B. Aspar, N. Azema, B. Armas, C. Combescure, J. Durand*, et al.*, "Morphological Properties of Chemical Vapor Deposited AlN Films," *Journal of Crystal Growth,* vol. 133, pp. 59-70, 1993.

[124] A. V. Sotnikov, H. Schmidt, M. Weihnacht, E. P. Smirnova, T. Y. Chemekova, and Y. N. Makarov, "Elastic and Piezoelectric Properties of AlN and LiAlO$_2$ Single Crystals," *IEEE Transactions on U ltrasonics Ferroelectrics and Frequency Control,* vol. 57, pp. 808 -811, 2010.

[125] S. Boeshore, "Aluminum Nitride Thin Films on Titanium: Piezoelectric Transduction on a Metal Substrate," Ph.D., Materials Science, University of California Santa Barbara, USA, 2006.

[126] Q. Chen, "Fabrication and Characterization of AlN Thin Film Bilk Acoustic Wave Resonator," Ph.D., Mechanical Engineering University of Pittsburgh, USA, 2005.

[127] S.-U. Hong, M.-C. Paek, G.-P. Han, Y.-J. Sohn, T.-Y. Kim, K.-I. Cho*, et al.*, "Characterization of Aluminum Nitride Thin Films on Silicon Substrates Grown by Plasma Assisted Molecu lar Beam Epitaxy," *Japanese Journal of Applied Physics,* vol. 41, pp. 5507-5512, 2002.

[128] W. Tian, W. Y. Yan, J. N. Dai, S. L. Li, Y. Tian, X. Hui*, et al.*, "Effect of growth temperature of an AlN intermediate layer on the growth mode of AlN grown by MOCVD," *Journal of Physics D: Applied Physics,* vol. 46, p. 065303(6pp), 2013.

[129] N. Tanaka, H. Okano, T. Usuki, and K. Shibata, "Preparation of Aluminum Nitride Epitaxial Films by Electron Cyclotron Resonance Dual-Ion-Beam Sputtering " *Japanese Journal of Applied Physics* vol. 33, pp. 5249-5254, 1994.

[130] J.-M. Liu, N. Chong, H. L. W. Chan, K. H. Wong, and C. L. Choy, "Pulsed-laser-deposited epitaxial aluminum nitride films on (111) Si for surface acoustic-wave applications," *Applied Physics A,* vol. 76, pp. 93-96, 2003.

[131] E. Iborra, M. Clement, J. Sangrador, A. Sanz-Hervas, L. Vergara, and M. Aguilar, "Effect of Particle Bombardment on the Orientation and the Residual Stress of Sputtered AlN Films for SAW Devices," *IEEE Transactions on U ltrasonics Ferroelectrics and F requency Control,* vol. 51, pp. 352-358, 2004.

[132] H.-C. Lee, J.-Y. Lee, and H.-J. Ahn, "Effect of the Substrate Bias Voltage on t he Crystallographic Orientation of Reactively Sputtered AlN Thin Films," *Thin Solid Films* vol. 251, pp. 136-140, 1994.

[133] M.-A. Dubois and P. Muralt, "Stress and Piezoelectric Properties of Aluminum Nitride Thin Films Deposited onto Metal Electrodes by Pulsed Direct Current Reactive Sputtering," *Journal of Applied Physics* vol. 89, pp. 6389-6395, 2001.

[134] J. W. Cho, "Pulsed DC Reactive Magnetron Sputtering of Aluminum Nitride Thin Films," Ph.D., Materials Science & Engineering North Carolina State University, United States, 2002.

[135] O. Baghriche, "Preparation and characterization of new materials based on TiO2 and silver. Application for elimination of microorganisms and harmful substances," Ph.D., Department of Chemistry, Université Constantine 1, Algeria, 2013.

[136] P. J. Kelly and R. D. Arnell, "Magnetron Sputtering: A Review of Recent Developments and Applications " *Vacuum* vol. 56, pp. 159-172, 2000.

[137] D. M. Mattox, *Handbook of physical vapor deposition (PVD) processing*: Elsevier Inc., 2010.

[138] L. B. Jonsson, T. Nyberg, I. Katardjiev, and S. Berg, "Frequency Response in Pulsed DC Reactive Sputtering Processes," *Thin Solid Films* vol. 365, pp. 43-48, 2000.

[139] A. Stoffel, A. Kovacs, W. Kronast, and B. Muller, "LPCVD Against PECVD for Micromechanical Applications " *Journal of Micromechanics & Microengineering,* vol. 6, pp. 1-13, 1996.

[140] M. Birkholz, *Thin Film Analysis by X-Ray Scattering* Wiley-VCH Verlag GmbH &Co. KGaA, 2005.

[141] F. Medjani, R. Sanjines, G. Allidi, and A. Karimi, "Effect of Substrate Temperature and Bias Voltage on the Crystallite Orientation in RF Magnetron Sputtered AlN Thin Films " *Thin Solid Films* vol. 515, pp. 260-265, 2006.

[142] C. Campbell, *Surface Acoustic Wave Devices and Their Signal Processing Applications* United Kingdom: Academic Press Inc., 1989.

[143] S. Datta, *Surface Acoustic Wave Devices*. New Jersey, USA: Prentice Hall, 1986.

[144] A. Technologies, "Network Analyzer Basics."

[145] D. Morgan, *Surface Acoustic Wave Filters, 2nd edition*: Academic Press, 2007.

[146] F. Moller and W. Buff, "Electromagnetic feedthrough in Si/ZnO-SAW-devices " presented at the Proceedings of the IEEE Ultrasonics Symposium Tucson, AZ, USA, 1992.

[147] M. Clement, L. Vergara, E. Iborra, A. Sanz-Hervas, J. Olivares, and J. Sangrador, "AlN-on-Si SAW filters: influence of film thickness, IDT geometry and substrate conductivity," presented at the IEEE Ultrasonics Sympsium, Rotterdam, Netherlands, 2005.

[148] E. Iborra, M. Clement, J. Sangrador, A. Sanz-Hervas, L. Vergara, and M. Aguilar, "Effecf of particle bombardment on the orientation and the residual stress of sputtered AlN films for SAW devices," *IEEE Transactions on Ultrasonics, Ferroelectrics and Frequency Control,* vol. 51, pp. 352-358, 2004.

[149] C.-M. Lin, Y.-Y. Chen, V. V. Felmetsger, W.-C. Lien, T. Riekkinen, D. G. Senesky*, et al.*, "Surface acoustic wave devices on A lN/3C-SiC/Si multilayer structures," *Journal of Micromechanics and Microengineering* vol. 23, p. 025019(8pp), 2013.

[150] K. Heller, L. J. Jacobs, and J. Qu, "Characterization of Adhesive Bond Properties using Lamb Waves " *NDT&E International* vol. 33, pp. 555-563, 2000.

[151] X. Xiao and X.-Y. You, "The determination for the adhesion of film and substrate by surface acoustic waves " *Surface Coatings & Technology,* vol. 201, pp. 9594-9597, 2007.

[152] J. P. Dunsmore, *Handbook of microwave component measurements: with advanced VNA techniques*. United States: John Wiley & Sons, 2012.

[153] J. Staudinger, *Vector network analyzer calibration in Commercial wireless circuits and components handbook*. United States: CRC Press, 2002.

[154] W. C. Wilson and G. M. Atkinson, "Mixed Modeling of a SAW Delay Line using VHDL," in *IEEE International Behavioral Modeling and Simulation Workshop*, September 14-15, 2006, pp. 34-39.

[155] H. N. Al-Shareef, D. Dimos, M. V. Raymond, and R. W. Schwartz, "Tunability and calculation of the dielectric constant of capacitor structures with interdigital electrodes," *Journal of Electroceramics* vol. 1, pp. 145-153, 1997.

APPENDIX A: MICROFABRICATION PROCEDURES

This section illustrates a detailed procedure of the steps involved in fabricating the SU-8/AlN/Si Surface Acoustic Wave Sensors. All the parameters for the processes used are listed.

Reactive Sputterig of AlN

- A Prime Si(100) wafer with 230nm LPCVD Si_3N_4 was used
- Two Al Target used
- Pump-down time: 4hrs30min
- Base Pressure: 2.3E-7Torr
- Conditioning for Target#1 was: 10min
- Conditioning for Target#2 was: 10min
- Deposition time: 180min
- Sputtering Pressure: 4mTorr
- Ar Flow: 8.57sccm
- N_2 flow: 20sccm
- Volt for Target#1 [Gun#2]: 252V
- Volt for Target#2 [Gun#1]: 254V
- Temperature: 28C
- Film thickness:1002.87nm
- Deposition Rate: 5.6nm/min

Al Deposition with Floyd

- Deposition Time: 17min

Lithography for Al Etching

- HPR504 used
- Exposure Time: 2.2sec
- Calibration done on November 8th 2013
- Exposure Factor: 76.4mW/cm^2
- Exposure Energy: 165mJ/cm2

Aluminum Etching

- Expected Etch Rate: 35nm/min

- Actual Etch Time: 8min
- Actual Etch Rate: 220/8.0=27.5nm/min

Lithography using AZ5214 for Au Films

- Exposure Time: 7sec
- Exposure Factor: 76.4mW/cm^2
- Exposure Energy: 514mJ/cm2
- Development Time: 60sec

Au+Cr Deposition with Floyd

For Chromium

- Dep Time: 120sec
- Power:75W
- Deposition Rate: 6nm/min
- Expected Film Thickness: 12nm

For Gold

- Dep Time: 7min
- Power: 80W
- Deposition Rate: 14.2nm/min
- Expected Film Thickness: 100nm

Au+Cr Lift-off

- Photoresist used is AZ5214
- Ultrasonic Bath is used
- Lift-off time: 13min

OMNICOAT Spinning Parameters

Add 5ml of OMNICOAT

- RPM1: 500 seconds
- Ramp1:5 seconds
- Time 1:5 seconds

- RPM2:3000 seconds
- Ramp2:10 seconds
- Time 2:30 seconds

Lithography using HPR504 for OMNICOAT Films

- Exposure Time: 2.2sec
- Exposure Factor: 76.4mW/cm^2
- Exposure Energy: 165mJ/cm^2

RIE Parameters
1. Power: 100Watts [33.3%]
2. Flow Rate: 35sccm
3. Pressure: 190mTorr
4. Time: 10sec

***EXCESS HPR504 Washed away with ACETONE

SU-8 Spinning Parameters

- Add 5ml of SU-8

- RPM1: 500 seconds
- Ramp1:5 seconds
- Time 1:5 seconds

- RPM2:5000 seconds
- Ramp2:10 seconds
- Time 2:30 seconds

Lithography for SU-8 2002

- Exposure Time: 5sec
- Exposure Factor: 76.4mW/cm^2
- Exposure Energy: 357mJ/cm2
- Development Time: 30sec

APPENDIX B: VECTOR NETWORK ANALYZER CALIBRATION PROCEDURE

The different types of errors in a network analyzer were introduced in chapter 5. The network analyzer calibration procedure can only eliminate the systematic errors. The experimental setup required for measuring the frequency responses of the sensors involves the use of multiple adapters and cables to connect the packaged sensor to the VNA. The use of adapters and cables can lead to variations in magnitude and phase that can mask the actual response of the device. Error correction through the measurement of known standard devices is a systematic approach that can help eliminate those errors and increase the accuracy of the measured signal. Known standards such as short/open/load/through are measured by the network analyzer and the measurements are compared to ideal models of these standards. The differences that arise between the measurements and the ideal models are the systematic errors introduced by the test setup and are removed later by error correction.

B.1 Error Models for One Port and Two Measurements

The influence of the systematic errors on the scattering parameters of the DUT can be represented using signal flow graphs. This facilitates the development of a mathematical model that represents how the systematic error terms affect the scattering parameters of the DUT. The signal flow graph for one-port reflection measurement is illustrated in Figure A. 1. A mathematical description illustrating the effect of the error terms on the scattering parameters is provided by error models. An error model will provide mathematical expressions for the scattering parameters of the DUT in terms of the systematic error terms. A signal flow graph for the error model in the case of one port reflection measurements is given [152]:
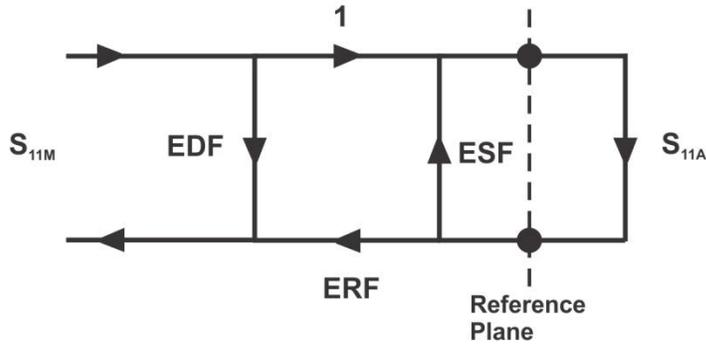
Figure B. 1 Signal flow graph for one-port reflection measurement

The actual reflection coefficient S_{11A} is the desired scattering parameter term of the DUT and is referenced with respect to the reference plane illustrated in Figure A. 1. However, the measured reflection coefficient S_{11M} includes the effect of the systematic errors. The S_{11A} parameter is related to the S_{11M} via [152]:

$$S_{11A} = \frac{S_{11M} - EDF}{ERF + (S_{11M} - EDF) \cdot ESF}$$

(B. 1)

The signal flow graph for two-port measurements illustrates the signal path in the forward (RF input at port 1) and reverse (RF input at port 2) directions. This is represented using two flow graphs as illustrated in Figure A. 2 and Figure A. 3, respectively. The error model consists of twelve error terms, 6 in the forward direction and 6 in the reverse direction. The actual S-parameters will be expressed in terms of the measured scattering parameters and the error terms.
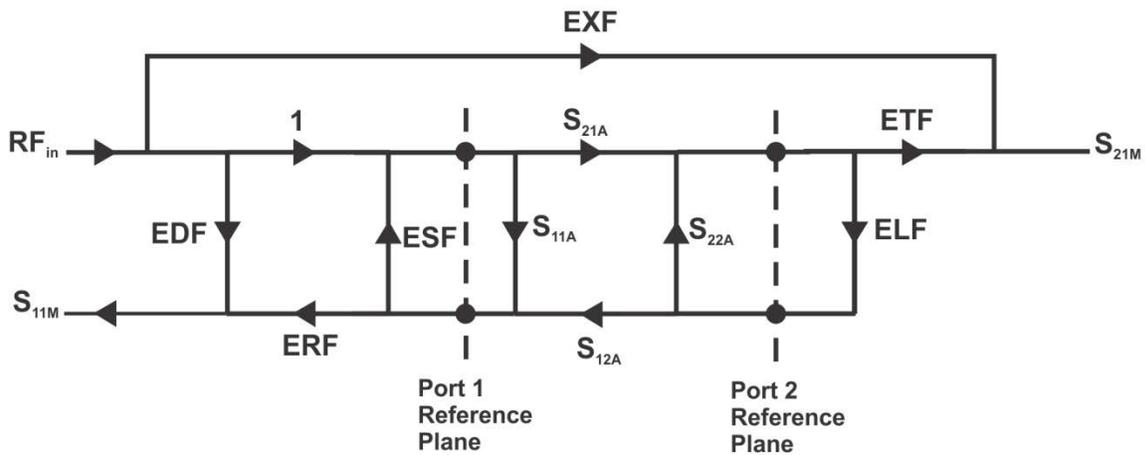
Figure B. 2 Signal flow graph for two port measurement in the forward direction
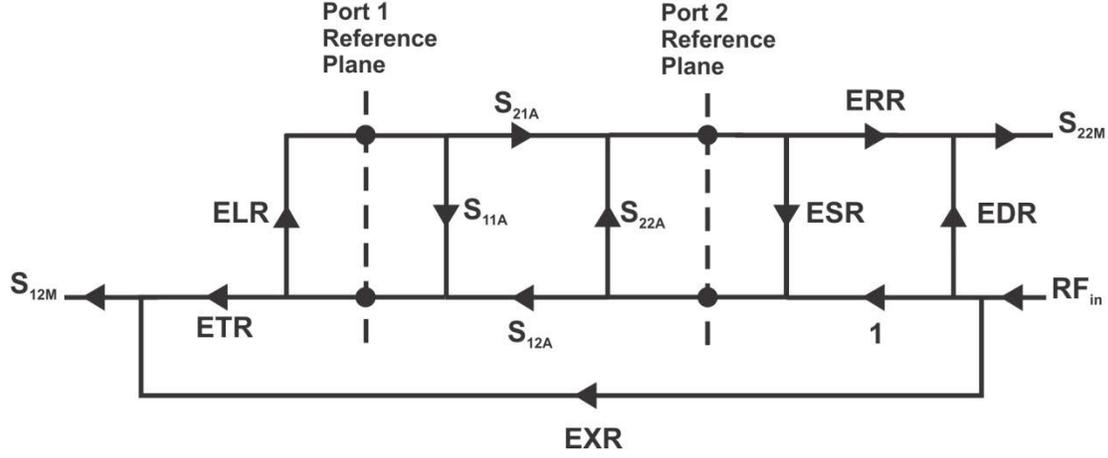
Figure B. 3 Signal flow graph for two port measurement in the reverse direction

The expressions for the actual forward and reverse scattering parameters can be derived from the signal flow graphs and are found to be [152]:

$$S_{11A} = \frac{S_{11N} \cdot (1 + S_{22N} \cdot ESR) - ELF \cdot S_{21N} \cdot S_{12N}}{(1 + S_{11N} \cdot ESF)(1 + S_{22N} \cdot ESR) - ELF \cdot ELR \cdot S_{21N} \cdot S_{12N}}$$

$$S_{21A} = \frac{S_{21N} \cdot (1 + S_{22N} \cdot (ESR - ELF))}{(1 + S_{11N} \cdot ESF)(1 + S_{22N} \cdot ESR) - ELF \cdot ELR \cdot S_{21N} \cdot S_{12N}}$$

$$S_{12A} = \frac{S_{12N} \cdot (1 + S_{11N} \cdot (ESF - ELR))}{(1 + S_{11N} \cdot ESF)(1 + S_{22N} \cdot ESR) - ELF \cdot ELR \cdot S_{21N} \cdot S_{12N}}$$

$$S_{22A} = \frac{S_{22N} \cdot (1 + S_{11N} \cdot ESF) - ELR \cdot S_{21N} \cdot S_{12N}}{(1 + S_{11N} \cdot ESF)(1 + S_{22N} \cdot ESR) - ELF \cdot ELR \cdot S_{21N} \cdot S_{12N}}$$

(B. 2)

where the normalized S-parameters are defined as [152]:

$$S_{11N} = \frac{S_{11M} - EDF}{ERF} \quad ; \quad S_{21N} = \frac{S_{21M} - EXF}{ETF}$$

$$S_{12N} = \frac{S_{12M} - EXR}{ETR} \quad ; \quad S_{22N} = \frac{S_{22M} - EDR}{ERR}$$

(B. 3)

The normalized scattering parameters are equivalent to the measured scattering parameters after subtracting the corresponding leakage terms and normalizing with respect to the corresponding tracking terms.

B.2 Vector Network Analyzer Calibration

The error models presented above illustrates how the actual scattering parameters are related to the error terms and the measured s-parameters. Therefore, when the error terms are determined it is possible to calculate the actual s-parameters from the measured ones. The process of determining the error terms is the calibration process, which is also referred to as the error correction technique. In order to determine the error terms a set of standards of known electrical properties are measured using network analyzer to generate one or more independent measurements. In a two port measurement there are 12 error terms; therefore 12 independent measurements (six in each direction) are needed to determine all the error terms.

Calibration of the vector network analyzer can be done either electronically using an electronic calibration module or mechanically using physical standards. In this study mechanical calibration was carried out using short, open, load and through standards, hence the process is known as SOLT calibration technique. The process involves making three measurements using one-port standards (open, short and load) and two measurements using a known through standard in each direction. This leads to a total of 12 independent measurements for determining 10 independent error terms. The scattering parameters of SOLT standards are illustrated in Figure A. 4.

Using the one-port calibration standards the measured scattering parameters due to the different standards in the forward direction can be expressed as:

$$
\begin{aligned}
S_{11M}^{O} &= EDF + \frac{ERF \cdot 1}{1 - ESF \cdot 1} \\
S_{11M}^{S} &= EDF + \frac{ERF \cdot (-1)}{1 - ESF \cdot (-1)} \\
S_{11M}^{L} &= EDF + \frac{ERF \cdot (0)}{1 - ESF \cdot (0)}
\end{aligned}
\tag{B. 4}
$$

This leads to three equations in three unknown error terms, which can be expressed as [152]:

$$EDF = S_{11M}^{O}$$

$$ESF = \frac{S_{11M}^{O} + S_{11M}^{S} - 2 \cdot EDF}{S_{11M}^{O} - S_{11M}^{S}}$$

$$ERF = \frac{-2 \cdot \left(S_{11M}^{O} - EDF\right) \cdot \left(S_{11M}^{S} - EDF\right)}{S_{11M}^{O} - S_{11M}^{S}}$$

(B. 5)

The three error terms in the reverse direction can be obtained in a similar manner, therefore a total of six error terms can be defined using one-port calibration standards. In order to complete the full two-port calibration procedure an additional six error terms need to be determined. These are the transmission tracking terms ETF and ETR, load match terms ELF and ELR and the isolation terms EXF and EXR.
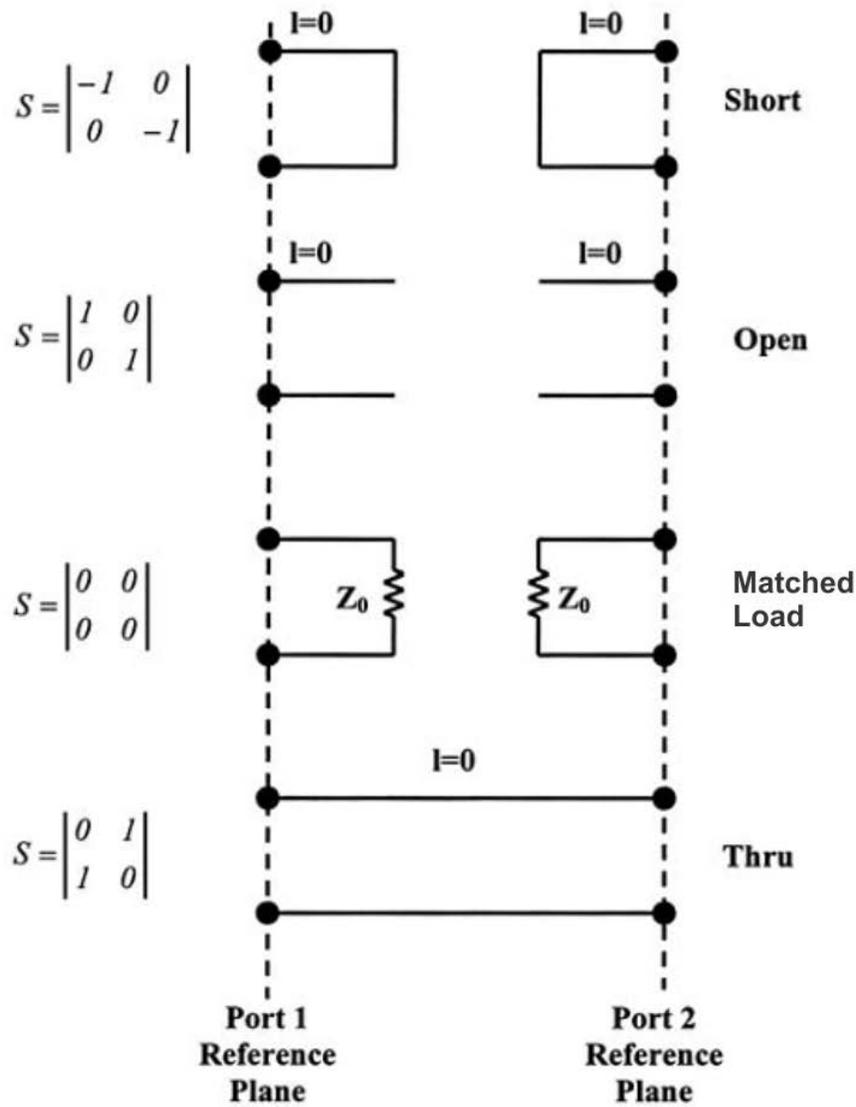
Figure B. 4 Electrical representation and scattering parameters of the SOLT standards (modified from [153])

Isolation Error Terms

In order to determine the isolation error terms i.e. the crosstalk that occurs between ports 1 and 2, two load standards need to be connected to both ports. By substituting the scattering parameter values for a load standard into the expressions for the actual transmission s-parameters given in equation (A.2) the isolation error terms are:

$$S_{21M} = EXF \quad ; \quad S_{12M} = EXR \tag{B. 6}$$

This implies that the error terms are equivalent to the transmission scattering parameters when load standards are connected to both ports.

<u>Transmission Tracking and Load Match Error Terms</u>

A through standard is a standard where all the scattering parameters are known. Using a through standard can be done by using an actual device with known scattering parameters (defined through) or basically connecting the two ports of the network analyzer (flush through). A flush through can be easily accomplished when the two ports have sexless connectors such as the APC-7 connector or if the two ports have opposite sexes. By substituting the scattering parameters for flush through in the expressions for the actual scattering parameters in equation(A.2) the measured s-parameters can be derived to be [153]:

$$S_{11M}^{T} = EDF + \frac{ERF \cdot ELF}{1 - ESF \cdot ELF} \quad ; \quad S_{22M}^{T} = EDR + \frac{ERR \cdot ELR}{1 - ESR \cdot ELR}$$

$$S_{21M}^{T} = \frac{ETF}{1 - ESF \cdot ELF} + EXF \quad ; \quad S_{12M}^{T} = \frac{ETR}{1 - ESR \cdot ELR} + EXR$$

(B. 7)

The expressions for the transmission tracking and load match error terms are found to be [152]:

$$ELF = \frac{S_{11M}^{T} - EDF}{ERF + ESF \cdot \left(S_{11M}^{T} - EDF \right)} \quad ; \quad ELR = \frac{S_{22M}^{T} - EDR}{ERR + ESR \cdot \left(S_{22M}^{T} - EDR \right)}$$

$$ETF = \left(S_{21M}^{T} - EXF \right) \cdot \left(1 - ESF \cdot ELF \right) \quad ; \quad ETR = \left(S_{12M}^{T} - EXR \right) \cdot \left(1 - ESR \cdot ELR \right)$$

(B. 8)

In order to determine the load match and transmission tracking error terms the one-port error terms and the cross-talk error terms should have been determined.

APPENDIX C: SCATTERING PARAMETER PLOTS FOR THE SAW SENSORS USED IN EVALUATING THE ADHESION OF SU-8 THIN FILM AND THE MASS LOADING EFFECT OF OMNICOAT

In Chapter 6 the full scattering parameter plots for the SAW sensors used in the characterization of SU-8 adhesion and in evaluation of the mass loading effect of omnicoat were not plotted for all the sensors. The full scattering parameters have been plotted for only two sensors; however the S_{21} parameter plots have been plotted for all the sensors. In this section the S_{11}, S_{21}, S_{22} and time domain plots for the S_{21} parameter are going to be plotted for the SU-8/AlN/Si sensors operating at 84, 125 and 208MHz. In addition, the S-parameter plots will be plotted for the Au/AlN/Si SAW sensors used in the characterization of the mass loading effect of omnicoat.

C.1 S-Parameter plots for the SU-8/AlN/Si SAW sensors operating at 84MHz
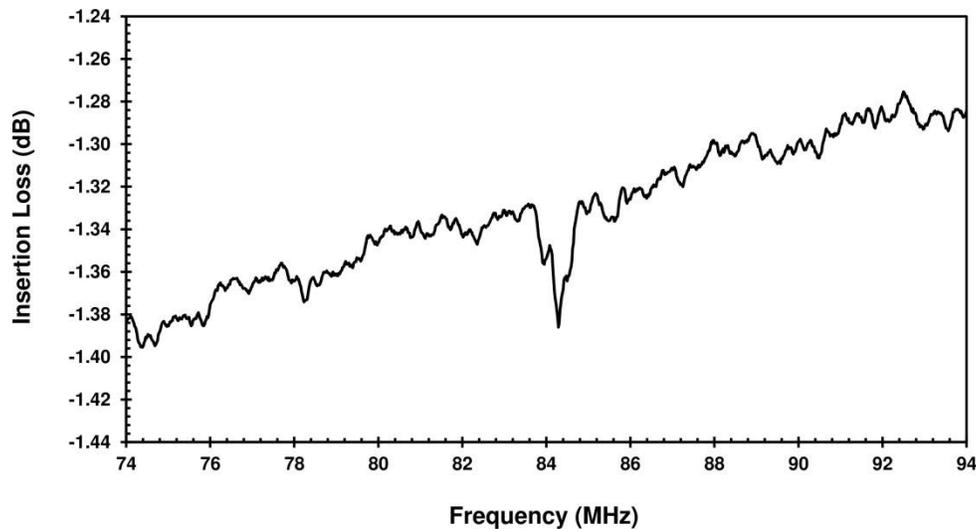
Figure C. 1 S_{11} parameter plot for the SU-8/AlN/Si SAW sensor with omnicoat operating at 84MHz
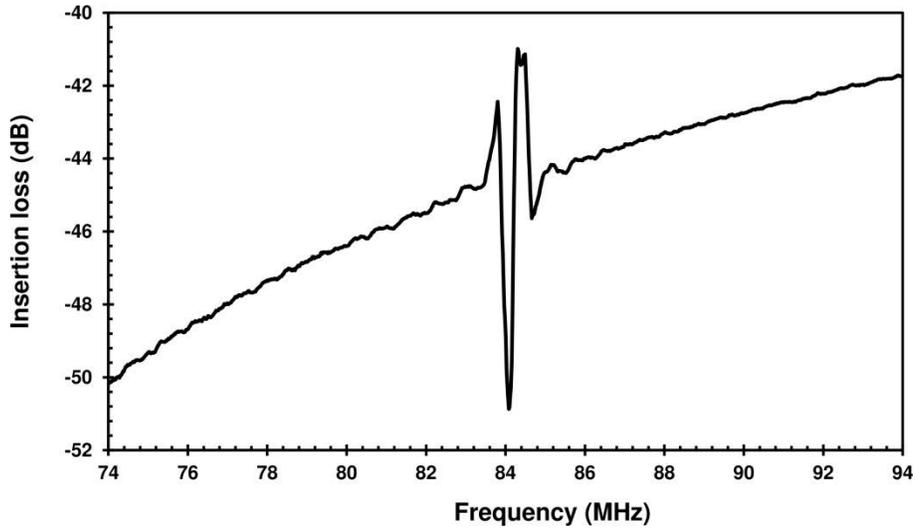
Figure C. 2 S$_{12}$ parameter plot for the SU-8 /AlN/Si SAW sensor with omnicoat operating at 84MHz
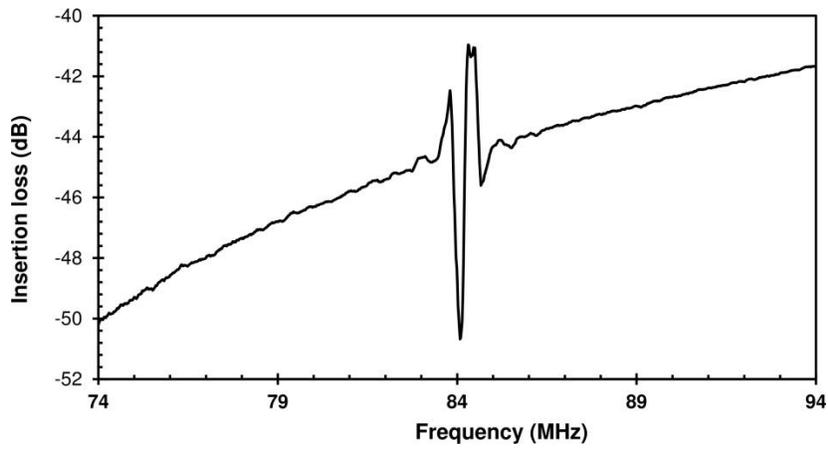
Figure C. 3 S$_{21}$ parameter plot without time gating for the SU-8/AlN/Si SAW sensor with omnicoat operating at 84MHz
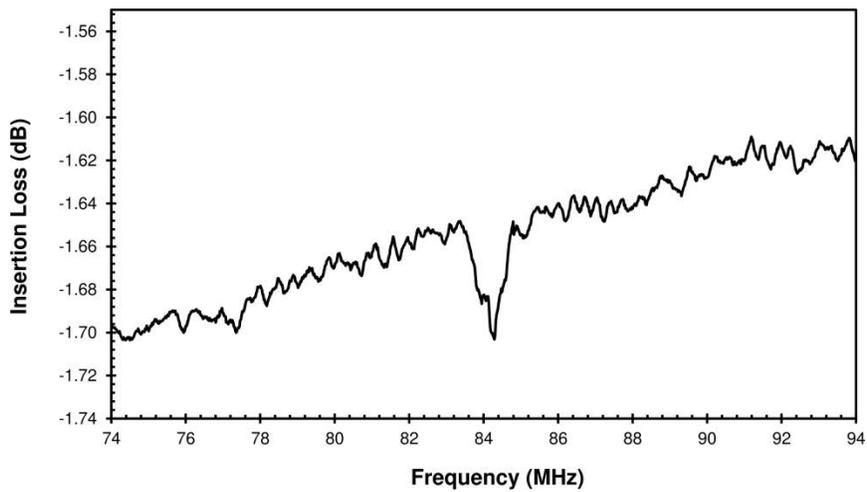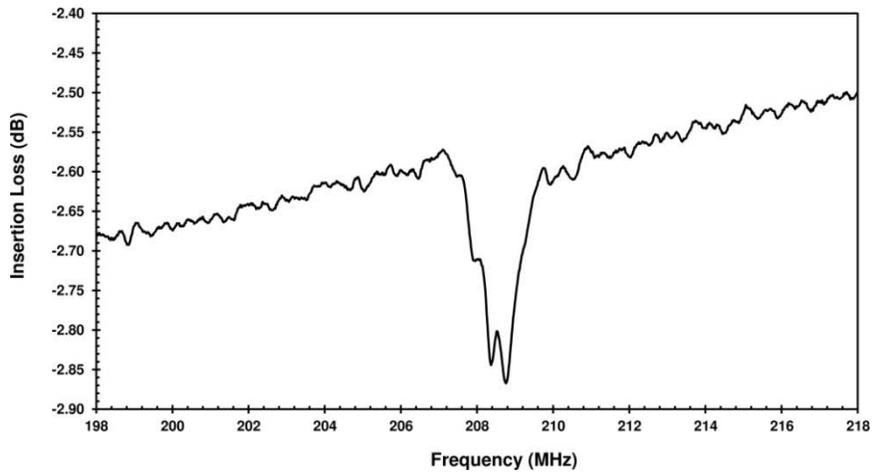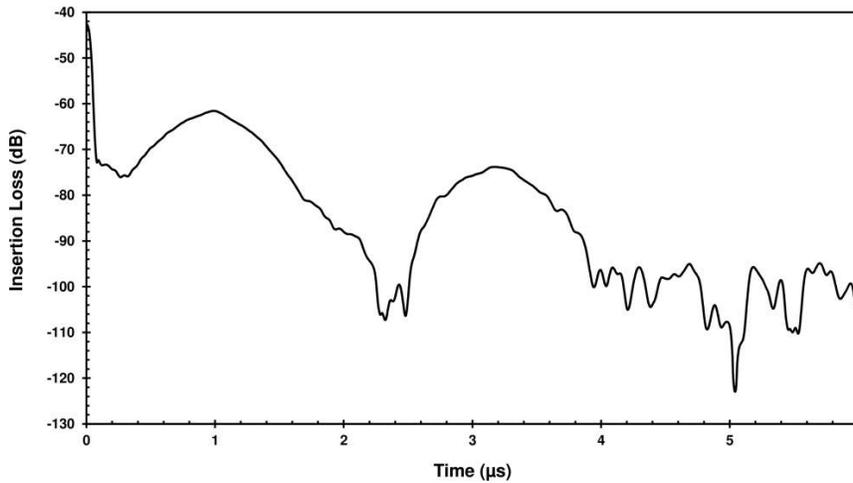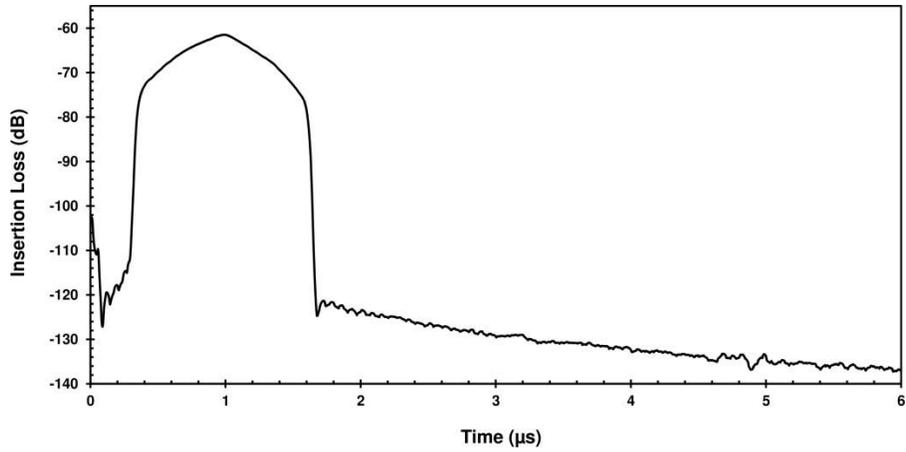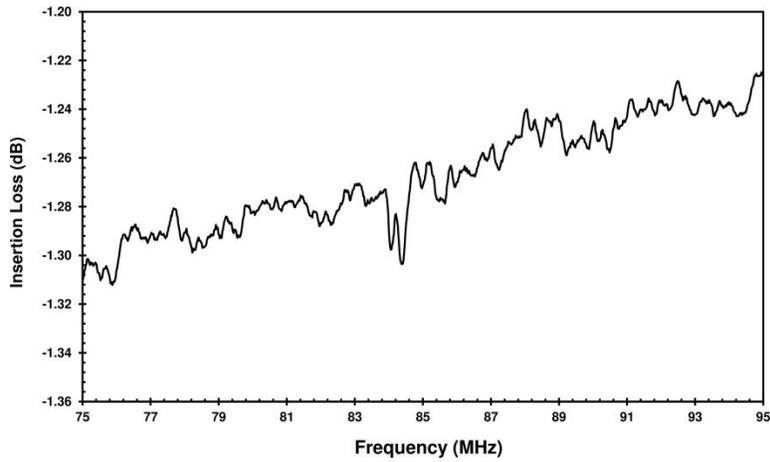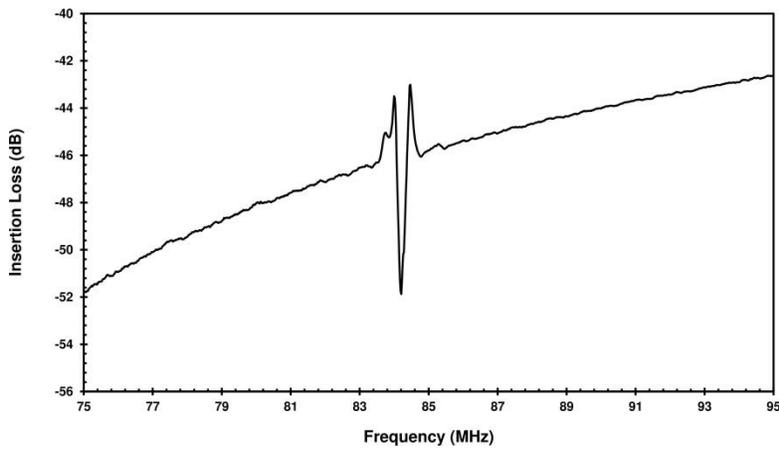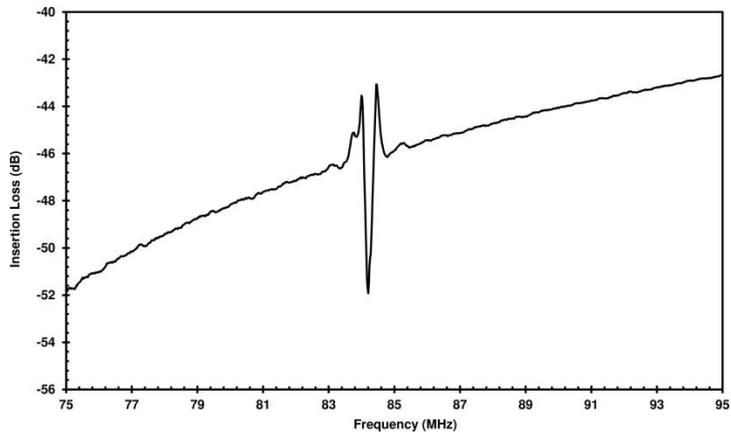

Figure C. 4 S$_{22}$ parameter plot for the SU-8/AlN/Si SAW sensor with omnicoat operating at 84MHz

183
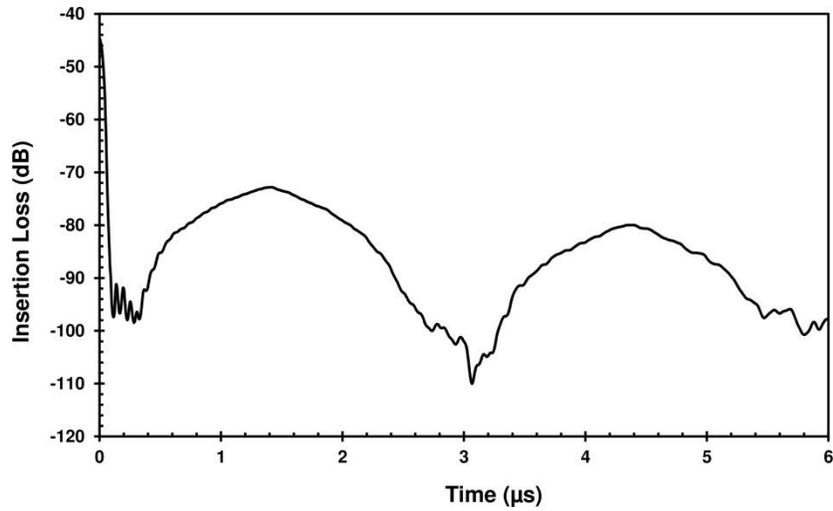
Figure C. 5 S_{21} **parameter plot in the time domain for the SU-8/AlN/Si SAW sensor with omnicoat operating at 84MHz**
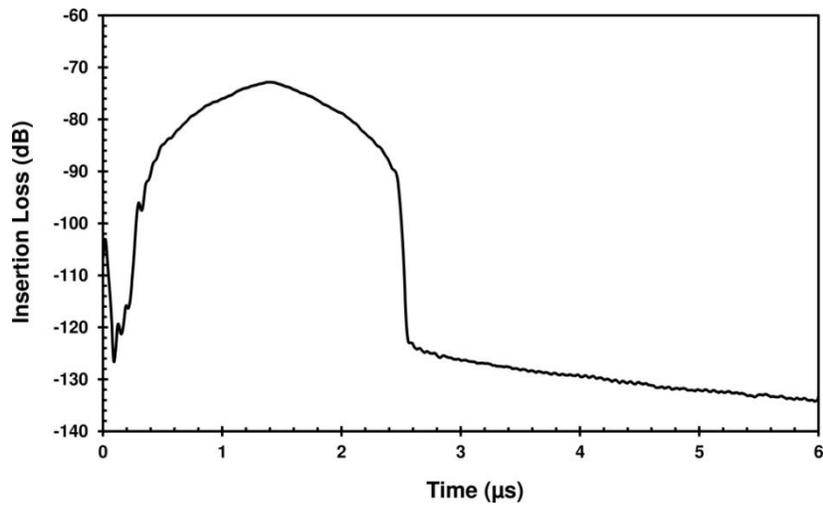
Figure C. 6 S_{21} **parameter plot with time gating for the SU-8/AlN/Si SAW sensor with omnicoat operating at 84MHz**
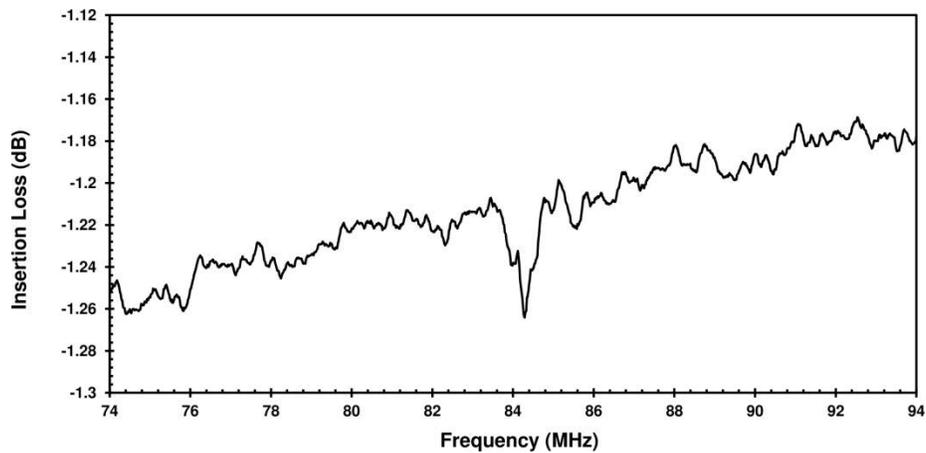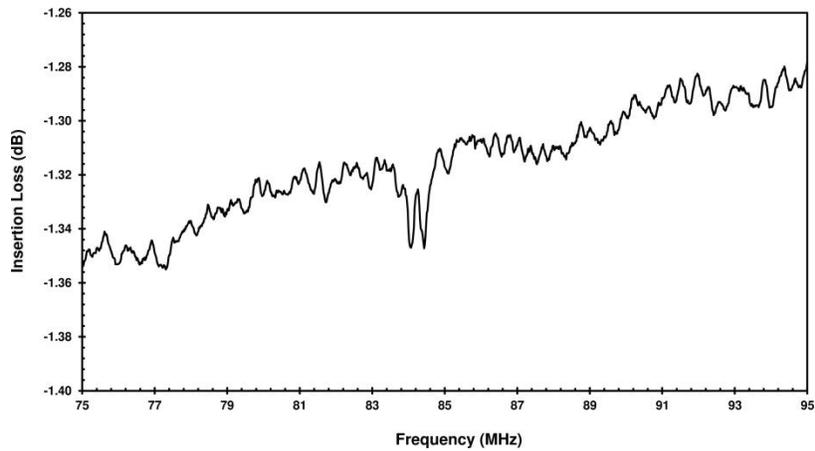

Figure C. 7 S_{11} **parameter plot for the SU-8/AlN/Si SAW sensor without omnicoat operating at 84MHz**
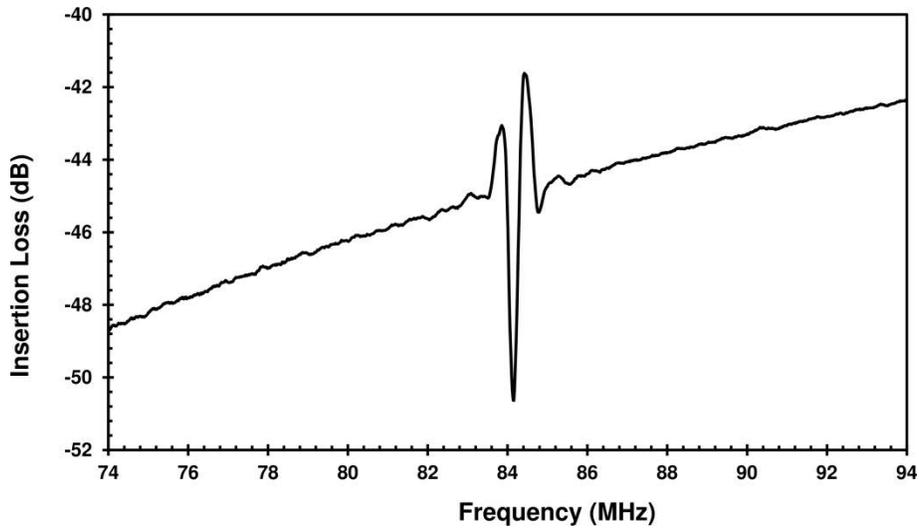
Figure C. 8 S$_{12}$ parameter plot for the SU-8/AlN/Si SAW sensor without omnicoat operating at 84MHz
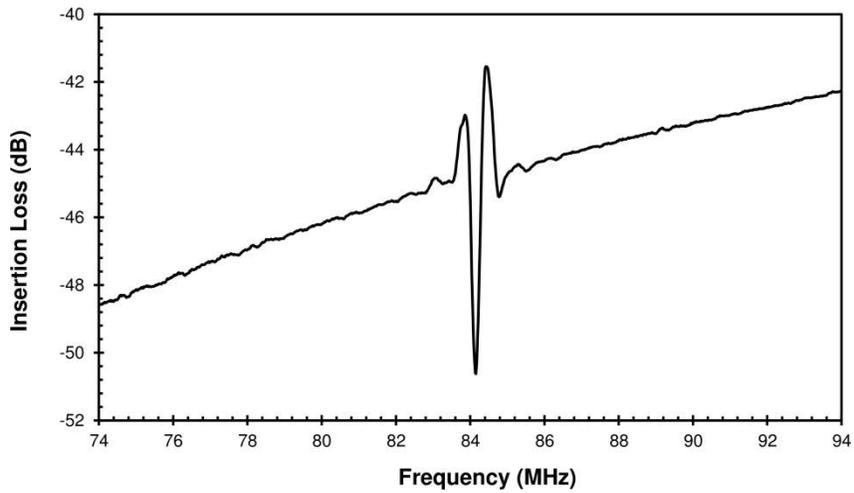
Figure C. 9 S$_{21}$ parameter plot for the SU-8/AlN/Si SAW sensor without omnicoat operating at 84MHz
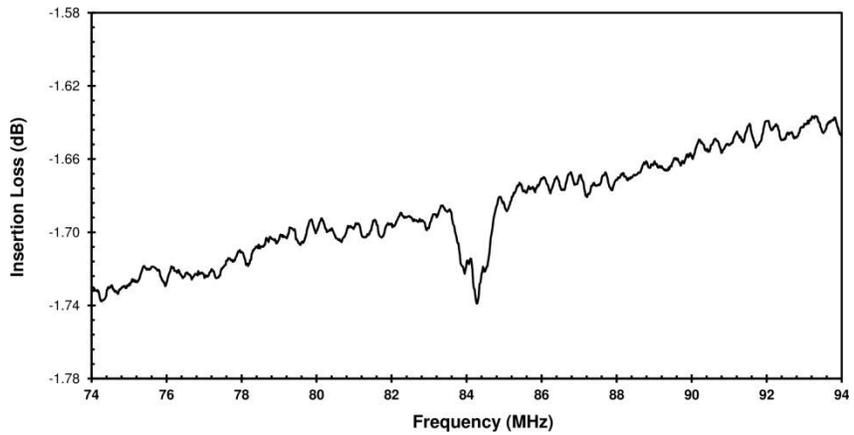
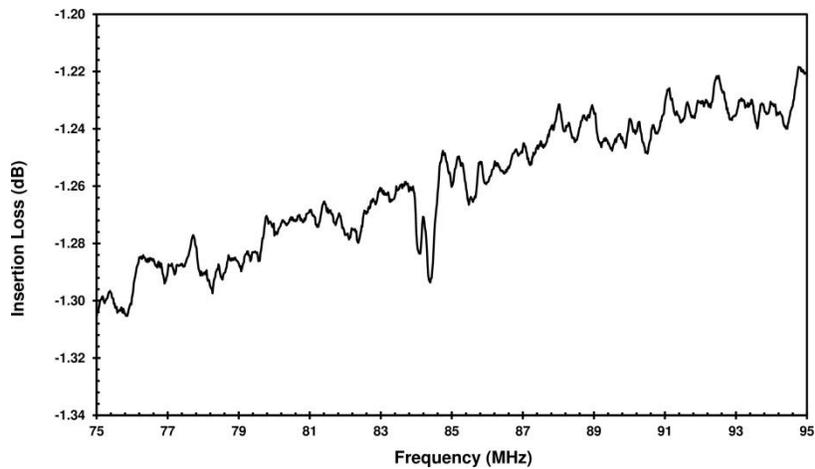**Figure C. 10 S$_{22}$ parameter plot for the SU-8/AlN/Si SAW sensor without omnicoat operating at 84MHz**
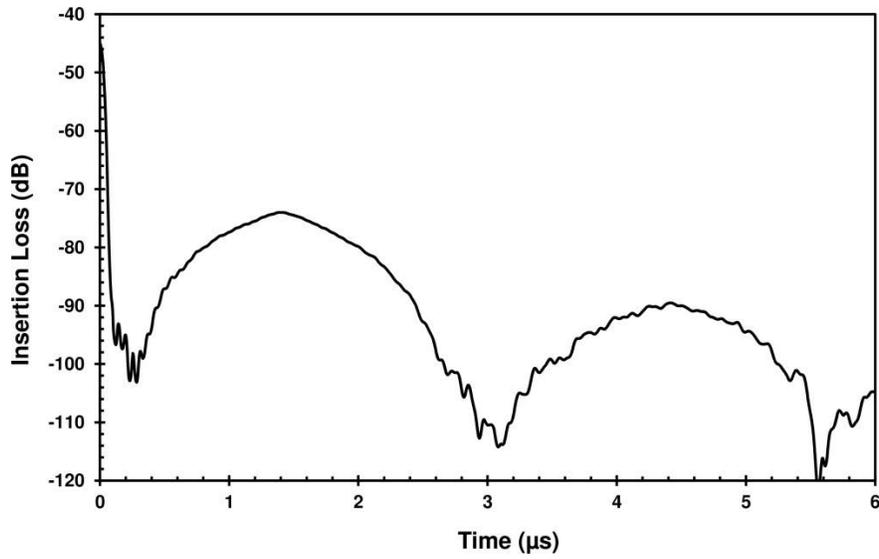
Figure C. 11 S$_{21}$ **parameter plot in the time domain for the SU-8/AlN/Si SAW sensor without omnicoat operating at 84MHz**
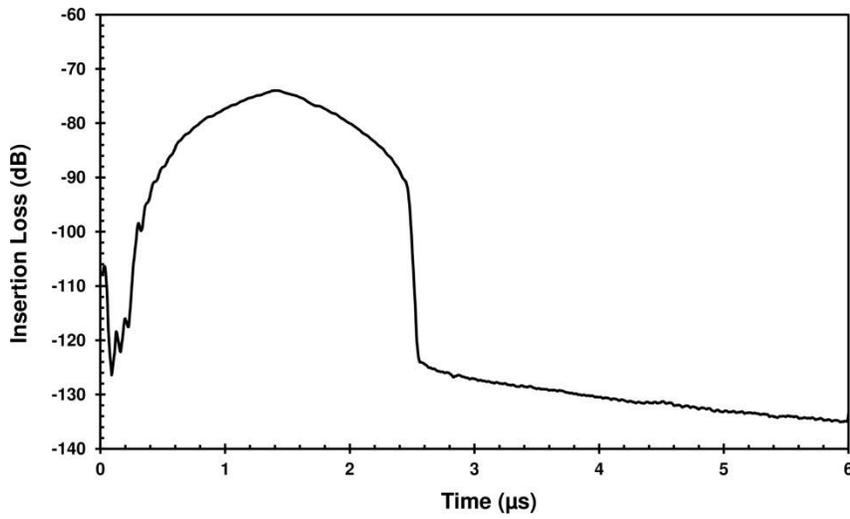
Figure C. 12 S$_{21}$ **parameter plot with time gating for the SU-8/AlN/Si SAW sensor without omnicoat operating at 84MHz**

C.2 S-Parameter plots for the SU-8 /AlN/Si SAW sensors operating at 125MHz
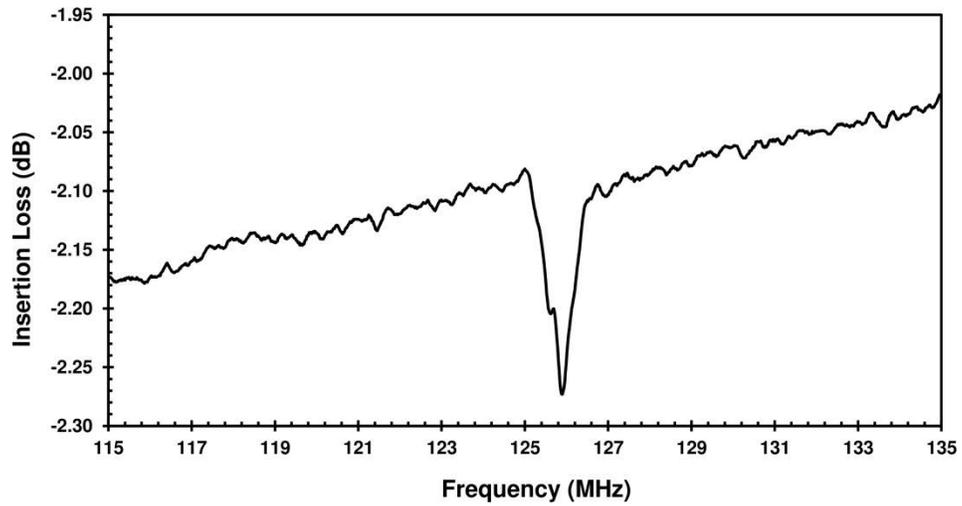
Figure C. 13 S_{11} parameter plot for the SU-8/AlN/Si SAW sensor with omnicoat operating at 125MHz
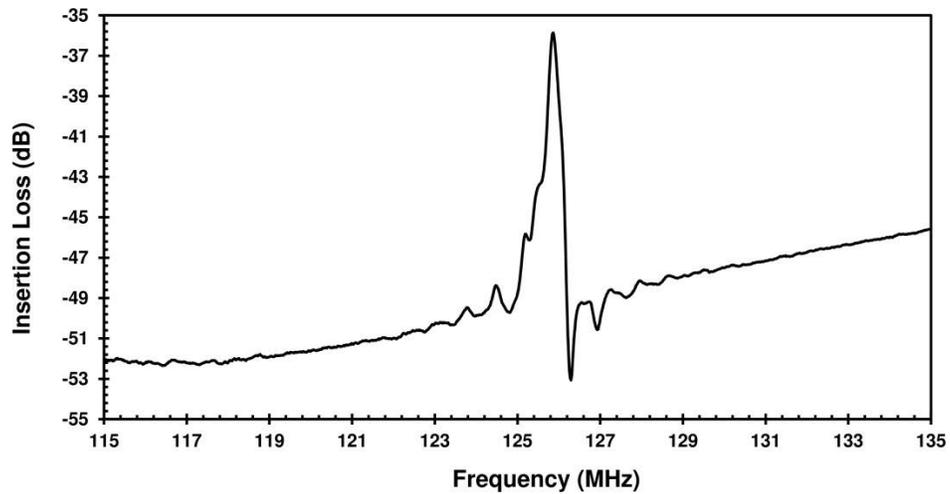
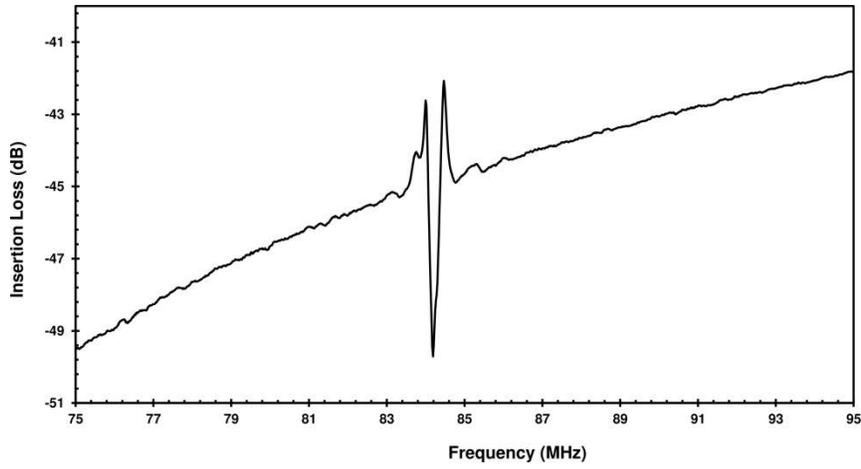**Figure C. 14 S_{12} parameter plot for the SU-8 /AlN/Si SAW sensor with omnicoat operating at 125MHz**
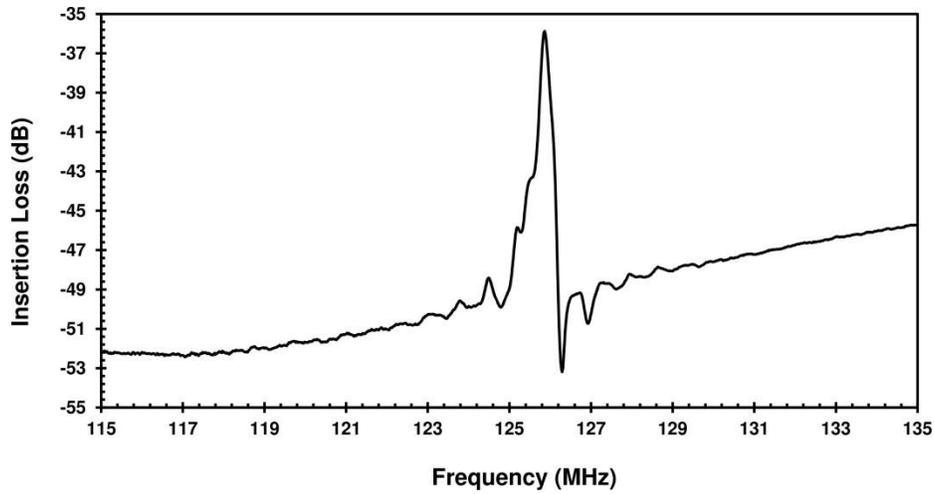
Figure C. 15 S_{21} parameter plot without time gating for the SU-8 /AlN/Si SAW sensor with omnicoat operating at 125MHz
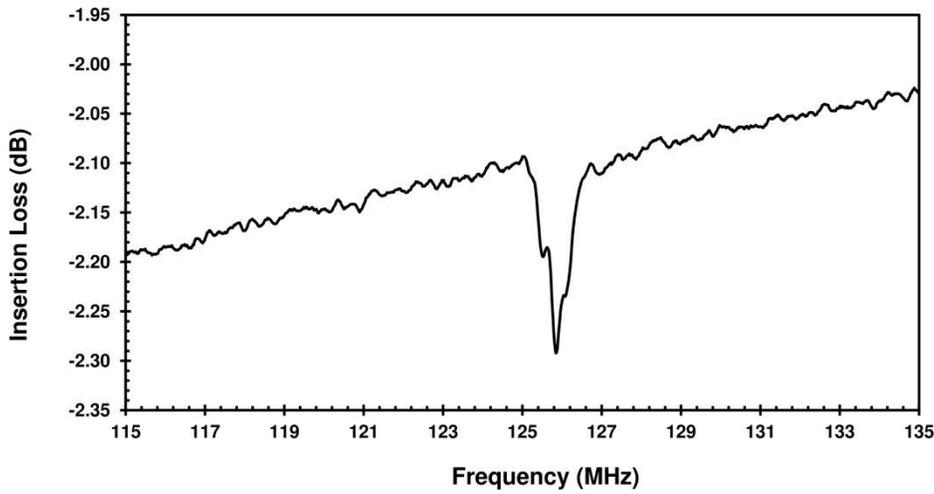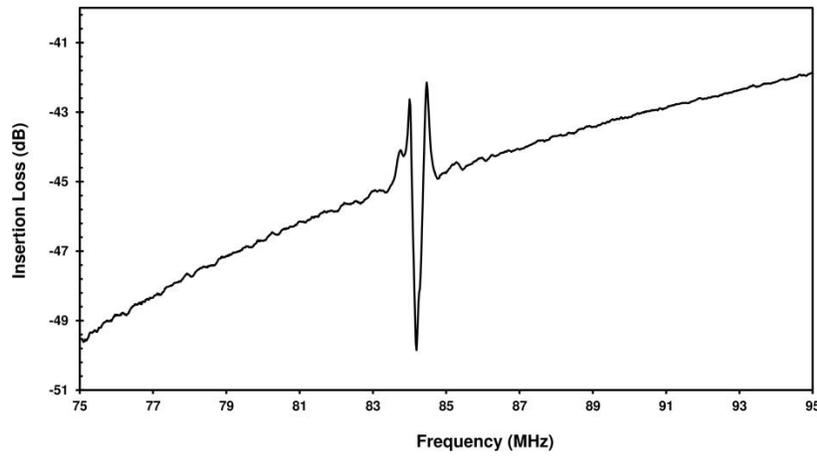

Figure C. 16 S_{22} parameter plot for the SU-8 /AlN/Si SAW sensor with omnicoat operating at 125MHz
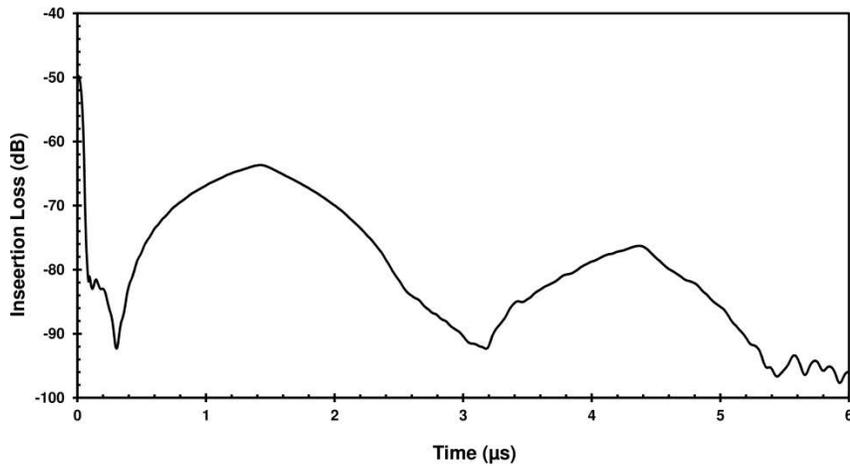
Figure C. 17 S_{21} parameter plot in the time domain for the SU-8 /AlN/Si SAW sensor with omnicoat operating at 125MHz
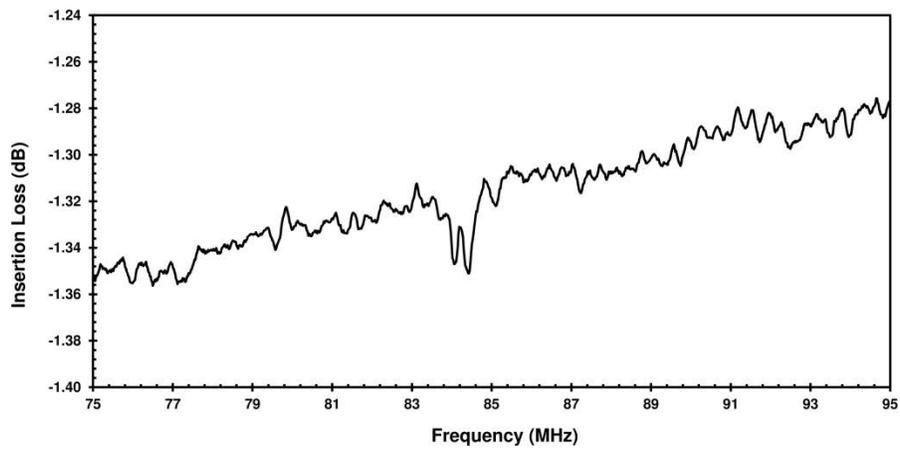
188
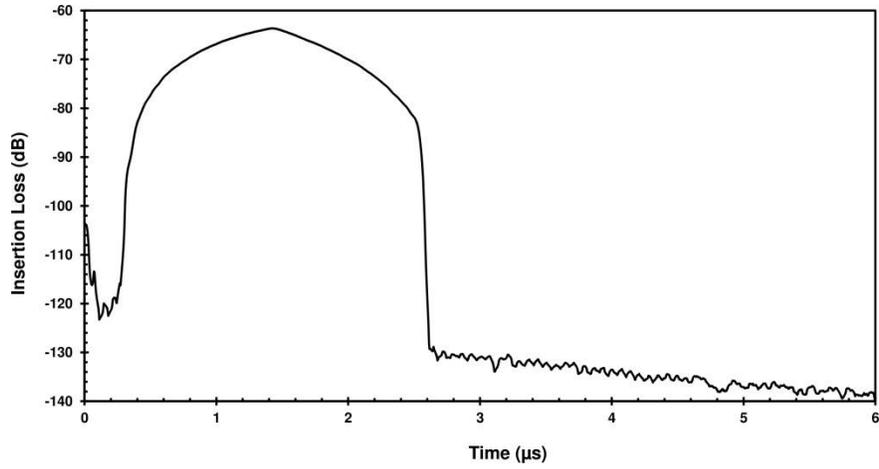
Figure C. 18 S_{21} **parameter plot with time gating for the SU-8 /AlN/Si SAW sensor with omnicoat operating at 125MHz**
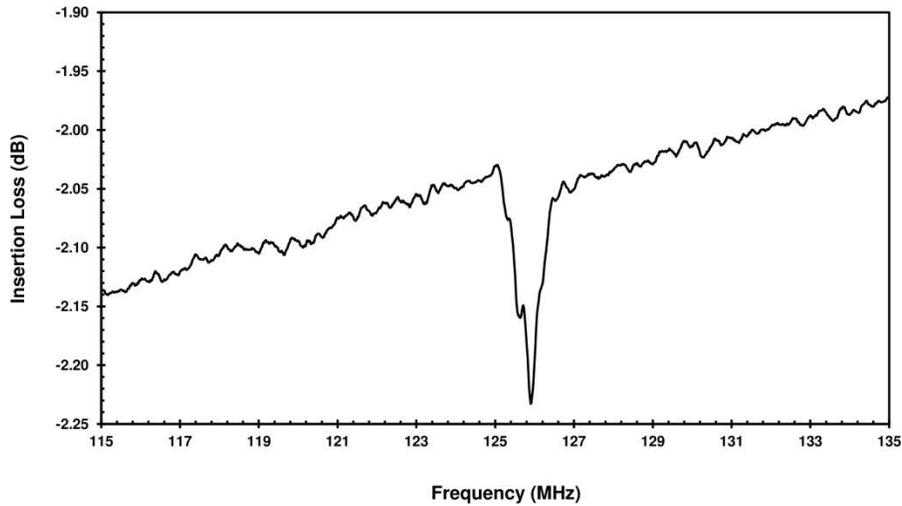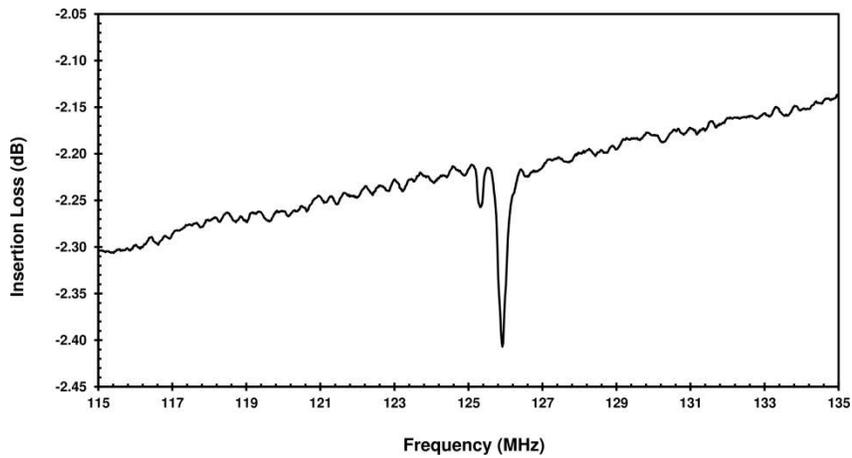

Figure C. 19 S_{11} **parameter plot for the SU-8/AlN/Si SAW sensor without omnicoat operating at 125MHz**
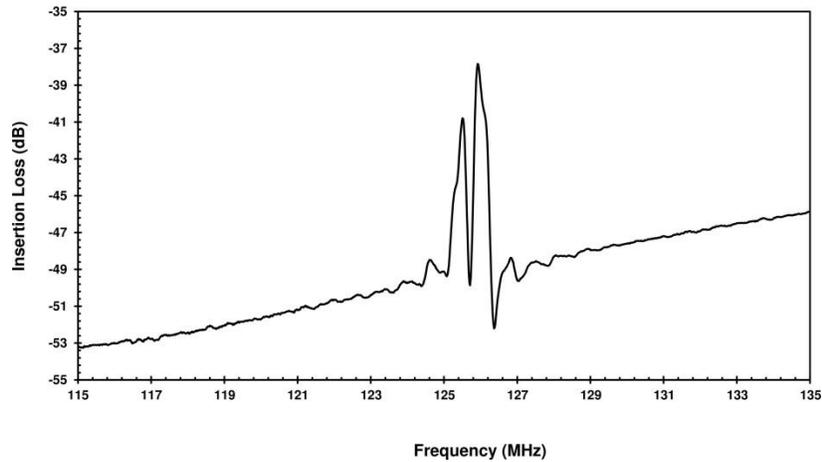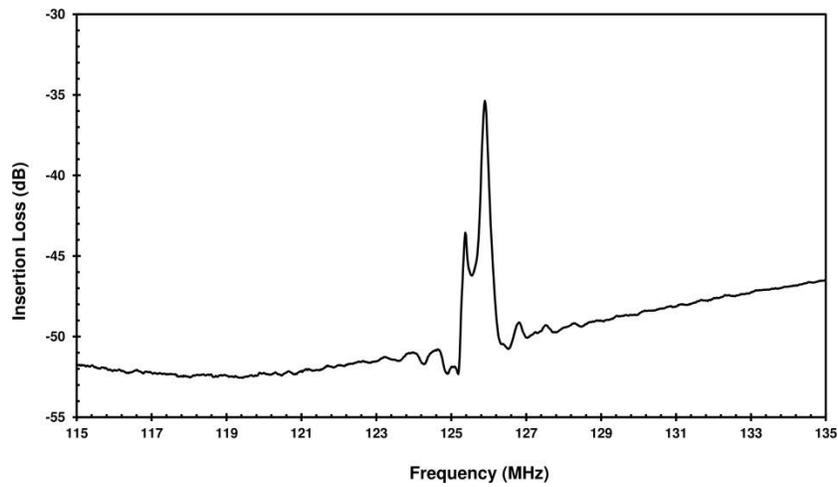

Figure C. 20 S_{12} **parameter plot without time gating for the SU-8/AlN/Si SAW sensor without omnicoat operating at 125MHz**
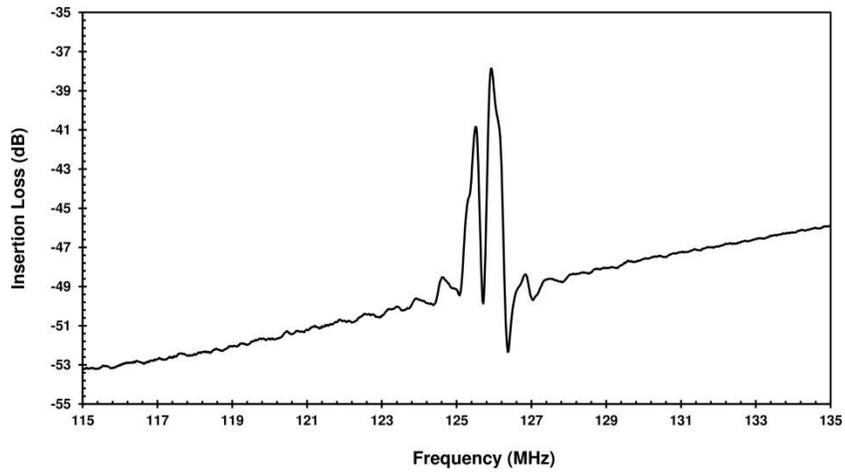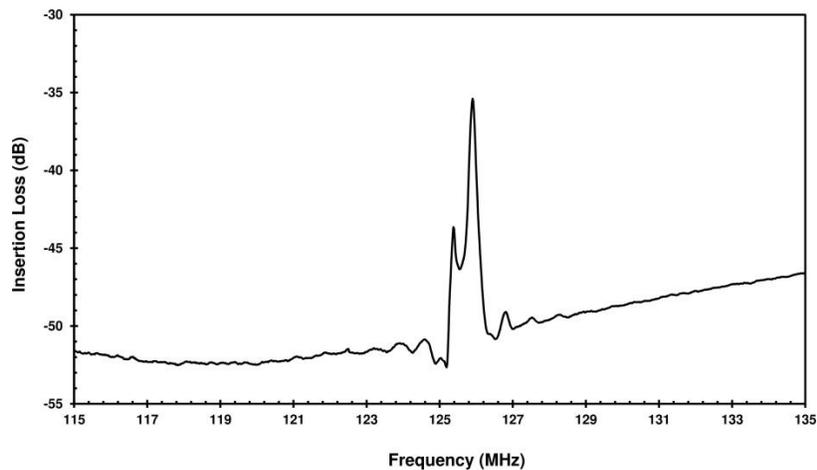
Figure C. 21 S_{21} **parameter plot without time gating for the SU-8/AlN/Si SAW sensor without omnicoat operating at 125MHz**
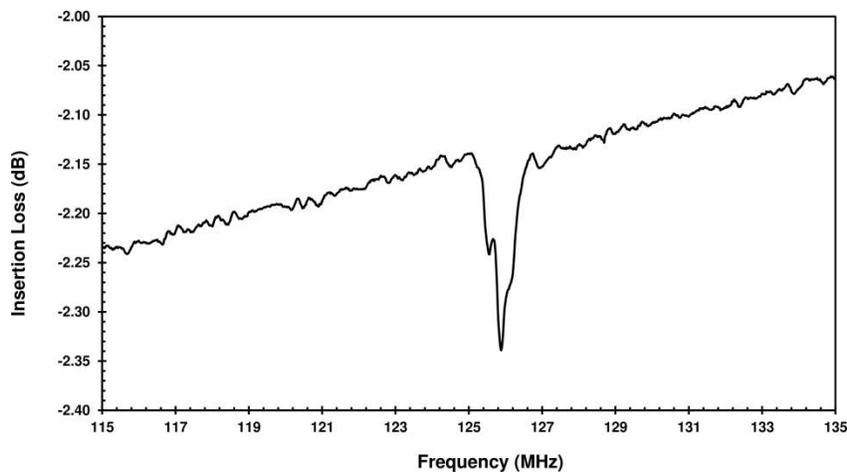
Figure C. 22 S_{22} **parameter plot for the SU-8/AlN/Si SAW sensor without omnicoat operating at 125MHz**
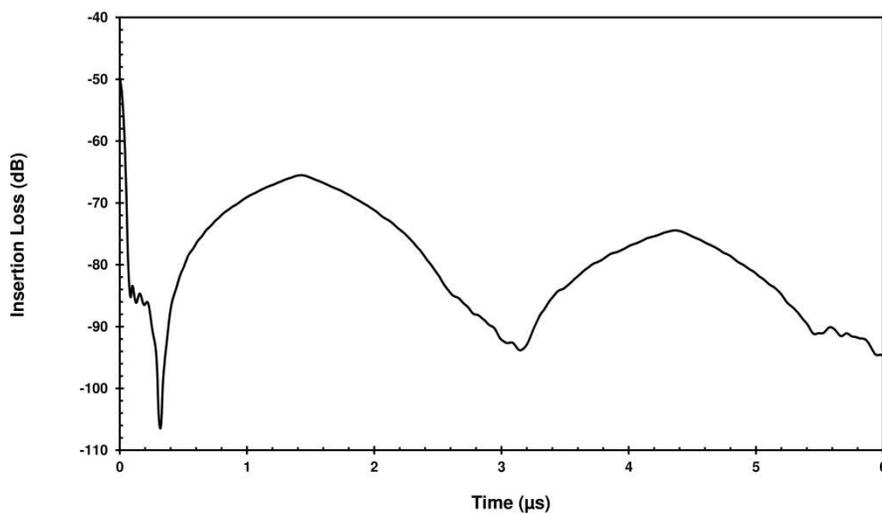
Figure C. 23 S_{21} **parameter plot in the time domain for the SU-8/AlN/Si SAW sensor without omnicoat operating at 125MHz**
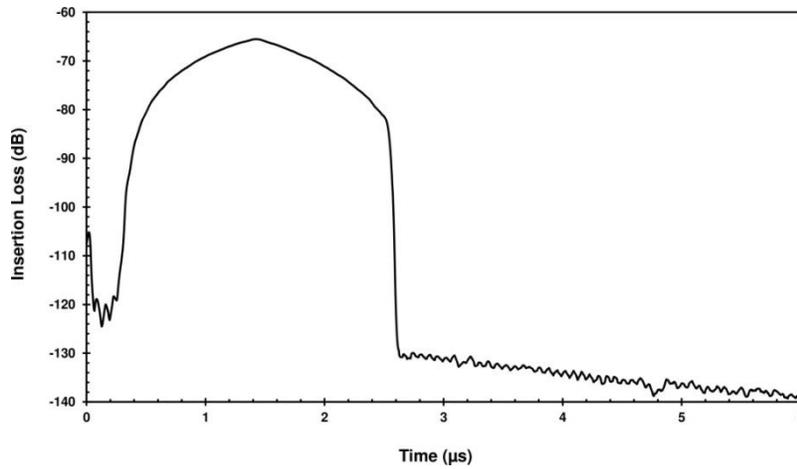
Figure C. 24 S_{21} **parameter plot with time gating for the SU-8/AlN/Si SAW sensor without omnicoat operating at 125MHz**
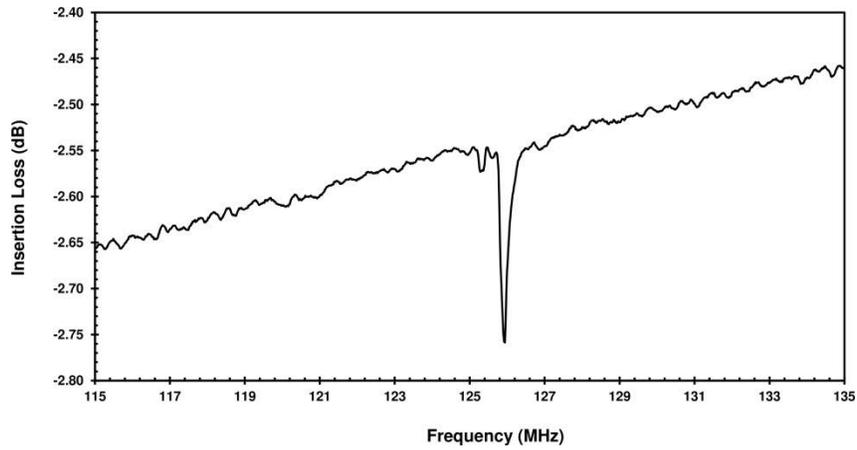
C.3 S-Parameter plots for the SU-8 /AlN/Si SAW sensors operating at 208MHz
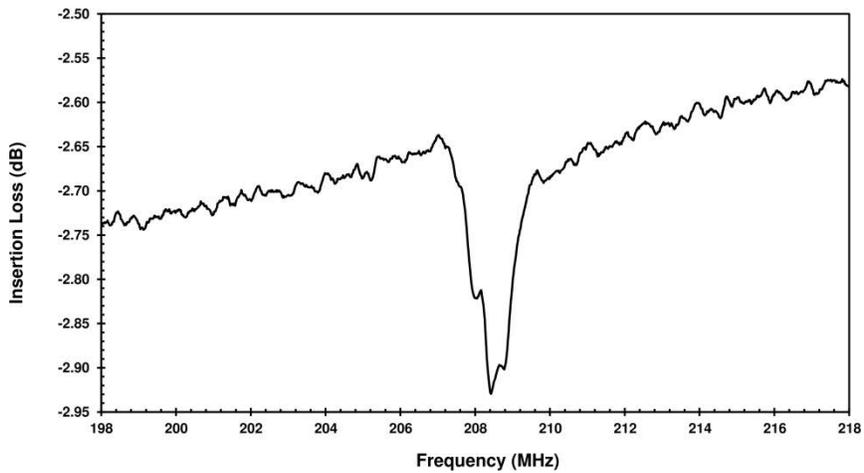
Figure C. 25 S_{11} **parameter plot for the SU-8/AlN/Si SAW sensor with omnicoat operating at 208MHz**
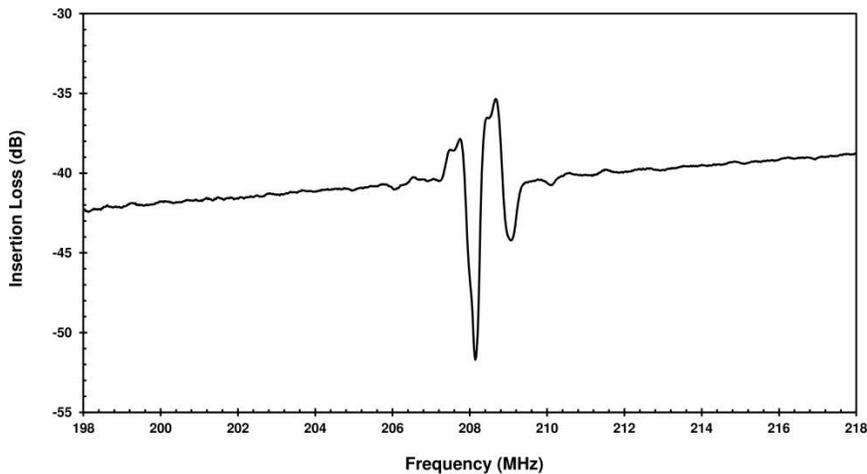
Figure C. 26 S_{12} **parameter plot without time gating for the SU-8/AlN/Si SAW sensor with omnicoat operating at 208MHz**
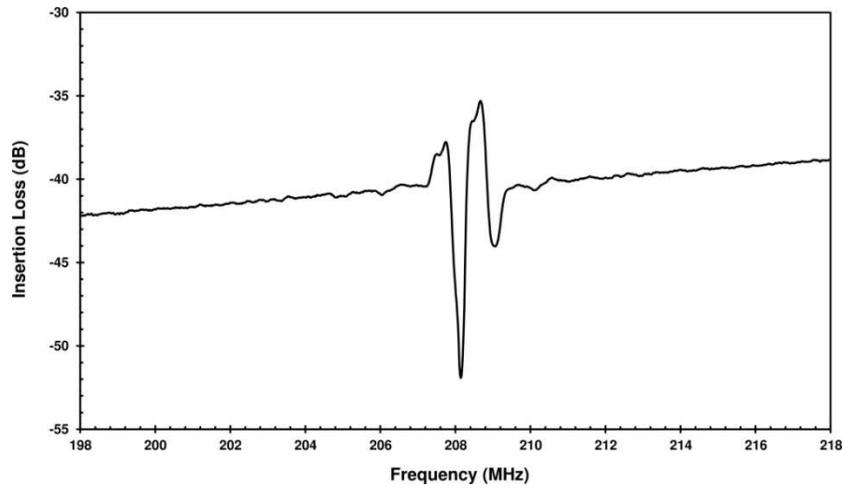
Figure C. 27   S$_{21}$ parameter plot without time gating for the SU-8/AlN/Si SAW sensor with omnicoat operating at 208MHz

Figure C. 28   S$_{22}$ parameter plot for the SU-8/AlN/Si SAW sensor with omnicoat operating at 208MHz


Figure C. 29   S$_{21}$ parameter plot in time domain for the SU-8/AlN/Si SAW sensor with omnicoat operating at 208MHz

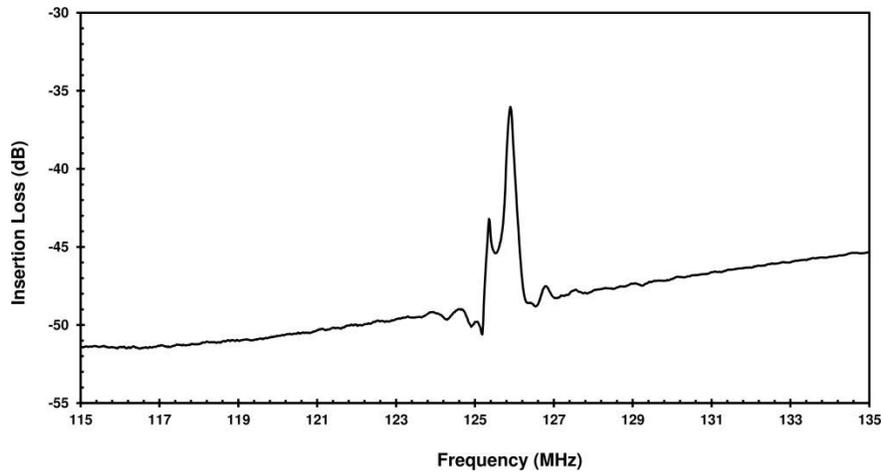**Figure C. 30** S_{21} parameter plot with time gating for the SU-8/AlN/Si SAW sensor with omnicoat operating at 208MHz

C.4 S-Parameter plots for the Au/AlN/Si SAW sensors operating at 84MHz

Figure C. 31 S_{11} parameter plot for the Au/AlN/Si SAW sensor with omnicoat operating at 84MHz

Figure C. 32 S_{12} parameter plot without time gating for the Au/AlN/Si SAW sensor with omnicoat operating at 84MHz
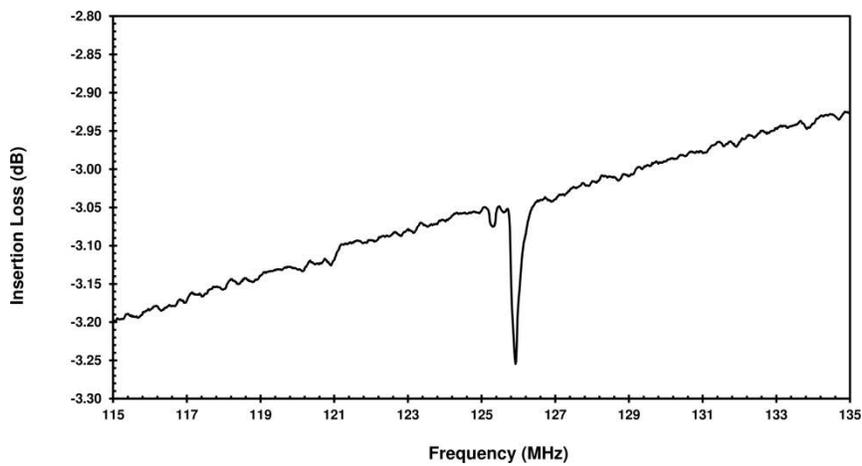
Figure C. 33 S_{21} **parameter plot without time gating for the Au/AlN/Si SAW sensor with omnicoat operating at 84MHz**

Figure C. 34 S_{22} **parameter plot for the Au/AlN/Si SAW sensor with omnicoat operating at 84MHz**

Figure C. 35 S_{11} **parameter plot for the Au/AlN/Si SAW sensor without omnicoat operating at 84MHz**

Figure C. 36 S_{12} **parameter plot without time gating for the Au/AlN/Si SAW sensor without omnicoat operating at 84MHz**

Figure C. 37 S_{21} **parameter plot without time gating for the Au/AlN/Si SAW sensor without omnicoat operating at 84MHz**

Figure C. 38 S_{22} **parameter plot for the Au/AlN/Si SAW sensor without omnicoat operating at 84MHz**

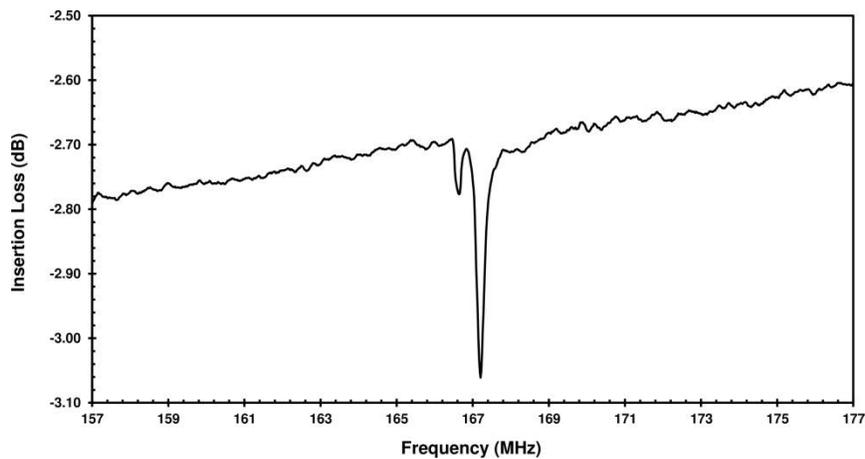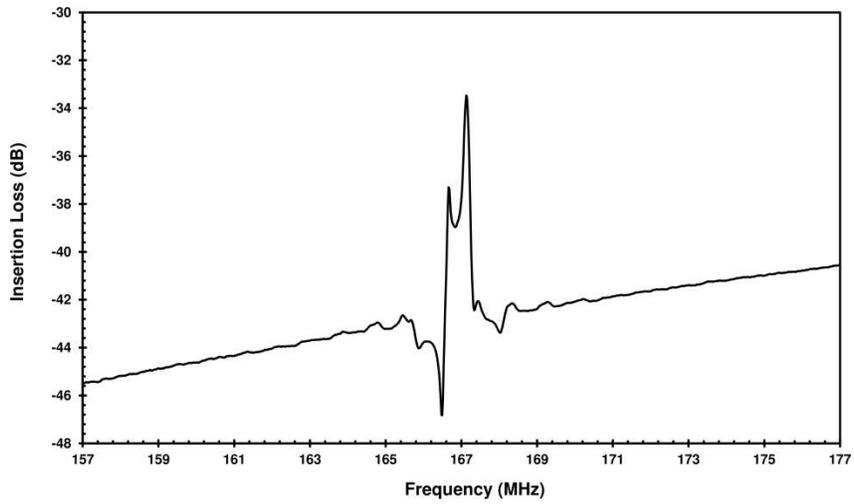## C.5 S-Parameter plots for the Au/AlN/Si SAW sensors operating at 208MHz

Figure C. 39   S$_{11}$ parameter plot for the Au/AlN/Si SAW sensor with omnicoat operating at 125MHz

Figure C. 40   S$_{12}$ parameter plot without time gating for the Au/AlN/Si SAW sensor with omnicoat operating at 125MHz
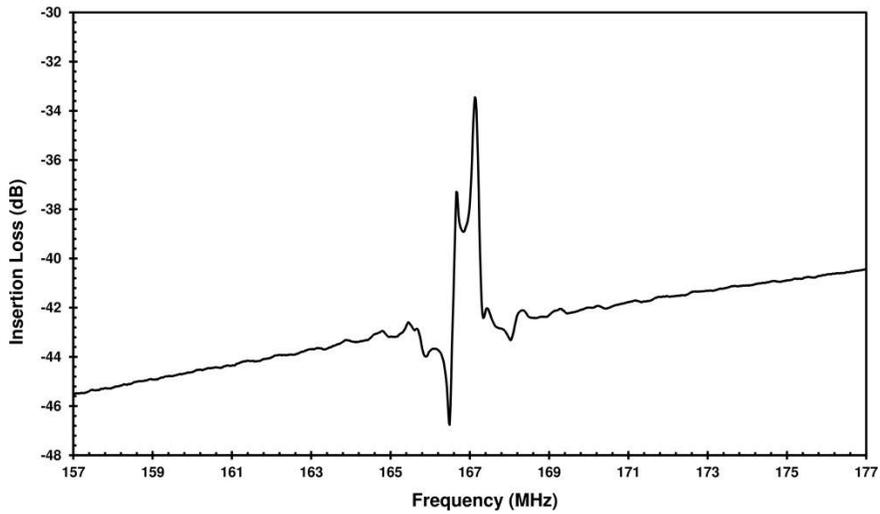

Figure C. 41   S$_{21}$ parameter plot without time gating for the Au/AlN/Si SAW sensor with omnicoat operating at 125MHz
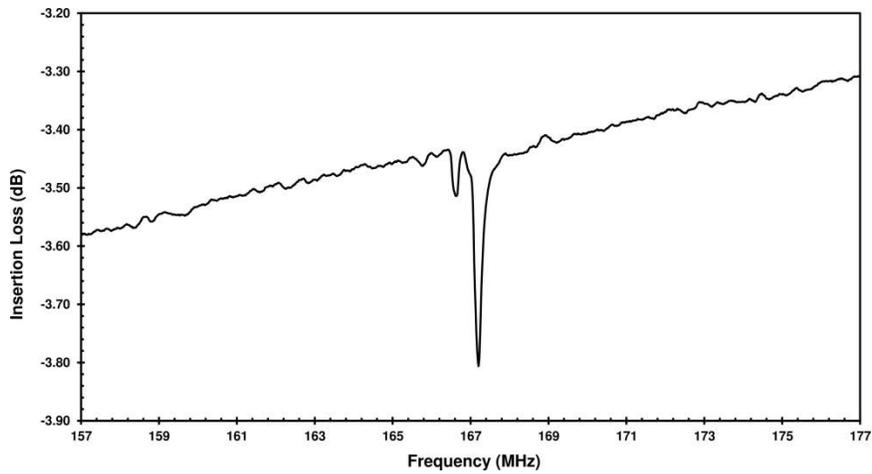
Figure C. 42 S$_{22}$ parameter plot for the Au/AlN/Si SAW sensor with omnicoat operating at 125MHz
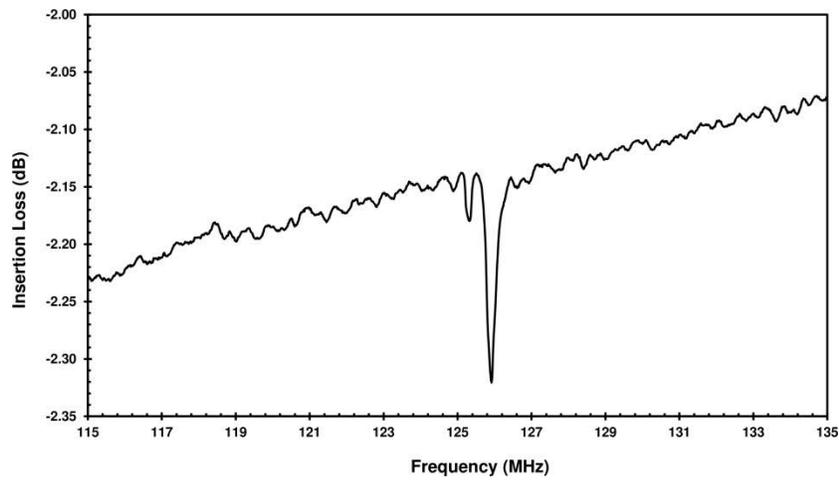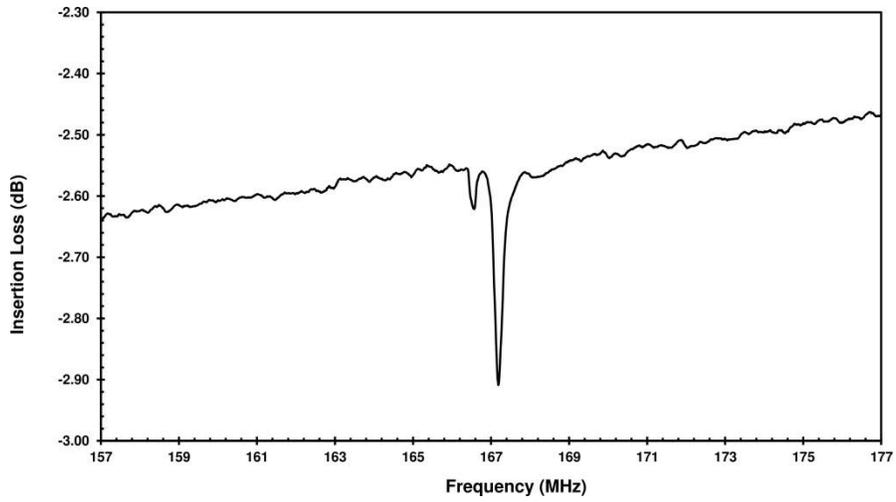

Figure C. 43 S$_{11}$ parameter plot for the Au/AlN/Si SAW sensor without omnicoat operating at 125MHz
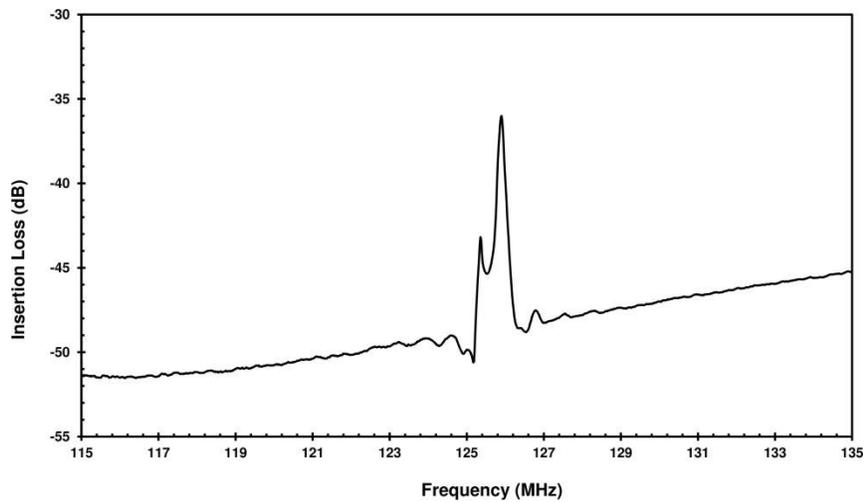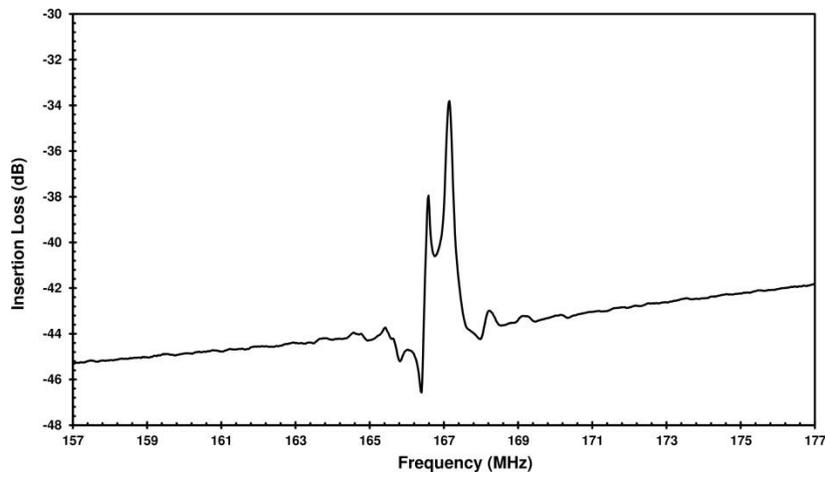

Figure C. 44 S$_{12}$ parameter plot without time gating for the Au/AlN/Si SAW sensor without omnicoat operating at 125MHz
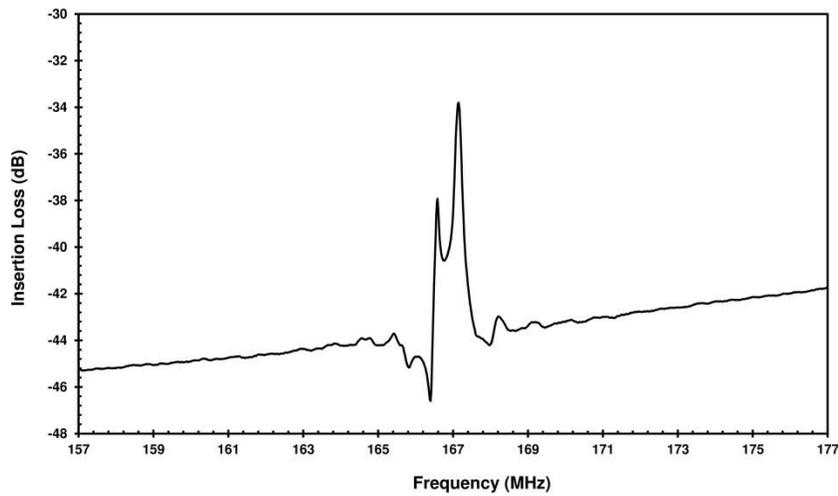
Figure C. 45 S_{21} **parameter plot without time gating for the Au/AlN/Si SAW sensor without omnicoat operating at 125MHz**

Figure C. 46 S_{22} **parameter plot for the Au/AlN/Si SAW sensor without omnicoat operating at 125MHz**

C.6 S-Parameter plots for the Au/AlN/Si SAW sensors operating at 167MHz

Figure C. 47 S_{11} **parameter plot for the Au/AlN/Si SAW sensor with omnicoat operating at 167MHz**

Figure C. 48 S_{12} **parameter plot without time gating for the Au/AlN/Si SAW sensor with omnicoat operating at 167MHz**

Figure C. 49 S_{21} **parameter plot without time gating for the Au/AlN/Si SAW sensor with omnicoat operating at 167MHz**
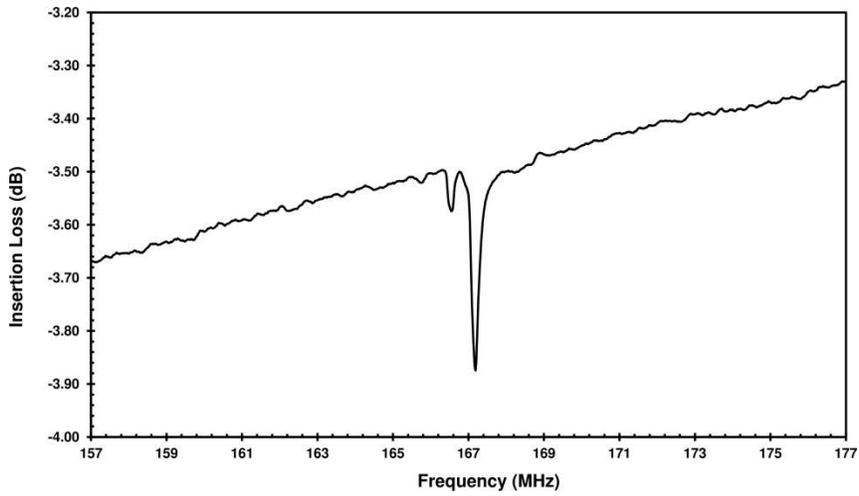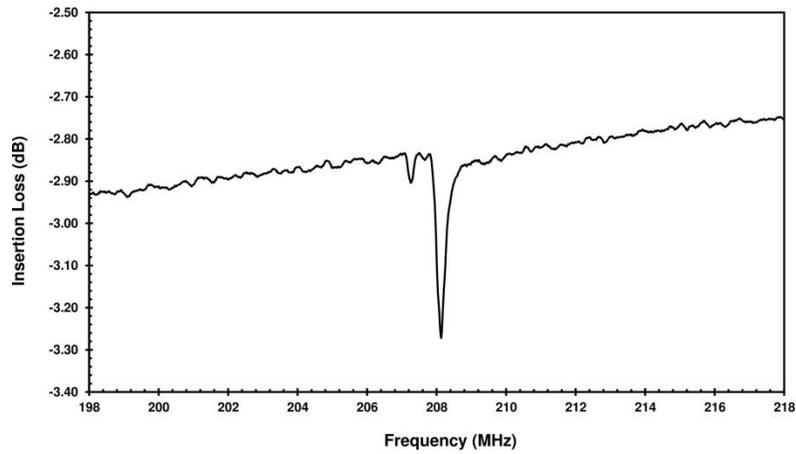

Figure C. 50 S_{22} **parameter plot for the Au/AlN/Si SAW sensor with omnicoat operating at 167MHz**

Figure C. 51 S_{11} parameter plot for the Au/AlN/Si SAW sensor without omnicoat operating at 167MHz

Figure C. 52 S_{12} parameter plot without time gating for the Au/AlN/Si SAW sensor without omnicoat operating at 167MHz

Figure C. 53 S_{21} parameter plot without time gating for the Au/AlN/Si SAW sensor without omnicoat operating at 167MHz

Figure C. 54   S$_{22}$ parameter plot for the Au/AlN/Si SAW sensor without omnicoat operating at 167MHz

C.7 S-Parameter plots for the Au/AlN/Si SAW sensors operating at 208MHz

Figure C. 55   S$_{11}$ parameter plot for the Au/AlN/Si SAW sensor with omnicoat operating at 208MHz
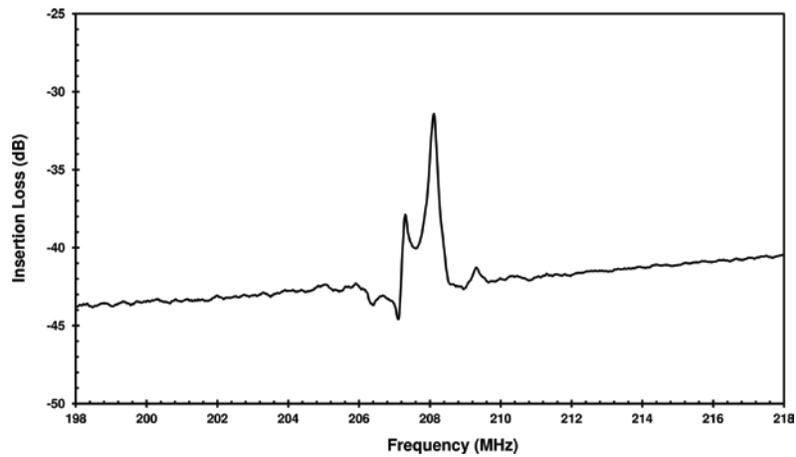

Figure C. 56   S$_{12}$ parameter plot without time gating for the Au/AlN/Si SAW sensor with omnicoat operating at 208MHz
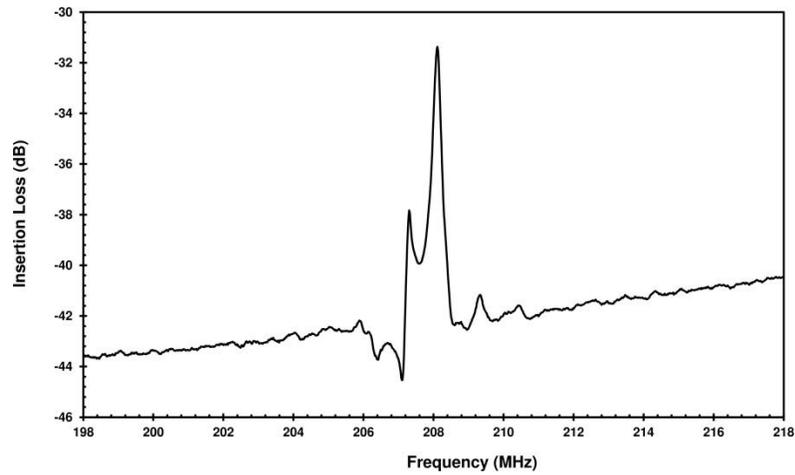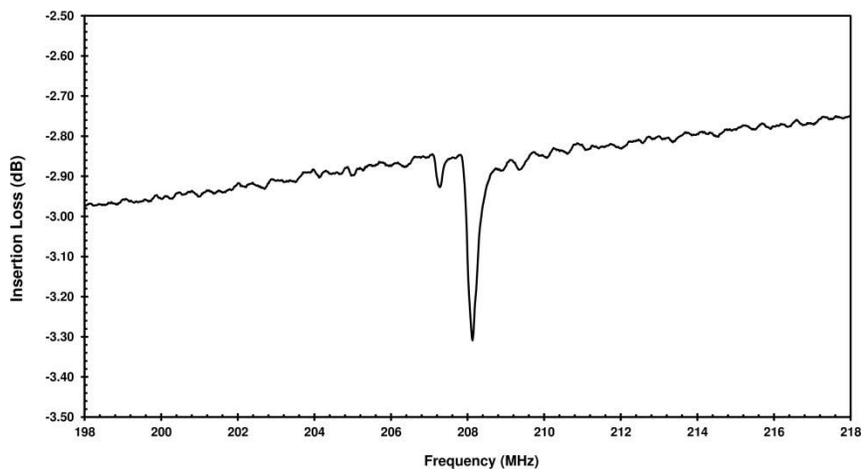
Figure C. 57 S$_{21}$ parameter plot without time gating for the Au/AlN/Si SAW sensor with omnicoat operating at 208MHz

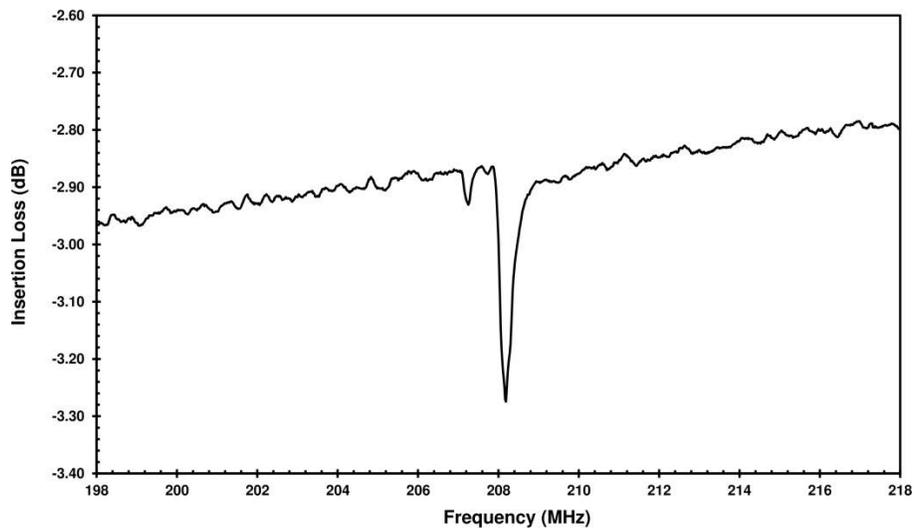**Figure C. 58** S$_{22}$ parameter plot for the Au/AlN/Si SAW sensor with omnicoat operating at 208MHz

Figure C. 59 S$_{11}$ parameter plot for the Au/AlN/Si SAW sensor without omnicoat operating at 208MHz
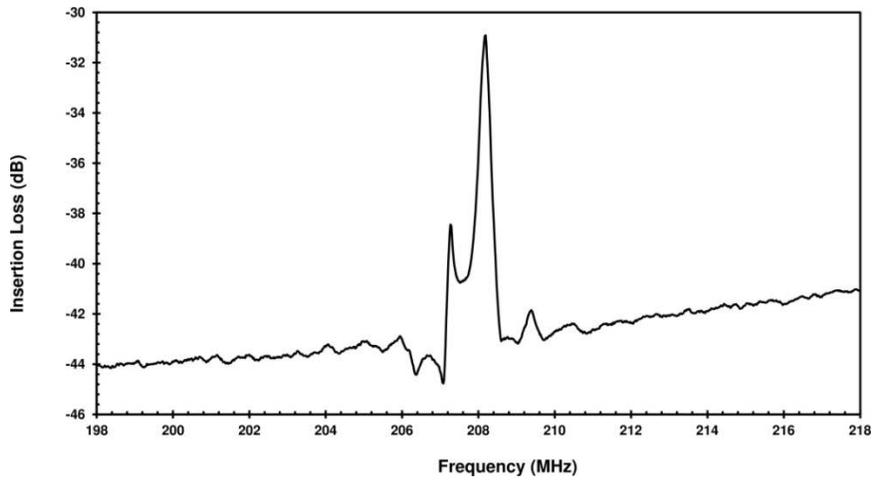
202

Figure C. 60   S$_{12}$ parameter plot without time gating for the Au/AlN/Si SAW sensor without omnicoat operating at 208MHz
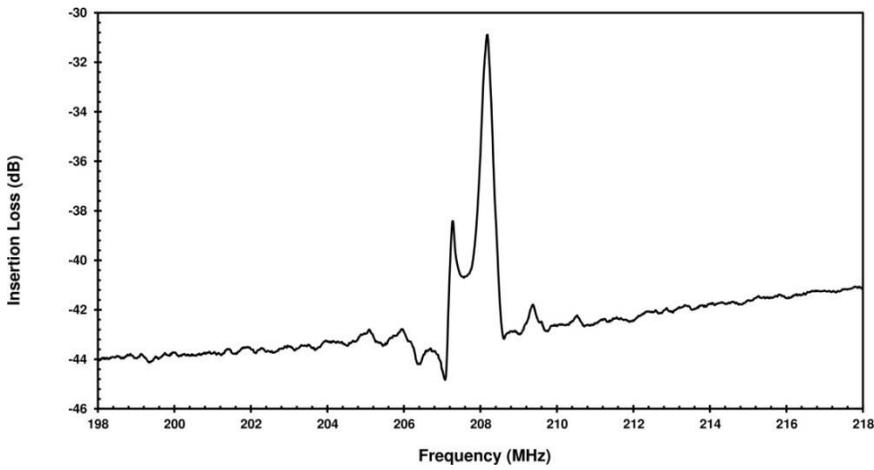

Figure C. 61   S$_{21}$ parameter plot without time gating for the Au/AlN/Si SAW sensor without omnicoat operating at 208MHz
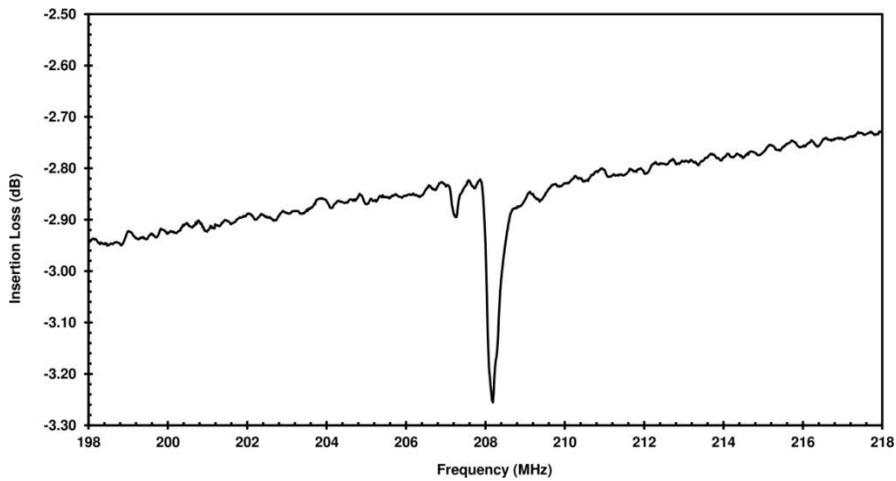

Figure C. 62   S$_{22}$ parameter plot for the Au/AlN/Si SAW sensor without omnicoat operating at 208MHz

APPENDIX D: EXPERIMENTAL MEASUREMENTS

This section details the procedures for the experiemental measurements. The experimental setup for conductig the frequency response measurements are explained in Chapter 5, which explains the cables and adapters used to connect the SAW sensors with the network analyzer. Figure 5-8 illustrates the schematic for the experimental setup adopted in this study and Figure 5-9 illustrates setup while conductig the frequency response measurement for one of the sensors. Upon connecting the SAW senosrs to the network analyzer the parameters used for the frequency response measurements are:

- Signal Power set to -10dBm.
- Apply a frequency sweep:
  - For the 84MHz sensor: 74-94MHz
  - For the 125MHz sensor: 116-136MHz
  - For the 167MHz sensor: 157-167MHz
  - For the 208MHz sensor: 198-218MHz
- The four scattering parameters of the sensors are recorded on the four channels.
- The S_{21} parameter is converted to the time domain.
- The time domain is plotted in the range of 0-6μs.
- A time gate is applied with the following parameters:
  - For the 84MHz sensor: Center: 1.392μs   Span: 2.2173μs
  - For the 125MHz sensor: Center: 1.4347μs   Span: 2.244μs
  - For the 167MHz sensor: Center: 1.136μs   Span: 1.833μs
  - For the 208MHz sensor: Center: 0.98133μs   Span: 1.2733μs
- The time domain response of the S_{21} parameter is converted to the frequency domain
- The center frequency value is determined by the network analyzer
- The same process is repeated for the S_{12} parameter

APPENDIX E: SAW SENSOR DESIGN PARAMETERS

This section discusses the design of the interdigital (IDT) electrodes of the SAW sensor. The parameters of interest are illustrated in Figure E. 1. The objective in designing the IDT parameters is to set the impedance of the IDT structure to 50 Ω. The impedance of the vector network analyzer is set to 50 Ω; therefore it is desired to match the impedance for maximum power transfer.
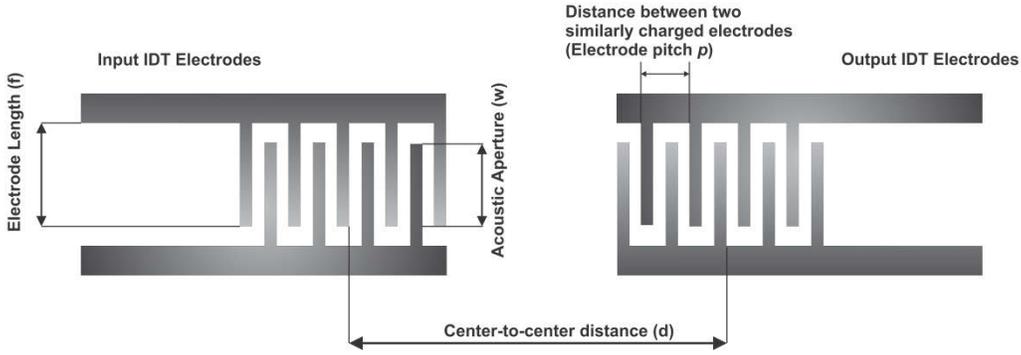

Figure E. 1: Parameters of the interdigital electodes (IDT) for the surface acoustic wave sensor

For each IDT the acoustic aperture (electrode overlap) w and the number of electrode pairs N_p are designed for impedance matching. Wilson and Atkinson [154] derive a relation where the acoustic aperture is dependent on the input resistance;

$$w = \frac{1}{R_{in}} \left(\frac{1}{2f \, C_s \, N_p} \right) \frac{4k^2 N_p}{\left(4k^2 N_p \right)^2 + \pi^2} \tag{E.1}$$

where R_{in} is the input impedance, f is the operating frequency, C_s is the capacitance per finger pair per unit length and k^2 is the electromechancial coupling coefficient. The capacitance per finger pair per unit length is calculated using [155]:

$$\varepsilon_f = \varepsilon_s + \left[\frac{C_s - \left(K(1+\varepsilon_s) \right)}{K \left(1 - \exp\left(\frac{-9.2h_{AlN}}{\lambda} \right) \right)} \right] \tag{E.2}$$

where ε_f and ε_s are the film and substrate dielectric constants, respectively, h_{AlN} is the film thickness and K is a constant that has a value of 4.535pF [155]: Using equations (E.1) and (E.2) the IDT design parameters in for the SAW sensors have been calculated.

Table E. 1: IDT design parameters for the SAW sensors

Design Parameters	Design 1	Design 2	Design 3	Design 4
Operating frequency (MHz)	84	125	167	208
Wavelength (λ) (μm)	60	40	30	24
Number of electrode pairs	100	150	150	150
Electrode length (f) (μm)	5,363	1,595	1,230	1,012
Acoustic aperture (w) ($x\lambda$)	90	40	41	42
Center-to-Center distance (d) (μm)	6,985	6,990	5,492	4,594
Sensor Length (L) (mm)	15.75	14.96	11.565	9.528
Normalized Film Thickness (h_{AlN}/λ)	0.01833	0.0275	0.03667	0.04583

A constant separation distance of 1mm was maintained between the input and output interdigital electrodes for all designs. The lengths of the gold and SU-8 films were equivalent to the acoustic aperture for each design and their widths were set to 0.72mm along the wave propagation direction. Figure E. 3 illustrates a substrate with the fabricated sensors and the four SAW sensor designs in Table E. 1 are highlighted. In addition, the thin films patterned on the surface of the SAW sensors for the two configurations adopted for each design are illustrated in Figure E. 3 with their corresponding thicknesses.
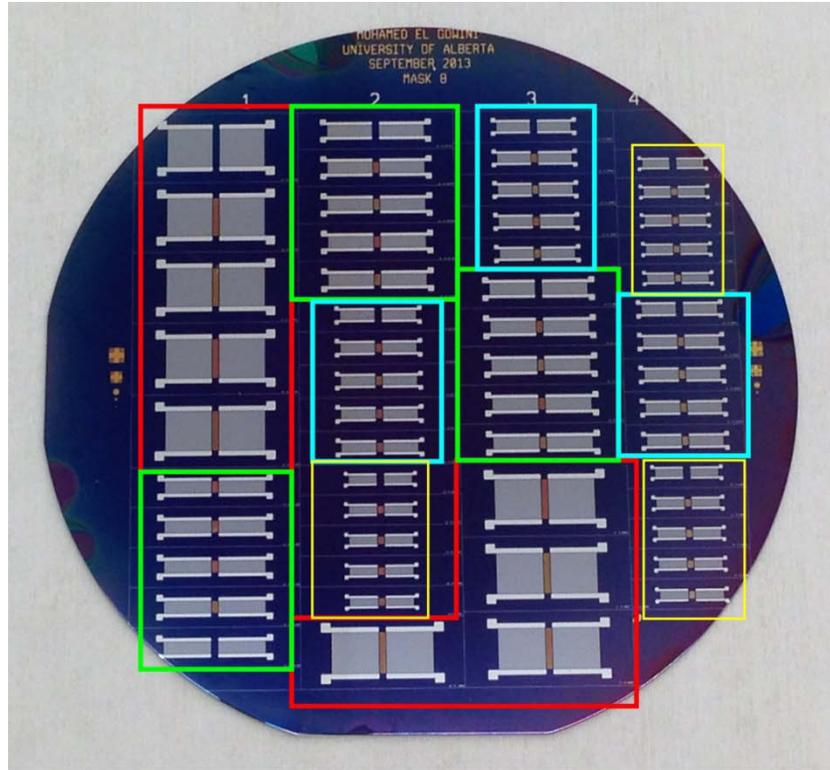
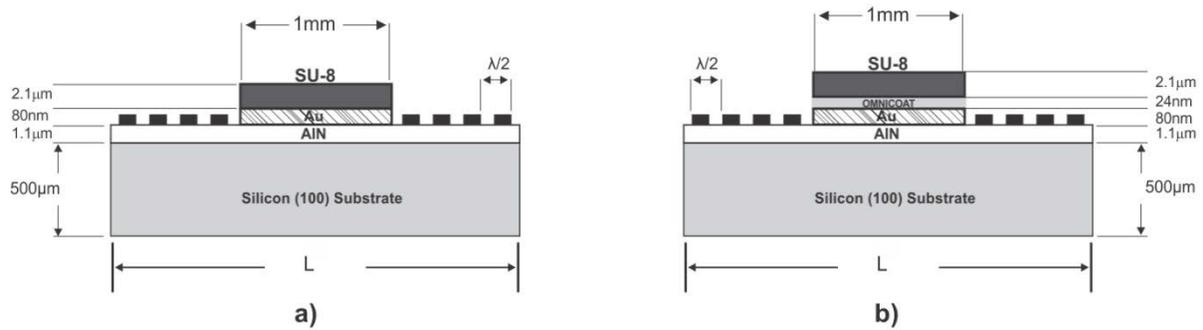**Figure E. 2: A substrate illustrating the fabricated SAW sensors with the four SAW sensor designs highlighted**

Figure E. 3: Schematic illustration of both sensor configurations with the dimension indicated (dimensions not to scale). The dimensions λ and L differ for each of the four designs and are listed in Table E.1. a) Sensor configuration without omnicoat. b) Sensor configuration with omnicoat.